From the Cosmic Web to the Bar: The Multiscale Drivers of Galaxy Spin Evolution

Tomas Hamish Rutherford

A thesis submitted in fulfilment of the requirements for the degree of

Doctor of Philosophy (PhD)

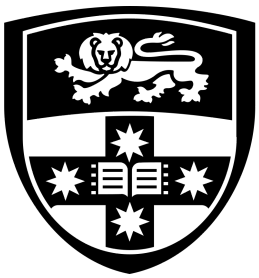

THE UNIVERSITY OF SYDNEY

Supervisors:
Prof. Scott Croom, Dr Jesse van de Sande

The University of Sydney
Faculty of Science
School of Physics

This research has been conducted with the support of an Australian Government Research Training Program Scholarship.

May 2026

Declaration

This is to certify that to the best of my knowledge, the content of this thesis is my own work. This thesis has not been submitted for any degree or other purposes.

GPT-5 was used for a small amount of grammatical editing, including spelling corrections and minor sentence restructuring. Where text was modified by generative AI, the content was reviewed for possible errors, inaccuracies, and biases. This usage was in accordance with University guidelines and policies.

I certify that the intellectual content of this thesis is the product of my own work and that all the assistance received in preparing this thesis and sources have been acknowledged.

Tomas Hamish Rutherford

May 20, 2026

This is one corner of one country, in one continent, on one planet that's a corner of a galaxy that's a corner of a universe that is forever growing and shrinking and creating and destroying and never remaining the same for a single millisecond. And there is so much, so much to see.

—The Eleventh Doctor

Abstract

The assembly and evolution of angular momentum in galaxies under the ΛCDM paradigm is shaped by a combination of internal and external processes. The development of integral field spectroscopy has revolutionised our ability to study spatially resolved galaxy properties across thousands of systems spanning a diverse range of masses, environments, and morphologies. In particular, measurements of stellar kinematics have revealed a vast array of dynamical structures and correlations with various global properties, raising questions about the specific evolutionary pathways of galaxy angular momentum. In this thesis, we investigate the physical drivers of galaxy spin evolution by combining the statistical power of the SAMI Galaxy Survey with the high spatial resolution of the GECKOS-MUSE Survey. We begin at the largest scales, using marked correlation functions to find an anti-correlation of λ_{R_e} with environment, where galaxies with low λ_{R_e} values are preferentially located in denser regions. We further show that neither stellar mass nor the slow rotator population alone can explain this relation, and that our results agree with mock observations from the cosmological EAGLE simulations.

Turning to individual galaxies, we examine how mergers drive spin-down and the formation of slow rotators. From deep HSC images of massive ($\log_{10}(M_*/M_\odot)$>10) early-type SAMI galaxies, we identify low surface brightness tidal features, classifying them as shells or streams. Although the full sample shows no spin difference, younger galaxies with shells exhibit lower spin and higher slow rotator fractions. We conclude that radial major mergers are the primary driver of spin-down in young early-type SAMI galaxies, with the lack of shells in older systems reflecting early Universe mergers whose shells have since faded.

In order to further link internal dynamics, age, and merger history, we derive orbital distributions for a subsample of SAMI early-types, using orbit-superposition Schwarzschild dynamical models. We find that the orbital fractions correlate strongly with λ_{R_e}, with the strongest relation arising from the merger-generated hot + counter-rotating fraction. Controlling for stellar mass and environment, hot and cold orbits correlate with stellar age, while warm orbits do not. We also find that the lower λ_{R_e} values in young shell galaxies arises from an excess of hot and a deficit of cold orbits, implying stars transition directly from cold to hot orbits. These results indicate that merger-driven heating dominates the spin-down of massive galaxies, rather than secular processes.

We next extend this to Milky-Way like disc-dominated late-types, where interactions may instead trigger bars that redistribute angular momentum internally. We use GECKOS-MUSE observations of seven edge-on disc galaxies to assess how the presence of dust affects axisymmetric JAM modelling and the recovery of kinematic structures. When dust is appropriately masked, the disc regions of galaxies are fit well. Analysis of residual velocity fields reveals coherent excesses in two galaxies that are aligned with bar orbits and supported by photometric bar signatures. A third galaxy displays off-plane velocity residuals consistent with a possible side-on bar. Collectively, this research contributes to a multiscale understanding of angular momentum evolution, connecting cosmological environment, mergers, age and the internal orbital structure of galaxies.

This thesis was primarily written at the University of Sydney, Country of the Gadigal people.

The work presented in this thesis uses observations from the Anglo-Australian Telescope, which stands in the Warrumbungle National Park, Country of the Gamilaraay people, and the Very Large Telescope, which stands in the Atacama desert in northern Chile.

Acknowledgements

We all change, when you think about it, we're all different people; all through our lives, and that's okay, that's good, you've gotta keep moving, so long as you remember all the people that you used to be. I will not forget one line of this, not one day, I swear.

—The Eleventh Doctor

I started my educational journey when I walked with my Oma to kindergarten at Milton Public School on a Summer's day in 2003, and now I will finish it with a PhD in Astronomy at the University of Sydney in 2025. It hasn't always been a straight line journey, but before I quite take my leave, I'd like to thank some of those who helped me along the way.

To my supervisors, Scott and Jesse, none of this would have been possible without you. Your constant support, positivity, endless knowledge of physics, and willingness to make time whenever I needed it went far beyond any expectation of academic supervisors. I am deeply grateful for the role you have played in getting me to where I am today. Scott, I know that "I can't remember if we discussed this or not" really means "We definitely discussed it and you forgot", but that's just proof of your kindness as a supervisor. It really almost, *almost*, makes up for your support of the English cricket team. Jesse, I don't think I could have imagined when I started my PhD that it would involve you testing my knowledge of German poetry in the foothills of the Alps around Neuschwanstein Castle, yet here we are. You took on the role of an academic supervisor brilliantly, always encouraging me to be bigger and better and expand my horizons. I am honoured to be your first PhD student.

To my ESO supervisors Amelia and Eric, I thank you deeply for all your help, I don't think I could have had any success at ESO without you. Eric, I very much appreciate your willingness to make time for me despite how busy you always were, your instinctual grasp of physics, and your constant upbeat attitude. Amelia, you went beyond your role as an academic supervisor, and truly helped me settle into living in a country on the other side of the world. It was more helpful than you know to have an Australian to be able to chat to each day.

I am deeply fortunate to have had and met so many fantastic friends during my time as a PhD student; I am indebted to you all. To Aman, one of the many who fell to the USyd-UNSW pipeline, always available for a laugh at ASTRO3D events and the only other person who knows of the "not really a club" in the upstairs of a bar in Munich that I was never quite able to find after that night. To Josh and Daan, two very politically informed friends who were always there for a chat. To Susie and Yifan, always sources of positivity and up for a good chat in the office, even if we disagreed occasionally on

optimal air-conditioner usage. To Hillary, a wonderful friend and source of support. To all my other officemates: Purmortal, Nabo, Matt, Pavadol, Dylan, Robin, Lachlan, you all helped create a fun office environment, and I apologise if I distracted you too often with chatting. To Will, I will miss our evenings ordering food to the Maths PhD offices, and your constant amusement at whatever new situation I'd managed to get myself into. To David, proof that you can combine study and fun successfully, and the source of many good pieces of advice. To Anuj, somehow wise about everything, always willing to help me with my coding and assure me it wasn't my fault I had no idea what I was doing, and of course a very good friend. To Rory, my first friend at ESO and founding member of Commonwealth Corner, and Jay, who mastered the German accent better than anyone I ever heard. To Louisa, who extended an invitation to join Garching Girlies, and an endless opportunity to mock the English. To Tommy and Felipe, founders of the troublemakers, nickname enjoyers, Dire Straits enthusiasts, the four-handed demon, always up for a night out or a game of table football, and two of the funniest people I've ever met. To Justyn, my ESO mentor, who supported me throughout my journey through ESO, both academically and socially. To Pierrick, my favourite French friend, I will never forget Starkbierfest (the craziest festival in ze vorld!). We made an excellent table football team (eventually, *me putain...*). To Lennart, the newest resident of Feilitzschstraße 33, Münchner Freiheit, who simply has never told a boring (or normal) story. To Julienne, of course my favourite of the people I met at ESO, a hike enthusiast, and a truly amazing person. To Matt Frosst, the human flag, Dietrich the board games legend, Jason the most reliable science coffee attendee, all the table football regulars, and everyone else!

My family has been beyond supportive throughout this PhD, and I thank you all immensely. Angus, despite how much you annoy me, I appreciate you more than I let on, and wouldn't take any other brother in the world. I know the Wado Berk adventures in Forest Lodge and Annandale are over now, but I'm sure there will be many, many more Wado Berk adventures to come. Thank you to Jen, Lauren and Lily for dinner clubs and board games, something I looked forward to every week. I still refuse to play Monopoly cards, though. To Oma and Grandpa, thank you for the endless love and support. I will never forget the ice cream at the harbour or the countless summer and winter days spent at Gallifrey, where a part of me will always reside. Oma, I model how to be kind off of you, and I think that may just be more important than any of this Astronomy business. Grandpa, you're the smartest man I've ever met, and my academic inspiration. I know I did, and hope I will continue to, make you proud. And finally, to Mum and Dad. You always ensured I had the best upbringing possible. You gave me equal appreciation for mathematics, science, sports, and the arts. You gave me my moral code, made sure I would never forget the value of public education, and always reminded me that we are all equal, and anyone is capable of anything if given the opportunity. I'm reminded of the story of the cosmonaut Yuri Gagarin, the first human we ever sent into outer space, a man who looked down on Earth from above – and the humble working-class son of a bricklayer and a milkmaid.

Statement of Attribution

This thesis contains material that was previously published in the following sources. I was the lead and corresponding author:

- Chapter 2 is published in the Astrophysical Journal as Rutherford et al. (2021). A detailed and complete authorship attribution is presented at the beginning of Chapter 2.
- Chapter 3 is published in Monthly Notices of the Royal Astronomical Society as Rutherford et al. (2024). A detailed and complete authorship attribution is presented at the beginning of Chapter 3.
- Chapter 5 is published in Astronomy & Astrophysics as Rutherford et al. (2025). A detailed and complete authorship attribution is presented at the beginning of Chapter 5.

This thesis also contains the following work:

- Chapter 4 will be drafted and submitted to a journal after thesis submission.

The published chapters included in this thesis are reproduced in their original form, with only small formatting changes to ensure a consistent style throughout the manuscript. I confirm that all of the work presented in this thesis is my own, except where indicated by specific reference in the text. I designed each study in these works, performed each analysis and wrote each manuscript.

Tomas H. Rutherford

May 20, 2026

As supervisor for the candidature upon which this thesis is based, I can confirm that the authorship attribution statements above are correct.

Professor Scott M. Croom

May 20, 2026

Contents

List of Figures

List of Tables

Chapter 1

Introduction

You should always waste time when you don't have any. Time is not the boss of you.

—The Eleventh Doctor

1.1 From Sky Stories to Cosmology

1.1.1 Cultural Astronomy

For almost the entirety of human history, we have looked to the sky. The Aboriginal and Torres Strait Islander people have lived on and around the Australian continent for at least 65,000 years (Clarkson et al., 2017), with over 500 recorded languages, traditions and cultures. The oral histories of many of these peoples shows evidence of astronomy going back tens of thousands of years (Hamacher & Banks, 2018). These stories show evidence that even in ancient times, humans were aware that the Sun, Moon and planets moved in the sky. For example, the Tiwi people tell stories of the Sun woman being followed by the Moon man, who is additionally followed by his four wives (Mars, Mercury, Venus and Jupiter) (Mountford, 1958).

Although the earliest cultures on Earth observed the objects in the sky and understood their motions, the idea of massive objects moving in three dimensions wasn't realised until classical antiquity, with the Ancient Greeks. The model of concentric spheres was developed by Eudoxus, Callippus, and Aristotle from the 4th century BCE (Neugebauer, 1975), and involved the celestial objects moving on spheres centred on Earth. Ptolemy's *Almagest* was published in the second century CE and showed that the Earth is a spherical object, further suggesting a geocentric model that placed Earth at the centre of the universe. This model was consistent with the prevailing theories at the time and stood as the accepted theory for over 1200 years. Although several people in the 3rd century BCE suggested that the Earth may move around the Sun instead, such as Aristarchus of Samos and Archimedes (Heath & Aristarchus of Samos, 1913), these models were not widely accepted.

1.1.2 The Birth of Scientific Astronomy

The next great leap in our understanding of the cosmos came when Nicholas Copernicus suggested his model of the Universe, which placed the Sun at the centre, with the planets orbiting it in circles (Copernicus, 1543). This was extended by Kepler, who adjusted the orbits to be elliptical, and placed the Sun at one of the two foci of these elliptic orbits (Kepler, 1609). Kepler also derived three laws of planetary motion, which allowed for the distances between the Sun and planets to be calculated, and first hinted that the Universe may be far larger than just our Solar System. Galileo Galilei further (controversially) proved the heliocentric model of our Solar System using observations (Galilei, 1610). With Newton's Law of Universal Gravitation (Newton, 1687) giving a mathematical model for how the planets moved around the Sun, the currently held heliocentric view on our Solar System was established.

The extension of astronomy outside of our Solar System developed with the understanding that distant stars are in fact the same class of objects as our Sun. This idea became mainstream by the 18$^{\text{th}}$ century (e.g. de Fontenelle & Gardiner, 1715), with the work of Edmond Halley showing that a set of "fixed" stars had moved since the Ancient Greek astronomers had observed them. Today, the total stellar mass of our Milky Way is estimated to be $(5 \pm 1) \times 10^{10}$ $M_{\odot}$ (Bland-Hawthorn & Gerhard, 2016), with approximately 100-400 billion stars. By the early 20$^{\text{th}}$ century, the idea of galaxies outside of our own Milky Way started to be realised. Vesto Slipher measured the redshifts of "spiral nebulae" using the newly developed technique of spectroscopy, and found they were almost all moving away from our Solar System, at far greater speeds than average resolved stellar speeds within our galaxy (Slipher, 1915). Edwin Hubble calculated the distances to these nearby spiral nebulae in 1929 and found they were too far away to be part of the Milky Way, effectively proving the existence of galaxies outside our own (Hubble, 1929). Today, we estimate there are approximately $2 \times 10^{11} - 10^{12}$ galaxies in the observable Universe (Lauer et al., 2021).

The field of astrophysics has taken many huge leaps since the early 20$^{\text{th}}$ century. The development of General Relativity in 1915 linked space and time in a fundamental manner, and predicted the existence of phenomena such as black holes (Oppenheimer & Snyder, 1939), gravitational lensing (Einstein, 1936) and gravitational waves (Einstein, 1918; Abbott et al., 2016). Inconsistencies in galaxy rotation curves and the amount of visible matter in galaxies led to the theory of dark matter (Babcock, 1939), which makes up ~85% of total matter in our Universe. Measurements of Type Ia supernovae in 1998 showed that the expansion of our Universe is accelerating (Riess et al., 1998), and an invisible dark energy contributes ~68% of the Universe's matter-energy budget. The currently accepted cosmological model is known as ΛCDM, where Λ is dark energy, and CDM is "Cold Dark Matter".

1.1.3 Modern Cosmology, Galaxy Formation and ΛCDM

Originally thought to be static and forever, the first hints that the Universe is instead evolving over time came in the early 20$^{\text{th}}$ century. Friedmann (1922) showed that Einstein's field equations (Einstein, 1916) were not only consistent with a static Universe, as Einstein had preferred, but with a Universe undergoing cosmological expansion. Edwin Hubble then

calculated the distance to several spiral nebulae, determining they were indeed beyond the Milky Way and in fact independent galaxies (Hubble, 1926a). Georges Lemaître and Hubble later both showed a relation between distance and recession velocity, known today as the Hubble-Lemaître Law (Lemaître, 1927; Hubble, 1929). Lemaître then first suggested in 1931 that if galaxies are all moving apart from one another, then at some point in the past they must have started from a single concentrated point (Lemaître, 1931). A very controversial idea at the time, it was strongly opposed by many physicists, including Fred Hoyle, who proposed his own steady-state model of the Universe that allowed it to be static in time (Hoyle, 1948). It was Hoyle who in 1949 attempted to discredit the idea of the Universe expanding from a single point by giving it what he thought was a fanciful name - the Big Bang.

Over time, the Big Bang hypothesis overtook the steady-state hypothesis, first through radio source counts (Shakeshaft et al., 1955), and finally beyond doubt with the discovery of the CMB (Penzias & Wilson, 1965) - the echo of the Big Bang 13.7 billion years later. Expansion was now established, and models of cosmological evolution and structure formation followed. Starting from the assumption of the Universe starting as almost entirely homogeneous and isotropic, theoretical work by Press & Schechter (1974) showed that structure could grow naturally from Gaussian initial quantum perturbations. This picture was later reinforced later reinforced by the inclusion of cold dark matter (White & Rees, 1978), a period of exponential inflation (Guth, 1981; Linde, 1982; Starobinsky, 1982), and N-body simulations (Efstathiou et al., 1988).

Building on this cosmological framework, galaxy formation theory traces the emergence of of galaxies from the abundances of primordial elements and dark matter established after Big Bang nucleosynthesis (Alpher et al., 1948; Wagoner et al., 1967; Steigman, 2007). Firstly, the quantum fluctuations during inflation create over-densities and under-densitites (Harrison et al., 1965; Zel'dovich, 1970; Mukhanov & Chibisov, 1981; Mukhanov et al., 1992). Galaxy formation then proceeds in a two-phase process, with dark matter first collapsing gravitationally around these over-densities to form dark matter haloes (Press & Schechter, 1974; White & Rees, 1978). Baryonic matter (primarily hydrogen gas) then follows, collapsing into dark matter potential wells and cooling radiatively (Rees & Ostriker, 1977; Silk, 1977). Once the gas has cooled enough, star formation begins (Spitzer, 1978). Early galaxies were turbulent and chaotic due to high star formation rates (Green et al., 2010), but further gravitational collapse, tidal torques and the conservation of angular momentum eventually leads to galaxies forming spinning discs, almost entirely dynamically supported by rotation. Hierarchical structure formation then follows, where matter collapses and merges into progressively larger structures over time, forming dispersion-supported elliptically shaped galaxies, and galaxy groups and clusters.

Although the basics of galaxy formation were established, work continued over the second half of the twentieth century. Analysis of merger rates and galaxy clusters agreed somewhat with theory (Kauffmann & White, 1993; Lacey & Cole, 1993), but models were underpredicting large-scale galaxy clustering. Analytical descriptions of dark matter haloes were developed (Navarro et al., 1996), but tensions remained, such as the Hubble constant (H_0) being too high in observations. Measurements of Type Ia supernovae solved most of these issues (H_0 tension between measurements remains a challenge, but at a much smaller amplitude than previously) and revealed the final component of the Universe, dark

energy. Dark energy, i.e. the cosmological constant, in fact makes up the largest fraction of the Universe's mass-energy budget (Riess et al., 1998), and implies that the Universe is not only expanding, but the speed of this expansion is increasing.

The currently accepted model for the Big Bang and following cosmology is called ΛCDM, and has been a highly successful theory in explaining and predicting many features of the evolution of our Universe (e.g. Baryon acoustic oscillation, Eisenstein et al., 2005). However, the detailed evolution of galaxies from the first structure formation early in the Universe to the complex structures we see today is inherently complex, and not yet fully understood. The development of large galaxy surveys in more recent times (e.g. York et al., 2000; Driver et al., 2011; Croom et al., 2012) has given us unprecedented data on large numbers of galaxies (e.g. measurements of stellar age, metallicity, kinematics), and allows us to start to investigate these problems.

1.2 Galaxy Photometry

Any examination of the physics of our Universe must involve what we can see when we look to the sky. With up to 2 trillion galaxies in the observable Universe (Conselice et al., 2016), they can be found across all sizes and masses. Ultra-compact dwarfs (Hilker et al., 1999; Drinkwater et al., 2000) have radii of $\sim$ 60pc and contain $\sim$ 100 million stars, and ultra-faint dwarfs (Willman et al., 2005a,b) have radii of $\sim$ 23pc and contain $\sim 100 - 1000$ stars. Conversely, there are massive brightest cluster galaxies (BCGs) such as ESO383-076, which has a radius of $\sim 5.4 \times 10^5$ pc and a mass of $2 \times 10^{12} M_\odot$ (Kemp & Meaburn, 1991).

With such a vast array of possible galaxy types, we start with the earliest classification of galaxy observations, which is their morphological projection onto the sky.

1.2.1 Visual Morphology

When Edwin Hubble first showed that spiral nebulae were too distant to be located within our Milky Way and thus must be extra-galactic, he also proposed a classification scheme for their morphology (i.e. their visual appearance on the sky, Hubble, 1926b). De Vaucouleurs extended it in 1959 (de Vaucouleurs, 1959) to a form what is commonly referred to as Hubble's tuning fork, shown in Figure 1.1. This diagram divides galaxies into several groups:
Early-Type Galaxies (ETGs):

- **Elliptical Galaxies:** Galaxies that feature a smooth light distribution. Ellipticals are labelled by the ratio of their minor (b) to major (a) axis, with the parameter defined as $10 \times (1 - \frac{b}{a})$. E0 galaxies are thus perfectly circular on the sky ($a = b$), E1 galaxies are slightly flatter, and so on, until about E7. However, E4-E7 galaxies are almost certainly misclassified lenticular galaxies, with their disc not clearly apparent due to inclination effects (Liller, 1966; Graham et al., 1998).
- **Lenticular Galaxies:** Galaxies that have a central bulge surrounded by a disc, but feature little to no active star formation or spiral arms.

Late-Type Galaxies (LTGs):

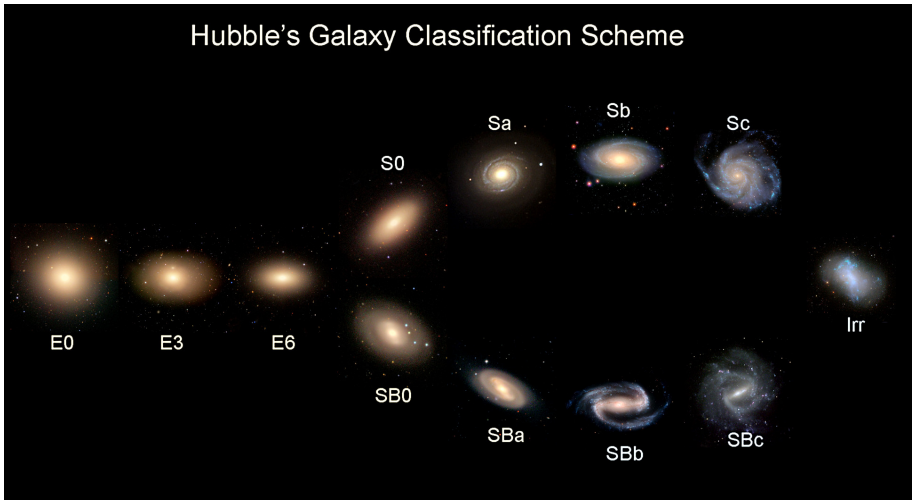

Figure 1.1: An illustration of Hubble's "tuning fork" diagram, displaying the various types of galaxy morphology we observe in the Universe. From left to right, we begin with spherical elliptical E0 galaxies, and progress as they become more flattened and disc-like. As they develop spiral arms, they split into two types, S and SB, depending on if they are barred or not. Finally, irregular (Irr) galaxies are galaxies that fit into none of the categories, and have generally more chaotic shapes. These are often a result of a recent merger, or are simply lower mass, so smooth disk features are not as clear. We stress here that although the left side of this diagram are referred to as "early-type" galaxies, and the right side as "late-type" galaxies, there is no explicit time evolution direction. Image taken from ESO/Zooniverse.

- **Spiral Galaxies:** Galaxies that feature a flattened disc, with spiral arms featuring active star formation. Spiral galaxies may also have a central concentration of older stars referred to as a "bulge".
- **Barred Spiral Galaxies:** A subset of spiral galaxies, barred spirals also feature a "bar" of stars through the centre of the galaxy. In the local Universe, approximately $\sim 60-65\%$ of spiral galaxies are barred (Menéndez-Delmestre et al., 2007).

Irregular Galaxies (Irr): Galaxies that feature no distinct shape, with little symmetry and are often chaotic in their appearance. They commonly do not display a bulge, disc, or spiral arms.

1.2.2 Surface Brightness Profiles

The galaxy components mentioned thus far, such as bulges, discs and bars, are often used to structurally decompose the light of a galaxy. A model of these components, as well as the total light of a galaxy, has various uses, such as dynamical modelling (e.g. Cappellari, 2008; Thater et al., 2022) and SED modelling (e.g. Robotham et al., 2020).

A galaxy's light distribution on the sky as a function of radius is commonly modelled with a Sérsic profile (Sérsic, 1963):

$$I(R) = I_0 e^{-kR^{1/n}} \tag{1.1}$$

where $I(R)$ is the intensity at $r = R$, I_0 is the intensity at $r = 0$, k is a free parameter, and n is the Sérsic index. Elliptical galaxies, as well as the bulges of spirals, generally

have profiles with $n = 4$, known as the de Vaucoulers profile (de Vaucouleurs, 1948). Disc components generally have profiles with $n = 1$, known as an exponential profile (Patterson, 1940; de Vaucouleurs, 1959; Freeman, 1970). These values, however, vary in practice across a population of galaxies.

Further, a galaxy's Sérsic index correlates with many photometrically derived properties of the galaxy. Blanton & Moustakas (2009) used data from the sixth data release of the Sloan Digital Sky Survey (SDSS, Adelman-McCarthy et al., 2008) and derived Sérsic indices for 77,153 galaxies. They showed each galaxy's relationship between its total r-band absolute magnitude M_r, $g - r$ colour, Sérsic index n, and effective radius r_{50}. These relationships can be seen in Figure 1.2. They found that while red galaxies show a range of Sérsic indices, blue galaxies generally show lower values. Additionally, a galaxy's Sérsic index correlates with M_r. While it should be noted that these relationships display a large amount of intrinsic scatter, it is clear that the Sérsic index is a key structural parameter. Other studies have decomposed galaxies into several physically motivated components, often a bulge+disc (e.g. Simard et al., 2011), but also allowing for bars and nuclear discs as well (e.g. Gadotti, 2009; Salo et al., 2015).

A further method for modelling the two-dimensional projection of galaxy light on the sky is Multi-Gaussian Expansion (MGE) (Monnet et al., 1992; Emsellem et al., 1994a). This models the surface brightness (Σ) at the *projected* position (x', y') as a sum of N two-dimensional Gaussians:

$$\Sigma(x', y') = \sum_{k=1}^{N} \frac{L_k}{2\pi\sigma_k^2 q'_k} \exp\left[-\frac{1}{2\sigma_k^2}\left(x'^2 + \frac{y'^2}{q'^2_k}\right)\right] \tag{1.2}$$

where each gaussian component has total luminosity L_k, observed axial ratio q'_k, and dispersion σ_k along the major axis. MGE models are useful as the Point Spread Function (PSF) may also be modelled with an MGE, and this may be analytically convolved with the light model and used for dynamical modelling (see Section 1.6).

1.3 Galaxy Spectroscopy

While the photometric imaging of galaxies is a powerful tool, it is limited in that each band of light (e.g. *u, g, r, i, z, y*) is integrated over a range of wavelengths. Although these can be used to examine galaxy visual morphology and estimate approximate redshifts; precise information on stellar populations, kinematics, chemistry and accurate redshift measurements requires a measurement of the galaxy's spectrum.

The use of spectra to study nature began with Newton's prism experiments (Newton, 1671), and were linked to astrophysics when Fraunhofer observed the spectrum of the Sun (Fraunhofer, 1817). The dark features in Fraunhofer's spectra were later identified as atomic absorption lines (Kirchhoff, 1860; Kirchhoff & Bunsen, 1860), and the era of spectroscopy in astronomy began.

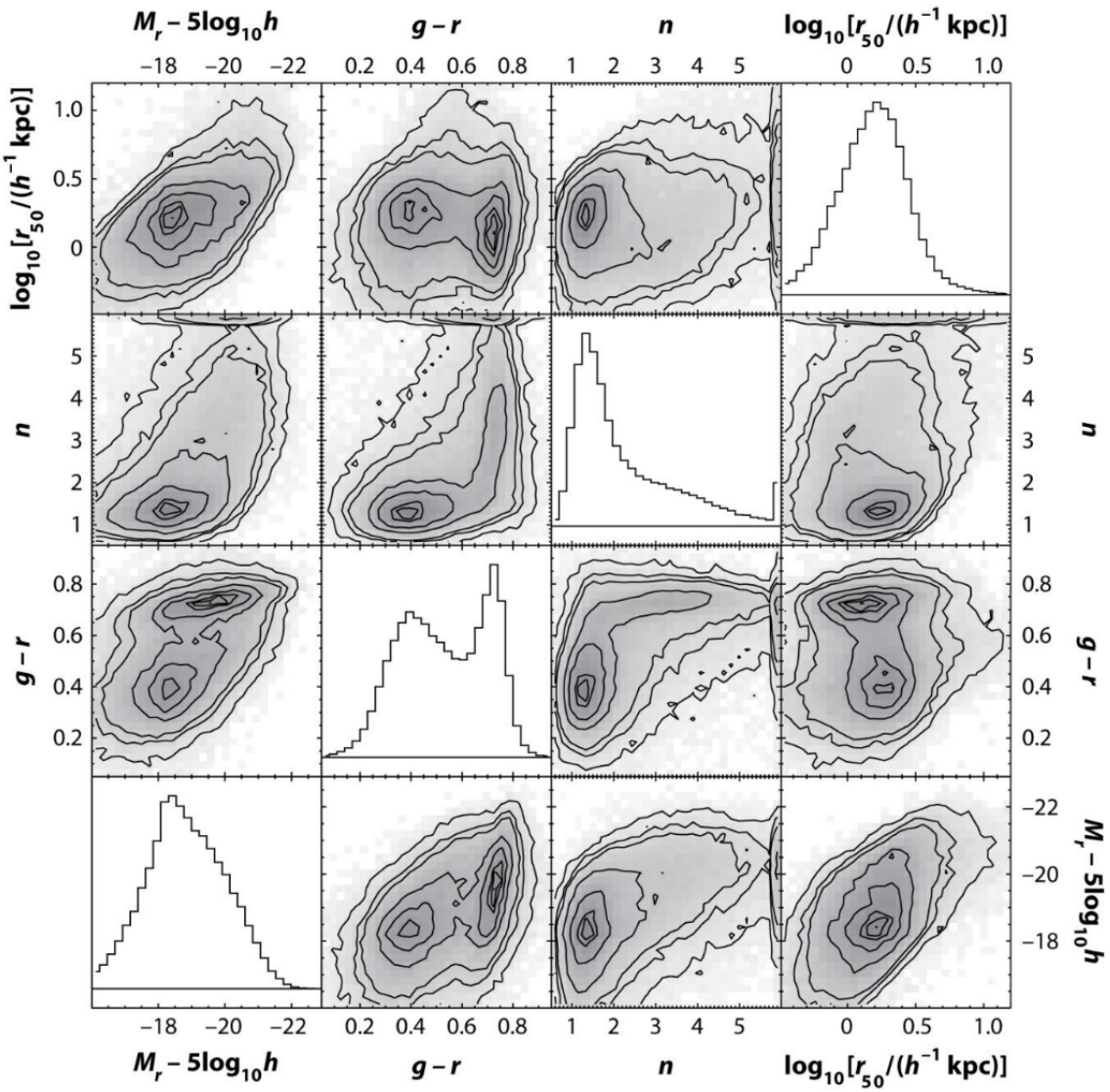

Figure 1.2: The distribution of broad-band galaxy properties from the sixth data release of the Sloan Digital Sky Survey. The parameters are total r-band magnitude M_r, $g-r$ colour, Sérsic index n, and effective radius r_{50}. Notably, n displays a correlation with M_r and $g-r$, albeit with large intrinsic scatter. Figure taken from Blanton & Moustakas (2009).

1.3.1 Long-Slit Spectroscopy

By the mid-20$^{\text{th}}$ century, astronomers extended the spectroscopy of single stars to obtain spatially resolved spectroscopy across the faces of galaxies. Long-slit spectrographs could sample multiple arcseconds along a galaxy (e.g. Babcock, 1939; Aller, 1942; Mayall, 1946; Burbidge et al., 1960), delivering spatially resolved spectroscopic measurements, discovering rotation curves and radial metallicity gradients in external galaxies. The technique works by observing an object in the sky through a narrow "slit" aperture. The light is then sent through a spectograph. This results in a two dimensional image, of which one dimension is spatial (along the slit), and one is spectral (i.e. wavelength data). This spatial resolution allows for the collection of spatial and spectral information about a

galaxy simultaneously, which is required for many important measurements (e.g. rotation curves, Courteau, 1997). There have also been several large surveys with long-slits (e.g. Thompson & Djorgovski, 1995), and multiple short slits (e.g. Le Fèvre et al., 2005). These surveys have the advantage that many objects can be observed at once ($\sim$ 600 for Le Fèvre et al. (2005)), which enables a very large number of galaxies to be observed within a reasonable timeframe.

The disadvantages of long-slit spectroscopy, however, come in three major categories. Firstly, the positioning of a slit on a galaxy requires forward planning, and errors in slit positioning can be common. Further, atmospheric differential refraction along a slit is a substantial effect (e.g. the Filippenko effect, Filippenko, 1982) which can lead to large uncertainties in derived velocities if not carefully accounted for. Finally, galaxies do not only vary along one axis (e.g. over one third of early-type galaxies are suspected to be triaxial (Emsellem et al., 2007; Cappellari et al., 2007)). A slit is fundamentally only capable of providing spatial variation along an axis. Although a second slit can be placed perpendicularly to the first slit, this only provides a second (thin) axis. Many galaxies appear *clumpy* (e.g. van den Bergh et al., 1996; Elmegreen & Elmegreen, 2005) as a result of their formation processes. These properties can't be properly explored with only slits, and require full two-dimensional spatially resolved data.

1.3.2 Single-Fibre Spectroscopy

The use of glass fibres in optics was first described by John Tyndall (Tyndall, 1873) in the 19$^{\text{th}}$ century, utilising the principle of total internal reflection. It would take until 1966 for the first patent for a fibre optic data transmission system, which was later used for the Moon landing (NASA, 1968).

The idea of fibre cables being used in Astronomy was an attractive one. The benefits of easily transferring light from a mirror to a spectrograph were obvious, with further ideas suggested by the 1970s, such as the potential application of fibre optics in creating telescope arrays (Angel et al., 1977). In 1979, the first spectrum was taken through a single silica fibre, the nucleus of NGC 4151 (Hubbard et al., 1979). This spectrum can be seen in Figure 1.3. The development of multi-object instruments utilising fibres followed quickly. Hill et al. (1980) developed the MEDUSA spectrograph, which obtained spectra from 26 galaxies within the galaxy cluster Abell 1904. Fibres were positioned at appropriate locations for each galaxy simultaneously.

In recent years, large, multi-object single fibre galaxy surveys have enabled the mapping of large-scale structure in the local Universe. The 2dF Galaxy Redshift Survey (Colless et al., 2001) obtained spectra (and thus redshifts) for over 200,000 galaxies. The Sloan Digital Sky Survey (SDSS) (York et al., 2000) continues to take data more than twenty years since it began, with over 3 million galaxy spectra obtained.

1.3.3 Integral Field Spectroscopy

Obtaining spatially resolved galaxy spectra across a galaxy's projection on the sky provides a wealth of information. To attain a genuinely comprehensive, three-dimensional, physically motivated understanding of galaxies, it is essential to gather data regarding how

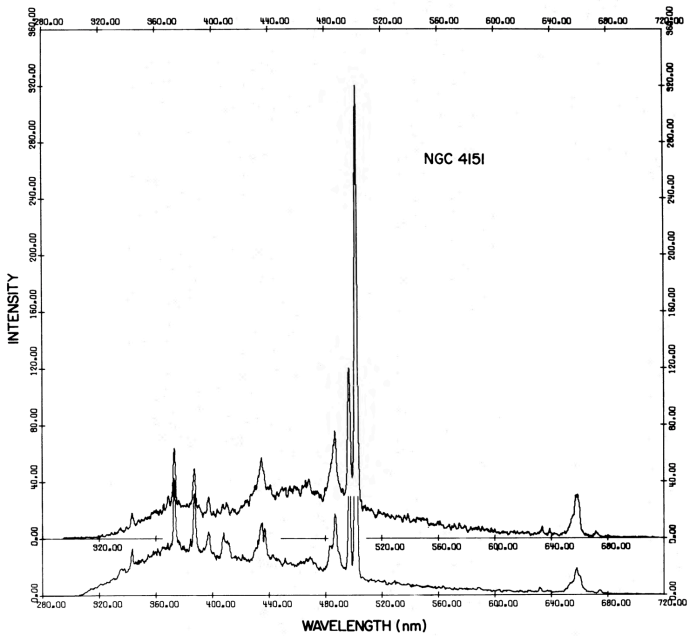

Figure 1.3: Two spectra of the nucleus of NGC 4151, taken by Hubbard et al. (1979). The spectra were taken with the 36 inch telescope at Steward Observatory, Arizona. The spectrograph used was the Boiler and Chivens Image Tube Spectrograph. The lower spectrum was taken with the spectrograph at the Cassegrain focus of the telescope. The upper spectrum, however, was taken with the spectrograph located in a floor below the telescope, connected with a silica fibre optic table. This was the first spectrum taken using fibre cables. Image taken from Hubbard et al. (1979).

a galaxy behaves in the *line of sight* dimension. This is done by providing a spectrum for each spatial pixel (or spaxel) across a galaxy. Early work used Fabry-Pérot instruments to obtain spatially resolved Hα spectroscopy of the Milky Way (Courtès, 1972), allowing for kinematic measurements of ionised gas. Measurements of velocity fields, position-velocity diagrams and Tully-Fisher relationships have also been derived for samples of nearby spirals from Fabry-Pérot data (Amram et al., 2002; Epinat et al., 2008). The most popular technique today to obtain spatially resolved galaxy spectra across a galaxy's optical spectral range and across its spatial projection on the sky is integral field spectroscopy (IFS). This enables the extraction of data such as spatially resolved star formation rates, metallicity, and stellar or gas kinematics.

Integral field spectroscopy has been developed over the end of the 20$^{\text{th}}$ and beginning of the 21$^{\text{st}}$ centuries. The first large spectrograph was TIGER, which was based on a lenslet array design (Bacon et al., 1995). The lenslet design exposes the sky to an array of many small lenses, which are then directed to a spectrograph. Although a lenslet array allows for up to 100% spatial filling with square or hexagonal lenses, it loses 50% of detector pixels on the CCD to avoid contamination between adjacent spectra. An alternate design for IFS is a fibre array. In this configuration, fibres are positioned across the image of the galaxy on the sky, which are then fed to a long-slit spectrograph. A fibre design can achieve high spatial filling, whilst not losing any CCD detector pixels. An image further illustrating the lenslet and fibre configurations, as well as the image slicer configuration,

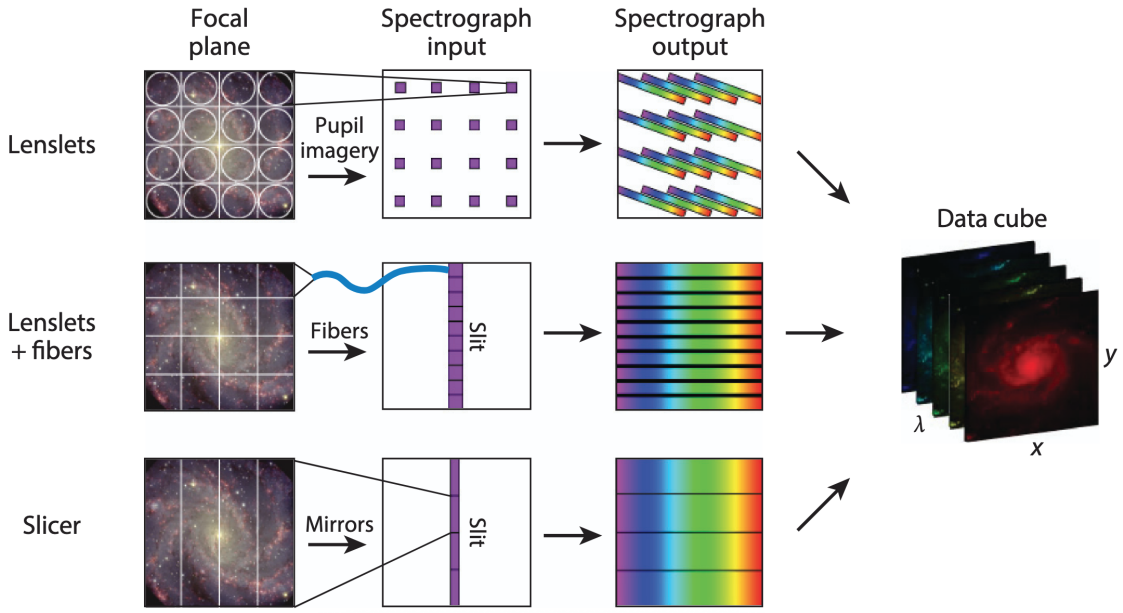

Figure 1.4: An illustration of how the lenslet, fibre and slicer designs for Integral Field Spectrographs are configured. Lenslets can achieve 100% spatial filling with many small lenses, however this design requires low efficiency with detector pixels. A fibre array can still reach high spatial filling, whilst also having ~ 100% detector pixel efficiency. Image slicers divide the field with mirror slices, reassembling the light into a pseudo-long-slit for the spectrograph. All arrangements provide a three-dimensional "datacube" of a galaxy, with two spatial dimensions and one spectral dimension. Each pixel of the galaxy has a provided spectra. Image adapted from Eisenhauer & Raab (2015).

can be seen in Figure 1.4.

The first large IFS project was SAURON (Bacon et al., 2001), which was inspired by TIGER. SAURON was both an instrument and a survey, and provided rich data for absorption-line kinematics for elliptical and lenticular galaxies (Emsellem et al., 2004), mass-to-light ratios, virial masses, and the fundamental plane for elliptical and lenticular galaxies (Cappellari et al., 2006) and more (e.g. de Zeeuw et al., 2002; Sarzi et al., 2006). SAURON was also used for the ATLAS^{3D} project, which captured IFS data for ~ 260 nearby ETGs (Cappellari et al., 2011a).

Despite the success of IFS science, the early surveys such as SAURON and ATLAS^{3D} were limited to single object instruments. Even CALIFA (Sánchez et al., 2012) which observed ~ 600 nearby galaxies could only observe one galaxy at a time. There was an early instrument in VLT FLAMES (Pasquini et al., 2002) that had 15 integral field units (IFUs) and could observe multiple objects simultaneously. However, its small FoV (2-3") and narrow wavelength range limited its use for large scale surveys. In order to explore the data that IFS instruments could provide over a large number of galaxies in a statistically significant way, a large-scale multi-object IFS survey was needed.

1.3.4 The SAMI Galaxy Survey

The Sydney-AAO Multi-Object Integral field spectrograph (SAMI) (Croom et al., 2012) was deployed on the Anglo-Australian Telescope and delivered an IFS instrument capable of simultaneous observation of 13 objects. SAMI was born of the desire to have an IFS survey which i) produced spatially resolved spectroscopy (with high spectral resolution), and ii) provided a statistically significant sample of galaxies over a full range of stellar masses and environments.

SAMI took advantage of advances in astrophotonic technology, utilising 13 hexabundles. Hexabundles (Bland-Hawthorn et al., 2011; Bryant et al., 2014) consist of a bundle of optical fibres, with stripped cladding to 5μm. This allows for a 75% fill factor. Each bundle accommodates 61 fibers of 1.6″ diameter, resulting in a 15″ diameter for each IFU. The SAMI instrument delivered a field of view with a 1-degree diameter. The AAOmega spectrograph (Sharp et al., 2006) processed the IFUs and 26 sky fibres. Utilising the 580V grating (3570-5750Å) achieved a resolution of R=1808 (σ=70.4 km s^{-1}), while the 1000R grating (6300-7400Å) provided a resolution of R=4304 (σ=29.6 km s^{-1}) (van de Sande et al., 2017b).

The SAMI Galaxy Survey (Croom et al., 2012; Bryant et al., 2015) based its target selection on the GAMA survey (Driver et al., 2011) and included data from eight low-redshift clusters (Owers et al., 2017). Reduced data cubes, detailed in (Sharp et al., 2015), are accessible through various SAMI Galaxy Survey data releases (Allen et al., 2015; Green et al., 2018; Scott et al., 2018; Croom et al., 2021), along with accompanying stellar kinematic maps.

The SAMI sub-sample selected from the GAMA survey consists of targets in three equatorial regions, each 4 × 12 degrees, and centred at approximate right ascensions (RAs) of 9, 12, and 15 hours. GAMA was selected as the background survey due to the ancillary data available in the ultraviolet, infrared, and radio wavelength regimes, as well as spectroscopic redshift measurements. Targets were selected from each region based on cuts in the redshift-stellar mass plane, where masses were derived from i-band magnitudes and $g - i$ colours (see Taylor et al., 2011; Bryant et al., 2015). These cuts are shown in Figure 1.5, where black dots represent all GAMA galaxies. Points within the red region ($0.004 < z < 0.095$) are high-priority targets, and points within the yellow and cyan regions are low-priority targets only observed if there were not 12 high-priority targets present in a pointing. The spatial distribution of SAMI galaxies within GAMA regions is shown in Figure 1.6. Each GAMA galaxy is represented by a grey dot, with SAMI high-priority observed targets shown in red, high-priority unobserved targets shown in blue, low-priority observed targets shown in magenta, and low-priority unobserved targets shown in cyan.

SAMI galaxies from cluster regions were defined in Owers et al. (2017), and we summarise the selection criteria here. Targets were selected such that, relative to the redshift of the cluster, $|v_{\rm pec}|/\sigma_{200} < 3.5$, where $v_{\rm pec}$ is the peculiar velocity of the galaxy relative to the cluster and σ_{200} is the cluster velocity dispersion at the overdensity radius R_{200}. These targets were further divided into primary and secondary targets within the redshift-stellar mass plane, as described in Owers et al. (2017). In Figure 1.7, we show the spatial distribution of galaxies within the eight cluster regions. Grey points represent cluster

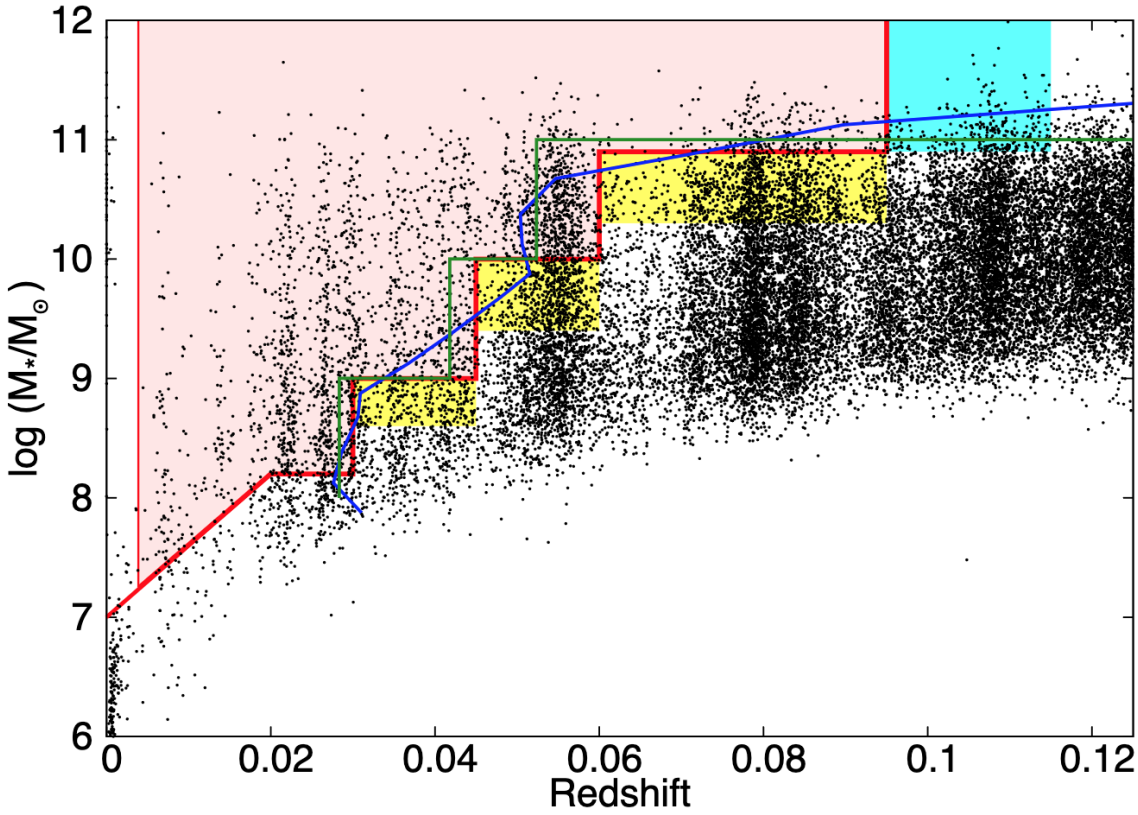

Figure 1.5: Stellar mass and redshift distribution of SAMI galaxies, and the background GAMA distribution from which they were selected. Black points represent GAMA galaxies, while all points within the red region ($0.004 < z < 0.095$) are high-priority SAMI targets. Galaxies within the yellow and cyan regions are low-priority targets, only observed if 12 high-priority targets were not present in a given pointing. The blue and green lines are not selection boundaries, but instead show flat stellar mass distributions. Figure taken from Bryant et al. (2015).

members from the SAMI Cluster Redshift Survey, from which the galaxy surface density isopleths were defined, which are shown as black contours. Observed primary galaxies (red circle), unobserved primary galaxies (blue circle), observed large radius secondary galaxies (magenta square), unobserved large radius secondary galaxies (cyan square), observed blue secondary galaxies (cyan star), and unobserved blue secondary galaxies (cyan star) are also shown. R_{200} is shown with green circles. The dashed green circle in Abell 168 represents the region used to define the cluster centre during the early survey.

SAMI is not alone in IFS surveys, however. Other surveys such as DiskMass (Bershady et al., 2010) and MASSIVE (Ma et al., 2014) have taken observations of discs and the most massive galaxies, respectively. MaNGA (Bundy et al., 2015) has observed 10,000 nearby galaxies, combining with SAMI for the largest resolved spectroscopic survey of the Universe to date. There are additionally new IFS surveys actively observing, such as Hector (Bryant et al., 2020, Oh et al. submitted), the follow-up to SAMI. Hector will observe up to 15,000 galaxies at low redshift, $z < 0.1$.

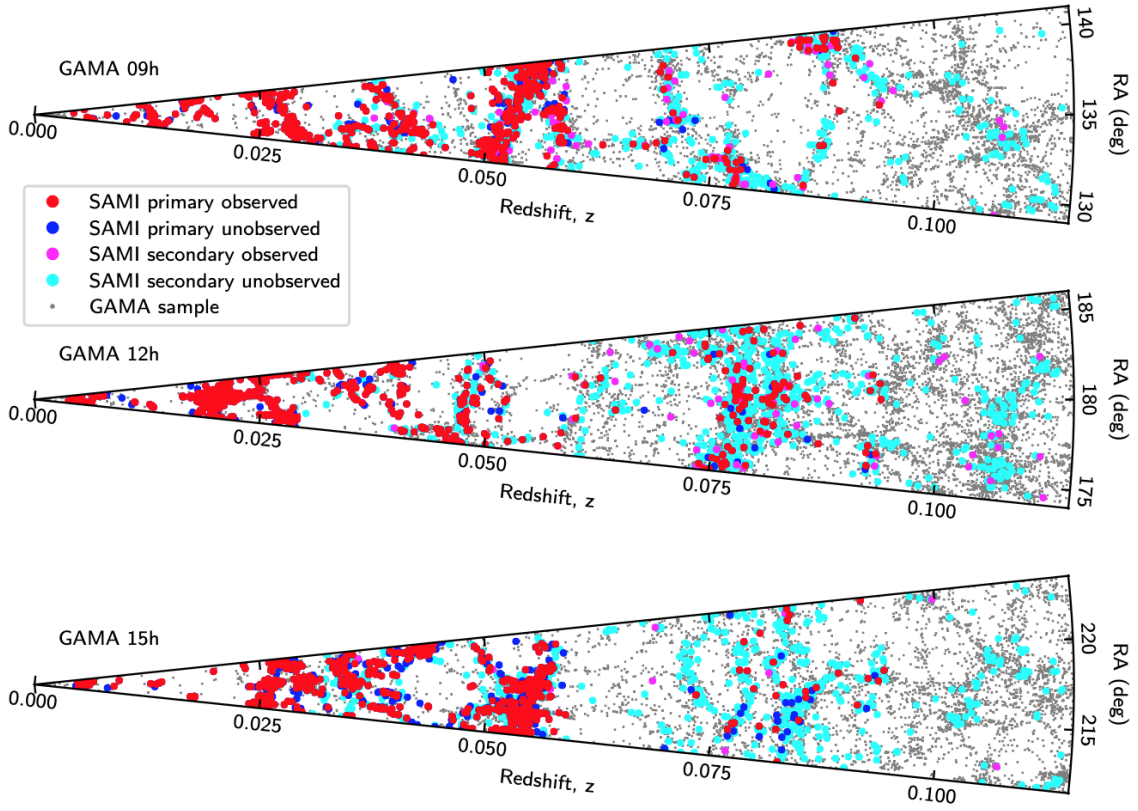

Figure 1.6: Spatial distribution of galaxies within the three GAMA regions (09h, 12h, 15h) that SAMI targets were selected from. Each GAMA galaxy is represented by a grey dot, with SAMI high-priority observed targets shown in red, high-priority unobserved targets shown in blue, low-priority observed targets shown in magenta, and low-priority unobserved targets shown in cyan. Figure taken from Croom et al. (2021).

1.3.5 The Multi Unit Spectroscopic Explorer (MUSE)

While SAMI covers a large area of the sky with 13 simultaneous IFUs, an alternative approach is to use a single IFU at much higher spatial resolution, as offered by the Multi Unit Spectroscopic Explorer (MUSE, Bacon et al., 2010, 2014). MUSE is a second generation instrument for the Very Large Telescope (VLT), operated by the European Southern Observatory (ESO). During observations, the field-of-view is split into 24 sub-fields, each directed to an IFU. Each IFU has an image slicer at the front end serving as an entrance slit. MUSE can operate in either Narrow Field Mode with a field-of-view of 7.5×7.5 arcsec^2 spatially sampled at 0.025×0.025 arcsec^2, or Wide Field Mode with a field-of-view of 1×1 arcmin^2 spatially sampled at 0.2×0.2 arcsec^2. MUSE also provides a large spectral range of $465 - 930$nm, with a resolution of R=2000 at 465nm, and R=4000 at 930nm.

MUSE has been used for a diverse range of scientific studies to date, from resolved stellar clusters (Husser et al., 2016; Kamann et al., 2018), to gravitational waves (Tanvir et al., 2017; Levan et al., 2017), and most relevant in the case of this thesis, galaxy evolution (e.g. Gadotti et al., 2019; Foster et al., 2021; Emsellem et al., 2022; van de Sande et al., 2024).

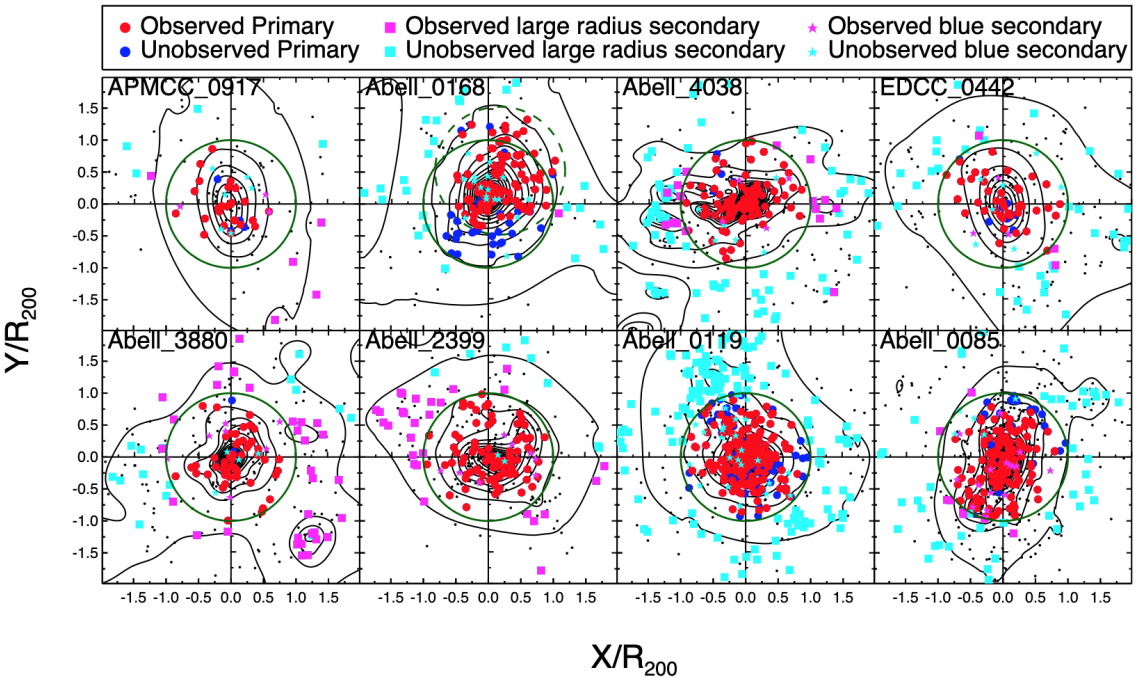

Figure 1.7: Spatial distribution of galaxies within the eight clusters that SAMI targets were selected from. Grey points represent cluster members from the SAMI Cluster Redshift Survey, from which the galaxy surface density isopleths were defined, which are shown as black contours. Observed primary galaxies (red circle), unobserved primary galaxies (blue circle), observed large radius secondary galaxies (magenta square), unobserved large radius secondary galaxies (cyan square), observed blue secondary galaxies (cyan star), and unobserved blue secondary galaxies (cyan star) are also shown. R_{200} is shown with green circles. The dashed green circle in Abell 168 represents the region used to define the cluster centre during the early survey. Figure taken from Croom et al. (2021).

1.3.6 Stellar Kinematics

While photometric observations provide a detailed view of a galaxy's structural components, a full understanding of galaxy evolution also requires knowledge of the motions of its stars. Galaxy kinematics trace many morphological substructures, which can themselves be evidence of specific evolutionary histories, e.g. bars (Hohl, 1971; Ostriker & Peebles, 1973; Noguchi, 1987; Salo, 1991), nuclear discs (Binney et al., 1991; Falcón-Barroso et al., 2006; Wozniak, 2015; Du et al., 2015; Méndez-Abreu et al., 2019), and boxy-peanut bulges (Combes & Sanders, 1981; Bureau & Freeman, 1999; Erwin & Debattista, 2017; Kruk et al., 2019). Indeed, studies of the dynamics of stars in galaxies give hints to their assembly histories regardless of kinematic components (e.g. de Zeeuw & Franx, 1991; Bender et al., 1994; Cappellari, 2016; Emsellem et al., 2022).

In principle, a galaxy can be represented by a six-dimensional distribution function $f(x, y, z, v_x, v_y, v_z)$, describing the positions and velocities of each of its stars. In reality, our observations must begin with what we can observe. The spectra emitted from galaxies show emission and absorption lines from a distribution of stars, shifted and broadened in wavelength space by the velocities of these stars (e.g. Minkowski, 1962; Morton & Thuan,

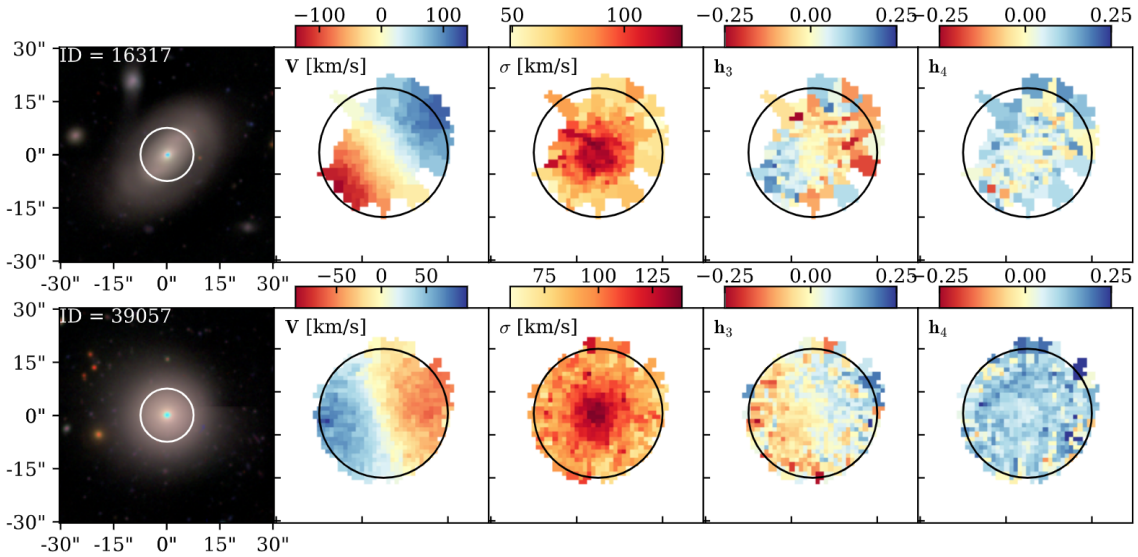

Figure 1.8: Stellar kinematic maps for two galaxies from the SAMI Galaxy Survey. In the top row, we show the galaxy with ID 16317. In the left-most panel, we show the *gri* image of the galaxy in HSC Wide data, from HSC data release 2 (Miyazaki et al., 2015). In the second panel from the left, we show the mean velocity V. In the third panel from the left, we show the velocity dispersion σ. In the fourth panel from the left, we show the skewness h_3. In the right-most panel, we show the kurtosis h_4. In each panel, we show a circle representing the SAMI field-of-view (diameter of 15 arcseconds). In the bottom row, we show the galaxy with ID 39057.

1973; Sargent et al., 1977; Franx & Illingworth, 1988). Analysis of these spectra allows for the derivation of velocity distributions. These velocity distributions are commonly represented with a truncated Gauss-Hermite series (van der Marel & Franx, 1993; Gerhard, 1993). This parametrises the distribution by its Gaussian mean velocity V, velocity dispersion σ, skewness h_3, and kurtosis h_4. With the use of integral field spectroscopy (IFS), it is possible to spatially resolve the line-of-sight velocity distributions (LOSVD) of stars across the spatial extent of galaxies. Each spaxel in an IFS datacube contains a spectrum, from which kinematic information can be extracted. By convolving templates of known stellar populations with a velocity distribution through full spectral fitting, the velocity distribution is solved for. The most common tool for extracting stellar kinematics from IFU data is Penalized PiXel-Fitting (pPXF) (Cappellari & Emsellem, 2004). When provided with appropriate stellar or stellar population model templates, pPXF derives the LOSVD in each spaxel, parameterised by V, σ, h_3, and h_4. In Figure 1.8, we show maps of these velocity moments for two galaxies from the SAMI Galaxy Survey (Croom et al., 2012; van de Sande et al., 2017b; Croom et al., 2021).

While spatially resolved maps of velocity moments offer a detailed view of a galaxy's internal kinematics, it is also practical to describe the kinematic properties of a galaxy in a single parameter. A proxy for the galaxy spin parameter λ_R can be measured within one

effective radius (R_e), to give λ_{R_e} (Emsellem et al., 2007):

$$\lambda_{R_e} \equiv \frac{\sum_i^{N_p} F_i R_i |V_i|}{\sum_i^{N_p} F_i R_i \sqrt{V_i^2 + \sigma_i^2}} \tag{1.3}$$

where F_i, R_i, V_i and σ_i are the flux, radius, velocity and velocity dispersion of the i^{th} bin respectively, where there are N_p bins in total. λ_{R_e} can be thought of as a measure of the ratio of ordered to random motion of stars: if $\lambda_{R_e} \sim 0$, then there is little ordered rotation in a galaxy, and it is mostly dispersion supported. If $\lambda_{R_e} \sim 1$, then the galaxy shows mostly ordered motion and very little dispersion, and is likely a cold disc.

1.4 Galaxy Environments

Just as "No man is an island" (Donne, 1624), galaxies must be considered in the context of their external influences. That is, galaxies in general do not evolve in isolation, and are strongly influenced by their environment. There are two main ways this influence occurs: through star formation quenching, and dynamical interactions. Ram pressure stripping occurs when a galaxy moves through a hot intra-cluster medium, and this medium is strong enough to strip gas from the galaxy (e.g. Gott & Gunn, 1971; Kenney et al., 2004; Koopmann & Kenney, 2004; Poggianti et al., 2017; Schaefer et al., 2019). Galaxies may also be quenched through the removal of the supply of new gas (e.g. Larson et al., 1980), which is often accreted along cosmic filaments. If quenching occurs early enough in the galaxy's lifetime, then there often hasn't been enough star formation to build a rotationally supported thin disc. The resulting galaxy will be more dispersion dominated, affecting the later-measured stellar kinematics (e.g. Kassin et al., 2012; Wisnioski et al., 2015; Übler et al., 2019).

Dynamical interactions between galaxies may also influence the gas fraction and stellar kinematics of galaxies. Dry mergers occur when there is little gas in a galaxy merger, and generally result in dynamical heating of the resulting system (Lagos, 2020b). In contrast, wet mergers involve a high gas fraction, and may result in dynamical heating or the re-building of a star-forming disc (Bois et al., 2010; Lagos et al., 2018a). Dynamical encounters that are either not full mergers (e.g. fly-bys, dynamical friction) or only minor mergers have also been shown to potentially drive a spin-down of galaxies (e.g. Choi & Yi, 2017; Lofthouse et al., 2017; Schulze et al., 2020).

The impacts of environment on galaxies affect the morphology, stellar kinematics, stellar age, kinematic/morphological components, gas content, and star formation rate. It is thus key to have a measure of the environment in which galaxies reside. The 5$^{\text{th}}$ nearest neighbour surface density, or Σ_5, is often used to measure this. Σ_5 is defined as $\Sigma_5 = 5/\pi d^2$, where d is the projected comoving distance to the 5$^{\text{th}}$ nearest galaxy in the tracer population (e.g. Brough et al., 2017). Additionally, it is possible to measure the total dark matter halo mass that a galaxy resides in. From the group a galaxy resides in, the group velocity dispersion is measured, and calibrated to simulations to get a halo mass (e.g. Robotham et al., 2011). This measure allows understanding of the size of a galaxy's group or cluster. Finally, it is also common to classify a galaxy based on its position in a group or cluster.

Robotham et al. (2011) classified the galaxy closest to the r-band centre of light as a central, and every other galaxy in the group or cluster as a satellite. Galaxies not in groups were classified as isolated. As galaxies in the centre of clusters are expected to experience more mergers, and indeed show a high fraction of slow rotators (e.g. van de Sande et al., 2021b), this statistic is useful to understand the difference in galaxy evolution in different regions of a given group.

Tools such as the 2-point real-space correlation function (Peebles, 1980) also make use of a galaxy tracer population to measure the "overdensity" of galaxies as compared to a random distribution, as a function of radial separation. This measure is extremely useful to measure large scale structure in the Universe. Hermit et al. (1996) used correlation functions to find that early-type galaxies cluster more than late-types, and Madgwick et al. (2003) found that passive galaxies cluster more strongly than star-forming galaxies. A 2-point correlation function was also used to measure baryon acoustic oscillations (e.g. Eisenstein et al., 2005). The fourier transform of the correlation function is known as the power spectrum, and has been used to measure fundamental cosmological parameters (e.g. Planck Collaboration et al., 2020).

It is also possible to weight galaxy counts in a correlation function by a given parameter, which gives the weighted correlation function (Sheth et al., 2005a). The ratio between this and the regular correlation function is the marked correlation function, and diverges from 1 at the radial separation where your chosen parameter is over or under-represented in galaxy clustering. This approach has been used as a powerful link between galaxy properties and environment, probing luminosity (Skibba et al., 2006), morphology (Skibba et al., 2009), and assembly bias (Contreras et al., 2019).

Understanding the environment provides essential context for interpreting the internal dynamics of galaxies, as these measures describe the external conditions that determine gas accretion, merger history, and thus the growth of angular momentum. This directly shapes the present-day stellar kinematics. Consequently, the next step is to examine how galaxies translate this environmental influence into their observed rotational support.

1.5 Fast Rotators, Slow Rotators, and the Company They Keep

With the wealth of measured morphological and kinematic properties in observed galaxies, attempting to understand the physical processes that drive the diversity in the galaxy population is the natural next step. Although there is not a one-to-one relationship between kinematics and morphology, elliptical ETGs tend to exhibit lower λ_{R_e} values on average, and late-type discs tend to have higher λ_{R_e}. This has led to the classification of galaxies into "fast rotators" and "slow rotators".

Slow rotators were first defined as a class of round galaxies with very little rotational support using data from the SAURON project (Emsellem et al., 2007; Cappellari et al., 2007), where it was suggested that slow rotators were galaxies with $\lambda_{R_e} < 0.1$. This was later adjusted to $\lambda_{R_e} < 0.31\sqrt{\varepsilon_e}$ (Emsellem et al., 2011) and then $\lambda_{R_e} < 0.08 + \varepsilon_e/4$, $\epsilon_e < 0.4$ (Cappellari, 2016; van de Sande et al., 2017a); where ε_e is the measured ellipticity

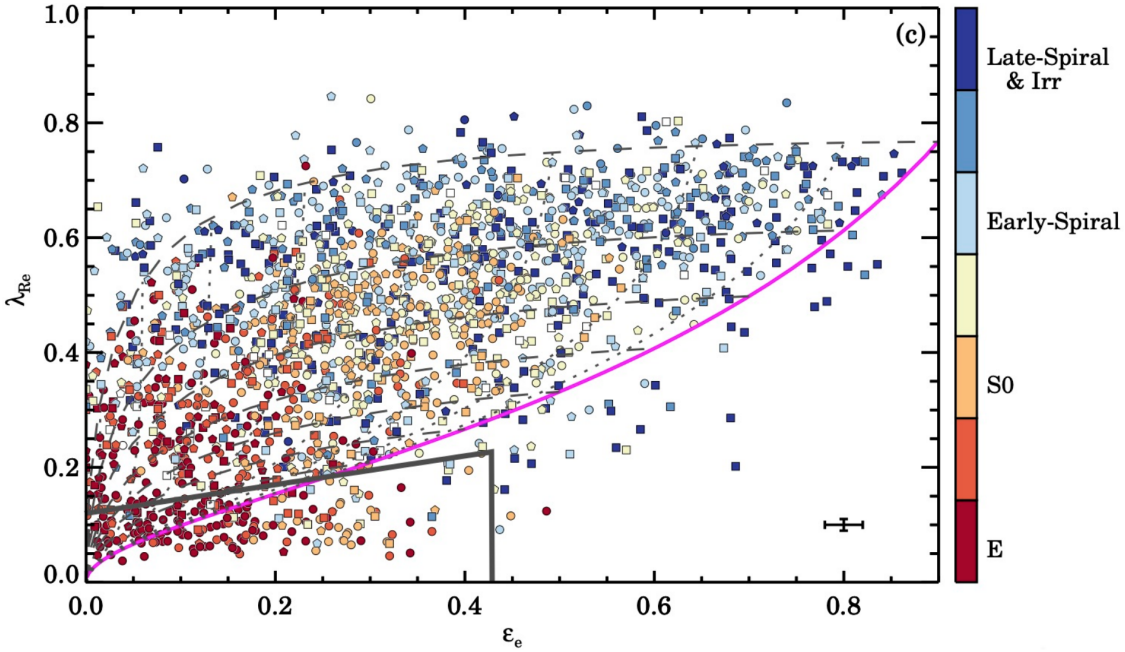

Figure 1.9: λ_{R_e} versus ε for the SAMI galaxy survey sample. Galaxies are further coloured by morphological type. The solid magenta line shows the theoretical prediction for edge-on regular rotators with anisotropy $\beta_z = 0.7$. Dashed lines show the same relation, but for varying intrinsic ellipticities, from 0.3-0.9. Dotted lines again show the same relation, but for varying inclinations from edge-on to face-on. The grey box in the bottom left corner shows the definition of slow rotators from van de Sande et al. (2021a), $\lambda_{R_e} < 0.12 + 0.25\varepsilon$, $\varepsilon < 0.428$. Figure taken from van de Sande et al. (2021a).

within $1R_e$. Finally, van de Sande et al. (2021a) used visual kinematic classification, the KINEMETRY measure (Krajnović et al., 2006, 2011), and the Matthews correlation coefficient (Matthews, 1975) to define slow rotators for the SAMI galaxy survey: $\lambda_{R_e} < 0.12 + 0.25\varepsilon$, $\varepsilon < 0.428$. This definition classifies visually round, dispersion supported galaxies as slow rotators, whilst allowing for projection effects. It also takes into account results from large surveys that suggest that genuine disk-less slow rotators are all rounder than $\varepsilon_e \lessapprox 0.4$ (CALIFA, SAMI, Falcón-Barroso et al., 2015; Fogarty et al., 2015). In Figure 1.9 we show this definition applied to galaxies from the SAMI galaxy survey, plotted in λ_{R_e} vs ellipticity ε_e space. Galaxies are coloured by morphological type, with the slow rotator region surrounded by a grey box in the bottom left. A clear correlation between morphology and slow rotators can be seen, with most slow rotators being an early-type elliptical or S0 galaxy. However, it's important to note that although the vast majority of slow rotators are ellipticals, 2/3 of ellipticals are fast rotators (Emsellem et al., 2011).

Galaxy morphology also correlates with environment, with Dressler 1980 showing that ETGs were preferentially found in high density environments, and LTGs in low density environments. With the advent of IFS surveys, this has been extended to a kinematic morphology-density relationship (KMDR) (Cappellari et al., 2011a). This KMDR shows that the fraction of slow rotator galaxies increases towards denser environments. Whilst there is strong evidence for this relationship (D'Eugenio et al., 2013; Houghton et al.,

2013; Scott et al., 2014; Fogarty et al., 2014), it is unclear to what degree it is truly driven by environment. Stellar mass might be the driver of the relationship (e.g. Brough et al., 2017; Veale et al., 2017; Greene et al., 2017; Lagos et al., 2017; Graham et al., 2019), or it could be *primarily* a mass driven relationship, with environment (van de Sande et al., 2021b) or age (van de Sande et al., 2018; Croom et al., 2024) as a second order effect. What is clear, however, is that the build-up of angular momentum, and thus λ_{R_e}, over the lifetime of the Universe is a very complex picture.

1.5.1 The Role of Mergers in Galaxy Evolution

The evolution of galaxies in the Universe under the ΛCDM paradigm (White & Rees, 1978) is strongly governed by the mergers galaxies undergo from their formation until $z = 0$. Whilst tracing the merger history of observed galaxies is a difficult task, N-body simulations (e.g. Kauffmann & White, 1993; Lacey & Cole, 1993) have shown that the current distribution of mass and clustering of galaxies requires the hierarchical build up of structure, where galaxies merge continuously over cosmological time.

Mergers may be classified in several ways, but are generally divided by the mass ratio, and the gas fraction of the merging galaxies. Major mergers are often defined as occurring when the mass ratio, μ, of the two galaxies is ≤ 3 (e.g. Conselice, 2006; Stewart, 2009), minor mergers when the ratio is $3 \leq \mu \leq 10$, and mini mergers for $10 \leq \mu \leq 100$ (Karademir et al., 2019). Wet mergers occur when the satellite galaxy is gas-rich, and dry mergers between two gas-poor galaxies (e.g. Lin et al., 2008).

While it is well established that the assembly of galaxy masses in the Universe requires mergers, the exact evolutionary pathways taken to reach the currently observed vast array of galaxy morphologies are less clear. Strongly negative metallicity gradients observed in elliptical galaxies (e.g. Parikh et al., 2019; Riffel et al., 2023) can be explained through monolithic collapse of primordial gas clouds at high redshifts ($z > 5$) (Larson, 1974; Chiosi & Carraro, 2002). Alternatively, simulations and observations of ellipticals with a flat metallicity gradient (e.g. Taylor & Kobayashi, 2017; Benedetti et al., 2023) can be explained through a merger scenario (Toomre & Toomre, 1972; Cole et al., 2000) which posits that modern-day ellipticals formed through a series of major and minor mergers over time. Today, a dual scenario for the formation of ETGs is preferred, where galaxies firstly undergo monolithic collapse, followed by a series of dry mergers (Kormendy, 1989).

Observationally identifying the earliest mergers in the Universe is a challenging task, as all morphological evidence of a past merger (e.g. tidal tails, streams, shells) settles into equilibrium within $\sim 2 - 4$ Gyr (Lotz et al., 2008, 2010a,b; Lofthouse et al., 2017; Mancillas et al., 2019; Nevin et al., 2021). Simulations are not bound in such ways as observations, and suggest that mergers kinematically and morphologically transform galaxies (e.g., Di Matteo et al., 2009; Jesseit et al., 2009; Bois et al., 2011; Naab et al., 2014; Choi & Yi, 2017; Lagos et al., 2017, 2018a; Penoyre et al., 2017; Schulze et al., 2020; Lagos, 2020b), causing a “spin-down" and transforming discs into ellipticals, and slow rotators. However, there is evidence that wet mergers may reform a fast-spinning disc post-merger (e.g. Lagos, 2020b), as well as induce starburst activity (e.g., Scott & Kaviraj, 2014; Knapen et al., 2015; Thorp et al., 2019; Bickley et al., 2022).

A significant consequence of both major, minor, wet, and dry mergers, is the production of extended, low surface brightness structures in galaxy outskirts. These features can extend up to several R_e in certain cases. The study of these faint features is thus a powerful tool for attempting to trace the recent merger histories of galaxies, and further, the formation and evolution of slow rotators.

1.5.2 Low Surface Brightness Features

Up to 40% of galaxies observed in the Universe show diffuse, extended, often difficult to detect structures at low surface brightness, understood to be relics of past interactions (e.g., Toomre & Toomre, 1972; van Dokkum, 2005; Hood et al., 2018; Mancillas et al., 2019; Huang & Fan, 2022; Khalid et al., 2024). Tidal forces during these interactions redistribute stars into diffuse features such as streams, shells, and plumes. The properties of these features are a function of the interaction that created them, and thus information can be gained from their size, shape, and colour (e.g. Johnston et al., 2008). See Figure 1.10 for an example of these tidal features.

Tidal tails and streams arise from the removal of stars and gas during interactions, either from a gas-rich, disc-dominated primary galaxy or a low-mass companion (Byrd & Howard, 1992; Oh et al., 2008; Hood et al., 2018). Streams are understood to result from circular infall interactions with high relative angular momentum between the two merging galaxies (i.e. high impact parameter), while shells result from radial orbits, often with higher mass ratios (e.g. Amorisco, 2015; Pop et al., 2018; Karademir et al., 2019; Yoon et al., 2024). Given this, mergers that leave shell remnants are more likely to have affected the inner regions of galaxies. This could impact their stellar kinematics within $1R_e$ more than mergers which leave stream/tail features.

Given the ΛCDM hierarchical structure formation theory discussed in Section 1.1.3, all galaxies are expected to have undergone multiple mergers over their lifetimes. If the mass ratio of the merger was small or the event occurred sufficiently long ago (e.g. $\gtrapprox$ 5 Gyr), any resulting tidal features may now be too faint to detect (e.g. Duc & Renaud, 2013; Ji et al., 2014). As a result, the observed fraction of galaxies exhibiting tidal features primarily depends on three factors: stellar mass ratio, time since merger, and the limiting surface brightness of the observations.

Simulations (e.g. Jian et al., 2012; Martin et al., 2022; Khalid et al., 2024) and observations (e.g. Atkinson et al., 2013; Huang & Fan, 2022; Sola et al., 2025) have consistently shown that the fraction of galaxies with tidal features increases with stellar mass. However, the relationship between limiting surface brightness (e.g. μ_r in the r-band) and detectability of tidal features in observations is more complex. Although most imaging surveys used for detection of low surface brightness features have limits of $\mu_r \lessapprox 30$ mag arcsec^{-2} (e.g. Duc et al., 2015; Ibata et al., 2017), many tidal features are expected to lie at $\mu_r \gtrapprox 30$ mag arcsec^{-2} (Johnston et al., 2008). Further, even at a nominal surface brightness limit, the identification of tidal features remains incomplete. For example, Kado-Fong et al. (2018) and Sola et al. (2022) demonstrated that tidal features injected into cutouts at a given surface brightness required a deeper limit for reliable detection.

Although tidal features allow us to infer information about recent interactions, they do

Figure 1.10: Multiple tidal tails and shells around NGC 474. These relics are understood to be a result of past interactions and mergers the galaxy has experienced. Image taken from Duc et al. (2015).

not probe how the dynamics of a galaxy have been affected, nor how the orbits of stellar populations may have been impacted. Progress can be made through the correlation of global kinematic measurements (e.g. λ_{R_e}), but for a more complete treatment, dynamical modelling provides methods of measuring kinematic structures and full orbital distributions.

1.6 Dynamical Modelling of Galaxies

Fundamentally, dynamical models of galaxies attempt to turn observed kinematic measurements of galaxies into physically meaningful quantities. In this thesis, we focus on two methods of dynamical modelling: Jeans Anisotropic MGE (JAM) models, and Schwarzschild orbit-superposition models.

1.6.1 Jeans Anisotropic MGE Models

Jeans' theorem (Jeans, 1922) is derived from the premise that the stars in a galaxy have positions ($\boldsymbol{x}$) and velocities ($\boldsymbol{v}$) that are described by some distribution function $f(\boldsymbol{x}, \boldsymbol{v})$. As a galaxy's stellar distribution is essentially entirely collisionless, $f(\boldsymbol{x}, \boldsymbol{v})$ should be well described by the steady-state collisionless Boltzmann equation (Binney & Tremaine, 1987):

$$\sum_{i=1}^{3} \left(v_i \frac{\partial f}{\partial x_i} - \frac{\partial \Phi}{\partial x_i} \frac{\partial f}{\partial v_i} \right) = 0 \tag{1.4}$$

where Φ is the gravitational potential. To enable solutions derived from observable kinematics, 1.4 is typically simplified under a series of standard assumptions, as described below.

Rewriting Equation 1.4 in cylindrical coordinates (R, z, ϕ) and assuming *axisymmetry* (i.e. $\partial\Phi/\partial\phi = \partial f/\partial\phi = 0$), the Jeans equations (Jeans, 1922) are obtained:

$$\frac{\nu\overline{v_R^2} - \nu\overline{v_\phi^2}}{R} + \frac{\partial(\nu\overline{v_R^2})}{\partial R} + \frac{\partial(\nu\overline{v_R v_z})}{\partial z} = -\nu\frac{\partial\Phi}{\partial R} \tag{1.5}$$

$$\frac{\nu\overline{v_R v_z}}{R} + \frac{\partial(\nu\overline{v_z^2})}{\partial z} + \frac{\partial(\nu\overline{v_R v_z})}{\partial R} = -\nu\frac{\partial\Phi}{\partial z} \tag{1.6}$$

where the following notation is used, with ν being the luminosity density:

$$\nu\overline{v_k v_j} \equiv \int v_k v_j f d^3v \tag{1.7}$$

These equations can now written in terms of the observable velocity moments, but further assumptions are needed to uniquely specify a solution. Firstly, it is assumed that the gravitational potential Φ can be derived from the observed luminosity distribution ν (if they are exactly equal, the solutions are *self-consistent*, however this is not required, and a dark matter profile may be added, for example). The next assumption is on the shape and alignment of the velocity ellipsoid. In principle, the velocity ellipsoid need not be aligned with any coordinate system, in which case all cross terms, $\overline{v_k v_j}$, are non-zero. However,

here we choose to align with cylindrical coordinates, as this is a reasonable assumption for spiral galaxies, particularly along the major and minor axis (e.g. Gerssen et al., 1997, 2000; Shapiro et al., 2003; Cappellari et al., 2007; Noordermeer et al., 2008). This assumption implies that the velocity dispersion tensor cross terms in cylindrical coordinates, $\overline{v_R v_z}$, are zero. It is also common to choose alignment with spherical, or prolate spheroidal coordinates, depending on the galaxies being modelled (Cappellari, 2008). Finally, we assume that the anisotropy is constant, and given by $\overline{v_R^2} = b\overline{v_z^2}$. Taking these assumptions with the boundary condition that $\nu\overline{v_z^2} = 0$ as $z \to \infty$, the Jeans equations (Equations 1.5 and 1.6) have the solutions:

$$\nu\overline{v_z^2}(R,z) = \int_z^\infty \nu \frac{\partial \Phi}{\partial z} dz \tag{1.8}$$

$$\nu\overline{v_\phi^2}(R,z) = b\left[\frac{\partial(\nu\overline{v_z^2})}{\partial R} + \nu\overline{v_z^2}\right] + R\nu\frac{\partial \Phi}{\partial R} \tag{1.9}$$

where ν is the luminosity density, R and z are the cylindrical coordinates, Φ is the gravitational potential, and b is an anisotropy parameter. Deprojecting an MGE model (Equation 1.2) obtains the luminous density ν:

$$\nu(R,z) = \sum_{k=1}^{N} \frac{L_k}{(\sqrt{2\pi}\sigma_k)^2 q_k} \exp\left[-\frac{1}{2\sigma_k^2}\left(R^2 + \frac{z^2}{q_k^2}\right)\right] \tag{1.10}$$

where N is the number of gaussian components, L_k the total luminosity of each component, σ_k the dispersion along the major axis, and q_k the intrinsic axis ratio. Φ, can be obtained by multiplying ν by a mass-to-light ratio, and a spherical NFW (Navarro et al., 1997) dark matter profile and central supermassive black hole may also be added as contributions to Φ. Equations 1.8 and 1.9 may then be solved to obtain the desired JAM models.

JAM models may be used to recover a galaxy's dynamical mass-to-light ratio, inclination, and dynamical mass. These models have been applied to early-type galaxies (e.g. Cappellari et al., 2013; Li et al., 2017; Ene et al., 2019) and spiral galaxies as well (e.g. Scott et al., 2015; Zhu et al., 2023). Additionally, JAM has been used to derive dark matter distributions from stellar dynamics and gravitational lensing (van de Ven et al., 2010; Barnabè et al., 2012), study initial mass function (IMF) variations (Cappellari et al., 2012), create discrete dynamical models of ω Centauri (Watkins et al., 2013), and perform time-delay cosmography (Shajib et al., 2023).

However, JAM is limited in its ability to model triaxial galaxies, or galaxies with distinct kinematic components (e.g. stellar bars) that arise from non-axisymmetric gravitational potentials. This is where orbit-superposition methods can become very useful, such as Schwarzschild's method.

1.6.2 Schwarzschild Models

Schwarzschild's method (Schwarzschild, 1979, 1982), also referred to as Schwarzschild modelling, is a flexible method to reconstruct the stellar dynamics of galaxies, while accommodating triaxial mass distributions. Rather than modelling the gravitational interaction each star within a galaxy (of which there may be up to $\sim 10^{12}$) has with every

other star, Schwarzschild's method models each star moving within a *global* gravitational potential. By constructing this potential $\Phi(x, y, z)$ with contributions from luminous and dark matter, building a library of allowed orbits, and numerically integrating these orbits within the potential, the model is obtained. LOSVDs are then derived from the integrated orbits and compared to observed LOSVDs as a measure of goodness-of-fit. The final model describes the full orbital distribution of the observed galaxy.

The calculation of a Schwarzschild model begins by estimating the gravitational potential for the galaxy, taking into account stellar mass and dark matter. Most Schwarzschild codes (e.g. DYNAMITE, Thater et al., 2022) use the MGE formalism (Emsellem et al., 1994a; Cappellari, 2002) to model a galaxy's observed luminosity density. The MGE is deprojected to a triaxial three-dimensional light distribution, constrained by the intrinsic shape of the flattest Gaussian component, parametrised by ($p_{\rm min}$,$q_{\rm min}$,$u_{\rm min}$). This is then multiplied by a M_*/L ratio, often taken to be globally constant. The resulting mass distribution specifies the stellar mass gravitational potential. A dark matter halo (e.g. NFW, Navarro et al., 1996) can then be added to form the full potential.

The second step is to calculate a library of stellar orbits allowed by the gravitational potential. These orbits are regular, i.e. they conserve three integrals of motion (E, I_2, I_3) and their trajectory lies on non-chaotic, predictable paths. The integrals of motion may be sampled several times, and further dithered over to smooth the model. Schwarzschild's method (Schwarzschild, 1979, 1982; Zhu et al., 2018b) may then be used to calculate the weight of each orbit's contribution to the LOSVD in each bin, recreating the observed velocity maps. These maps are convolved with a PSF and divided by the observational error to obtain a χ^2 comparison.

Finally, a grid search is run over the free parameters of the model to minimise χ^2. The free parameters depend on the chosen parameterisations, but they commonly include $p_{\rm min}$, $q_{\rm min}$, $u_{\rm min}$, M_*/L, and the parameters of a dark matter halo. For example, for an NFW halo, the parameters are the concentration c and fraction of dark matter within R_{200}, f. For 4-moment velocity maps, the grid search seeks to minimise χ^2, defined as:

$$\chi^2 = \sum_{n=1}^{N_{\rm kin}} \left[\left(\frac{V^n_{\rm mod} - V^n_{\rm obs}}{V^n_{\rm obserr}} \right)^2 + \left(\frac{\sigma^n_{\rm mod} - \sigma^n_{\rm obs}}{\sigma^n_{\rm obserr}} \right)^2 + \left(\frac{h^n_{3,\,\rm mod} - h^n_{3,\,\rm obs}}{h^n_{3,\,\rm obserr}} \right)^2 + \left(\frac{h^n_{4,\,\rm mod} - h^n_{4,\,\rm obs}}{h^n_{4,\,\rm obserr}} \right)^2 \right]$$

where $V^n_{\rm mod}$, $\sigma^n_{\rm mod}$, $h^n_{3,\,\rm mod}$, $h^n_{4,\,\rm mod}$ are the model velocities for bin n in the velocity maps, $V^n_{\rm obs}$, $\sigma^n_{\rm obs}$, $h^n_{3,\,\rm obs}$, $h^n_{4,\,\rm obs}$ are the observed velocities, $V^n_{\rm obserr}$, $\sigma^n_{\rm obserr}$, $h^n_{3,\,\rm obserr}$, $h^n_{4,\,\rm obserr}$ are the observational errors and $N_{\rm kin}$ is the number of bins. Each model velocity is convolved with the same PSF as the observations prior to calculating χ^2. Once a best-fit model is obtained, the orbital distributions, velocity anisotropy, triaxilality, total mass and spin parameter $\lambda_{R_{\rm e}}$ can be derived for a given galaxy.

Schwarzschild models have been used to model supermassive black holes (e.g. Krajnović et al., 2009; Thater et al., 2019; Quenneville et al., 2021), globular clusters (e.g. van de Ven et al., 2006; Feldmeier-Krause et al., 2017), and galaxies of all morphologies (e.g. Zhu et al., 2018a; Poci et al., 2019; Jin et al., 2020; Vasiliev & Valluri, 2020). Further,

the orbital distributions obtained from these models has been used to identify dynamical components within galaxies (e.g. Cappellari et al., 2007; van den Bosch et al., 2008; Breddels & Helmi, 2014; Krajnović et al., 2015). Combining such orbit-based dynamical models with environmental metrics therefore provides a direct bridge between the internal stellar kinematics of galaxies and the environments in which they reside.

1.7 Thesis Goals

The advent of large IFS surveys has enabled the statistical study of spatially resolved properties of galaxies in the nearby Universe. In this thesis, we study the connection between stellar kinematics and environment. We investigate measurements of large-scale structure to statistically link dynamical support to environmental density, and extend this to galaxy mergers through the detection of tidal features in deep imaging. We derive the orbital distribution of galaxies through orbit-superposition modelling to further establish the impact of mergers on stellar dynamics. Finally, we demonstrate that when kinematic measurements are available at spatial resolutions of ~10s of parsecs, axisymmetric modelling of galaxies provides clear identification of non-axisymmetric kinematic structure such as stellar bars and nuclear discs.

In Chapter 2, we present results that were published in the Astrophysical Journal. In this paper, we investigate the kinematic morphology density relation. We use marked correlation functions to explore the relationship between large-scale structure and the galaxy spin parameter λ_{R_e}, and attempt to determine whether it persists independently of any stellar mass correlations.

In Chapter 3, we present results that were published in the Monthly Notices of the Royal Astronomical Society. In this paper, we analyse the relationship between tidal features detected in deep imaging of galaxies and their kinematic properties. Taking our sample as SAMI early-type galaxies with $M_* > 10^{10} M_\odot$, we investigate the relationship between merger history, galaxy spin λ_{R_e}, and stellar age. We further attempt to identify the formation pathway for slow rotator galaxies.

In Chapter 4, we further analyse the relationship between tidal features and λ_{R_e}, by creating orbit superposition-based Schwarzschild dynamical models of our sample. We investigate how the proportion of cold, warm and hot orbits, as well as triaxiality, depends on merger history, stellar age and environment.

In Chapter 5, we present work that was published in Astronomy & Astrophysics. In this paper, we model GECKOS galaxies with axisymmetric Jeans Anisotropic MGE models. We apply these models to extremely highly spatially resolved MUSE data. We attempt to detect the excess velocities in edge-on disc galaxies typical of the end of a stellar bar. We further explore the impact of dust on dynamical modelling, with an aim to provide a basis for future, more detailed dynamical models.

Finally, in Chapter 6, we summarise this thesis and conclude all results. Additionally, we outline the next steps and prospects in this topic that will can inform future work.

Chapter 2

The SAMI Galaxy Survey: Detection of Environmental Dependence of Galaxy Spin in Observations and Simulations Using Marked Correlation Functions

Never be cruel. Never be cowardly. Hate is always foolish. Love is always wise. Always try to be nice, but never fail to be kind. Laugh hard. Run fast. Be kind.

—The Twelfth Doctor

Tomas H. Rutherford,[1,2] Scott M. Croom,[1,2] Jesse van de Sande,[1,2] Claudia del P. Lagos,[3,2] Joss Bland-Hawthorn,[1,2] Sarah Brough,[4,2] Julia J. Bryant,[1,5,2] Francesco D'Eugenio,[6] and Matt S. Owers[7,8]

[1]Sydney Institute for Astronomy, School of Physics, A28, The University of Sydney, NSW, 2006, Australia
[2]ARC Centre of Excellence for All Sky Astrophysics in 3 Dimensions (ASTRO 3D), Australia
[3]International Centre for Radio Astronomy Research (ICRAR), M468, University of Western Australia, 35 Stirling Hwy, Crawley, WA 6009, Australia
[4]School of Physics, University of New South Wales, NSW 2052, Australia
[5]Australian Astronomical Optics, AAO-USydney, School of Physics, University of Sydney, NSW 2006, Australia
[6]Sterrenkundig Observatorium, Universiteit Gent, Krijgslaan 281 S9, B-9000 Gent, Belgium
[7]Department of Physics and Astronomy, Macquarie University, NSW 2109, Australia
[8]Astronomy, Astrophysics and Astrophotonics Research Centre, Macquarie University, Sydney, NSW 2109, Australia

This chapter is reproduced from Rutherford et al. (2021), which was published in the Astrophysical Journal as "The SAMI Galaxy Survey: Detection of Environmental Dependence of Galaxy Spin in Observations and Simulations Using Marked Correlation Functions". I wrote all the text, produced all figures, and wrote all code for analysis. Scott M. Croom and Jesse van de Sande supervised the work and assisted in revising the text. Claudia del P. Lagos provided the EAGLE simulation measurements for comparison with SAMI observational measurements.

Abstract

The existence of a kinematic morphology-density relation remains uncertain, and instead stellar mass appears the more dominant driver of galaxy kinematics. We investigate

the dependence of the stellar spin parameter proxy λ_{R_e} on environment using a marked cross-correlation method with data from the SAMI Galaxy Survey. Our sample contains 710 galaxies with spatially resolved stellar velocity and velocity dispersion measurements. By utilising the highly complete spectroscopic data from the GAMA survey, we calculate marked cross-correlation functions for SAMI galaxies using a pair count estimator and marks based on stellar mass and λ_{R_e}. We detect an anti-correlation of stellar kinematics with environment at the 3.2σ level, such that galaxies with low λ_{R_e} values are preferably located in denser galaxy environments. However, a significant correlation between stellar mass and environment is also found (correlation at 2.4σ), as found in previous works. We compare these results to mock-observations from the cosmological EAGLE simulations, where we find a similar significant λ_{R_e} anti-correlation with environment, and a mass and environment correlation. We demonstrate that the environmental correlation of λ_{R_e} is not caused by the mass-environment relation. The significant relationship between λ_{R_e} and environment remains when we exclude slow rotators. The signals in SAMI and EAGLE are strongest on small scales (10-100 kpc) as expected from galaxy interactions and mergers. Our work demonstrates that the technique of marked correlation functions is an effective tool for detecting the relationship between λ_{R_e} and environment.

2.1 Introduction

A relationship exists between galaxy properties and local environmental density (Dressler, 1980), such that early-type galaxies (ETGs) are preferably found in denser environments. Although the kinematic properties of galaxies do not correlate one-to-one with visual morphology, a tentative relationship between a proxy for the spin parameter, λ_{R_e}, and environmental density was presented by Cappellari et al. (2011b). This kinematic morphology-density relation (KMDR) suggests that the fraction of slow rotating galaxies (low λ_{R_e}) increases towards denser environments. However, galaxy stellar mass also correlates with both environment and the intrinsic properties of galaxies. Thus, the question arises what the true physical driver of the KMDR is.

Further work supported the picture of a KMDR (D'Eugenio et al., 2013; Houghton et al., 2013; Scott et al., 2014; Fogarty et al., 2014). More recent results with larger galaxy samples find that the KMDR is driven mostly by stellar mass (Brough et al., 2017; Veale et al., 2017; Greene et al., 2017), but that the KMDR may also still exist at fixed stellar mass (Graham et al., 2019). There is also evidence from simulations that points towards environmental dependence as a weaker secondary effect, but mass as the primary physical driver (e.g. Lagos et al., 2017). Some clear results have emerged, i.e. the trend with mass, but it is evident that any environmental dependence is likely to be a second order effect.

Multi-object integral field spectroscopy has revolutionised the number of galaxies with spatially resolved kinematic measurements. The Sydney-Australian-Astronomical-Observatory Multi-object Integral-Field Spectrograph (SAMI) galaxy survey has observed ~3000 galaxies (Croom et al., 2012), while the Mapping Nearby Galaxies at Apache Point Observatory (MaNGA) survey aims to observe ~10,000 galaxies (Bundy et al., 2015). Other ancillary surveys such as the Sloan Digital Sky Survey (SDSS; York et al., 2000) and the Galaxy and Mass Assembly Survey (GAMA; Driver et al., 2011) enable an ac-

curate definition of environment, tracing the underlying large scale structure that exists in the Universe.

With the growing wealth of spatially resolved kinematic data, the statistical tool of correlation functions becomes more powerful. It allows us to connect large scale structure in galaxy clustering to internal galaxy properties, in our case galaxy spin, parameterised by λ_{R_e}Correlation functions have already demonstrated a relation between environment and the star-forming and morphological properties of galaxies (e.g. Madgwick et al., 2003; Hermit et al., 1996). Marked correlation functions, where galaxies are marked by some physical parameter, are even more effective at detecting and quantifying weak correlations with environment (Sheth & Tormen, 2004; Harker et al., 2006), making this method ideal for detecting a possible relation between λ_{R_e} and environment.

Most papers look at the fraction of fast and slow rotators as a function of mass and environment (Cappellari et al., 2011b; Brough et al., 2017; Veale et al., 2017; Greene et al., 2017; Graham et al., 2019), whereas a broader analysis of the λ_{R_e} distribution as a function of mass and environment shows that environment might have a small impact on λ_{R_e} (Wang et al., 2020).

In this paper we aim to investigate the correlation between λ_{R_e} and environmental density. We present an analysis using marked cross correlation functions applied to SAMI (Croom et al., 2012) and GAMA (Driver et al., 2011) data, as well as mock observations from the EAGLE Simulations (Schaye et al., 2015). We adopt a ΛCDM cosmology, with $H_0 = 70$ km s^{-1} Mpc^{-1}, $\Omega_m = 0.3$, $\Omega_\Lambda = 0.7$.

2.2 Observations and Simulations

2.2.1 Observations

The SAMI instrument (Croom et al., 2012) is mounted on the Anglo-Australian Telescope and provides a 1 degree diameter field of view. SAMI employs 13 fused fibre bundles (Hexabundles; Bland-Hawthorn et al., 2011; Bryant et al., 2014) with a high (75%) fill factor. Each bundle contains 61 fibres of 1.6″diameter resulting in each IFU having a diameter of 15 ″. The IFUs, as well as 26 sky fibres, are fed to the AAOmega spectrograph (Sharp et al., 2006), using the 580V grating at 3570-5750A giving a resolution of R=1808 (σ=70.4 km s^{-1}), and the R1000 grating from 6300-7400A giving a resolution of R-4304 (σ=29.6 km s^{-1}) (van de Sande et al., 2017b).

The SAMI Galaxy survey (Croom et al., 2012; Bryant et al., 2015) selected galaxies from the GAMA (Driver et al., 2011) survey, in addition to eight low-redshift clusters (Owers et al., 2017). Reduced data cubes (Sharp et al., 2015) and stellar kinematic maps are available with the SAMI Galaxy Survey data releases (Allen et al., 2015; Green et al., 2018; Scott et al., 2018; Croom et al., 2021).

Our sample contains 1832 galaxies with λ_{R_e} measurements, derived from spatially resolved kinematic measurements as described in van de Sande et al. (2017b), and include an aperture correction (van de Sande et al., 2017a) and a seeing correction (Harborne et al., 2020; van de Sande et al., 2020). Furthermore, we define a volume-limited sample by

selecting galaxies at: 1) $z < 0.06$ to avoid biases in the marked correlation function as the SAMI selection function results in different distributions of galaxy stellar masses in different volumes, and 2) $M/M_{\odot} > 10^{10}$ to avoid low-completeness in the stellar kinematic sample. Alternatively, we could have treated each redshift section within the SAMI function selection individually, and taken a variance weighted mean of each resulting correlation function. While this achieves a stronger signal, the result becomes more difficult to interpret due to our ranking method for weights (Section 2.3). The final sample contains 710 galaxies, of all morphological types. This sample is unique amongst other similar surveys. For example, ATLAS^{3D}'s sample for kinematic analysis (Cappellari et al., 2011b) only contained 260 field ETGs, and MaNGA (10,000 galaxies, Bundy et al., 2015) is only a narrow band in the mass redshift plane, with a complicated selection function that may make analyses that require volume limited samples more difficult to replicate.

Galaxies from the GAMA survey (Driver et al., 2011; Liske et al., 2015) serve as a background galaxy distribution for our analysis. GAMA adopted an r-band magnitude limit of $r_{\rm pet} < 19.8$ mag. For our analysis, we restrict the GAMA sample at $z < 0.06$ ($z_{\rm max}$ of SAMI) and define a volume-limited sample in redshift and r-band apparent magnitude. This was done so that the background distribution was not biased by a higher density of fainter galaxies at lower redshifts in an apparent magnitude limited sample. The GAMA data used in this paper came from three equatorial regions centred at 9^h, 12^h and 14.5^h in RA, each of 12×4 deg^2.

2.2.2 Simulations

We use galaxy mock-observations from the EAGLE hydrodynamical cosmological simulation suite (Schaye et al., 2015) as presented by Lagos et al. (2018b). A total of 7×10^8 galaxies were extracted from the 100 Mpc^3 box, where each baryonic particle has an initial mass of 1.8×10^6M$_{\odot}$, with a maximum gravitational softening length of 0.7 kpc. We adopt a stellar mass cut of $\rm M_{stars} > 5 \times 10^9$ M$_{\odot}$, to ensure galaxies had angular momentum profiles that converged. λ_{R_e} values were derived for mock-observations of this sample, leaving us with 5587 galaxies. A sample of 29737 galaxies not subjected to the stellar mass cut serves as the background galaxy distribution. These samples have an effective mass limit of $M/M_{\odot} > 10^{8.5}$.

Additionally, as the mass distributions of SAMI and EAGLE galaxies are significantly different, we use a set of galaxies sampled from EAGLE in such a way to match the SAMI mass distribution. The initial distributions can be seen in Figure 2.1.

2.3 Marked Correlation Functions

Marked statistics are a powerful tool to determine whether correlations between galaxy parameters depend on environment or not. Galaxies are assigned a mark, corresponding to some physical parameter, and a marked correlation function (Sheth & Tormen, 2004; Sheth et al., 2005a) is calculated. We begin by defining the 2-point real-space correlation

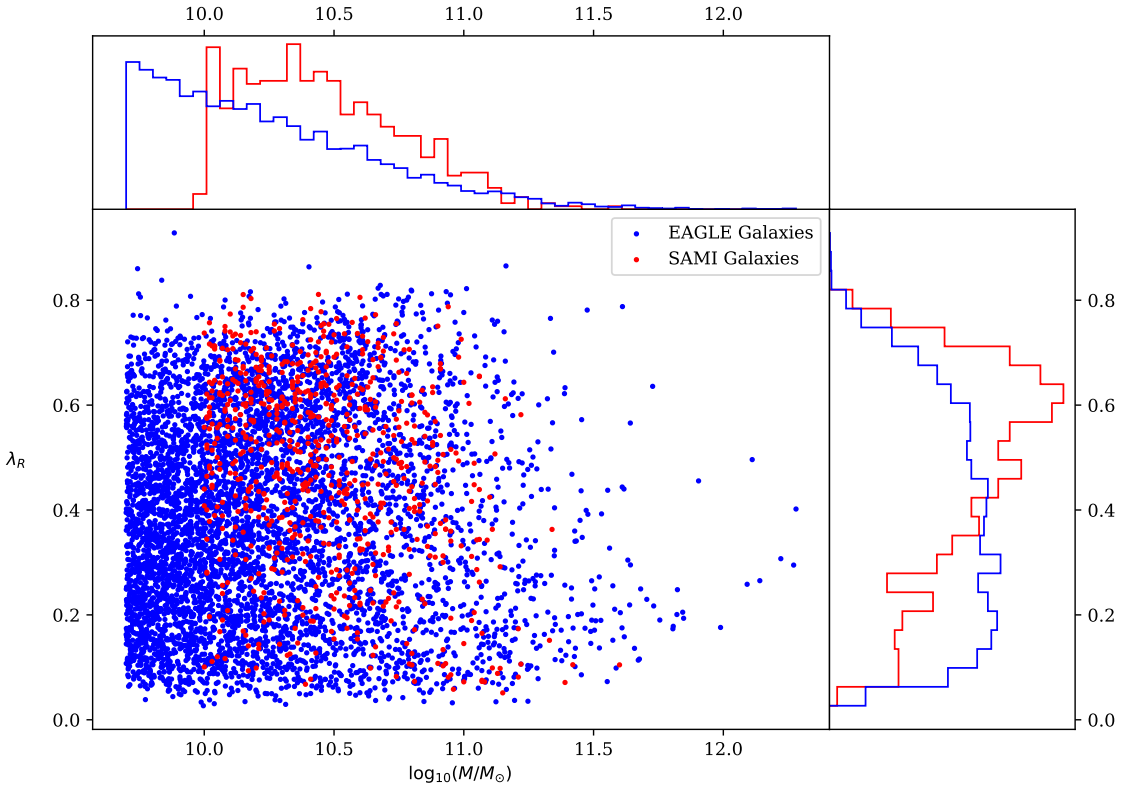

Figure 2.1: The distribution of SAMI (red) and EAGLE (blue) galaxies in $\log_{10}(M/M_\odot)$-λ_{R_e} space. The normalised histograms of both samples for both parameters is also included. In this paper we adopt a mass limit for SAMI of $\log_{10}(M/M_\odot) > 10$.

function $\xi(r)$, given by Peebles (1980):

$$dP = \rho^2[1 + \xi(r)]dV_1 dV_2, \tag{2.1}$$

where dP is the probability for two galaxies to be located at a distance r from each other, in volume elements dV_1 and dV_2. ρ is the mean density of galaxies in the volume considered. The correlation function $\xi(r)$ measures the "overdensity" of galaxies. In our case, we assume that redshift gives the radial distance to a galaxy. This is known as a redshift-space (s) correlation function, $\xi(s)$.

In practice, estimators are used to calculate $\xi(s)$. We use an estimator introduced by Peebles (1980):

$$1 + \xi(s) = \frac{\langle SG(s)\rangle}{\langle SG_R(s)\rangle}, \tag{2.2}$$

where $\langle SG(s)\rangle$ and $\langle SG_R(s)\rangle$ are pair counts between a SAMI (S) and GAMA (G) galaxy, and a SAMI and random GAMA (G_R) galaxy respectively. These pair counts are calculated by first defining radial bins, equally spaced in $\log_{10}(s)$. A SAMI galaxy is selected, and the distance to each GAMA galaxy is calculated. A count is then added to each relevant radial bin. This is repeated for all SAMI galaxies. Random GAMA galaxies are a sample of GAMA-like galaxies, created in such a way to match GAMA's selection function.

We now assign SAMI galaxies marks (m). Galaxies are ranked in λ_{R_e} and log stellar mass, with the mark taken as the rank, to ensure an equivalent dynamical range for both marks.

Marked correlation functions can then be thought of as a ratio of galaxy marks to the mean mark, $\overline{m}$, as a function of galaxy separation (Sheth et al., 2005a):

$$M(s) \equiv \frac{\sum m(\boldsymbol{x})m(\boldsymbol{y})\mathcal{I}(|\boldsymbol{x}-\boldsymbol{y}|-s)}{\overline{m_x m_y}\sum \mathcal{I}(|\boldsymbol{x}-\boldsymbol{y}|-s)} = \frac{\sum m(\boldsymbol{x})\mathcal{I}(|\boldsymbol{x}-\boldsymbol{y}|-s)}{\overline{m}\rho^2[1+\xi(s)]}, \tag{2.3}$$

where $m(\boldsymbol{x})$ is the mark of a SAMI galaxy. We have defined the mark of all GAMA galaxies $[m(\boldsymbol{y})]$ to be 1, $\mathcal{I}(x) = 0$ unless $x = 0$, and the sum is over all SAMI-GAMA galaxy pairs. As we have divided by $\overline{m}$, $M(s) = 1$ for all s if no correlation between marks and environment exists.

We can also consider Equation 2.3 in an alternate way. By a simple re-arrangement, the denominator can be expressed as one plus the regular correlation function, defined in Equation 2.1, and the numerator as one plus a "weighted" correlation function. This weighted correlation function, defined as $W(s)$, can be calculated using the same estimator as $\xi(s)$, except the i^{th} SAMI galaxy contributes a weight of $m_i/\overline{m}$ to the relevant radial bins:

$$M(s) \equiv \frac{\sum (m(\boldsymbol{x})/\overline{m})\mathcal{I}(|\boldsymbol{x}-\boldsymbol{y}|-s)}{\sum \mathcal{I}(|\boldsymbol{x}-\boldsymbol{y}|-s)} \equiv \frac{1+W(s)}{1+\xi(s)} = \frac{\langle WG(s)\rangle}{\langle SG(s)\rangle}, \tag{2.4}$$

where $\langle WG(s)\rangle$ are *weighted* pair counts between weighted SAMI (W) and GAMA (G) galaxies, and $\langle SG(s)\rangle$ are *unweighted* pair counts between SAMI (S) and GAMA galaxies. Marked correlation functions with random marks are also calculated, as a check that any signal seen in the real functions is legitimate. Once our correlation functions are calculated, we use the Python emcee package (Foreman-Mackey et al., 2013a) to fit a function of the form:

$$M(s) = 1 + As^{-m} \tag{2.5}$$

We use this functional form as we expect $M(s) \approx 1$ for all scales other than small scales, where it may deviate according to possible spin-environment and mass-environment relations. Uncertainties are calculated from the 16^{th} and 84^{th} percentiles.

2.3.1 Uncertainty Calculation

We choose bootstrap re-sampling for our uncertainty estimate, as bootstrap re-sampling is robust and as shown by Fisher et al. (1994), at worst overestimates error in correlation functions. Importantly, bootstrap uncertainties assume zero correlation between points, which is not strictly true in our case, as single galaxies contribute to multiple pair counts. However, on small scales the data points are largely independent, due to the small number of galaxies contributing to pairs at such small separation. As another test, we also evaluated another two different error estimations. We divided our sample into nine regions, and calculated a correlation function in each region, taking the standard deviation between the regions. We also calculated Poissonian errors for each bin. We found that the bootstrap errors were similar to Poissonian at small scales, and similar to the nine region standard

deviation at large scales. Due to this, and our largely independent points at small scales, we use ordinary bootstrap re-sampling as a close approximation of errors.

As bootstrap re-sampling generally overestimates uncertainties at small scales by a factor $\sqrt{3}$ (Croom & Shanks, 1996), the number of SAMI galaxies drawn per bootstrap sample was $3N$, where N is the total number of galaxies, as also suggested by Norberg et al. (2001). Previous galactic correlation function works have used 10 re-samples (Hermit et al., 1996) or 20 re-samples (Madgwick et al., 2003). Due to our smaller data set in SAMI, we created 10,000 re-samples for each correlation function.

2.4 Results

2.4.1 SAMI Galaxies

We present marked correlation functions for SAMI Galaxies, with ranked λ_{R_e} and stellar mass marks, in Figure 2.2.

Towards small scales s we find that the marked correlation measurements (orange symbols) are significantly less than 1, i.e., there is a significant anti-correlation of ranked λ_{R_e} with environment. The best-fit power-law (Equation 2.5, Figure 2.2a, red line), shows a significant turn below $M(s) = 1$, beginning at around $s = 1$ Mpc. We find a best-fit value for $A = -0.038^{+0.012}_{-0.013}$, 3.2σ below zero. This implies that galaxies with low λ_{R_e} start being preferentially located in dense environments at scales of $s \approx 1$ Mpc. As done by Harker et al. (2006), we also take one large radial bin out to 1 Mpc to find significance at small scales ($M(< 1Mpc)$). We find $M(< 1Mpc) = 0.925 \pm 0.034$, 2.2σ below 1. Randomised marks are consistent with $M(s) = 1$ at all scales.

In Figure 2.2b we also detect a significant correlation of ranked stellar mass with environment. The best-fit power-law (red line) shows a significant up turn above $M(s) = 1$ towards small scales in s, beginning at around $s = 1$ Mpc. We find a best-fit value of $A = 0.036^{+0.015}_{-0.015}$, 2.4σ above zero. This result implies that galaxies with high stellar mass start being preferentially located in dense environments at scales of ≈ 1 Mpc. We find $M(< 1Mpc) = 1.058 \pm 0.042$, 1.4σ above zero. This result is consistent with previous work, as galaxies are well known to cluster according to mass (or luminosity) (e.g. Norberg et al., 2002). Randomised marks are consistent with $M(s) = 1$ at all scales.

Further Analysis of SAMI Results

We have found an anti-correlation of λ_{R_e} with environment, and a positive correlation of stellar mass with environment. We can compare these results with different tests. First, we reverse the rank order for λ_{R_e} and compare $M(< 1Mpc)$ for these reverse λ_{R_e} ranks and stellar mass ranks. We find $M(< 1Mpc) = 1.075 \pm 0.043$ for reverse λ_{R_e} and $M(< 1Mpc) = 1.058 \pm 0.041$ for stellar mass. This gives a difference of 0.017 ± 0.059. Using this metric, mass and reverse λ_{R_e} rank marks are consistent. However, this simplistic approach of assuming a one-to-one relationship between reversed λ_{R_e} ranks and stellar mass ranks is not entirely supported, as there is a lot of scatter in this relationship (Croom et al., 2021). In Figure 2.3, we present two methods of testing for the physical driver of our SAMI λ_{R_e}-environment anti-correlation. Bins are defined in stellar mass of 0.1 dex

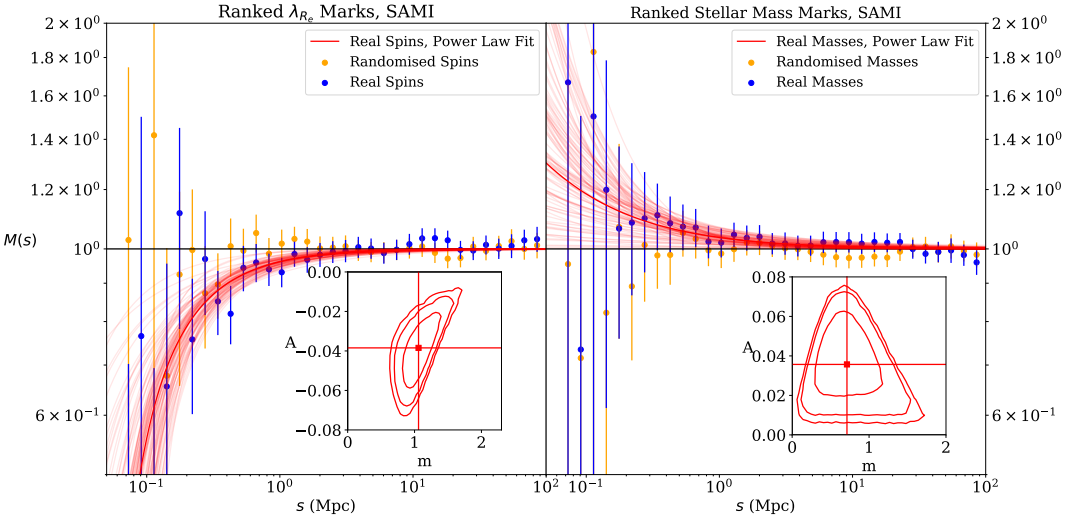

Figure 2.2: Marked correlation functions for ranked λ_{R_e} (left panel) and ranked stellar mass marks (right panel), with SAMI galaxies (blue data). Randomised marks are plotted as a test of our method (orange data). We plot the best-fit power law (dark red line). One hundred samples from the MCMC chain (light red lines) are plotted, as a representation of the uncertainty in the fits. Contours for the 68^{th}, 90^{th} and 95^{th} percentiles are plotted for the real data in A and m space, as explored by the emcee algorithm, in the inset. The red overlay lines in these parameter spaces represent the values of A and m selected at the 50^{th} percentile. Measures of the significance can be found in Table 2.1. λ_{R_e} is negatively correlated with environment, while stellar mass is positively correlated with environment in SAMI galaxies.

in width. Galaxies are then assigned a λ_{R_e} value from another random galaxy in their mass bin. This failed to reproduce a negative correlation with environment. The lack of correlation in this case implies that the signal we see between λ_{R_e} and environment cannot be caused purely by a mass-environment relation. Removing slow rotators ($\lambda_{R_e} < 0.2$) from the sample did reproduce a negative correlation with environment. This existence of a correlation implies that the observed correlation between λ_{R_e} and environment cannot be attributed solely to slow rotators.

2.4.2 EAGLE Galaxies

We show the distribution in λ_{R_e} and stellar mass of SAMI and EAGLE galaxies in Figure 2.1. As the mass distributions are significantly different, we create a set of observations sampled from EAGLE in such a way to match the SAMI mass distribution. Fifty bins spaced in $\log(M/M_\odot)$ were defined across the mass range for SAMI, and EAGLE galaxies in each bin were drawn randomly until there were three times as many EAGLE galaxies in each bin as SAMI.

We present marked correlation functions for these re-sampled EAGLE galaxies, with ranked λ_{R_e} and stellar mass marks, in Figure 2.4. We see a significant anti-correlation of ranked λ_{R_e} with environment in our marked correlation function for EAGLE (Figure 2.4a).

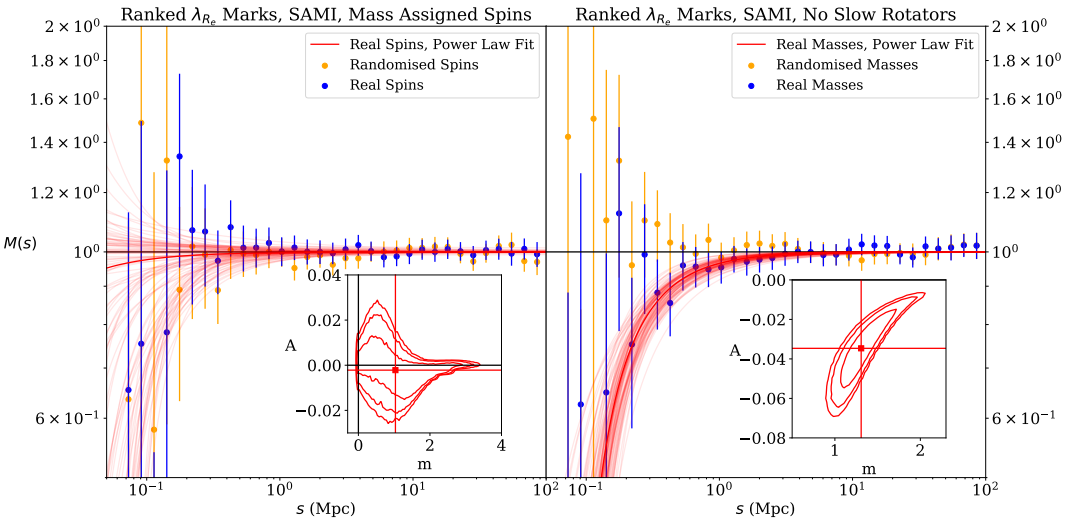

Figure 2.3: Marked correlation functions for different tests exploring whether our SAMI λ_{R_e} anti-correlation with environment can be explained by mass trends. Selecting a galaxy's λ_{R_e} value at random from 0.1 dex mass bins failed to reproduce a negative correlation (left panel). Removing slow rotators from the SAMI sample ($\lambda_{R_e} < 0.2$) still reproduces a negative correlation (right panel). Randomised marks are also plotted as a test of our method. Symbols and lines are similar as in Figure 2.2, but now presented for mass-defined λ_{R_e} and for a sample with slow rotators removed. The anti-correlation of λ_{R_e} with environment is not driven purely by stellar mass, or by slow rotators.

The best-fit power-law shows a significant downward trend towards small scales in s. m is lower for EAGLE than for SAMI, so the correlation between λ_{R_e} and environment extends to larger scales in EAGLE than in SAMI. We find a best-fit value of $A = -0.020^{+0.003}_{-0.003}$, 6.6σ below zero. This implies that in the EAGLE mock-observations, low-λ_{R_e} galaxies are preferentially located in dense environments, out to scales of the order ~1 Mpc. This is consistent with our SAMI results. We find $M(< 1Mpc) = 0.966 \pm 0.008$, 4.2σ below 1. Randomised marks are consistent with $M(s) = 1$ at all scales.

We see a significant correlation of ranked stellar mass with environment in our marked correlation function for EAGLE. The best-fit power-law shows a significant upwards trend towards small scales in s. We find a best fit value of $A = 0.030^{+0.003}_{-0.003}$, 10σ above zero. This implies that in the EAGLE mock-observations, high stellar mass galaxies are preferentially located in dense environments, out to scales of the order ~ 10 Mpc. We find $M(< 1Mpc) = 1.066 \pm 0.015$, 4.4σ above 1. Randomised marks are consistent with $M(s) = 1$ at all scales, as expected.

2.5 Conclusion

We investigate the existence of a kinematic morphology-density relation (KMDR) using the technique of marked correlation functions. Ranking galaxies by their spin (parametrised by λ_{R_e}) and stellar mass allows us to investigate whether the relation is driven purely

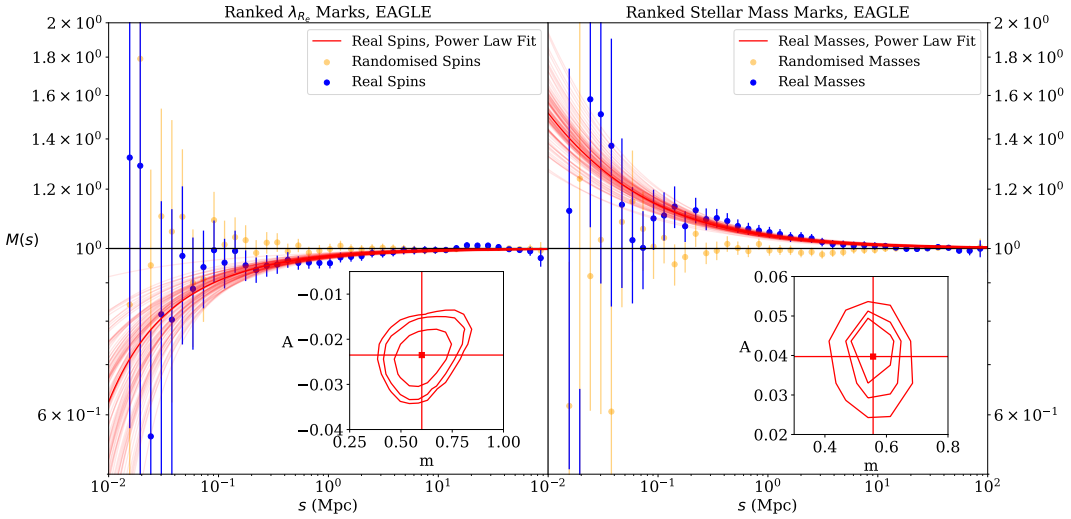

Figure 2.4: Marked correlation functions for ranked λ_{R_e} (left panel) and ranked stellar mass marks (right panel). Symbols and lines are similar as in Figure 2.2, but now presented for the EAGLE data. λ_{R_e} is negatively correlated with environment, while stellar mass is positively correlated with environment in EAGLE galaxies.

Table 2.1: Measurements of the significance of the signals in the correlation functions for SAMI and EAGLE data. We present the values of A and m for each data type and mark type, and the value of a single bin below 1 Mpc for each data type and mark type. The significance for the single bin is taken as the distance away from $M(s) = 1$, the expected value given no correlation.

Data Type	Mark Type	A	m	Single Bin Value
SAMI Spin Data	Real	$-0.038^{+0.012}_{-0.013}$	$1.060^{+0.196}_{-0.179}$	0.925 ± 0.035
	Random	$-0.008^{+0.005}_{-0.008}$	$1.850^{+0.412}_{-0.317}$	0.981 ± 0.038
SAMI Mass Data	Real	$0.036^{+0.015}_{-0.015}$	$0.713^{+0.320}_{-0.255}$	1.058 ± 0.041
	Random	$-0.003^{+0.009}_{-0.011}$	$0.795^{+0.706}_{-0.512}$	1.019 ± 0.039
Re-sampled EAGLE Spin Data	Real	$-0.020^{+0.003}_{-0.003}$	$0.529^{+0.092}_{-0.094}$	0.966 ± 0.008
	Random	$-0.001^{+0.002}_{-0.003}$	$0.530^{+0.480}_{-0.332}$	1.000 ± 0.008
Re-sampled EAGLE Mass Data	Real	$0.030^{+0.003}_{-0.003}$	$0.488^{+0.045}_{-0.046}$	1.066 ± 0.015
	Random	$-0.003^{+0.003}_{-0.003}$	$0.379^{+0.414}_{-0.225}$	1.005 ± 0.015
Mass Assigned Spin Data, SAMI	Real	$-0.002^{+0.009}_{-0.008}$	$1.035^{+0.807}_{-0.641}$	0.984 ± 0.038
	Random	$-0.014^{+0.011}_{-0.013}$	$0.792^{+0.536}_{-0.412}$	0.989 ± 0.038
No Slow Rotators Spin Data, SAMI	Real	$-0.035^{+0.013}_{-0.014}$	$1.308^{+0.218}_{-0.183}$	0.937 ± 0.037
	Random	$0.005^{+0.014}_{-0.009}$	$0.812^{+0.662}_{-0.460}$	1.008 ± 0.041

by stellar mass or if some residual spin correlation exists. This is the first time that marked correlation functions have been applied to galactic spin. We apply our analysis to both the SAMI observations and EAGLE simulation mock-observations, allowing us to compare SAMI to simulated results. The GAMA dataset is used as the "background" in the SAMI analysis for measuring large scale structure, due to GAMA's highly complete spectroscopic data. We estimate uncertainties in all our correlation functions through bootstraps with 10,000 re-samples, and estimate significance by fitting power laws of the form $M(s) = 1 + As^{-m}$ and looking at single bins below 1 Mpc.

We find the following results:

- Mass is positively correlated with environment. Fitting our ranked mass mark correlation function by a power law gave parameters $A = 0.036^{+0.015}_{-0.015}$, and $m = 0.713^{+0.320}_{-0.255}$. These results are consistent with previous work (e.g. Norberg et al., 2002).
- Spin (parametrised by λ_{R_e}) is negatively correlated with environment. Fitting our ranked λ_{R_e} mark correlation function by a power law gave parameters $A = -0.038^{+0.012}_{-0.013}$, and $m = 1.060^{+0.196}_{-0.179}$. This is consistent with previous work that found evidence of a KMDR (Cappellari et al., 2011b; D'Eugenio et al., 2013; Houghton et al., 2013; Scott et al., 2014; Fogarty et al., 2014), and the presence of an environmental effect on spin (Choi et al., 2018).
- Spin anti-correlation with environment is not driven solely by stellar mass. Defining bins in stellar mass of 0.1 dex, galaxies are assigned random λ_{R_e} values corresponding to their mass bin. This failed to reproduce a negative correlation with environment.
- The anti-correlation between spin and environment is not driven purely by slow rotators. When slow rotators are removed from the SAMI sample ($\lambda_{R_e} < 0.2$), the anti-correlation is found to still be present.
- Using mock-observations from the EAGLE simulations we find qualitatively consistent results as compared to observed data. Mass is correlated with environment, and spin is anti-correlated with environment with EAGLE galaxies as well as SAMI galaxies. A larger sample size in EAGLE allows us to see to larger scales than SAMI with high signal to noise, but the overall qualitative result remains the same. Although the relationship extends to larger scales for EAGLE, we know there are offsets between SAMI and EAGLE spin values (van de Sande et al., 2019). Investigation of whether these offsets can fully explain the larger scale result is beyond the scope of this paper.

Previous work has suggested that the λ_{R_e}-environment anti-correlation is simply a manifestation of the mass-environment correlation, caused by dynamical friction (Brough et al., 2017; Houghton et al., 2013; Cappellari, 2016; Veale et al., 2017; Greene et al., 2017). Our results suggest that the λ_{R_e}environment anti-correlation is not as simple as a re-statement of the mass-environment correlation. Physical process such as environmental quenching, mergers and interactions may drive galaxies towards lower λ_{R_e} values in denser environments (see also van de Sande et al., 2021b). The connection between mean stellar population age and environment (e.g. Scott et al., 2017) combined with the relation between mean stellar age and the dynamical thickness or intrinsic shape of galaxies (van de Sande et al., 2018) indicates that the star-formation history of a galaxy, its environment,

and dynamical properties are closely connected.

Future IFS surveys such as HECTOR (Bryant et al., 2016) will improve the statistics that we find here, in particular at small separation.

ACKNOWLEDGEMENTS

The SAMI Galaxy Survey is based on observations made at the Anglo-Australian Telescope. SAMI was developed jointly by the University of Sydney and the Australian Astronomical Observatory (AAO). The SAMI input catalogue is based on data taken from the Sloan Digital Sky Survey, the GAMA Survey and the VST ATLAS Survey. The SAMI Galaxy Survey is supported by the Australian Research Council (ARC) Centre of Excellence ASTRO 3D (CE170100013) and CAASTRO (CE110001020), and other participating institutions. The SAMI Galaxy Survey website is http://sami-survey.org/

JvdS, JJB, JBH, SB, MSO acknowledge support of the ARC (DE200100461, FT180100231, FL140100278, FT140101166, FT140100255). The SAMI instrument was funded by the AAO and JBH through FF0776384, LE130100198. FDE acknowledges funding through the H2020 ERC Consolidator Grant 683184.

Chapter 3

The SAMI Galaxy Survey: using tidal streams and shells to trace the dynamical evolution of massive galaxies

Never knowingly be serious.

—The Eleventh Doctor

Tomas H. Rutherford,[1,2] Jesse van de Sande,[1,2] Scott M. Croom,[1,2] Lucas M. Valenzuela,[3] Rhea-Silvia Remus,[3] Francesco D'Eugenio,[4,5] Sam P. Vaughan,[2,6,7,8] Henry R. M. Zovaro,[9,2] Sarah Casura,[10] Stefania Barsanti,[9,2,1] Joss Bland-Hawthorn,[1,2] Sarah Brough,[11,2] Julia J. Bryant,[1,2,12] Michael Goodwin,[13] Nuria Lorente,[13] Sree Oh,[14,9,2] and Andrei Ristea[15,2]

[1]Sydney Institute for Astronomy, School of Physics, A28, The University of Sydney, NSW, 2006, Australia
[2]ARC Centre of Excellence for All Sky Astrophysics in 3 Dimensions (ASTRO 3D), Australia
[3]Universitäts-Sternwarte, Fakultät für Physik, Ludwig-Maximilians-Universität München, Scheinerstr. 1, 81679 München, Germany
[4]Kavli Institute for Cosmology, University of Cambridge, Madingley Road, Cambridge, CB3 0HA, UK
[5]Cavendish Laboratory - Astrophysics Group, University of Cambridge, 19 JJ Thomson Avenue, Cambridge, CB3 0HE, UK
[6]School of Mathematical and Physical Sciences, Macquarie University, NSW 2109, Australia
[7]Astronomy, Astrophysics and Astrophotonics Research Centre, Macquarie University, Sydney, NSW 2109, Australia
[8]Centre for Astrophysics and Supercomputing, School of Science, Swinburne University of Technology, Hawthorn, VIC 3122, Australia
[9]Research School of Astronomy and Astrophysics, Australian National University, Canberra, ACT 2611, Australia
[10]Hamburger Sternwarte, Universität Hamburg, Gojenbergsweg 112, 21029 Hamburg, Germany
[11]School of Physics, University of New South Wales, NSW 2052, Australia
[12]Astralis-USydney, School of Physics, University of Sydney, NSW 2006, Australia
[13]AAO-MQ, Faculty of Science & Engineering, Macquarie University. 105 Delhi Rd, North Ryde, NSW 2113, Australia
[14]Department of Astronomy and Yonsei University Observatory, Yonsei University, Seoul 03722, Republic of Korea
[15]International Centre for Radio Astronomy Research, The University of Western Australia, 35 Stirling Highway, Crawley WA 6009, Australia

This chapter is reproduced from Rutherford et al. (2024), which was published in the Monthly Notices of the Royal Astronomical Society as "The SAMI Galaxy Survey: using tidal streams and shells to trace the dynamical evolution of massive galaxies". I

wrote all the text, produced all figures, and wrote most of the code for analysis. Francesco D'Eugenio provided the code for Multi-Gaussian Expansion models of SAMI galaxies which I modified for my use. Jesse van de Sande and Scott M. Croom supervised the work and assisted in revising the text. Lucas M. Valenzuela and Rhea-Silvia Remus provided the simulation data from Magneticum. Sam Vaughan provided light-weighted average ages for SAMI galaxies, and Henry Zovaro provided Hα equivalent width measurements.

Abstract

Slow rotator galaxies are distinct amongst galaxy populations, with simulations suggesting that a mix of minor and major mergers are responsible for their formation. A promising path to resolve outstanding questions on the type of merger responsible, is by investigating deep imaging of massive galaxies for signs of potential merger remnants. We utilise deep imaging from the Subaru-Hyper Suprime Cam Wide data to search for tidal features in massive ($\log_{10}(M_*/M_\odot) > 10$) early-type galaxies (ETGs) in the SAMI Galaxy Survey. We perform a visual check for tidal features on images where the galaxy has been subtracted using a Multi-Gauss Expansion (MGE) model. We find that 31^{+2}_{-2} percent of our sample show tidal features. When comparing galaxies with and without features, we find that the distributions in stellar mass, light-weighted mean stellar population age and Hα equivalent width are significantly different, whereas spin (λ_{R_e}), ellipticity and bulge to total ratio have similar distributions. When splitting our sample in age, we find that galaxies below the median age (10.8 Gyr) show a correlation between the presence of shells and lower λ_{R_e}, as expected from simulations. We also find these younger galaxies which are classified as having "strong" shells have lower λ_{R_e}. However, simulations suggest that merger features become undetectable within $\sim 2-4$ Gyr post-merger. This implies that the relationship between tidal features and merger history disappears for galaxies with older stellar ages, i.e. those that are more likely to have merged long ago.

3.1 Introduction

Galaxy mergers play an important role in the hierarchical structure formation theory of the Universe (White & Rees, 1978), being a key aspect of mass build-up in the ΛCDM paradigm. While the overall picture is well established, the impact of mergers on specific sub-classes or individual galaxies is less well understood. Slow rotator galaxies are a subset of galaxies characterised by a low spin parameter (λ_{R_e}) (Emsellem et al., 2007), large stellar mass and old stellar ages. However, it is not clear which processes cause the morphological (spin-down) and quenching transformation of these galaxies (e.g. Lagos et al., 2022). Evidence from simulations (e.g., Di Matteo et al., 2009; Jesseit et al., 2009; Bois et al., 2011; Naab et al., 2014; Choi & Yi, 2017; Lagos et al., 2017, 2018a; Penoyre et al., 2017; Schulze et al., 2020; Lagos, 2020b) suggests that galaxy mergers are capable of kinematically transforming these galaxies. However when these mergers happen, the ratio of minor to major mergers and the importance of gas are still outstanding questions. Indeed, some observational studies have found no link between merger signatures and slow rotators (e.g., Oh et al., 2016).

Galaxy interactions and mergers leave remnants of their existence in the form of tidal features, long understood to be relics of past encounters (e.g., Toomre & Toomre, 1972; van Dokkum, 2005; Hood et al., 2018; Mancillas et al., 2019; Huang & Fan, 2022). Tidal

tails and streams are formed when material is stripped from a primary gas-rich, disc-dominated galaxy or from a low-mass companion during interactions (Byrd & Howard, 1992; Oh et al., 2008; Hood et al., 2018). Simulations have suggested that streams indicate a circular infall of a companion (large impact parameter), and shells a nearly complete radial infall (Karademir et al., 2019). However, it should be noted that the evolution from a radial merger to a shell is not one-to-one, as radial infall mergers can also form other structures such as diffuse fans (Weil et al., 1997).

If slow rotators (SRs) are formed through galaxy mergers (Lagos et al., 2022), we expect to see a higher fraction of recent merger features around these slow rotator galaxies. The galaxy spin parameter λ_{R_e} has traditionally been used to classify galaxies as slow rotators ($\lambda_{R_e} \lesssim 0.1$) or fast rotators ($\lambda_{R_e} > 0.1$) (Emsellem et al., 2007). λ_{R_e} is defined as $\lambda_{R_e} = \langle R|V|\rangle / \langle R\sqrt{V^2 + \sigma^2}\rangle$, a luminosity-weighted rotational velocity, normalised by the second velocity moment $V^2 + \sigma^2$. λ_{R_e} can be interpreted as a measure of how rotationally or dispersion supported a galaxy is. More recently, slow rotators have been defined within a region of λ_{R_e}-ε (spin-ellipticity) space (e.g., Emsellem et al., 2011; Cappellari, 2016; van de Sande et al., 2021a), with low λ_{R_e} ($\lesssim 0.2$) and low ε (≤ 0.4).

The role of major versus minor mergers in the evolution of slow rotators is not yet clear from simulations. Whilst major mergers have long been believed to be essential for spinning-down galaxies, it is also known that processes such as minor mergers, secular evolution, fly-by encounters, harassment and dynamical friction can impact and even dominate spin evolution (Choi & Yi, 2017). Indeed, slow rotators can form from a series of minor mergers (Schulze et al., 2020), and this may even be the dominant driver of morphological transformations over cosmic time (Choi & Yi, 2017; Lofthouse et al., 2017). λ_{R_e} has been shown to decrease in simulations and observations from a maximum at $z = 1$ (Bezanson et al., 2018), however, this is independent of merger history in the case of simulations (Walo-Martín et al., 2020). Choi & Yi (2017) and Lofthouse et al. (2017) argue that major mergers are not the main driver of the spin-down of galaxies over cosmic time.

In order to confidently link tidal features to a potential merger history, an understanding of the timescale on which these features fade to be undetectable, or settle back into the main body of the galaxy is required. Post-merger galaxies can mostly only be identified via their tidal features during this timescale, which may differ from the timescale for λ_{R_e} to settle post-merger. Generally, tidal features are visible for a few Gyr (e.g., Lotz et al., 2008, 2010a,b; Lofthouse et al., 2017; Mancillas et al., 2019; Nevin et al., 2021), although various studies have a large variation in timescales. The best combination of techniques can make detection possible up to $\lesssim 2$ Gyr (Nevin et al., 2021), or potentially $\lesssim 4$ Gyr (Pop et al., 2018). However, these times have been shown to be dependent on gas fraction (Hood et al., 2018), decreasing to ≤ 300 Myr for low gas fractions ($\sim 20\%$), and reaching up to ≥ 1 Gyr for higher gas fractions ($\sim 50\%$) (Lotz et al., 2010a). Huang & Fan (2022) estimate that for massive early-type galaxies (ETGs), the lifetime of tidal features is ~ 3 Gyr. It should be noted, however, that these timescales are often related to identifying a merger in progress (e.g., Lotz et al., 2010b,a; Nevin et al., 2019, 2021), and the timescale for tidal features at large radii to exist may be significantly longer. Additionally, different classes of features may have different detectability timescales. Mancillas et al. (2019) investigated the lifetime of different types of features. They estimated a survival time of ~ 2 Gyr for tidal tails, ~ 3 Gyr for streams, and ~ 4 Gyr for shells.

The detection of tidal features is also strongly dependent on surface brightness limits. Ji et al. (2014) found that the detection time was on average $\sim$ 2 times as long for a surface brightness limit of 28 mag arcsec^{-2} as compared to 25 mag arcsec^{-2}. They found environment had an important effect, where a cluster potential was able to strip merger features and reduce the detection time. Martin et al. (2022) also found that detection rates depend on surface brightness limits, with 80 per cent of flux in features around Milky Way like galaxies identified at 30-31 mag arcsec^{-2}, falling to 60 per cent at 29.5 mag arcsec^{-2}.

The vast array of different merger scenarios can have a strong impact on the evolution of the galaxy, with the importance of gas specifically impacting both the kinematic evolution and star formation quenching. Whilst mergers may kinematically spin-down a galaxy (e.g., Naab et al., 2014; Lagos, 2020b) and leave an SR remnant, a fast-rotating disc can be subsequently formed post merger. However, the formation of a fast-rotating disc post-merger is dependent on the gas fraction (Lagos, 2020b), where wet mergers can even spin-up a galaxy post-merger, via newly-formed stars of high rotational speed. Mergers can also cause quenching in galaxies provided there is strong active galactic nuclei (AGN) feedback (Sparre & Springel, 2017), but this strong feedback is generally only induced by the gaseous disc being disrupted (Pontzen et al., 2017). Dry mergers tend to spin-down and morphologically disrupt galaxies, and wet mergers are capable of inducing star formation in a new disk. If this disk has enough stellar mass to counteract the stars sent to hotter orbits when the merger occurred, there can be little to no change in λ_{R_e}.

The identification and analysis of galaxy mergers from observations is complicated by the low surface brightness of the tidal features, and the large radii at which they often occur. Studies using simulations often analyse λ_{R_e} and studies using observations perform visual merger checks, and thus work that bridges this gap is a key part of identifying the impact of galaxy mergers on slow rotator formation. Recent work by Valenzuela & Remus (2022), building on tidal feature classification by Bílek et al. (2020) on the MATLAS sample (Duc et al., 2015; Habas et al., 2020) has shown a correlation between shells and low λ_{R_e} values.

In this paper, we use the recent wealth of deep optical imaging from the Subaru Hyper-Suprime Cam (HSC) to expand on the MATLAS (Mass Assembly of early-Type GaLAxies with their fine Structures) work with a significantly larger sample size. We use visual identification of tidal features in model-subtracted massive galaxies (e.g., shells, tidal streams, tails) from HSC-SSP (Aihara et al., 2019) in addition to standard cutout feature visual identification, complemented by kinematic data from the SAMI Galaxy Survey (Croom et al., 2021). We aim to address some of the questions surrounding the role of galaxy mergers in the formation pathway of slow rotators.

Our work is structured as follows. Section 2 discusses the data used in this paper. Section 3 describes our method. Section 4 states the results. Section 5 discusses these results in context with previous work. Section 6 presents a conclusion to this work. Throughout this paper, we adopt a ΛCDM cosmology, with $H_0 = 70$ km s^{-1} Mpc^{-1}, $\Omega_m = 0.3$, $\Omega_\Lambda = 0.7$. We further assume a Chabrier (Chabrier, 2003) stellar initial mass function (IMF), and an AB magnitude system (Oke & Gunn, 1983).

3.2 Data

3.2.1 The SAMI Survey

The SAMI instrument (Croom et al., 2012) provides a 1 degree diameter field of view and is mounted on the Anglo-Australian Telescope. SAMI uses 13 fibre bundles (Hexabundles; Bland-Hawthorn et al., 2011; Bryant et al., 2014), each having a 75% fill factor. There are 61 fibres of 1.6″diameter within each bundle, giving a diameter of 15″to each IFU. The IFUs and 26 sky fibres are fed to the AAOmega spectrograph (Sharp et al., 2006). The 580V grating at 3570-5750Å is used, giving a resolution of R=1808 (σ=70.4 km s^{-1}), as well as the 1000R grating from 6300-7400Å, which gives a resolution of R=4304 (σ=29.6 km s^{-1}) (van de Sande et al., 2017b).

The SAMI Galaxy survey (Croom et al., 2012; Bryant et al., 2015) target selection came from the GAMA (Driver et al., 2011) survey, as well as eight low-redshift clusters (Owers et al., 2017). Reduced data cubes (Sharp et al., 2015) are available with the SAMI Galaxy Survey data releases (Allen et al., 2015; Green et al., 2018; Scott et al., 2018; Croom et al., 2021), as well as stellar kinematic maps.

Our sample contains λ_{R_e} values derived from spatially resolved kinematic measurements, detailed in van de Sande et al. (2017b), with both an aperture correction (van de Sande et al., 2017a), and a seeing correction (Harborne et al., 2020; van de Sande et al., 2021a). R_e is defined as the semimajor axis effective radius of a galaxy, and the ellipticity ε is defined in terms of the axis ratio, $b/a = 1 - \varepsilon$. R_e and ε values are taken from MGE fits derived by D'Eugenio et al. (2021), using code from Cappellari (2002). Stellar mass measurements are taken from Bryant et al. (2015), using Milky-Way-extinction-corrected apparent g and i magnitudes, using the technique from Taylor et al. (2011).

Luminosity-weighted age measurements were derived by Vaughan et al. (2022). The PPXF code (Cappellari & Emsellem, 2004; Cappellari, 2017) was used to fit MILES single-age, single-metallicity stellar populations (SSP) models (Vazdekis et al., 2015). The SSP models used templates from Pietrinferni et al. (2004, 2006). Bulge to total flux ratios were derived by Casura et al. (2022), using the PROFOUND (Robotham et al., 2018) and PROFIT (Robotham et al., 2017) codes, applied to r-band KiDS (Kilo-Degree Survey) DR4.0 photometry (Kuijken et al., 2019). In our analysis, we begin by including bulge to total ratios of galaxies that have an appropriate two component fit[1]. We then extend this, by assigning bulge to total ratios of 1 to one component fit galaxies with Sérsic indices above 2.5, and bulge to total ratios of 0 to one component fit galaxies with Sérsic indices below 1. This allows us to include pure ellipticals and disks which cannot be fit with two components in our analysis.

For each galaxy, the Hα emission line equivalent width ($H_{H\alpha}$) was measured within a circular apertures with radius $1R_e$, where we adopted the MGE measurements from SAMI DR3 (D'Eugenio et al., 2021; Croom et al., 2021). The equivalent width is measured as the total Hα flux (not corrected for extinction) divided by the mean continuum level within the rest-frame wavelength range from 6500 Å to 65400 Å.

[1]To have an appropriate fit, a galaxy was required to have the flag R_N_COMP = 2, i.e. that the recommended number of Sérsic components was 2. For more detail, see Casura et al. (2022).

3.2.2 The HSC SSP Survey

Located on the summit of Maunakea in Hawaii, the wide-field imaging camera Hyper-Suprime-Cam (HSC) is mounted on the prime focus of the 8.2m Subaru telescope (Aihara et al., 2018a; Miyazaki et al., 2015). HSC utilises the full 1.5 degree diameter field of view of the Subaru telescope, with 116 Hamamatsu Deep Depletion CCDs, with 2000×4000 pixels each. Each of the $15\mu m$ pixels covers $0.168''$ on the sky. There are five broad-band (*grizy*) and 4 narrow band filters.

This paper uses the HSC *r*-band Wide data from HSC data release 2, which has a surface brightness limit of 27.8 ± 0.5 mag arcsec^{-2}, derived in Section 3.2.4. We use the Wide data due to its overlap with the GAMA/SAMI sample, and data release 2 was shown by Huang & Fan (2022) to be most suitable for extended, LSB objects. Image cutouts of 361×361 pixels (approximately $60'' \times 60''$), centred on the chosen galaxy, were used for model subtraction images. Greyscale inspection images were taken to be at least $10R_e$ in size, requiring cutouts of 829×829 pixels (approximately $140'' \times 140''$) as standard, with larger taken when necessary.

3.2.3 Sample Selection

We take our sample to be non-cluster SAMI ETGs from SAMI DR3 (Croom et al., 2021), as these galaxies have HSC imaging coverage. Morphology measurements were taken from Cortese et al. (2016), which used the classification method from Kelvin et al. (2014) on SDSS DR9 colour images (Ahn et al., 2012). We selected all galaxies above $\log_{10}(M_*/M_\odot) = 10$ to balance our aim to investigate massive slow rotators, and to appropriately compare to Valenzuela & Remus (2022). Some galaxies in this sample are discarded due to issues with their imaging (artefacts impacting the galaxy image), or identifiable spiral arms in HSC-SSP despite their previous morphological classification from SDSS imaging. Not all galaxies have values for all parameters. This is due to several factors, most importantly low signal to noise and insufficient radial coverage. The final sample contains 411 ETGs with good imaging, of which:

- 325 galaxies have λ_{R_e} values.
- 268 have B/T ratios.
- 405 have ellipticity values.
- 386 have light-weighted age measurements.

3.2.4 HSC Surface Brightness Limits

The identification of low surface brightness (LSB) features in galaxy surveys is limited by the minimum surface brightness of a survey. Previously unobserved features often appear in a deeper survey, and these features can be required to be several magnitudes brighter than the reported depth of a survey to be identified at a high completeness level (Kado-Fong et al., 2018).

However, it should be noted that the effect of surface brightness limits differs for different tidal features. Mancillas et al. (2019) found that the detection of streams is highly sensitive to surface brightness limits ($2-3\times$ more streams with a brightness cut of 33 mag arcsec^{-2}

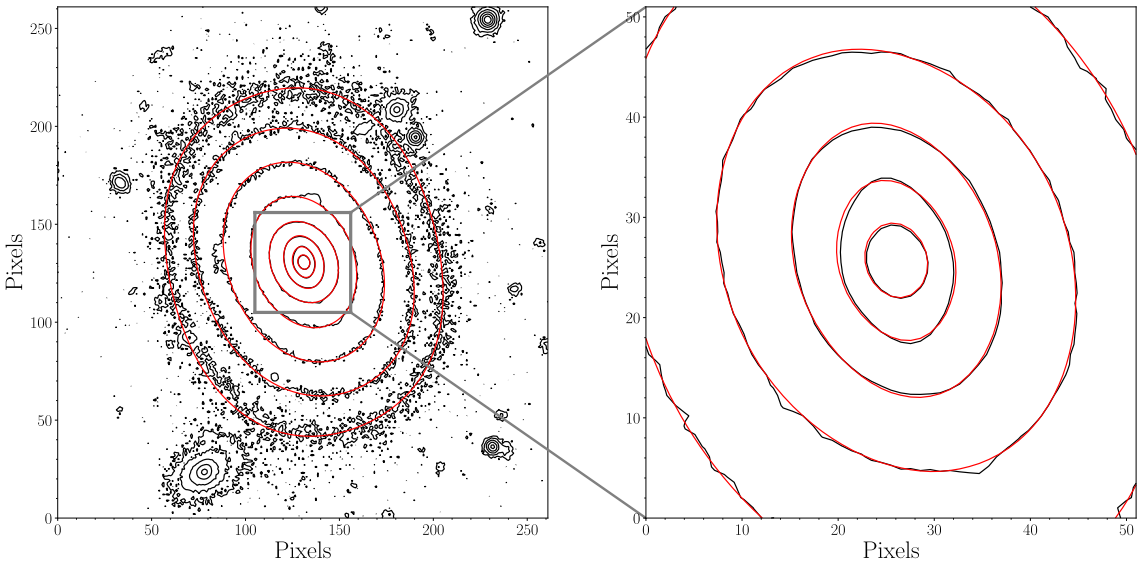

Figure 3.1: An example of an MGE model of galaxy with CATID 91697. The left panel has flux contour lines in black, with MGE model contour lines in red. Contour lines are spaced by 1 mag arcsec^{-2}. The grey square contains the central region of the galaxy, and is enlarged and shown in the right-hand panel. The pixel scale of all cutouts is 0.168 arcsec pixel^{-1}.

compared to 29 mag arcsec^{-2}). There was no sensitivity dependence found for tails, and only a mild dependence for shells.

The various surveys on LSB features use different methods and aperture sizes to estimate the limiting surface brightness. Atkinson et al. (2013) note that differences as large as 2-3 mag arcsec^{-2} can exist between surveys, making comparison extremely difficult. For completeness, we will describe here our derivation of our surface brightness limits.

Similarly to Atkinson et al. (2013), we placed 40 circular apertures of area 1 arcsec^2 on empty fields of 20 HSC cutouts. The root-mean-square variations between the total sum of flux within each aperture, for each cutout, was calculated. These values were then converted to mag arcsec^{-2} with Equation 3.1, where FLUXMAG0 = 63095734448.0194.

$$SB_{\text{mag arcsec}^{-2}} = 2.5 \times \log_{10}\left(\frac{\text{FLUXMAG0}}{\text{flux}}\right) \tag{3.1}$$

This resulted in a distribution of surface brightness limits, where we took the mean and standard deviation to be our limiting surface brightness, and its uncertainty. This estimation of our surface brightness limit was found to be 27.8 ± 0.5 mag arcsec^{-2}.

3.3 Method

3.3.1 MGE Galaxy Profile Modelling

The visual inspection and analysis of LSB tidal features in deep imaging is complicated by separating these features from the bright, smoothly varying flux of the main body of

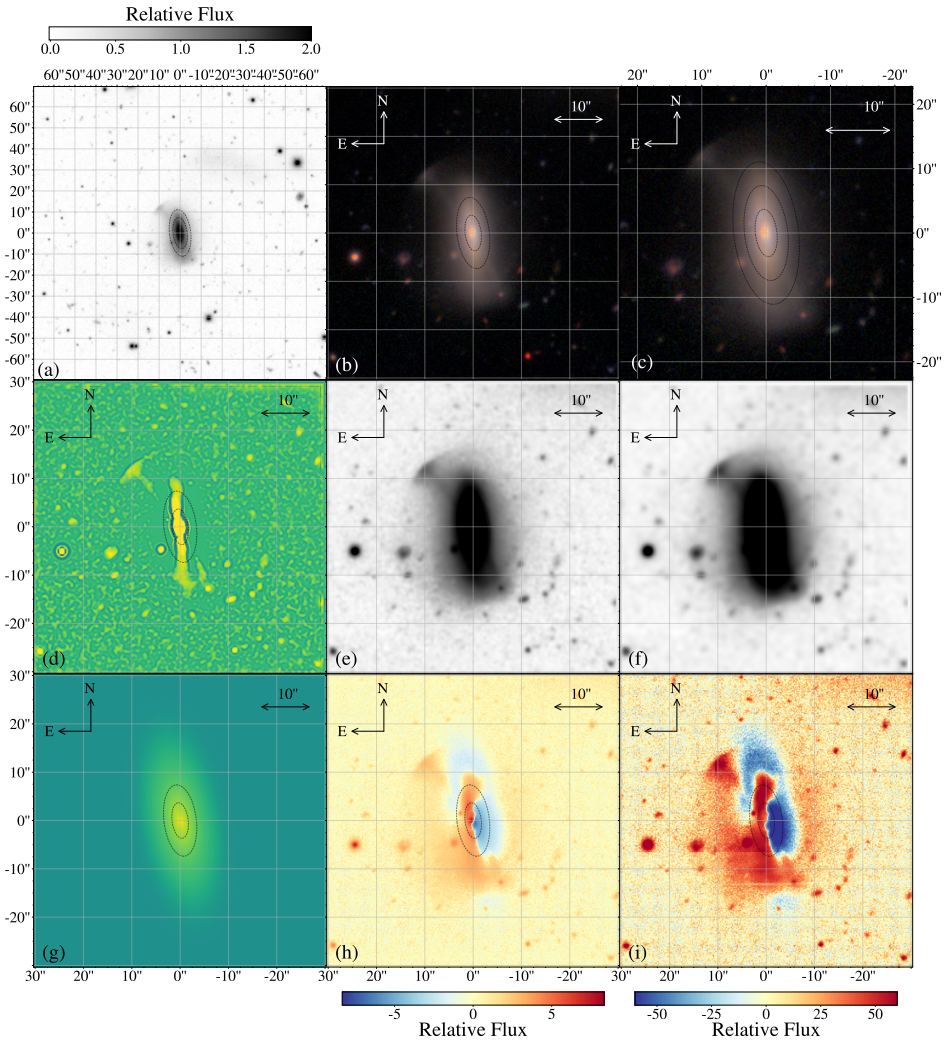

Figure 3.2: An example image (DEC vs RA) for analysis of galaxy with CATID 49734. Panel (a) contains the r-band cutout for the galaxy. Panels (b) and (c) contain an rgb image of the galaxy, and an enlarged version of the rgb image respectively. Panel (d) contains the r-band cutout for the galaxy, with the spatial frequency filters from Kado-Fong et al. (2018) applied, and panels (e) and (f) contain r-band cutouts with increased contrast. Panel (g) contains an MGE model of the galaxy, panel (h) contains the MGE model-subtracted residual, and panel (i) contains the same residual divided by noise. The dashed ellipses represent the radii $1R_e$ and $2R_e$ (and $3R_e$ in panel (c)). A shell-like tidal feature can be seen to the upper left of the images.

the galaxy. To overcome this issue, analysis of model-subtracted residual images has been employed in previous work (e.g., Bell et al., 2006; McIntosh et al., 2008; Mantha et al., 2019). The modelling code GALFIT (Peng et al., 2002) has traditionally been used to fit physically motivated Sérsic profiles for the required flux models. MGE is an alternate method, being significantly faster than GALFIT with high-efficiency algorithms delivering a fit in $\sim$ 2 minutes. The efficiency of MGE comes from the fitting of a number of sectors of a given flux profile, rather than pixel-by-pixel. Given our desire for fast model generation which can give us the smallest residuals after model subtraction, physical motivation is less important than efficiency, and we utilise MGE in this work.

We follow the MGE fitting code from D'Eugenio et al. (2021). The code starts by using SEXTRACTOR (Bertin & Arnouts, 1996) to identify all sources in the HSC cutout. SEXTRACTOR provides an image mask to all sources other than the central galaxy. The point-spread function (PSF) is characterised by fitting 2-5 stacked circular Gaussians.

Provided with a PSF and image mask, the galaxy flux is fit. We do not use regularised fits (Scott et al., 2009), which require the flattest Gaussian to have the roundest axial ratio which still reproduces observations (Cappellari, 2002). Unregularised fits yield the lowest χ^2 values and more realistic galaxy shapes (D'Eugenio et al., 2021). We present an example MGE fit in Figure 3.1.

The MGE modelling code used in this work (Cappellari, 2002) fits an integer pixel to the galaxy centre. As a result, the flux in the centre of a galaxy is usually not fit as well as the outer regions, and thus model subtraction near the galaxy centre is poor. This can be seen in examining panel (i) in Figure 3.2. However, as we expect tidal features at large radii, this sub-pixel shift does not affect the identification of these features.

3.3.2 Model Subtraction and Visual Inspection

The visual inspection of each galaxy for tidal features utilised an image with multiple panels. Each image includes: r-band image, rgb image, MGE model, model-subtracted residuals, and relative model-subtracted residuals. An example image can be seen in Figure 3.2. Panel (a) shows an r-band cutout for the galaxy. Panels (b) and (c) show an rgb image for the galaxy. Panel (d) shows the r-band cutout, with spatial frequency filters from Kado-Fong et al. (2018), with the goal of making non-spherically-symmetric features more apparent. Panels (e) and (f) show increased contrast versions of the r-band cutout. Panel (g) shows the MGE model for the galaxy, with panels (h) and (i) showing the model subtracted residual, and model subtracted residual divided by uncertainty respectively.

Tidal features are often divided into classes, based on the physical process they formed from (e.g., Atkinson et al., 2013; Bílek et al., 2020; Desmons et al., 2023a). We divide these into two for this work: tidal streams, and shells. Tidal streams are seen as "streams" of stars, appearing to move radially inwards to the galaxy, and in some cases the satellite galaxies associated with these streams are still visible. We acknowledge here that there is significant ambiguity between a shell, stream, ring and a weak spiral arm in LSB imaging. Although our sample was selected to contain only ETGs, the morphological classifications used were taken from visual inspection of SDSS imaging. The increased depth of HSC imaging allows for visual identification of rings and spiral arms previously

unseen. We defined a shell as a feature that curves around a galaxy with approximately constant radius, and unlike most spiral arms or rings, is separate from the main body of the galaxy. We made a point to only classify galaxies without knowing their λ_{R_e} values, to avoid any unconscious bias. This also meant we did not downselect our galaxies after re-examination. There are some fast rotating disc galaxies with weak shell features that could plausibly be a ring within the disc, rather than a shell. We accept this as a reality of our method, which cannot be easily reduced without biasing our sample (examples can be seen in Figure A.2).

Each HSC model-subtracted residual image was inspected individually by a group of three people (THR, JvdS, SMC). Each person was able to individually decide if an image had any stream or shell-like tidal features, and give a 1-5 value for the "strength" of that feature. This strength classification represented the confidence a classifier had in a feature existing, and often correlated with how bright and separated from the main galaxy body the feature was. When inspecting the image seen in Figure 3.2, one could focus on the top left panel, panel (a). The dynamic range of the greyscale image could be changed interactively for each galaxy, allowing for the user to select a unique scaling to best identify features for a given galaxy. A feature was determined to be significant if at least two people identified it. The strength was taken to be the average strength selected.

Once individual classifications were complete, a set of galaxies which had disagreements in strength of ≥ 2 were selected, and inspected as a group. Disagreements were identified and a group classification was agreed upon. Most disagreements were due to ambiguity between a shell and a stream. We note that other galaxy observables, such as metallicity, kinematics and HI maps, can also be used alongside visual features to identify past interactions (e.g., López-Sánchez, 2010). However, this work is focused on correlating these observables to tidal features and thus we will not be using this technique.

3.4 Results

3.4.1 Merger/Tidal Features in the SAMI Galaxy Survey

Here, we present the results of our analysis of the merger features of our SAMI galaxies in the GAMA field regions with $\log_{10}(M_*/M_\odot) > 10$. In total, we have 411 galaxies with classifications. 129 galaxies have a feature identified (71 shells, 76 streams and 18 with both). For simplicity, we refer to galaxies with shells as "Shell Galaxies", galaxies with streams as "Stream Galaxies", galaxies with a shell and/or stream as "Feature Galaxies", and galaxies with no shell or stream as "Regular Galaxies". Feature classifications are used alongside SAMI kinematic data to examine the link between merger features and slow rotators.

We begin by presenting the distributions of our regular galaxies, shell galaxies and stream galaxies in several parameter spaces, using the parameters λ_{R_e}, $\log_{10}(M_*/M_\odot)$, Age and B/T. This can be seen in Figure 3.3. Galaxies with no features are coloured in sky blue, galaxies with shells are coloured in red, galaxies with streams are coloured in dark blue, and galaxies with streams and shells are coloured in orange. Shell galaxies classified with a strength of at least 3 are circled in black, referred to as "strong" shells. In panel (b), we

Table 3.1: We present p-values from comparing distributions for an array of parameters for all galaxies and young galaxies, splitting our feature sample into shells and streams separated, and strong features only. A two sample KS test is applied to a set of feature galaxy parameters (e.g. shell galaxy λ_{R_e} values) and the regular galaxy parameters (e.g. regular galaxy λ_{R_e} values). Strong features are defined as features which were identified with a confidence level of at least 3/5 during classification. Significant p-values ($p < 0.05$) are highlighted in bold.

	Tidal Features			Strong Tidal Features		
All Galaxies	Shells	Streams	Streams & Shells	Shells	Streams	Shells & Streams
λ_{R_e}	4.38×10^{-1}	6.12×10^{-1}	8.97×10^{-1}	5.23×10^{-2}	8.07×10^{-1}	1.80×10^{-1}
ε	9.77×10^{-1}	2.43×10^{-1}	5.51×10^{-1}	6.05×10^{-1}	4.27×10^{-1}	8.93×10^{-1}
$\log_{10}(\mathrm{Age/Gyr})$	$\mathbf{6.28 \times 10^{-5}}$	$\mathbf{5.44 \times 10^{-5}}$	$\mathbf{1.98 \times 10^{-6}}$	$\mathbf{2.08 \times 10^{-2}}$	2.60×10^{-1}	$\mathbf{1.47 \times 10^{-2}}$
$\log_{10}(\mathrm{W_{H\alpha}})$	$\mathbf{2.68 \times 10^{-6}}$	$\mathbf{4.85 \times 10^{-6}}$	$\mathbf{5.90 \times 10^{-7}}$	$\mathbf{1.40 \times 10^{-2}}$	$\mathbf{3.26 \times 10^{-2}}$	$\mathbf{1.52 \times 10^{-3}}$
B/T	5.73×10^{-1}	4.95×10^{-1}	2.57×10^{-1}	7.44×10^{-1}	2.96×10^{-1}	4.92×10^{-1}
$\log_{10}(M_*/M_\odot)$	$\mathbf{2.25 \times 10^{-4}}$	$\mathbf{2.33 \times 10^{-5}}$	$\mathbf{1.12 \times 10^{-6}}$	1.12×10^{-1}	3.72×10^{-1}	5.91×10^{-2}
Young Galaxies	Shells	Streams	Streams & Shells	Shells	Streams	Shells & Streams
λ_{R_e}	$\mathbf{3.82 \times 10^{-2}}$	6.79×10^{-1}	3.01×10^{-1}	5.93×10^{-2}	2.91×10^{-1}	5.60×10^{-2}
ε	7.92×10^{-1}	$\mathbf{3.72 \times 10^{-2}}$	2.93×10^{-1}	9.95×10^{-1}	7.59×10^{-1}	9.34×10^{-1}
$\log_{10}(\mathrm{Age/Gyr})$	1.40×10^{-1}	2.78×10^{-1}	1.36×10^{-1}	$\mathbf{3.90 \times 10^{-2}}$	4.29×10^{-1}	8.88×10^{-2}
$\log_{10}(\mathrm{W_{H\alpha}})$	$\mathbf{5.66 \times 10^{-3}}$	$\mathbf{4.22 \times 10^{-4}}$	$\mathbf{8.62 \times 10^{-4}}$	3.05×10^{-1}	2.61×10^{-1}	9.80×10^{-2}
B/T	9.73×10^{-2}	3.95×10^{-1}	1.98×10^{-1}	7.33×10^{-1}	6.29×10^{-1}	5.20×10^{-1}
$\log_{10}(M_*/M_\odot)$	$\mathbf{9.14 \times 10^{-5}}$	$\mathbf{2.39 \times 10^{-4}}$	$\mathbf{8.22 \times 10^{-6}}$	1.11×10^{-1}	4.25×10^{-1}	1.95×10^{-1}

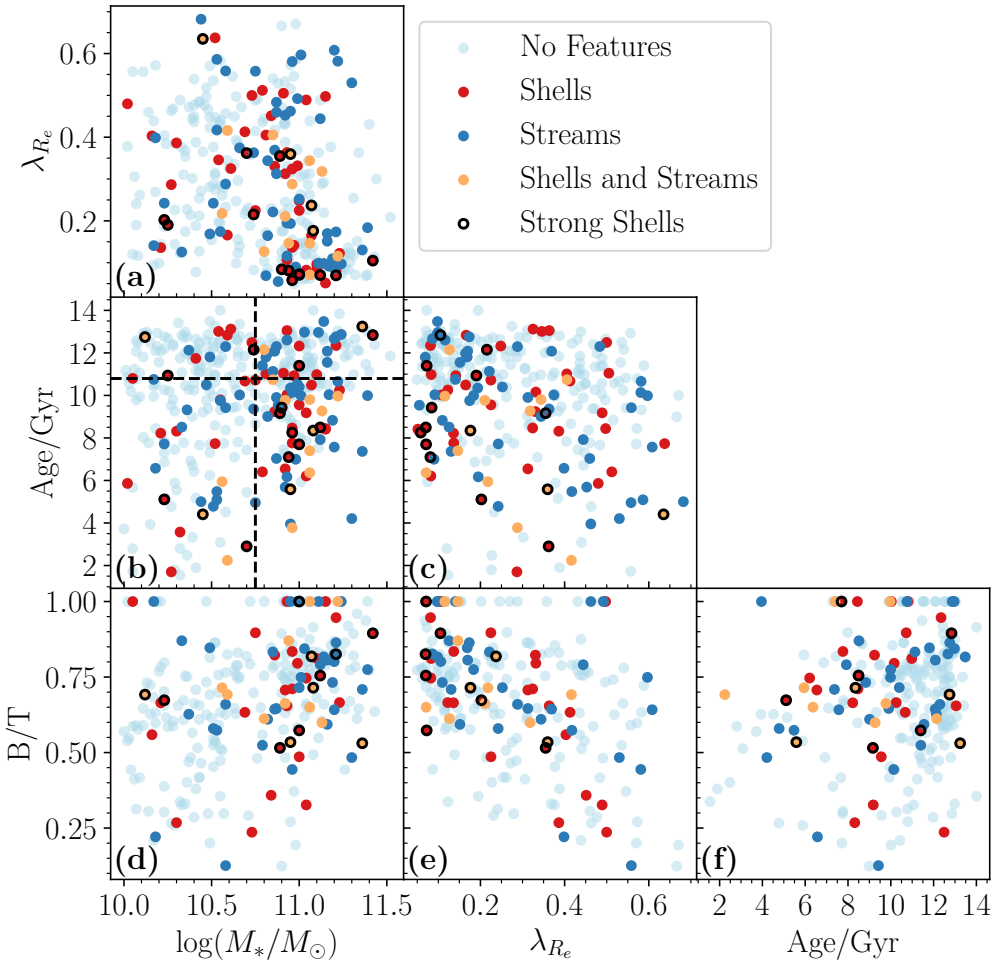

Figure 3.3: Distributions of our sample galaxies in all relevant parameter spaces, using the parameters λ_{R_e}, $\log_{10}(M_*/M_\odot)$, Age and B/T. Galaxies with no features are coloured in sky blue, galaxies with shells are coloured in red, galaxies with streams are coloured in dark blue, and galaxies with streams and shells are coloured in black. Shell galaxies classified with a strength of at least 3 are circled in black. The median stellar mass and age are shown as dashed lines in panel (b).

show the median stellar mass and age with dashed lines.

We see evidence in panel (b) of galaxy shells being correlated with both age and mass, with neither being the sole driver of the relation. When splitting this panel into four quadrants by the median stellar mass and median age ($\log_{10}(M_*/M_\odot) = 10.75$ and Age/Gyr = 10.80 respectively, shown by dashed lines), we find the following shell feature fractions:

- Low mass, high age galaxies: 9/90, $10.0^{+4.1}_{-2.3}$%
- High mass, high age galaxies: 11/103, $10.7^{+3.8}_{-2.3}$%
- Low mass, low age galaxies: 13/104, $12.5^{+4.0}_{-2.6}$%

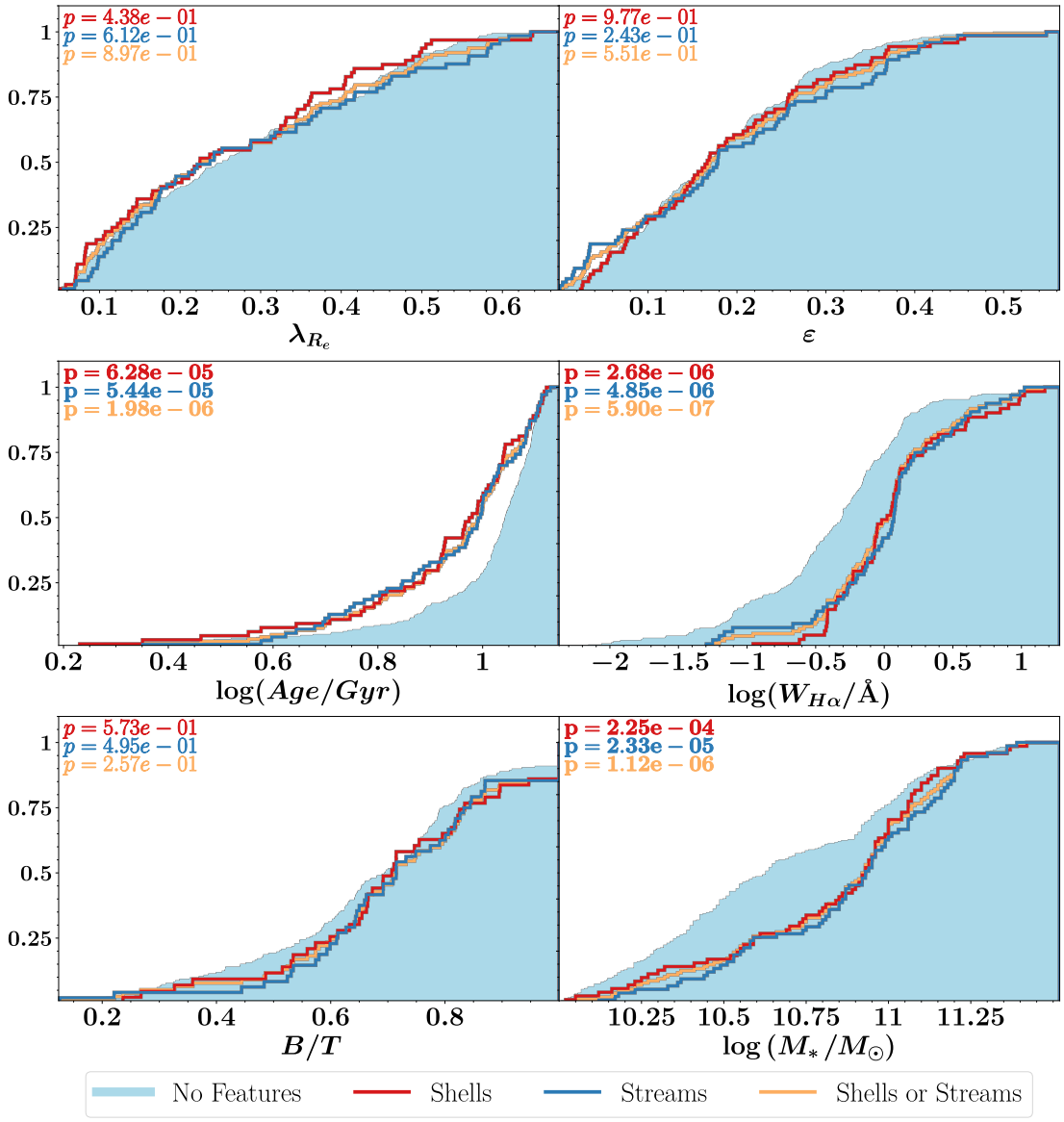

Figure 3.4: The cumulative distribution for all relevant parameters and tidal feature samples. Regular galaxies (sky blue), shells (red), streams (dark blue) and shells or streams (orange) are all shown. In each panel, we show different parameters. We show the p-values from a KS test between regular galaxies and shells (red), regular galaxies and streams (dark blue), and regular galaxies and combined features (orange). P-values less than $p = 0.05$ are shown in bold. We don't consider p-values above $p = 0.05$ to be significant correlations. We find that while features are correlated with lower stellar ages and higher $W_{H\alpha}$, there is no such correlation with λ_{R_e} or B/T.

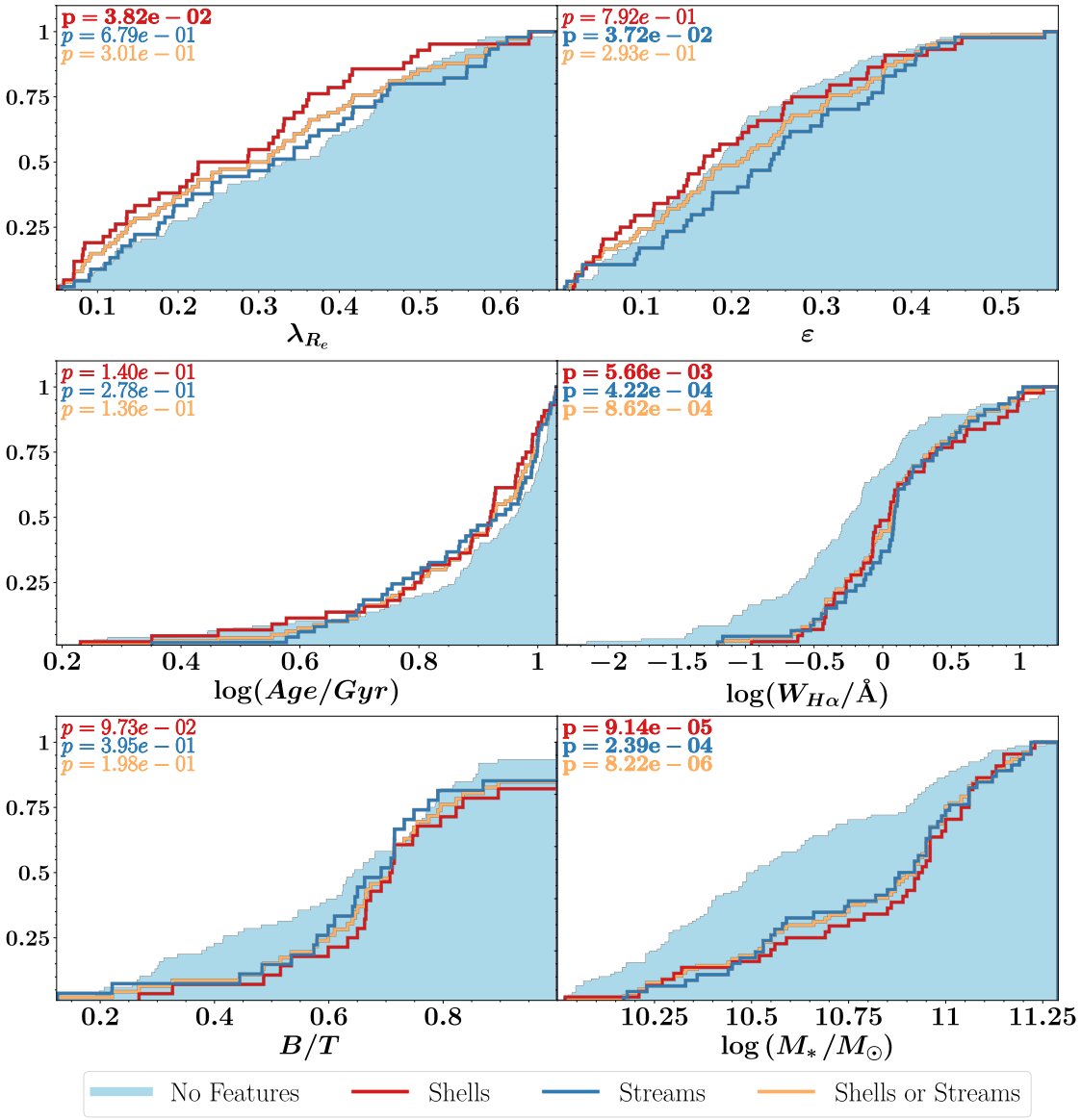

Figure 3.5: The cumulative distribution for all relevant parameters and tidal feature samples, for galaxies with stellar ages below the median light-weighted stellar age. All cumulative distributions and labels are the same as Figure 3.4. We find that for these galaxies with low stellar ages, shells are correlated with lower λ_{R_e} and higher $W_{H\alpha}$.

- High mass, low age galaxies: 31/89, $34.8^{+5.3}_{-4.7}$%

There is a substantial number and fraction of galaxies with features at high mass and low age, with the fraction of features clearly affected by both age and mass.

We also visually represent and quantify the difference between shell galaxies, stream galaxies, and regular galaxies using cumulative distributions and Kolmogorov–Smirnov (KS) tests. The cumulative distributions for all relevant parameters and feature samples can be seen in Figure 3.4. We analyse feature galaxies split into shell (red) and stream (dark blue) samples, and combined (orange). The resulting p-values from each KS test are given in Figure 3.4 and Table 3.1. Table 3.1 also includes p-values for when galaxy

features are only considered for a classified strength greater than three. Each p-value comes from a two sample KS test applied to a set of feature galaxy parameters (e.g. shell galaxy λ_{R_e} values) and the set of regular galaxy parameters (e.g. regular galaxy λ_{R_e} values). Essentially, they quantify the probability that these merger features are not correlated with a given parameter. If a p-value is higher than 0.05, we don't consider this to be a significant correlation. To test whether there are any significant differences in the tails of the distribution, we also employ the Anderson-Darling test. We find that all p-values from Figures 3.4 and 3.5 stay either significant or non-significant under this test, with the exception that the difference between the ellipticity (ε) of young stream and regular galaxies in Figure 3.5 is no longer significant.

We see in Figure 3.4 that λ_{R_e}, ε and B/T are not correlated with any type of tidal feature. We additionally find that the mean stellar age is significantly lower, and Hα emission line equivalent width ($W_{H\alpha}$) and stellar mass ($\log_{10}(M_*/M_\odot)$) are significantly higher, for feature galaxies versus regular galaxies. Specifically, lower stellar age ($p = 6.28 \times 10^{-5}$, $p = 5.44{\times}10^{-5}$), higher $W_{H\alpha}$ ($p = 2.68{\times}10^{-6}$, $p = 4.85{\times}10^{-6}$) and higher $\log_{10}(M_*/M_\odot)$ ($p = 2.25 \times 10^{-4}$, $p = 2.35 \times 10^{-5}$) are correlated with both shells and streams. A lower mean stellar age is an expected result, as models and observations have shown that cold gas may be funnelled to the centre of galaxies during a merger, giving rise to central starburst activity and thus lower mean stellar ages (e.g., Scott & Kaviraj, 2014; Knapen et al., 2015; Thorp et al., 2019; Bickley et al., 2022). An alternative interpretation is that features fade over time, so older galaxies may have had an earlier merger but have no identifiable features remaining. We also expect a higher stellar mass, given the correlation between stellar mass, number of mergers, and total flux in tidal features (i.e. identifiability of features) (e.g. Martin et al., 2022). We note here that we choose to analyse $W_{H\alpha}$ instead of sSFR for our sample. We do this for several reasons. Firstly, as we have selected only ETGs, Hα based star formation rate measurements for these mostly passive galaxies are not very physically meaningful, and SED-fitted SFR values (Ristea et al., 2022) show no correlation. Secondly, $W_{H\alpha}$ goes approximately with sSFR, without assumptions that Hα flux is from star formation sources.

The correlation of higher stellar masses with tidal features as shown in Figures 3.4 and 3.5 is significant, however we found that it does not drive our strong mean stellar age result. In Figure A.1, we show that when restricting to galaxies with stellar masses above the median stellar mass ($\log_{10}(M_*/M_\odot) = 10.75$), there is no significant correlation between features and stellar mass. However, when we apply the same restriction, the qualitative results from Figure 3.9 (see below) remain (The mean spin values from this figure while only considering high-mass galaxies can additionally be seen in Table 3.4). Specifically, we still see a lower spin for shell galaxies in the central age bin as compared to regular galaxies, and strong shell galaxies show the same relation with a larger gap in average spin.

The stellar kinematics of galaxies are also well known to be affected by mergers (e.g., Naab et al., 2014; Lagos, 2020b; Schulze et al., 2020). Given these results, an increase in B/T ratio and a decrease in ε and λ_{R_e} in feature galaxies is similarly expected, as slow rotators are described as high dispersion oblate spheroids. The lack of these results in Figure 3.4, as well as the results from Figure 3.3 leads us to consider the role of stellar age, which we investigate in section 3.4.2.

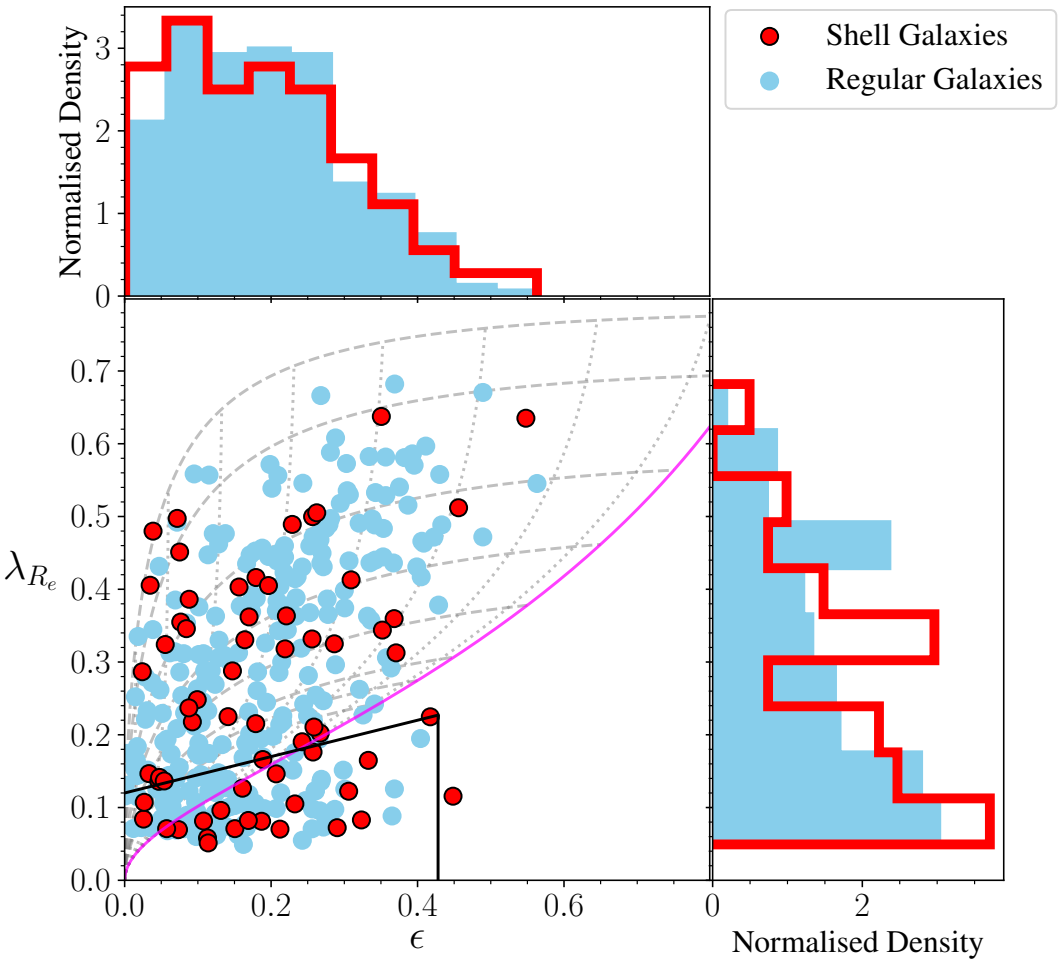

Figure 3.6: The distribution of selected SAMI galaxies in λ_{R_e}-ε space. Galaxies are coloured as red if they were identified as having shells, and by blue if they had no features identified. The solid magenta line shows the expected relation for edge-on oblate rotators with anisotropy $\beta_z = 0.7$. The dotted grey lines represent the same relation, but for varying inclinations ($10° - 80°$). The dashed grey lines represent the same relation again, but for fixed ellipticity ($0.35 - 0.9$), changing with inclination. The black line denotes the separation between fast and slow rotators from van de Sande et al. (2021a), $0.12 + 0.25\varepsilon$ for $\varepsilon < 0.428$. Distributions of λ_{R_e} and ε are in the side panels, in red for galaxies with identified shells, and in blue for galaxies with no tidal features. The galaxies with shells do not have significantly different λ_{R_e} values than galaxies without, and are not preferentially located in the slow rotator region.

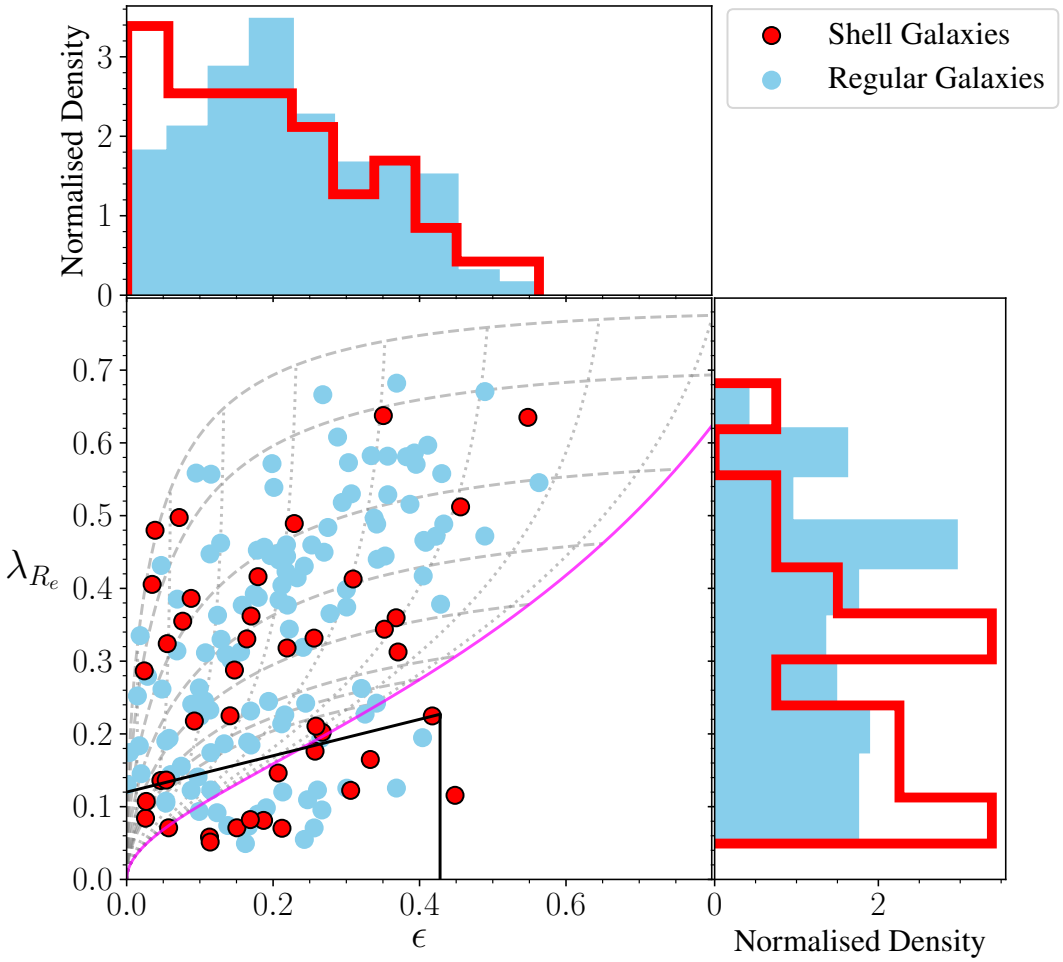

Figure 3.7: The distribution of selected SAMI galaxies with a mean stellar age below the median age in λ_{R_e}-ε space. The layout is similar to Figure 3.6. The young galaxies with shells have significantly different λ_{R_e} values than galaxies without, and are preferentially located in the slow rotator region.

3.4.2 Merger/Tidal Features in Galaxies with Relatively Young Age

We present our analysis of the galaxies in our sample with stellar ages below the median light-weighted stellar age (10.80 Gyr), henceforth referred to as younger galaxies. As tidal features are only detectable for $\sim 2-4$ Gyr (Lotz et al., 2008, 2010b,a; Lofthouse et al., 2017; Nevin et al., 2021; Mancillas et al., 2019), we expect that younger mean stellar age should be correlated with identifiable merger features. This can also be seen in Figure 3.4. The cumulative distributions for our young galaxies can be seen in Figure 3.5, presented similarly to Figure 3.4.

We find that when we restrict to lower ages, the presence of shells is correlated with lower λ_{R_e} ($p = 0.038$), while the stellar age correlation disappears. This is likely due to

reducing the dynamic range in stellar age. The correlation of lower $W_{H\alpha}$ with features is maintained ($p = 0.0057$ for shells, $p = 0.00042$ for streams), as well as the correlation with higher $\log_{10}(M_*/M_\odot)$ ($p = 9.14 \times 10^{-5}$ for shells, $p = 2.39 \times 10^{-4}$ for streams). The B/T ratio is not significantly correlated with features, however this is likely due to low number statistics. 268 of 411 galaxies have B/T ratios, of which only 77 ($\sim 29\%$) have features. This can be compared to 325 galaxies with λ_{R_e} measurements, of which 114 ($\sim 35\%$) have features. It should also be noted that λ_{R_e} is measured within one effective radius, while B/T is a measurement taken from the full photometry of a galaxy, and thus the parameters are not indicative of the same physical scale.

From Figure 3.5, we see that even though the presence of shells is correlated with lower λ_{R_e}, streams are not. Indeed, the analysis done to shell galaxies in Sections 3.4.3 and 3.5.3 below can be done to stream and combined feature galaxies as well, but all results remain strongly driven by shells. We also acknowledge that while streams may be more important than shells at lower stellar masses (e.g., Desmons et al., 2023b), our mass cut at $\log_{10}(M_*/M_\odot) = 10$ means our sample contains a reasonable fraction of shells. As a result of these considerations, this paper will henceforth be largely focused on shell features only.

3.4.3 Spin, Ellipticity and Slow Rotators

When considering slow rotators, we look in more detail at the parameters that define a slow rotator, λ_{R_e} and ε (ellipticity). Figure 3.6 shows our galaxies with classifications in λ_{R_e}-ε space, where slow rotators are traditionally classified (e.g., Emsellem et al., 2011; Cappellari, 2016; van de Sande et al., 2021a). We plot galaxies with shell features as red points, and galaxies without any type of feature as blue points. The magenta line represents the expected relation between λ_{R_e} and ellipticity for edge-on oblate rotators with varying intrinsic ellipticity ε_i and anisotropy $\beta_z = 0.7\varepsilon_i$. Dotted grey lines show the same relation but for varying inclinations, with the grey dashed lines showing galaxies with fixed intrinsic ellipticity, changing with inclination. The black lines denote the separation between fast and slow rotators for seeing-corrected SAMI data, from van de Sande et al. (2021a). We find that feature galaxies are not preferentially located in the slow rotator region compared to regular galaxies ($32.8^{+6.3}_{-5.3}\%$ vs $30.7^{+3.0}_{-2.7}\%$ respectively)[2]. We note that the slow rotator fraction is particularly high here overall, due to a high mass, early-type sample. The distribution of younger galaxies in λ_{R_e}-ε space is shown in Figure 3.7, with the same layout as Figure 3.6. Shell galaxies in the younger sample are found to be significantly more preferentially located in the slow rotator region than regular younger galaxies ($31.0^{+7.9}_{-6.1}\%$ vs $17.39^{+4.1}_{-3.0}\%$ respectively). Note that the increase in significance when we cut by stellar age is due to the fraction of regular slow rotators falling, rather than the fraction of shell slow rotators rising.

3.5 Discussion

In this section, we discuss the implications and limitations of our results and place them in context with similar studies.

[2]Uncertainties are calculated as binomial confidence intervals from Cameron (2011).

3.5.1 Effectiveness of Visual Classification

In this work, visual classification of merger features using the combination of model subtraction with an interactive dynamic range in image cutouts provided a consistent method for identifying any apparent merger features. However, the completeness of our classifications is hampered by two factors. Firstly, the majority of tidal features are expected to lie at $\gtrsim$ 30 mag arcsec^{-2} (Johnston et al., 2008), and our derived surface brightness limit for HSC r-band cutouts is 27.8 ± 0.5 mag arcsec^{-2}. Secondly, identification of tidal features at nominal surface brightness limits is significantly incomplete. Detectability is also strongly dependent on radial extent. For example, Kado-Fong et al. (2018) injected features into cutouts, with various surface brightnesses for each feature, and a derived surface brightness limit of $\sim$ 28 mag arcsec^{-2}. They identified only 14.3% of shells at $4R_e$ with a shell surface brightness of 27.0 mag arcsec^{-2}, as compared to a shell surface brightness of 25.125 mag arcsec^{-2} which gave 64.3% at $4R_e$ and 89.3% at $5R_e$. Sola et al. (2022) similarly were unable to find any tidal features fainter than 27.5 mag arcsec^{-2}, despite their nominal surface brightness limits of 28.3 – 29 mag arcsec^{-2}.

Given these challenges in defining a completeness for our visual classifications, we can look to similar studies, examining the fraction of features as a comparison. The MATLAS survey (Duc et al., 2015; Bílek et al., 2020; Habas et al., 2020; Sola et al., 2022) was examined by Bílek et al. (2020) similarly to this work, classifying tidal features visually. Valenzuela & Remus (2022) further investigated the correlation between tidal features and λ_{R_e} for MATLAS, as well as a hydrodynamical cosmological simulation (*Magneticum Pathfinder*[3], Dolag et al., in prep.). Comparing MATLAS to this work is appropriate, given the similar surface brightness limits (28.3 – 29 mag arcsec^{-2} for MATLAS, 27.5 ± 0.5 mag arcsec^{-2} here, noting the discussion in Section 3.2.4 above concerning differences in calculated surface brightness limits) and target galaxies (field ETGs). The feature fractions from this work and from MATLAS can be seen in Table 3.2. The feature and shell fractions agree remarkably well between SAMI and MATLAS galaxies. Whilst the stream fractions are in slight disagreement, the overall results suggests that our work detects as many features as Bílek et al. (2020). Indeed, noting that MATLAS contains only galaxies in a local volume with distance below 42 Mpc, and SAMI contains galaxies out to a redshift of $\sim$ 0.1 ($\sim$ 420 Mpc), cosmological surface brightness dimming reduces intensities by a factor $(1+0.056)^4 = 1.246$ at the median redshift of our sample, and $(1+0.11)^4 = 1.509$ at the maximum redshift. This effectively reduces our surface brightness limit by 0.3 mag arcsec^{-2} and 0.5 mag arcsec^{-2} respectively.

Additionally, other observations and simulations of samples like ours report similar fractions of features to this work. Kluge et al. (2020) found a lower bound of $\sim$ 9.4% of galaxies in local clusters showing shell features, and $\sim$ 22% showing streams. Pop et al. (2018) found in the Illustris simulation that 18 ± 3% of massive, $z = 0$ galaxies exhibited shells. Other studies (e.g. Schweizer & Seitzer, 1988; Tal et al., 2009) have found shells in between $\sim$ 10% and $\sim$ 22% of elliptical galaxies.

Given the similar results and surface brightness limits between our work and MATLAS, as well as similar feature fraction rates between our work and similar studies, our combination of model subtraction with an interactive dynamic range in image cutouts likely provides a

[3] www.magneticum.org

Table 3.2: The number of galaxies with shells, streams and any feature for SAMI ($n_{\rm SAMI}$) and MATLAS ($n_{\rm MATLAS}$). We also show the fraction of features found as compared to the total number of galaxies for SAMI ($f_{\rm SAMI}$) and MATLAS ($f_{\rm MATLAS}$).

	Shells	Streams	Features	Total
$n_{\rm SAMI}$	71	76	129	411
$f_{\rm SAMI}$	$17.3^{+2.0}_{-1.7}$%	$18.5^{+2.1}_{-1.8}$%	$31.4^{+2.4}_{-2.2}$%	−−
$n_{\rm MATLAS}$	23	33	41	131
$f_{\rm MATLAS}$	$17.6^{+3.8}_{-2.8}$%	$25.2^{+4.2}_{-3.4}$%	$31.3^{+4.3}_{-3.8}$%	−−

consistent and appropriate method of identifying tidal features around ETGs.

Instead of human visual classifications, machine learning techniques have recently shown promise in automatic classification (e.g., Bottrell et al., 2022; Bottrell, 2022; Bickley et al., 2022; Domínguez Sánchez et al., 2023), and make classifying very large datasets ($\gtrsim 10,000$ galaxies) possible in a reasonable amount of time. Whilst this is a method with a lot of potential, visual classification currently remains necessary for training these algorithms on real observations. However, developments in self-supervised learning could change this in the near future (e.g., Desmons et al., 2023a).

The identification of LSB tidal features around galaxies is difficult, but future surveys which reach deeper surface brightness limits will be able to identify higher fractions of galaxies with features. Martin et al. (2022) showed that at a surface brightness limit of $\mu_r = 35$, close to 100 percent of galaxies show some type of feature. Although a limiting surface brightness of 35 is still somewhat unrealistic, the importance of ranking the strength of tidal features as well as identification will become more important as they become more ubiquitous around galaxy images.

3.5.2 Interpretation of Hα Equivalent Widths

In Figures 3.4 and 3.5, we showed that shell and stream galaxies have significantly higher Hα emission line equivalent width ($W_{H\alpha}$) values than regular galaxies. We are careful not to interpret larger amounts of Hα emission as indicative of star formation, given our sample was selected to be massive ETGs which are likely to be mostly passive. While a thorough investigation of the nature of Hα emission in these galaxies is beyond the scope of this paper, we use the classification method from Cid Fernandes et al. (2011), which utilises $W_{H\alpha}$ and the [NII]/Hα line ratio to classify the emission source of weak-lined galaxies.

In Figure 3.8 we show [NII]/Hα line ratio versus $W_{H\alpha}$ values of regular (blue) and feature (orange) galaxies. Of the 314 galaxies with measured line ratios, 105 (33%) are feature galaxies. Table 3.3 shows the proportion of galaxies within each region of Figure 3.8. We note that galaxies with a $W_{H\alpha}$ S/N < 1 are still included in our analysis (empty sumbols in Figure 3.8, because these low S/N values are typically driven by low $W_{H\alpha}$ values, and removing them would heavily bias our sample.

We find that feature galaxies are over-represented in the sAGN and wAGN regions ($50.0^{+13.4}_{-13.4}$% and $66.7^{+9.6}_{-13.5}$% vs $33.4^{+2.8}_{-2.6}$% overall), and under-represented in the passive

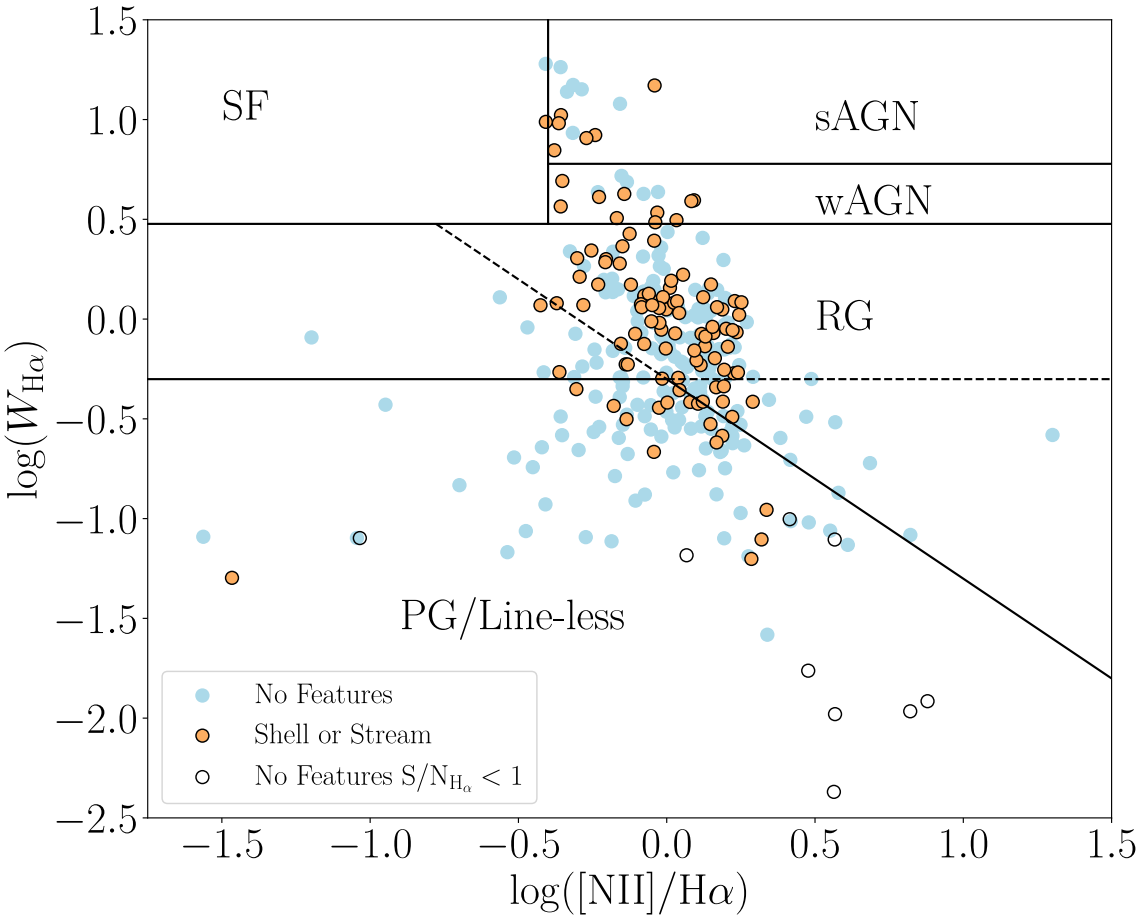

Figure 3.8: Distributions of our regular galaxies (blue) and feature galaxies (orange) in an emission line classification diagram, with [NII]/Hα line ratios plotted against $W_{H\alpha}$. Galaxies with signal-to-noise ratios in $W_{H\alpha}$ of below one are plotted as empty symbols, of which there are no feature galaxies. The following regions are defined: SF (star forming), sAGN (strong AGN), wAGN (weak AGN), RG (retired galaxies) and PG/Line-less (Passive galaxies/Line-less galaxes). The dashed lines denote areas that have one requirement for being a PG ($W_{H\alpha}$ < 0.5 or $W_{[NII]}$ < 0.5). Feature galaxies are over-represented in the AGN regions, and under-represented in the PG region (see Table 3.3.

galaxy regions ($17.6^{+4.7}_{-3.3}$% vs $33.4^{+2.8}_{-2.6}$% overall). We also note that there are only 2 galaxies in the SF region, as expected given our ETG selection.

Herpich et al. (2018) suggests that it is possible that the difference in emission between liny RGs (those with emission lines) and line-less RGs (PGs in this work) is due to warm gas content. They suggest RGs experienced a recent wet merger, providing gas and possibly inducing a period of star formation. This agrees broadly with our work, where we find feature galaxies under-represented in the PGs population. This is consistent with a scenario where ETGs that have recently experienced a merger (RGs) have increased their gas fraction, and thus show stronger emission lines from this gas than ETGs which have not experienced a recent merger (PGs). We also note that if mergers lead to rapid star formation, they should result in a population of post-starburst galaxies. Such galaxies

Table 3.3: The number of galaxies within each region of Figure 3.8, separated into feature and regular galaxies. Percentages represent what fraction of each region comprises of regular and feature galaxies.

	Regular Galaxies	Feature Galaxies	Total
SF	1 $50.0^{+24.8}_{-24.8}$%	1 $50.0^{+24.8}_{-24.8}$%	2
sAGN	6 $50.0^{+13.4}_{-13.4}$%	6 $50.0^{+13.4}_{-13.4}$%	12
wAGN	5 $33.3^{+13.5}_{-9.6}$%	10 $66.7^{+9.6}_{-13.5}$%	15
RG	122 $62.9^{+3.3}_{-3.6}$%	72 $37.1^{+3.6}_{-3.3}$%	194
PG	75 $82.4^{+3.3}_{-4.7}$%	16 $17.6^{+4.7}_{-3.3}$%	91
All	209 $66.6^{+2.6}_{-2.8}$%	105 $33.4^{+2.8}_{-2.6}$%	314

have been shown to display specific line features (e.g. Dressler & Gunn, 1983; Wild et al., 2007; Pawlik et al., 2019) which could be examined further in future work.

3.5.3 The Role of Galaxy Mergers in Kinematic Evolution and the Formation of Slow Rotators

Although slow rotators are an important subset of galaxy populations, their formation pathway remains unclear. Simulations have suggested that galaxy mergers are capable of providing the required (spin-down) morphological transformation (e.g., Di Matteo et al., 2009; Jesseit et al., 2009; Bois et al., 2011; Naab et al., 2014; Choi & Yi, 2017; Lagos et al., 2017; Lagos, 2020b; Lagos et al., 2018b; Penoyre et al., 2017; Schulze et al., 2020), but conclusive observational evidence linking tidal features to slow rotators is yet to be found. Indeed, recent studies (e.g., Lagos et al., 2022; Bílek et al., 2023) suggest that there is a diverse number of formation pathways for slow rotator galaxies.

We find that for early type galaxies with relatively young stellar ages of $\lesssim$ 10Gyr, the presence of a shell is correlated with lower λ_{R_e}. We further show this relationship in Figure 3.9, with mean values in Table 3.4. In this figure, we show SAMI and MATLAS galaxies above $\log_{10}(M_*/M_\odot) > 10$ in λ_{R_e}-Light Weighted Age space. Galaxies are coloured by stellar mass, and galaxies with identified shells are circled in black. Further, each sample is divided into three equally spaced age bins. The average spin in each bin for both galaxies with no features, and galaxies with shells, is plotted for each bin. Panel (a) contains SAMI galaxies, panel (b) is the same as panel (a) but with the adjustment that only *strong* shells are considered (classified strength of at least 3/5), and panel (c) contains MATLAS galaxies.

The age values shown in Figure 3.9 have different physical interpretations for SAMI and MATLAS. Stellar ages for SAMI are derived from full spectral fitting to SSP models, with

Table 3.4: The mean spin (λ_{R_e}) within each of the three light-weighted age bins in Figure 3.9, for panels (a), (b) and (c). We also include the values for an equivalent plot to Figure 3.9, but only considering galaxies with $\log_{10}(M_*/M_\odot) \geq 10.75$.

		Regular Galaxies λ_{R_e} Values	Shell Galaxies λ_{R_e} Values	Massive Regular Galaxies λ_{R_e} Values	Massive Shell Galaxies λ_{R_e} Values
SAMI (a)	Lowest Age Bin	0.39 ± 0.04	0.36 ± 0.05	0.35 ± 0.07	0.24 ± 0.06
	Middle Age Bin	0.34 ± 0.02	0.25 ± 0.03	0.31 ± 0.03	0.21 ± 0.03
	Highest Age Bin	0.25 ± 0.01	0.24 ± 0.03	0.21 ± 0.02	0.23 ± 0.04
SAMI Strong Shells (b)	Lowest Age Bin	0.38 ± 0.03	0.39 ± 0.08	0.31 ± 0.05	0.22 ± 0.09
	Middle Age Bin	0.33 ± 0.02	0.13 ± 0.04	0.29 ± 0.02	0.14 ± 0.09
	Highest Age Bin	0.25 ± 0.01	0.15 ± 0.03	0.21 ± 0.01	0.09 ± 0.01
MATLAS (c)	Lowest Age Bin	0.48 ± 0.03	0.30 ± 0.08	0.51 ± 0.07	0.38 ± 0.09
	Middle Age Bin	0.38 ± 0.02	0.29 ± 0.05	0.36 ± 0.04	0.17 ± 0.06
	Highest Age Bin	0.44 ± 0.03	0.27 ± 0.06	0.39 ± 0.08	0.21 ± 0.04

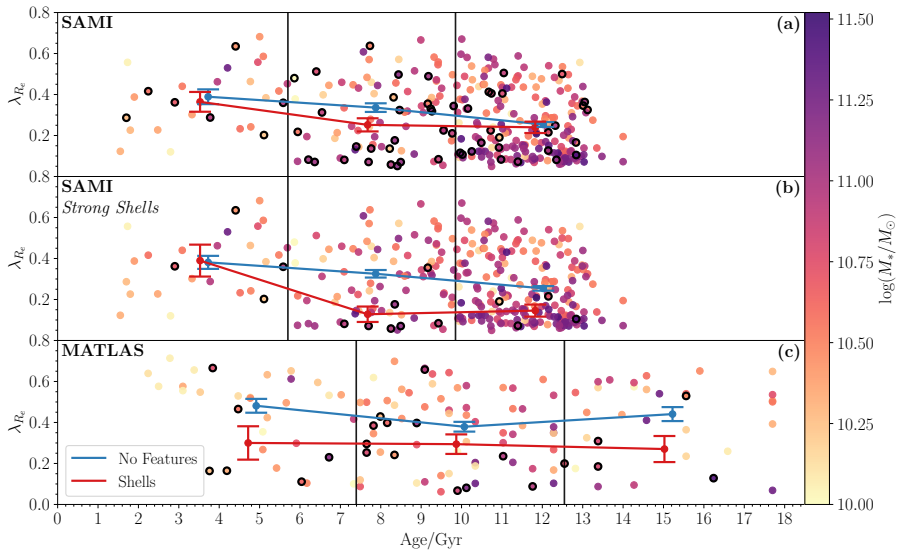

Figure 3.9: The distribution of SAMI and MATLAS galaxies in λ_{R_e}-mean light-weighted stellar age space. Galaxies are coloured by $\log_{10}(M_*/M_\odot)$, and galaxies with shells are circled in black. The average λ_{R_e} value in 3 age bins is drawn for regular galaxies in blue, and for shell galaxies in red. Panel (a) shows SAMI galaxies, panel (b) shows SAMI galaxies with only strong shells considered (strength classified as 3/5 or higher), and panel (c) shows MATLAS galaxies. The age bins are taken to be equally spaced between the minimum and maximum stellar ages. As MATLAS stellar ages are derived differently to SAMI's and have significant differences (such as different maximum ages), we don't compare them numerically, and thus using the same age bins is not necessary. We see that in the central age bin, SAMI galaxies have a correlation between shells and lower λ_{R_e}. This correlation grows stronger when only considering strong shells.

a maximum stellar age of 14 Gyr. The age measurement is derived as a light-weighted mean within $1R_e$. Age measurements for MATLAS are derived in McDermid et al. (2015), from SSP models which used Hβ, Fe5015, Mgb and Fe5270 line indices. These SSP ages also differ from SAMI's in that they go to ages above the currently accepted age of the universe (Planck Collaboration et al., 2016). As a result, we treat them as relative ages, which we will not compare numerically to the SAMI ages. We choose to focus on light-weighted ages here as they may be a better proxy for the time since the last major merger than mass-weighted ages.

We first see the overall trend in Figure 3.9 that spin decreases towards higher ages in SAMI galaxies (van de Sande et al. (2018), Croom et. al in prep). However, we also see a separation in the mean spin of shell and regular galaxies in the central age bin for all panels.

The results in Figure 3.9, panel (a), suggest that for SAMI galaxies in the lowest age bin, there is no difference in λ_{R_e} for galaxies that have a shell and those that do not. There is an indirect link between stellar age and time since merger, as mergers can induce star formation and a light-weighted mean stellar age approximately measures the time since

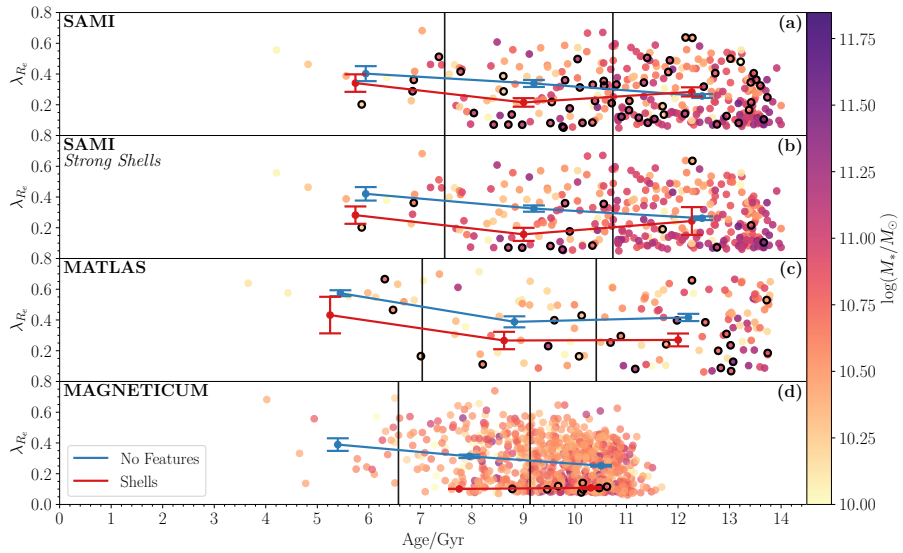

Figure 3.10: The distribution of SAMI, MATLAS and Magneticum galaxies in λ_{R_e}-mean mass-weighted stellar age space. Galaxies are coloured by $\log_{10}(M_*/M_\odot)$, and galaxies with shells are circled in black. The average λ_{R_e} value in 3 age bins is drawn for regular galaxies in blue, and for shell galaxies in red. Panel (a) shows SAMI galaxies, panel (b) shows SAMI galaxies with only strong shells considered (strength classified as 3/5 or higher), panel (c) shows MATLAS galaxies, and panel (d) shows Magneticum galaxies. Mass-weighted stellar ages show a typical lack of ages below $\sim$ 6 Gyr as compared to the light-weighted ages (seen in Figure 3.9), due to light-weighted averages favouring young, bright stars.

the last period of star formation. This is not a direct correlation however, as dry mergers for example may not induce star formation, and may result in a galaxy with a mean stellar age older than the time since the dry merger. We suggest that feature galaxies in the lowest stellar age bin may have only recently merged. At this stage, the galaxy is still disk-like and has not yet undergone the spin-down morphological transformation. Alternatively, galaxies in the lowest age bin may also have merged longer ago, but experienced a wet merger which re-built a star-forming disc. These two possible scenarios both result in shell galaxies with no difference in λ_{R_e} to regular galaxies. A further possibility is simply that a combination of low number statistics and noise results in no significant difference between shell galaxies and regular galaxies in the low age bin.

For the central age bin, we see significantly lower spin for galaxies with shells than galaxies with no features. This is an expected relationship between merger features and kinematics from simulations (e.g., Di Matteo et al., 2009; Jesseit et al., 2009; Bois et al., 2011; Naab et al., 2014; Choi & Yi, 2017; Penoyre et al., 2017; Lagos et al., 2017, 2018a; Schulze et al., 2020; Lagos, 2020b), which suggest that galaxy mergers spin down galaxies.

Finally, in the oldest age bin, we see no difference in the spin of galaxies with shells and those without. This could be due to several reasons. Firstly, some of the oldest galaxies may have simply been born hot, with any mergers having no effect on spin. Additionally,

it could plausibly be because the spin-down merger occurred long enough ago ($\gtrsim$ 4 Gyr) that the shell features are no longer identifiable. In these cases, the correlation between shells and spin disappears.

The scenario of fading tidal features is further supported by the transition of shell and regular galaxies from the central to the oldest age bin in panel (a) in Figure 3.9. While the shell galaxies do not change their spin, the regular galaxies have lower spin at older ages. This would be consistent with a contamination of regular galaxies with merger galaxies that no longer have identifiable shells. Further, Figures 3.6 and 3.7 show that when only considering younger galaxies, feature galaxies are preferentially located in the slow rotator region of a λ_{R_e}-ε diagram. This is not the case when considering all galaxies, regardless of age. The difference between this younger galaxy result and the result when considering all galaxies is driven not by fewer shell galaxy slow rotators at older ages, but more regular galaxy slow rotators at older ages. This is again consistent with merger-induced slow rotators no longer having identifiable shells at long enough times post-merger.

We address the possibility of weak shells in actuality being rings or weak spiral arms in panel (b) of Figure 3.9. By selecting only shells identified with an average strength of at least 3/5, we have much higher confidence that we are not selecting any fast rotating discs without any real features. The strength measurement both correlates with higher confidence in a feature being real, and the visual strength of the feature. We see, that in comparison to panel (a), the difference in mean spins in the middle age bin is much more significant, and a significant difference arises in the highest age bin. This is likely due to almost all of the high spin shell galaxies in the central and highest age bin only having low strengths, reducing the impact of fading shells on this metric.

An alternative to the shell features fading in the oldest galaxies is that the mergers that generate features add mass with a lower mean stellar age. Given the median ages and masses for our shell and regular samples, we can estimate the mass ratio of mergers required to form a shell galaxy from a regular galaxy.

If we assume that a galaxy from the regular population undergoes a merger event(s), it needs enough mass added to match the median shell galaxy stellar mass. In order to match the lower stellar age of shell galaxies, we need a mass-weighted stellar age estimate for a galaxy of a given mass. We fit a linear relation between stellar mass and mass-weighted stellar age for all SAMI ETGs, shown in Equation 3.2:

$$\text{Age/Gyr} = 2.10 \times \log_{10}(M_*/M_\odot) - 10.86 \tag{3.2}$$

We note here that there is considerable scatter in this relation, and this approach only provides a simplified assessment of the types of mergers required. We can calculate the mass-weighted stellar age for a galaxy after it has experienced a series of mergers. We find that, given our results, a galaxy needs to undergo several $\sim 1:4-6$ mergers to transform from a regular galaxy to a shell galaxy. Two equal mass mergers will not work, as the galaxies will typically have similar age. However, it's worth bearing in mind that we do expect features to fade over time, and this may be the main reason for not seeing shells in the oldest galaxies. If this is the case, high-redshift 1:1 mergers could form the oldest galaxies without features.

3.5.4 Comparison of SAMI, MATLAS and Magneticum

Due to MATLAS light-weighted ages being derived signficantly differently to SAMI light-weighted ages, we do not make direct numerical comparisons between these ages. Rather, we use *mass*-weighted SAMI ages from full spectral fitting, as mass-weighted ages derived in a similar way are available for MATLAS. This gives the additional advantage that we can compare to the simulated Magneticum galaxies which were also analysed by Valenzuela & Remus (2022), as they have mass-weighted age measurements available. We show this comparison in Figure 3.10, with a similar layout to Figure 3.9. The Magneticum galaxies used in this work come from Box4 (uhr), a $(48\mathrm{Mpc}/h)^3$ box, initially containing 2×576^3 particles of DM (dark matter) and gas. The particles have masses of $m_{\mathrm{DM}} = 3.6\times10^7 M_\odot/h$ and $m_{\mathrm{gas}} = 7.3\times10^6 M_\odot/h$, with a gravitational softening length of 1.4 kpc$/h$ for DM and gas, and 0.7 kpc$/h$ for star particles. More detail on the Magneticum simulations can be found in Teklu et al. (2015).

MATLAS shows no difference in spin in the lowest age bin, and a lower spin for shell galaxies in the central and oldest age bin in panel (c), Figure 3.10, consistent with our SAMI results in the central bin. The main disagreement between SAMI and MATLAS is in the oldest age bin, where SAMI does not show a difference in spin. There are several possible reasons for this. Firstly, linear age measurements for galaxies, particularly at old ages, have an inherently large scatter. The oldest age bin may not be particularly meaningful physically as an age measurement. Secondly, LSB features in SAMI are more affected by cosmological redshift surface brightness dimming than MATLAS (see Section 3.5.1). We expect that galaxies in the oldest age bin are more likely to have experienced the longest time since their latest merger, and thus their features are expected to be fainter, and more susceptible to becoming undetectable through redshift dimming.

Magneticum galaxies ages are represented by mass-weighted mean stellar lookback time within $1R_{\mathrm{half}}$, and shown in panel (d) of Figure 3.10. Whilst SAMI and MATLAS galaxies are sorted by visual morphology to exclusively examine early types, Magneticum defines morphology in terms of their kinematics, and as such correlating to their kinematics after a kinematics based cut is not appropriate. We attempt to account for this by performing a cut between ETGs and LTGs on the star forming main sequence of Magneticum, in comparison to SAMI (see Figure A.4). We find that Magneticum shell galaxies have exclusively low spin values compared to regular galaxies in both the central and oldest age bins, with no detected shell galaxies in the lowest age bin. While Magneticum galaxies do trend towards lower spin with age as SAMI does, the lack of any scatter in the spin of shell galaxies is clearly different from our SAMI and MATLAS results. Whilst it is possible that this is caused by low number statistics, it is also possible that Magneticum is not fully capturing the possibility of a galaxy rebuilding a star-forming disc post radial infall merger.

3.5.5 Radial Infall Galaxy Mergers

Our results show that there is an excess of shells around younger slow rotator galaxies. We suggest that radial path mergers play an important role in the formation of the slow rotator population. Given the diverse formation pathways of slow rotators (Lagos et al., 2022), the existence of shells around a slow rotator is a potential method to distinguish this formation

scenario from others. However, galaxies which had these mergers early have shells which are very difficult to detect with current methods and surveys. These features are likely to be undetectable after ~ 4 Gyr even with improved surveys (Mancillas et al., 2019; Martin et al., 2022). A more significant result can be found by only considering "strong" shells, but the number of detections drops significantly (71 total shells vs 19 strong shells in this work).

These merger scenarios would also result in an excess of shells around galaxies with a higher B/T ratio, as mergers are known to impact the growth of the bulge component of galaxies (e.g., Sales et al., 2012; Wilman et al., 2013; Barsanti et al., 2022). However, we do not see a correlation of B/T with shell galaxies. In Figure 3.3, we examined this by showing the distributions of our galaxies in all relevant parameter spaces, using the parameters λ_{R_e}, $\log_{10}(M_*/M_\odot)$, Age and B/T.

In panel (e), although all shell galaxies are spread throughout the λ_{R_e}-B/T distribution, strong shell galaxies are much more tightly clustered in a high B/T, low λ_{R_e} region. Similarly in panel (d), strong shell galaxies are mostly clustered in a high $\log_{10}(M_*/M_\odot)$region. Low λ_{R_e}, high B/T and high stellar mass define a slow rotator. Indeed, $52.9^{+11.1}_{-11.8}$% (9/17) of strong shell galaxies are slow rotators (cf. $32.8^{+6.3}_{-5.3}$% (21/64) for all shell galaxies).

There is a possible correlation between B/T, λ_{R_e} and shells, but it is complex, and the strength of the shells as well as stellar age plays an important role. Although the strength represents the classifiers' confidence of a shell, it also correlates with the surface brightness of the feature, and thus likely increases with the mass of the most recent merger.

3.6 Conclusions

We investigated the role of mergers in the formation of slow rotator galaxies through the identification of low surface brightness tidal features in deep HSC imaging. We performed a visual inspection of HSC images, with surface brightness model subtracted residuals and galaxy cutouts with an interactive dynamic range to classify SAMI ETGs with $\log_{10}(M_*/M_\odot) > 10$ as either galaxies with shells, galaxies with streams, or galaxies with no tidal features. We further connected these features to stellar kinematics and morphology to investigate a link between galaxy mergers and the removal of angular momentum in galaxies.

We find that shell features are correlated with lower λ_{R_e} in early-type galaxies with stellar ages below the median (Age/Gyr = 10.8), with a p-value of $p = 3.82 \times 10^{-2}$. Further, the signal is strongest at intermediate ages ($7.39 <$ Age/Gyr < 12.55), with the average λ_{R_e} for galaxies with shell features being significantly lower than for galaxies with no features. Additionally, although our results show that feature fraction depends on both age and stellar mass, this result is not driven by stellar mass. At high stellar masses, our relation between λ_{R_e}, age and shells remains, and the fraction of galaxies with shells has a strong dependence on age ($34.8^{+5.3}_{-4.7}$% for low age, high mass galaxies; $10.7^{+3.8}_{-2.3}$% for high age, high mass galaxies).

Galaxies with obvious, high surface brightness shells are correlated with lower λ_{R_e} in all but the youngest mean stellar age galaxies. These galaxies generally have low λ_{R_e}, high

B/T, high stellar mass, and are more likely to be slow rotators ($52.9^{+11.1}_{-11.8}$% (9/17) for strong shells vs $31.1^{+2.7}_{-2.5}$% (101/325) for our full sample).

Radial galaxy merger events (i.e. those with small impact parameter) likely play an important role in the formation of the slow rotator population. These radial mergers additionally produces shell-like tidal features, which can further be used to distinguish this formation pathway for slow rotators from others. The relation between radial mergers and angular momentum is complex, with our results showing that shell features, shell feature strength, λ_{R_e}, stellar age, stellar mass and B/T ratio all play a role.

We find that lower mean stellar age ($p = 1.98\times10^{-6}$) and higher Hα EW ($p = 3.32\times10^{-6}$) are correlated with tidal features in early-type galaxies. The emission line properties of feature galaxies are consistent with a scenario in which ETGs experience a merger, increasing both their gas content and emission line strength.

Future surveys (such as the LSST, Ivezić et al., 2019; Brough et al., 2020; Martin et al., 2022) which reach even fainter surface brightness limits, as well as more advanced feature identification through potential methods such as machine learning, will allow for higher completeness in feature identification, and the possibility of orders of magnitude more galaxies inspected. A more detailed and quantitative analysis of the impact of mergers on slow rotator evolution will then be possible. Additionally, methods such as dynamical modelling of orbital populations in slow rotators will provide an alternate method to identify merger histories via the modelled orbital populations. Finally, the in-progress Hector Survey will be able to explore the environmental effects on mergers (Bryant et al., 2016), enabling a similar analysis as performed here in diverse environments such as the outskirts of clusters.

Acknowledgements

The SAMI Galaxy Survey is based on observations made at the Anglo-Australian Telescope. SAMI was developed jointly by the University of Sydney and the Australian Astronomical Observatory (AAO). The SAMI input catalogue is based on data taken from the Sloan Digital Sky Survey, the GAMA Survey and the VST ATLAS Survey. The SAMI Galaxy Survey is supported by the Australian Research Council (ARC) Centre of Excellence ASTRO 3D (CE170100013) and CAASTRO (CE110001020), and other participating institutions. The SAMI Galaxy Survey website is `http://samisurvey.org/`.

The calculations for the Magneticum Box4 hydrodynamical simulation were carried out at the Leibniz Supercomputer Center (LRZ) under the project pr83li (Magneticum).

The SAMI instrument was funded by the AAO and JBH through FF0776384, LE130100198. JBH is supported by an ARC Laureate Fellowship and an ARC Federation Fellowship that funded the SAMI prototype. FDE acknowledges funding through the H2020 ERC Consolidator Grant 683184. SO acknowledges support from the NRF grant funded by the Korea government (MSIT) (No. 2020R1A2C3003769 and No. RS-2023-00214057). LMV acknowledges support by the German Academic Scholarship Foundation (Studienstiftung des deutschen Volkes) and the Marianne-Plehn-Program from the Elite Network of Bavaria. JvdS acknowledges support of an Australian Research Council Discovery Early

Career Research Award (project number DE200100461) funded by the Australian Government. JJB acknowledges support of an Australian Research Council Future Fellowship (FT180100231). AR acknowledges the receipt of a Scholarship for International Research Fees (SIRF) and an International Living Allowance Scholarship (Ad Hoc Postgraduate Scholarship) at The University of Western Australia.

The Hyper Suprime-Cam (HSC) collaboration includes the astronomical communities of Japan and Taiwan, and Princeton University. The HSC instrumentation and software were developed by the National Astronomical Observatory of Japan (NAOJ), the Kavli Institute for the Physics and Mathematics of the Universe (Kavli IPMU), the University of Tokyo, the High Energy Accelerator Research Organization (KEK), the Academia Sinica Institute for Astronomy and Astrophysics in Taiwan (ASIAA), and Princeton University. Funding was contributed by the FIRST program from the Japanese Cabinet Office, the Ministry of Education, Culture, Sports, Science and Technology (MEXT), the Japan Society for the Promotion of Science (JSPS), Japan Science and Technology Agency (JST), the Toray Science Foundation, NAOJ, Kavli IPMU, KEK, ASIAA, and Princeton University.

This paper makes use of software developed for Vera C. Rubin Observatory. We thank the Rubin Observatory for making their code available as free software at http://pipelines.lsst.io/.

This paper is based on data collected at the Subaru Telescope and retrieved from the HSC data archive system, which is operated by the Subaru Telescope and Astronomy Data Center (ADC) at NAOJ. Data analysis was in part carried out with the cooperation of Center for Computational Astrophysics (CfCA), NAOJ. We are honored and grateful for the opportunity of observing the Universe from Maunakea, which has the cultural, historical and natural significance in Hawaii.

The Pan-STARRS1 Surveys (PS1) and the PS1 public science archive have been made possible through contributions by the Institute for Astronomy, the University of Hawaii, the Pan-STARRS Project Office, the Max Planck Society and its participating institutes, the Max Planck Institute for Astronomy, Heidelberg, and the Max Planck Institute for Extraterrestrial Physics, Garching, The Johns Hopkins University, Durham University, the University of Edinburgh, the Queen's University Belfast, the Harvard-Smithsonian Center for Astrophysics, the Las Cumbres Observatory Global Telescope Network Incorporated, the National Central University of Taiwan, the Space Telescope Science Institute, the National Aeronautics and Space Administration under grant No. NNX08AR22G issued through the Planetary Science Division of the NASA Science Mission Directorate, the National Science Foundation grant No. AST-1238877, the University of Maryland, Eotvos Lorand University (ELTE), the Los Alamos National Laboratory, and the Gordon and Betty Moore Foundation.

Data Availability

The results of the data displayed in the figures can be obtained by contacting the corresponding author upon request. The images originate from the Hyper-Suprime Cam Public Data Release 2 (HSC-PDR2; Aihara et al., 2019) and are accessible at https://hsc-release.mtk.nao.ac.jp/doc/index.php/tools-2/. The data utilized in this paper, including kinematic measurements, originate from SAMI Data Release 3

(Croom et al., 2021). This data is accessible through Australian Astronomical Optics' Data Central at https://datacentral.org.au/.

Chapter 4

The SAMI Galaxy Survey: Linking Tidal Features and Orbit Populations Using Schwarzschild Modelling

There's no point in being grown up if you can't be childish sometimes.

—The Fourth Doctor

Tomas H. Rutherford,[1,2] Jesse van de Sande,[3,1,2] Scott M. Croom,[1,2]

[1]Sydney Institute for Astronomy, School of Physics, A28, The University of Sydney, NSW, 2006, Australia
[2]ARC Centre of Excellence for All Sky Astrophysics in 3 Dimensions (ASTRO 3D), Australia
[3]School of Physics, University of New South Wales, NSW, 2052, Australia

This chapter presents an investigation linking the orbital populations derived from Schwarzschild models of SAMI galaxies to their merger histories. I wrote all the text, produced all the figures, and ran all the models. The DYNAMITE code was used to create the models. Jesse van de Sande and Scott Croom supervised the work and assisted in revising the text. This chapter is being prepared for publication.

Abstract

The evolution of angular momentum in galaxies is shaped by a combination of internal secular processes and external mechanisms such as mergers. Orbit-superposition based dynamical modelling provides a powerful means of linking the intrinsic orbital structures of galaxies to their global properties and merger histories. We construct Schwarzschild orbit-superposition models of massive ($\log_{10}(M_*/M_\odot)$>10) SAMI galaxies using the DYNAMITE code, utilising deep KiDS photometry to accurately reproduce each galaxy's mass distribution. We find that the fractions of hot, cold, warm, and counter-rotating orbits all show significant correlations with the spin parameter proxy λ_{R_e}, with the strongest correlation arising from the combined hot + counter-rotating fraction. When controlling for stellar mass and environment, we find that hot and cold orbits show significant correlations with stellar age, whereas warm orbits do not. We further find that the reduction in λ_{R_e} for young galaxies with shell merger features in our sample is driven by an excess of hot orbits

and a deficit of cold orbits, with no dependence on warm orbits. We suggest that the kinematic transformation in this SAMI sample proceeds through stars transitioning directly from cold to hot orbits. Together, these findings indicate that merger-driven heating is the dominant mechanism governing the loss of angular momentum in massive galaxies.

4.1 Introduction

The mass assembly of galaxies in the Universe is the result of hierarchical processes (White & Rees, 1978), where many systems merge together over cosmic time. The merger history of galaxies can impact both the internal stellar dynamics (e.g. White, 1979; Fall & Efstathiou, 1980; Naab et al., 2014), and the external morphology, where tidal features formed from stellar debris serve as long-lived evidence of interactions (e.g. Toomre & Toomre, 1972; van Dokkum, 2005; Hood et al., 2018; Mancillas et al., 2019; Huang & Fan, 2022). These features are often classified into two broad categories: shells and streams. Streams form when material can be tidally stripped either from the disc of a massive, gas-rich system or from a low-mass satellite, giving rise to extended features (Byrd & Howard, 1992; Oh et al., 2008; Hood et al., 2018). Simulations suggest that shells form from nearly radial accretion events, in contrast to streams, which require a much more circular infall (Karademir et al., 2019). These classifications of tidal debris provide a method for interpreting the kinematic signatures observed in merger remnants, linking visible features to the intrinsic stellar dynamics.

Simulations have shown that mergers can reduce the rotational support of galaxies, as quantified by the spin parameter proxy λ_{R_e} (e.g., Di Matteo et al., 2009; Jesseit et al., 2009; Bois et al., 2011; Naab et al., 2014; Lagos et al., 2017, 2018a; Penoyre et al., 2017; Lagos, 2020b). However, the evolution of stellar dynamics is not solely governed by major mergers. Secular evolution, harassment, fly-by encounters, dynamical friction (Choi & Yi, 2017), minor mergers (Schulze et al., 2020), and cold accretion (Lofthouse et al., 2017) have also been shown in simulations to drive spin evolution. Simulations also display a trend for slow rotator galaxies to be preferentially created in dry rather than wet mergers (e.g. Lagos et al., 2018a). Observational studies have confirmed a link between mergers and kinematic spin-down (e.g. Bílek et al., 2023; Yoon et al., 2024), but the relation shows a large amount of scatter (e.g. Oh et al., 2016) and depends on parameters such as stellar age and environmental density (e.g. Rutherford et al., 2024; Croom et al., 2024). While simulations and observations both point to merger-driven spin evolution, the large variability in the relation suggests that the integrated dynamical support measured by λ_{R_e} cannot fully capture the variety of dynamical responses to mergers. Indeed, although λ_{R_e} has become the standard for distinguishing between fast and slow rotators (e.g. Emsellem et al., 2011; Cappellari, 2016; van de Sande et al., 2021a), it is sensitive to effects such as inclination, kinematic twists, decoupled components, and seeing (e.g. Emsellem et al., 2011; van de Sande et al., 2017a; Harborne et al., 2020). Furthermore, galaxies with different orbital structures can have the same value of λ_{R_e} (e.g. Jesseit et al., 2009), and while merger remnants change the orbital distribution of galaxies, λ_{R_e} is not always strongly affected (Bois et al., 2011; Naab et al., 2014). Therefore, a full understanding of how merger processes impact stellar dynamics requires an understanding of the detailed orbital structures within a galaxy, beyond what is captured by an average value of λ_R within one effective radius.

Stellar motions in galaxies can be separated into various orbital families, determined by the underlying gravitational potential, their angular momentum, and the axis around which they rotate. In practice, the gravitational potential of most galaxies is well represented by a Stäckel potential (Stäckel, 1891), for which the Hamilton–Jacobi equation is separable

and all orbits conserve the three integrals of motion E, I_2, I_3 (de Zeeuw, 1985). In such a triaxial system, there are four families of orbits: box orbits, inner long-axis tube orbits, outer long-axis tube orbits, and short-axis tube orbits. Box orbits have zero net angular momentum and oscillate along all three spatial axes. Because the frequencies of motions of a box orbit around any two axes are generally not commensurable, this orbit will pass through every point inside a rectangular box (Binney & Tremaine, 2008). Tube orbits conserve angular momentum around a particular axis, with short-axis tubes looping around the z-axis, and long-axis tubes looping around the x-axis (Binney & Tremaine, 2008). Tube orbits around the y-axis do exist, but they are unstable and therefore don't contribute much to orbital distributions. An alternate method of classifying orbits is by using their circularity parameter $\lambda_z = J_z/J_c(E)$, which is the ratio of the specific angular momentum to that of a circular orbit with the same energy (Abadi et al., 2003). Zhu et al. (2018b) classified orbits with $\lambda_z > 0.8$ as cold (near circular orbits), orbits with $-0.25 < \lambda_z < 0.25$ as hot (mostly radial orbits), orbits with $0.25 < \lambda_z < 0.8$ as warm (a mixture) and orbits with $\lambda_z < -0.25$ as counter-rotating. Galaxies with a large proportion of cold and warm orbits over hot orbits will display $\lambda_{R_e} \gtrapprox 0.5$, whereas galaxies with a large proportion of hot orbits will show $\lambda_{R_e} \lessapprox 0.3$ (Santucci et al., 2022). However, such orbital classifications cannot be derived from velocity moment maps, as λ_{R_e} is. Measuring orbital distributions from observations requires dynamical modelling techniques that recover the intrinsic dynamical structure (e.g. Zhu et al., 2018b; Jin et al., 2019).

The Schwarzschild orbit-superposition method (Schwarzschild, 1979, 1982) can be used to create dynamical models of galaxies that gives insight into their intrinsic orbital structures. By populating a triaxial gravitational potential with a comprehensive library of stellar orbits and fitting to the observed velocity maps, a representation of the galaxy's internal dynamics can be obtained. There have been many implementations of Schwarzschild models over time, both axisymmetric and triaxial (e.g. Cretton et al., 1999; Gebhardt et al., 2003; Valluri et al., 2004; van den Bosch et al., 2008; Vasiliev & Athanassoula, 2015; Vasiliev & Valluri, 2020; Neureiter et al., 2021). In this work, we employ DYNAMITE[1] (Jethwa et al., 2020; Thater et al., 2022) due to its ability to model triaxial potentials and its flexible, documented[2] python wrapper. By reconstructing the three-dimensional orbital distribution, these Schwarzschild models provide the means to quantify the variety of internal dynamics within a galaxy.

In this paper, we take advantage of the recent wealth of deep imaging from the Hyper-Suprime-Cam (HSC) (Aihara et al., 2018b) and Kilo-Degree Survey (KiDS) (Kuijken et al., 2019) optical galaxy surveys, complemented by kinematic data from the SAMI Galaxy Survey (Croom et al., 2012; van de Sande et al., 2021a; Croom et al., 2021) to construct orbit-superposition Schwarzschild models of a sample of massive, early-type galaxies. We base our sample on the sample in Rutherford et al. (2024), who use deep HSC imaging to investigate merger features around ETGs with $M_* > 10^{10} M_\odot$. We re-create and expand the sample of models of SAMI galaxies created by Santucci et al. (2022), by modelling our luminosity density with KiDS imaging rather than Sloan Digital Sky Survey (SDSS) imaging (Abazajian et al., 2009). As KiDS goes to deeper surface brightness limits than SDSS with better seeing, we expect the outer isophotes of each

[1] DYnamics, Age and Metallicity Indicators Tracing Evolution

[2] https://dynamics.univie.ac.at/dynamite_docs/index.html

galaxy's luminosity density, and thus mass distribution, to be more accurately modelled. We aim to investigate the impact of mergers on a galaxy's internal dynamics by combining the merger feature classifications with orbital distributions derived from these dynamical models.

This paper is structured as follows. Section 4.2 describes the data used in this paper and sample selection. Section 4.3 discusses our method. Section 4.4 presents the results. Section 4.5 discusses the results in the context of previous work. Section 4.6 presents a conclusion to this work. Throughout this paper, we adopt a flat ΛCDM cosmology, with $H_0 = 70\text{km s}^{-1}\text{ Mpc}^{-1}$, $\Omega_m = 0.3$, $\Omega_\Lambda = 0.7$. We further assume a Chabrier (Chabrier, 2003) initial mass function (IMF), and the AB magnitude system (Oke & Gunn, 1983).

4.2 Data

4.2.1 The SAMI Galaxy Survey

The SAMI instrument (Croom et al., 2012) was installed on the Anglo-Australian Telescope and offered a 1 degree diameter field of view. SAMI utilised 13 fibre bundles (Hexabundles; Bland-Hawthorn et al., 2011; Bryant et al., 2014), each with a 75% fill factor. Within each bundle, there were 61 fibres, each with a diameter of 1.6″, resulting in a 15″diameter for each IFU. These IFUs, along with 26 sky fibres, were connected to the AAOmega spectrograph (Sharp et al., 2006). The spectrograph employed the 580V grating covering the wavelength range of ~3700-5750Å, providing a resolution of R=1808 (σ=70.4 km s^{-1}). The 1000R grating was additionally used, covering 6300-7400Å, offering a resolution of R=4304 (σ=29.6 km s^{-1}) (van de Sande et al., 2017b).

The SAMI Galaxy Survey (Croom et al., 2012; Bryant et al., 2015) targeted galaxies selected from the GAMA survey (Driver et al., 2011) and eight low-redshift clusters (Owers et al., 2017). Reduced data cubes (Sharp et al., 2015) are accessible through SAMI Galaxy Survey data releases (Allen et al., 2015; Green et al., 2018; Scott et al., 2018; Croom et al., 2021), including stellar kinematic maps. The λ_{R_e} values used in our sample are derived from spatially resolved kinematic measurements (van de Sande et al., 2017b), incorporating corrections for aperture (van de Sande et al., 2017a) and seeing (Harborne et al., 2020; van de Sande et al., 2021a).

Light-weighted stellar ages are derived from full spectrum fitting of SAMI data, as described in Vaughan et al. (2022). The average light-weighted stellar age for a galaxy was calculated by summing all pixels within one effective radius (R_e), and fitting to this aperture spectrum. The environmental metric used in this work is the fifth nearest neighbour surface density, Σ_5. This density is defined as $\Sigma_5 = 5/\pi d^2$, where d is the projected comoving distance to fifth nearest neighbour galaxy, as described in Brough et al. (2017). We adopt stellar mass estimates from Bryant et al. (2015), calculated from Milky Way–extinction–corrected apparent g and i magnitudes, following the technique of Taylor et al. (2011).

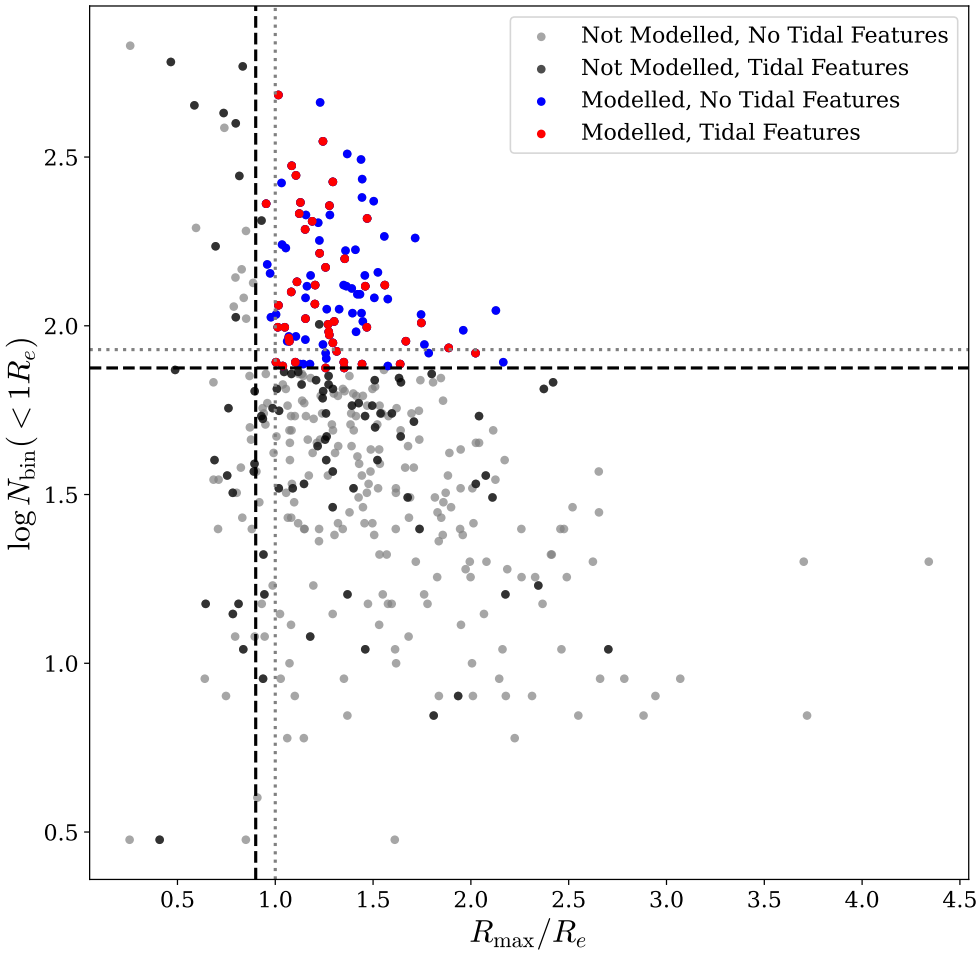

Figure 4.1: SAMI ETGs with $M_* > 10^{10} M_\odot$, plotted in $\log N_{\rm bin}(<1R_e)$ versus $R_{\rm max}/R_e$. $\log N_{\rm bin}(<1R_e)$ is the log of the number of Voronoi bins within $1R_e$, and $R_{\rm max}/R_e$ is the maximum radius reached by a galaxy's kinematic maps, divided by R_e. We expand the selection criteria from Santucci et al. (2022) from $\log N_{\rm bin}(<1R_e) \geq 85$ and $R_{\rm max}/R_e \geq 1$ (black dashed lines), to $\log N_{\rm bin}(<1R_e) \geq 75$ and $R_{\rm max}/R_e \geq 0.9$ (grey dotted lines). Galaxies plotted as black and grey dots are not within our selection criteria, and do and do not show tidal features, respectively. Galaxies plotted as red and blue dots are within our selection criteria, and do and do not show tidal features, respectively. There are two galaxies that lie within our selection criteria, but the model fitting failed to converge, and they were thus excluded from our sample.

4.2.2 The Kilo-Degree Survey (KiDS)

In this paper we use the Kilo-Degree Survey (KiDS) r-band data from KiDS data release 4, which achieves a limiting surface brightness of 25.02 ± 0.13 mag arcsec^{-2} (5σ in a 2" aperture, Kuijken et al., 2019). KiDS is an optical imaging survey covering 1500 degrees^2 (de Jong et al., 2013), and utilises the OmegaCAM instrument (Kuijken, 2011)

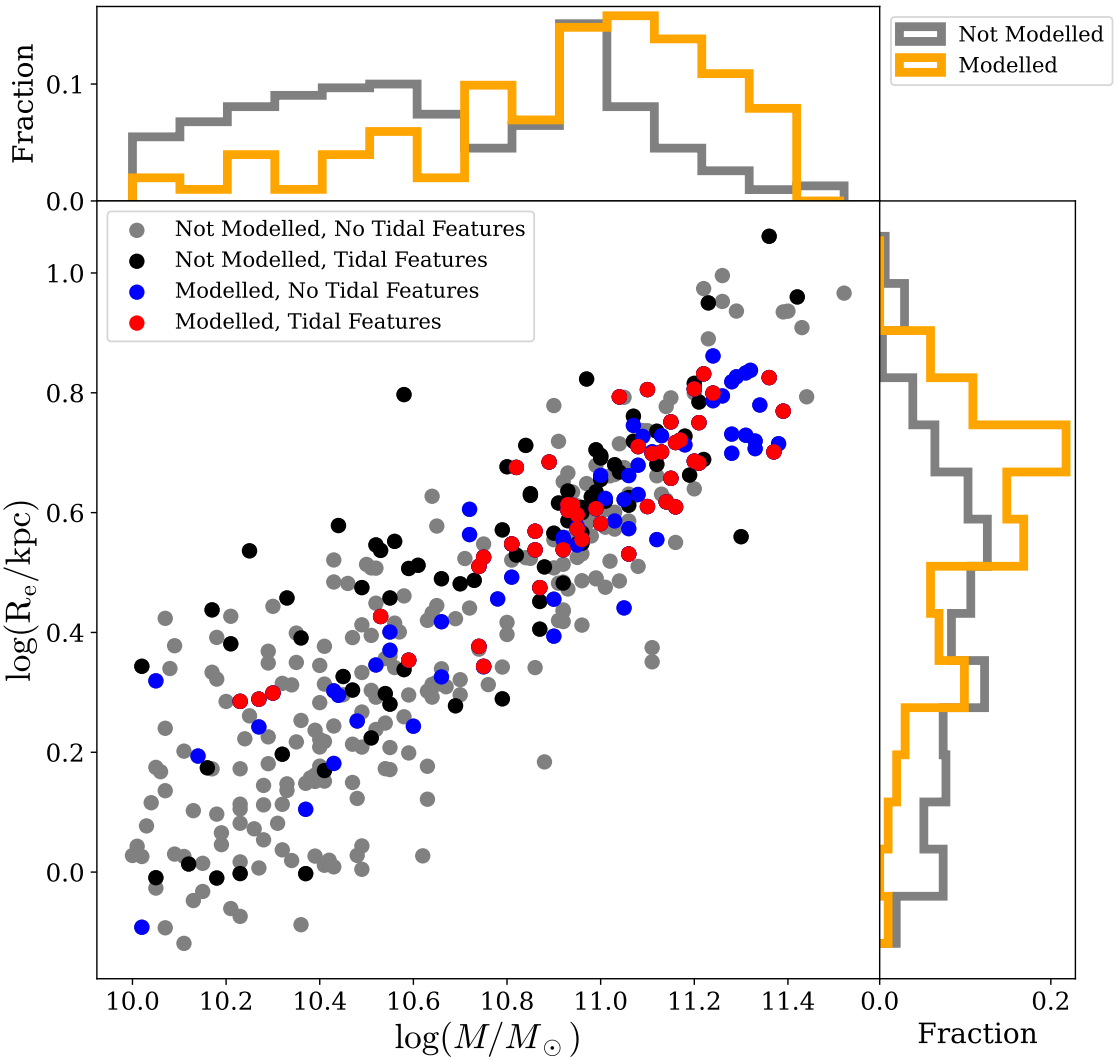

Figure 4.2: SAMI ETGs with $M_* > 10^{10} M_\odot$, plotted in $\log_{10}(M_*/M_\odot)$versus $\log(R_e/kpc)$. $\log(R_e/kpc)$ is the circular radius of the galaxy in kpc. Galaxies plotted as black and grey dots are not within our selection criteria, and do and do not show tidal features, respectively. Galaxies plotted as red and blue dots are within our selection criteria, and do and do not show tidal features, respectively. The fractions of galaxies as a function of $\log_{10}(M_*/M_\odot)$and $\log(R_e/kpc)$ are also shown as marginalised histograms for galaxies modelled and galaxies not modelled in orange and grey respectively. We observe that the galaxies that fall into our selection criteria are larger and more massive on average than the full sample. This is due to the selection requirement of at least 75 Voronoi bins within $1R_e$. However, the galaxies with the largest $\log(R_e/kpc)$ values are not modelled, as the stellar kinematics do not meet the required value of $R_{max}/R_e \geq 0.9$.

on the VLT Survey Telescope (VST), which has a 2.6m diameter and is located at the Paranal Observatory in Chile. OmegaCAM has a 268 Megapixel camera, providing a $1^\circ \times 1^\circ$ field of view. A focal plane array of 32 CCDs, each with 2048×4096 pixels, gives a total of $16,000 \times 16,000$ pixels, and a scale of 0.214 arcseconds/pixel.

The motivation for using KiDS imaging over SDSS imaging to model the luminosity

density of the galaxies in our sample is improved imaging depth and seeing. A direct comparison of surface brightness limits derived under the same assumptions is not readily available, however, KiDS r-band observations were obtained with an exposure time of 1800 seconds on a 2.6m telescope under a mean seeing of 0.70" (Kuijken et al., 2019). In comparison, SDSS DR7 achieved an effective exposure time of 54.1 seconds on a 2.5m telescope, with a median seeing of 1.40" (Abazajian et al., 2009). KiDS is thus significantly deeper than SDSS, and the advantage of deep imaging is that reaching the outermost isophotes of a galaxy provides the most accurate model of its light, and hence mass distribution.

However, imaging surveys that achieve the most extreme depths often suffer from saturation in the bright centres of massive galaxies. The HSC-SSP survey (Aihara et al., 2018a; Miyazaki et al., 2015) achieves a high surface brightness limit of 27.8 ± 0.5 mag arcsec^{-2} in the r-band (1σ noise in 1" apertures, Rutherford et al., 2024), but experiences point source saturation at $\mu < 17.5$. Given our sample of massive early-types, this results in a significant proportion of galaxies displaying saturation in the centre.

In Figure 4.3 we show an example of this saturation, and compare the HSC light profile to the KiDS and SDSS light profile for a galaxy in our sample with CATID = 70802. In panels (a), (b), and (c) we show this galaxy in HSC, KiDS, and SDSS imaging, respectively, with a horizontal dashed line across the centre. In panel (d), we show the surface brightness profile along this horizontal cut for HSC in black, KiDS in red, and SDSS in blue. A clear non-physical decrease in peak surface brightness is seen for HSC, absent in KiDS or SDSS, which is a result of saturation in the HSC imaging. The surface brightness of SDSS peaks lower than KiDS, because of the poorer seeing conditions of SDSS (1.4" vs 0.7"). Outside of the centre, the profiles agree well, with HSC going deeper than KiDS, which itself goes deeper than SDSS. Finally, HSC imaging has been shown to have issues with over sky-subtraction around bright, extended sources such as galaxies (e.g. Huang & Fan, 2022; Li et al., 2022). This is visible when comparing panels (a) and (b), with the HSC flux decreasing with radius faster than KiDS. As a result of the over sky-subtraction and clear saturation in HSC, we choose to use KiDS imaging, as it remains a substantial improvement in depth and seeing over SDSS.

4.2.3 Sample Selection

To investigate the relations between stellar age, stellar kinematics, and tidal features, we adopt the galaxy sample of Rutherford et al. (2024). This sample comprises early-type galaxies from the GAMA fields, taken from SAMI DR3 (Croom et al., 2021), with a mass cut of $\log_{10}(M_*/M_\odot) >= 10$. Galaxy morphologies were taken from Cortese et al. (2016), obtained using the classification approach of Kelvin et al. (2014) on SDSS DR9 data (Ahn et al., 2012). The mass cut was performed as the primary focus of Rutherford et al. (2024) was slow rotators, whose fraction increases strongly with stellar mass (e.g. van de Sande et al., 2017a). Additionally, the stellar kinematic completeness in the SAMI Galaxy Survey falls below 50% for $\log_{10}(M_*/M_\odot) < 9.5$, necessitating a mass cut for robust dynamical modelling. This sample contains 411 galaxies.

We adopt the spaxel quality criteria from van de Sande et al. (2017b) to ensure reliability in the kinematic measurements, but increase the minimum signal to noise per Voronoi

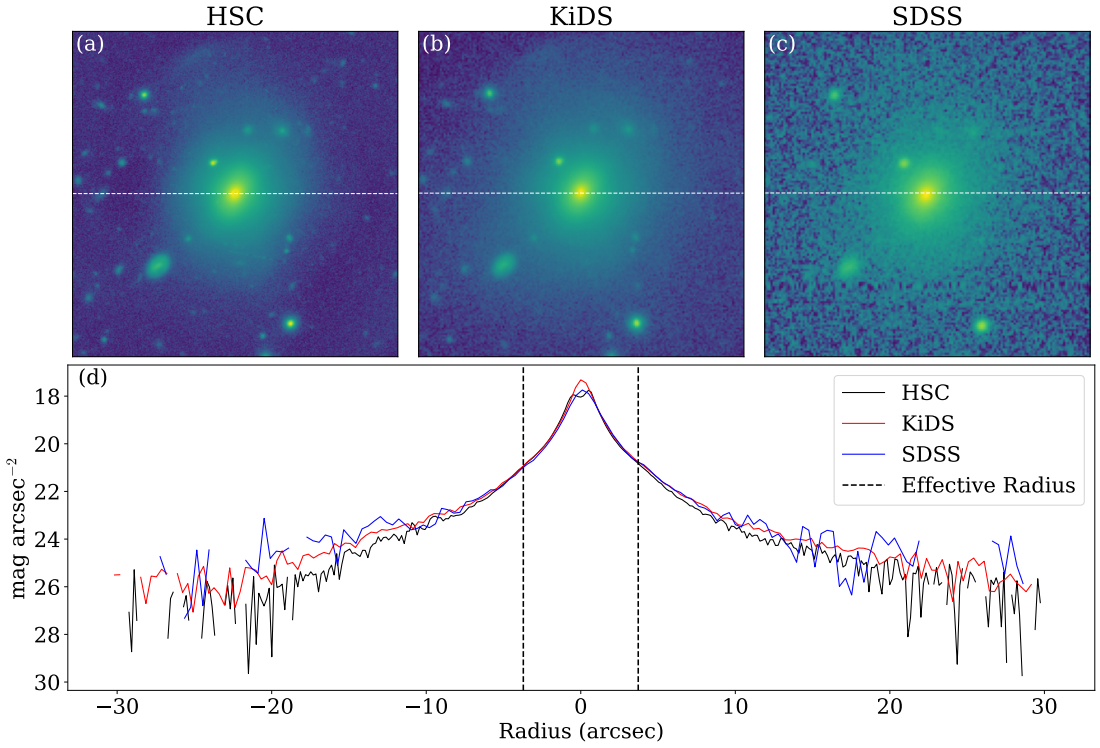

Figure 4.3: A comparison of imaging and surface brightness profiles for HSC DR2, KiDS DR4, and SDSS DR12 imaging for the SAMI galaxy with CATID = 70802. In panels (a), (b), and (c) we show a cutout for the galaxy in HSC, KiDS, and SDSS imaging, respectively. We also show a dashed horizontal white line through the centre, which we take a one-dimensional surface brightness profile from. In panel (d), we show this surface brightness profile in mag arcsec^{-2} for HSC (black), KiDS (red), and SDSS (blue). We also show the effective radius of the galaxy in vertical dashed lines. A clear non-physical decrease in peak surface brightness in the centre is clear in HSC that is not present in KiDS or SDSS, a result of saturation in HSC. SDSS peaks at a lower surface brightness than KiDS due to the poorer seeing conditions of SDSS (1.4" vs 0.7").

bin from $S/N > 3$ Å^{-1} to $S/N > 10$ Å^{-1}. This higher threshold provides more robust measurements while allowing us to work with a reduced minimum number of spaxels within one effective radius. These criteria are therefore:

$$Q_1) \;\; S/N > 10 \text{ Å}^{-1} \;\; \& \;\; \sigma > 35 \text{ km/s} \tag{4.1}$$

$$Q_2) \;\; V_{\text{error}} < 30 \text{ km/s} \;\; \& \;\; \sigma_{\text{error}} < \sigma \times 0.1 + 25 \text{ km/s} \tag{4.2}$$

The final step of the sample definition is to select from our sample based on the radial coverage of SAMI. In Figure 4.1, we show our initial sample, displayed as the number of Voronoi bins within 1R$_e$vs radial coverage. We also show our sample in Figure 4.2, displayed in the mass-size plane. We extend the selection criteria from Santucci et al. (2022), and require each galaxy to have a minimum number of bins within 1R$_e$of 75, and the minimum radius reached in the kinematic maps to be 0.9R$_e$. These cuts in sampling and radial coverage are displayed as the black dashed lines in Figure 4.1, with the selection criteria of Santucci et al. (2022) displayed as grey dotted lines. Galaxies shown as black

(with tidal features) and grey (without tidal features) dots do not fall within our selection criteria. Galaxies shown as red (with tidal features) and blue (without tidal features) dots are within our selection criteria. Finally, two galaxies that satisfy our selection criteria failed to converge during model fitting, and they were consequently excluded from our sample. The final sample thus consists of 102 galaxies.

4.3 Orbit-Superposition Modelling

We use the Schwarzschild's method (Schwarzschild, 1979, 1982) to create orbit-superposition models for our galaxies, using the DYNAMITE (Jethwa et al., 2020; Thater et al., 2022) implementation and code. We use DYNAMITE, as it accommodates triaxial models, provides multiple grid-search algorithms for efficient convergence of our free parameters, and offers a well-documented python wrapper.

The derivation of a Schwarzschild model can be summarised in three steps: 1) create a model for the gravitational potential, 2) derive a library of stellar orbits allowed by this potential, and 3) calculate which combination of orbits best reproduces the observed kinematic maps. These steps are described in detail in van den Bosch et al. (2008), and we summarise them in Sections 4.3.1-4.3.3.

4.3.1 Gravitational Potential

We model the gravitational potential as consisting of a stellar mass, dark halo, and supermassive black hole component.

Stellar Potential

The stellar mass distribution is modelled with the Multi-Gaussian Expansion (MGE) formalism (Monnet et al., 1992; Emsellem et al., 1994a; Cappellari, 2002). This method is adopted by the DYNAMITE code that we use in this paper to construct our Schwarzschild models. MGE assumes that a galaxy's projected luminosity on the sky, I, can be represented by a sum of N two-dimensional Gaussians:

$$I(x', y') = \sum_{k=1}^{N} \frac{L_k}{2\pi\sigma_k'^2 q_k'} \exp\left[-\frac{1}{2\sigma_k'^2}\left(x'^2 + \frac{y'^2}{q_k'^2}\right)\right] \tag{4.3}$$

where x' and y' are the projected coordinates on the sky, and each Gaussian component has total luminosity L_k, observed axial ratio q_k', and dispersion σ_k along the major axis.

We create MGE models of KiDS r-band images for each galaxy in our sample. The galaxy mask and PSF for each image are derived using the source-extraction and star-fitting procedures of PROFOUND and PROFUSE respectively (Robotham et al., 2018, 2022). The PSF, provided by PROFUSE as a Moffat profile image (Moffat, 1969), is then modelled with MGE so it may be analytically convolved with the MGE model of the relevant galaxy during fitting.

Although DYNAMITE is capable of allowing small isophote twists in the MGE model, we fix the position angles of each Gaussian to be constant. We do this as these twists greatly

reduce the available viewing angle parameter space for deprojection into three-dimensional luminosity densities. We show an example MGE fit in Figure 4.4.

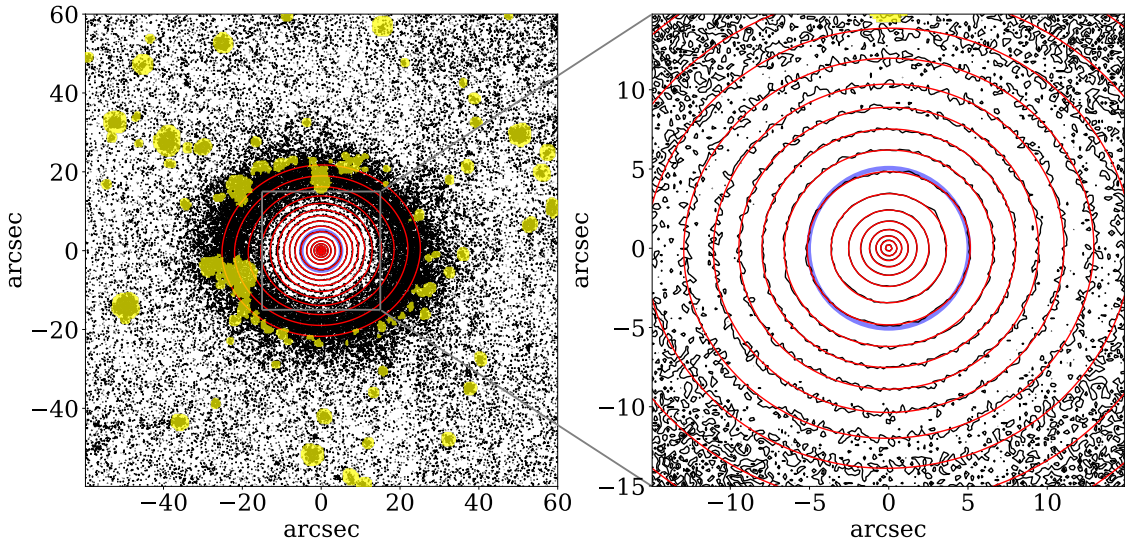

Figure 4.4: MGE fit to the galaxy with CATAID = 39057. KiDS r-band imaging contours are shown in black, the MGE model contours are shown in red, and masked regions (other sources) are shown in yellow. The effective radius of the galaxy (R_e=5.05") is shown in blue. The contours are spaced by 0.5 mag arcsec^{-2}. The right side panel is a zoomed-in version of the left side panel, with the scale shown by a box around the central region in the left side panel.

The MGE model of the projected luminosity is then deprojected into a three-dimensional luminosity density, given some set of viewing angles (ϑ, ϕ, ψ). These viewing angles are fitted for by first converting them into the intrinsic shape parameters $(p_k, q_k, u_k = \sigma'_k/\sigma_k)$, using the relation for ellipsoidal bodies from de Zeeuw & Franx (1989), as described in Cappellari (2002):

$$1 - q^2 = \frac{\delta'[2\cos 2\psi + \sin 2\psi(\sec\vartheta\cot\phi - \cos\vartheta\tan\phi)]}{2\sin^2\vartheta[\delta'\cos\psi(\cos\psi + \cot\phi\sec\vartheta\sin\psi) - 1]} \tag{4.4}$$

$$p^2 - q^2 = \frac{\delta'[2\cos 2\psi + \sin 2\psi(\cos\vartheta\cot\phi - \sec\vartheta\tan\phi)]}{2\sin^2\vartheta[\delta'\cos\psi(\cos\psi + \cot\phi\sec\vartheta\sin\psi) - 1]} \tag{4.5}$$

where $\delta' = 1 - q'^2$, $p_k = B_k/A_k$, and $q_k = C_k/A_k$, with A_k, B_k, and C_k being the major, medium, and minor axes of the k^{th} 3D Gaussian component. The luminosity density ρ is then given by:

$$\rho(x,y,z) = \sum_{k=1}^{N} \frac{L_k}{(\sigma_k\sqrt{2\pi})^3 q_k p_k} \exp\left[-\frac{1}{2\sigma_k^2}\left(x^2 + \frac{y^2}{p_k^2} + \frac{z^2}{q_k^2}\right)\right] \tag{4.6}$$

where (x, y, z) is a set of coordinates centred on the Gaussians and aligned with the principal axes. Further, the deprojection requires that $q_k \leq p_k \leq 1$, $q'_k \leq q_k$ and $\max(q_k/q'_k, p_k) \leq u_k \leq \min(p_i/q'_i, 1)$. In DYNAMITE, the deprojection is fit for by taking $(p_{\min}, q_{\min}, u_{\min})$ as the free parameters. Finally, a globally constant mass-to-light

ratio Υ_* multiplies the luminosity density to obtain the stellar mass distribution, with Υ_* the 4$^{\text{th}}$ free parameter included in our fit. One advantage of using r-band KiDS photometry for our MGE model is that it traces the older stellar population that makes up the majority of the stellar mass. It is possible to derive a spatially varying mass-to-light ratio for a Schwarzschild mass model (e.g. for an edge-on disc, Poci et al., 2019), but keeping Υ_* constant has been shown for CALIFA galaxies to not impact the internal dynamics of a Schwarzschild model (Zhu et al., 2018b), and hence we use a constant value here.

Dark Matter Halo and Supermassive Black Hole

The dark matter halo is taken to be a spherical NFW halo (Navarro et al., 1996), with an enclosed mass profile given by:

$$M(<r) = M_{200}[\ln(1+c) - c/(1+c)]^{-1}\left[\ln(1+cr/r_{200}) - \frac{cr/r_{200}}{1+cr/r_{200}}\right] \tag{4.7}$$

where c is the dark matter halo concentration, and M_{200} is the mass within the virial radius r_{200}. The virial mass and virial radius are related via the relation $M_{200} = \frac{4}{3}\pi 200\rho_c r_{200}^3$, with the critical density $\rho_c = 1.37\times10^{-7}M_\odot \text{pc}^{-3}$. However, the concentration c has been shown to be poorly constrained by kinematics only extending to $\sim 2\text{R}_e$, such as SAMI (e.g. Zhu et al., 2014). We therefore fix c according to M_{200} and the relation of Dutton & Macciò (2014). Finally, we define the dark matter fraction as $f = M_{200}/M_*$, and take $\log f$ as the sole free parameter to characterise the dark matter halo, and thus dark matter contribution to the gravitational potential.

The black hole contribution is modelled as a Plummer potential (Plummer, 1911), which is parametrised by its total mass M_{BH}, and scale radius a. As the spatial resolution of SAMI kinematic maps is lower than the region where the black hole's mass dominates the potential, we fix $a = 0.001"$ and the potential becomes essentially point-like. The black hole is therefore represented solely by M_{BH}, which we choose to parametrise as $\log(M_{BH})$. Combining all components of the potential, we have six free parameters characterising it: $p_{\text{min}}, q_{\text{min}}, u_{\text{min}}, \Upsilon_*, \log f,$ and $\log(M_{BH})$.

4.3.2 Orbit Library

The construction of a Schwarzschild model requires a library of all allowable stellar orbits within the gravitational potential, a linear combination of which will reconstruct the observed kinematics. As our potential is triaxial and separable (i.e. the Hamilton-Jacobi equation is separable), all orbits are regular and conserve three integrals of motion: Energy E, I_2, and I_3 (e.g. de Zeeuw, 1985; Binney & Tremaine, 2008). There are four families of orbits that exist in this potential: three types of tube orbits (inner long axis, outer long axis, short axis), and box orbits. We initiate our orbits by sampling from the three integrals of motion.

The number of points sampled across the three integrals is $n_E \times n_\theta \times n_R$, where n_E, n_θ, n_R denote the number of intervals taken across the energy E, azimuthal angle θ and radius R on the (x, z) plane. The E values are sampled logarithmically in radius, with E calculated as the potential at $x = r$. This grid spans $0.5\sigma'_{min}$ to $5\sigma'_{max}$, where σ'_{min} and σ'_{max} are the

minimum and maximum observed dispersions of the MGE model. R and θ are sampled in a linear open polar grid. Each initial condition sampled is then used to seed three orbits: a box orbit, a tube orbit, and a counter-rotating tube orbit. Finally, DYNAMITE allows each orbit to be dithered $n_{\rm dither}$ times (as done in e.g. van den Bosch et al., 2008; Zhu et al., 2018b; Santucci et al., 2022), where there are $n^3_{\rm dither}$ orbits seeded in a grid around each set of initial conditions. This is done to smooth the model, and results in a "bundle" of orbits for each integral value. Overall, the total number of orbits generated in an orbit library is $3 \times n_E \times n_\theta \times n_R \times n^3_{\rm dither}$.

We calculate two libraries of orbits for each galaxy. For the first library, we add $3 \times n_E \times n_\theta \times n_R = 3 \times 21 \times 18 \times 9 = 10206$ orbits. This library is used to coarsely sample the parameter space to get initial estimates for the free parameters of the model, and we refer to it as our coarse library. The second library contains $3 \times n_E \times n_\theta \times n_R \times 3^3 = 3 \times 30 \times 20 \times 10 \times 3^3 = 486000$ orbits, where we have dithered each orbit 3 times for each integral value. We use this library to fit for and build our final, best-fit model, and refer to it as our "fine" library.

4.3.3 Orbit Weighting

To find the best-fit model, we define a goodness-of-fit, χ^2, and find values for our free parameters $(p_{\rm min}, q_{\rm min}, u_{\rm min}, \Upsilon_*, \log f, M_{BH})$ such that χ^2 is minimised. In DYNAMITE, the best-fit model is taken to be that with the minimum *kinematic* χ^2:

$$\chi^2 = \sum_{n=1}^{N_{\rm kin}} \left[\left(\frac{V^n_{\rm mod} - V^n_{\rm obs}}{V^n_{\rm obserr}} \right)^2 + \left(\frac{\sigma^n_{\rm mod} - \sigma^n_{\rm obs}}{\sigma^n_{\rm obserr}} \right)^2 + \left(\frac{h^n_{3,\,\rm mod} - h^n_{3,\,\rm obs}}{h^n_{3,\,\rm obserr}} \right)^2 + \left(\frac{h^n_{4,\,\rm mod} - h^n_{4,\,\rm obs}}{h^n_{4,\,\rm obserr}} \right)^2 \right]$$

where $V^n_{\rm mod}$, $\sigma^n_{\rm mod}$, $h^n_{3,\,\rm mod}$, $h^n_{4,\,\rm mod}$ are the model velocities for bin n in the velocity maps, $V^n_{\rm obs}$, $\sigma^n_{\rm obs}$, $h^n_{3,\,\rm obs}$, $h^n_{4,\,\rm obs}$ are the observed velocities, $V^n_{\rm obserr}$, $\sigma^n_{\rm obserr}$, $h^n_{3,\,\rm obserr}$, $h^n_{4,\,\rm obserr}$ are the observational errors and $N_{\rm kin}$ is the number of bins. Each model velocity is convolved with the same PSF as the observations prior to calculating χ^2. The reduced χ^2, $\chi^2_{\rm red}$ is defined as $\chi^2_{\rm red} = \frac{\chi^2}{4N_{\rm kin} - N_{\rm par}}$, where $N_{\rm par}$ is the number of free parameters, with $N_{\rm par} = 6$ in this work. We expect $\chi^2_{\rm red}$ to approach 1 for the best-fit model. For each model fitting step, we use DYNAMITE's "LegacyWeightSolver" implementation of Lawson and Hanson's non-negative least-squares algorithm (Lawson & Hanson, 1974).

We begin with our coarse library of orbits. Similarly to Derkenne et al. (2024), we use this library to first run a coarse grid search over the structural parameters $p_{\rm min}, q_{\rm min}, u_{\rm min}$, with minimum steps of 0.03, 0.03, and 0.01 respectively. We use DYNAMITE's "FullGrid" parameter search setting, which creates a Cartesian grid for all free parameters, and searches through it with the minimum step size. We then use the coarse library of orbits again, to run another coarse grid search over the parameters $\log f, \Upsilon_*$, with minimum steps of 0.01 each. We again run this search with the "FullGrid" parameter search setting.

For the final step, we use our fine library of orbits. We run a grid search over the full parameter space of $p_{\rm min}, q_{\rm min}, u_{\rm min}, \Upsilon_*, \log f, \log(M_{BH})$, with minimum step sizes of

0.01,0.01,0.01,0.01,0.01, and 0.1 respectively. We limited Υ_* between 0.1 and 10, log f between -3 and 3, and log(M_{BH}) between 1 and 10. We use the best-fit values from the first two coarse grid searches as the starting values for each parameter, and the relation from Reines & Volonteri (2015) for black hole masses from stellar mass for the starting value of M_{BH}. We use the "LegacyGridSearch" search setting, which takes smaller and smaller steps towards the best fit solution.

4.4 Results

4.4.1 Schwarzschild Models

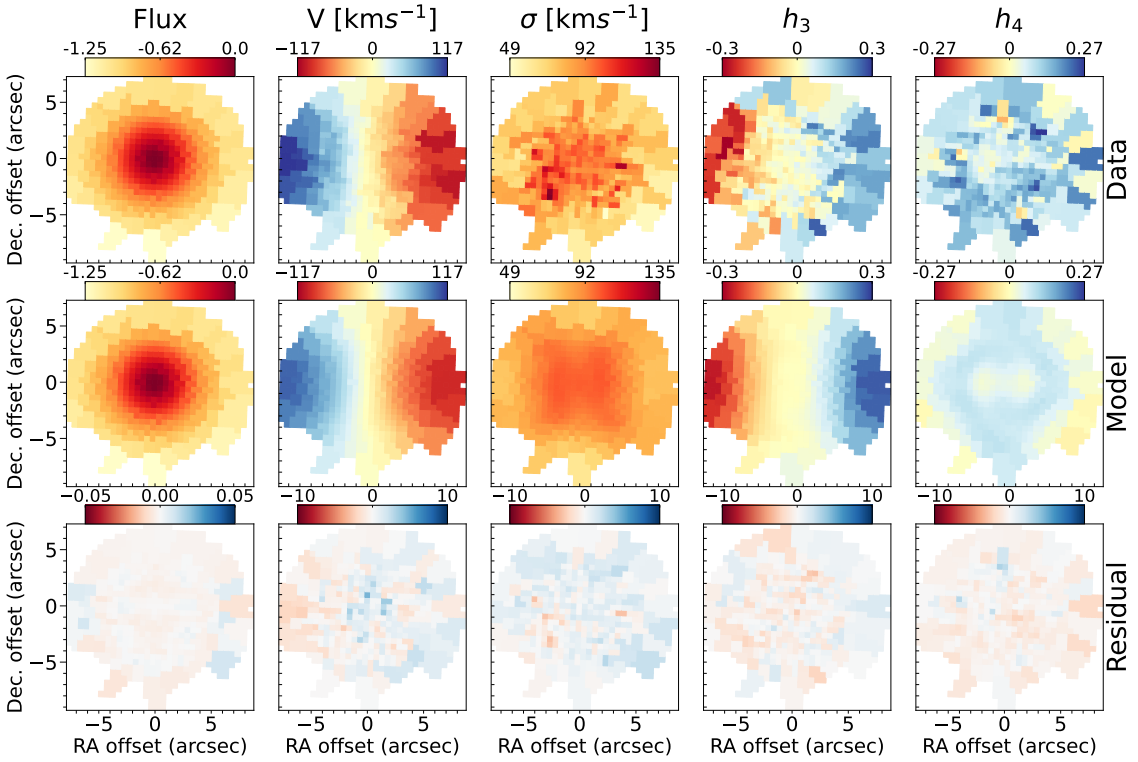

Figure 4.5: The best-fitting Schwarzschild model for SAMI galaxy with CATID = 220394, and $\chi^2_{\rm red}$ = 0.94. This galaxy displays a good fit at high spatial sampling, with a stellar mass of $\log_{10}(M_*/M_\odot)$ = 10.3, λ_{R_e} = 0.39, $R_{\rm max}/R_e$ = 1.28, and $N_{\rm bins}$ = 227. From top to bottom, we show the input data, the model, and the relative residual respectively. Some spaxels approach relative residual values of ~ 10, or 1000%, but due to the large number of well-fit spaxels, $\chi^2_{\rm red}$ remains close to unity and indicates a good fit to the data. From left to right, we show the flux, velocity, velocity dispersion σ, h_3, and h_4 respectively. The model reconstructs all velocity moments accurately, as the residual panels show low values and no structure.

We fit Schwarzschild orbit-superposition models to the 102 galaxies in our sample. For each galaxy, we explored up to 2000 models in the coarse parameter searches, and 2000 models in the final grid search. This is comparable to previous works with large sample sizes (e.g. 1000-2000 models for Jin et al. 2019, 2020, 1250 for Santucci et al. 2022), and slightly lower than previous works with smaller sample sizes (e.g. up to 8000 models

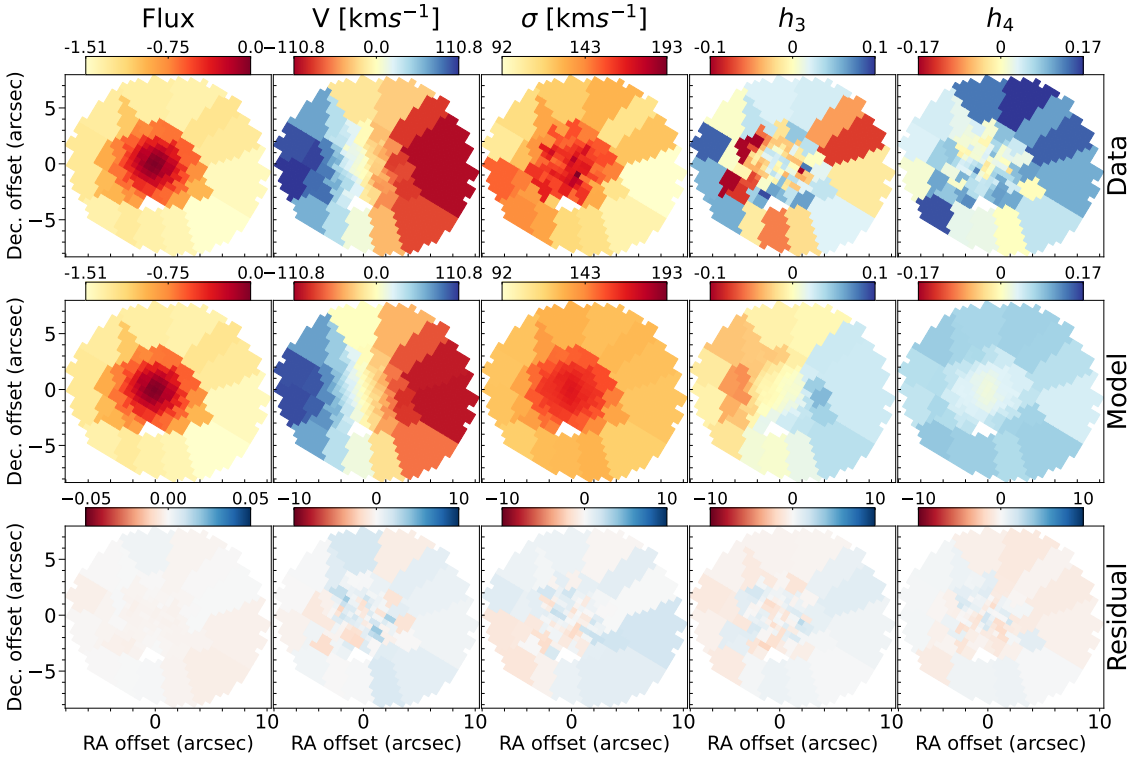

Figure 4.6: The best-fitting Schwarzschild model for SAMI galaxy with CATID = 511892, and $\chi^2_{\rm red} = 1.13$. This galaxy displays a good fit at low spatial sampling, with a stellar mass of $\log_{10}(M_*/M_\odot) = 10.86$, $\lambda_{R_e} = 0.33$, $R_{\rm max}/R_e = 1.36$, and $N_{\rm bins} = 78$. Panels are arranged as in Figure 4.5. The model reconstructs all velocity moments accurately, as the residual panels show low values and no structure.

for Derkenne et al. 2024). From each model we extract the velocity moment maps V, σ, h_3, and h_4. Additionally, from the best-fit parameters and derived orbit library, we extract fractions of λ_z and triaxiality, both as a function of radius.

We present the velocity moment maps of four galaxies representative of our sample, labelled here with their CATID:

- 220394: A galaxy with many spatial bins, 227 bins within R_e, $\chi^2_{\rm red} = 0.94$. Shown in Figure 4.5.
- 511892: A galaxy close to the minimum number of spatial bins, 78 bins within R_e, $\chi^2_{\rm red} = 1.13$. Shown in Figure 4.6.
- 79733: A triaxial galaxy, 164 bins within R_e, $\chi^2_{\rm red} = 0.86$. Shown in Figure 4.7.
- 289102: An oblate galaxy, 120 bins within R_e, $\chi^2_{\rm red} = 1.07$. Shown in Figure 4.8.

For Figures 4.5-4.8, the first row shows the observed flux, V, σ, h_3, and h_4 from left to right. The middle row shows the same, but for the model. The bottom row shows the relative residual, where we subtract the model from the data and divide by the observational uncertainties. Some spaxels approach 1000% relative residual even for well fit galaxies, but due to the large number of spaxels, these galaxies display a $\chi^2_{\rm red}$ value close to unity, indicative of a good fit to the data.

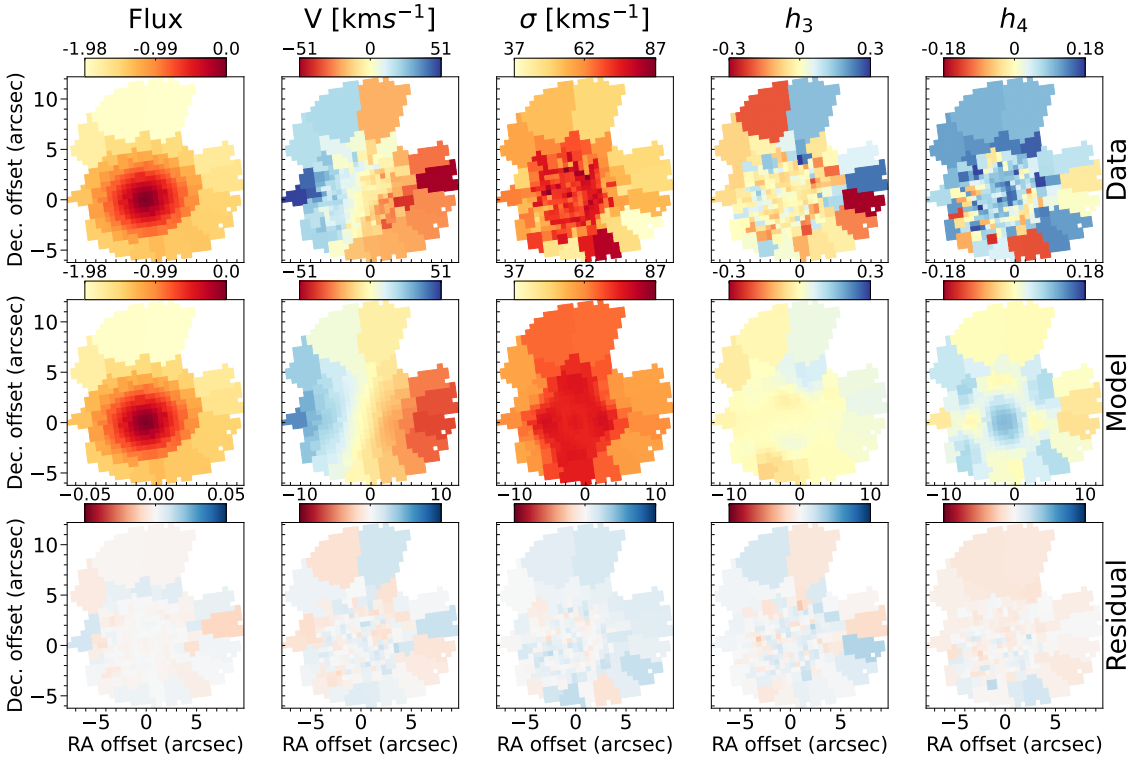

Figure 4.7: The best-fitting Schwarzschild model for SAMI galaxy with CATID = 79733, and $\chi^2_{\rm red} = 0.86$. This galaxy displays a good fit with a triaxial shape, with a stellar mass of $\log_{10}(M_*/M_\odot) = 10.23$, $\lambda_{R_e} = 0.20$, $R_{\rm max}/R_e = 1.23$, and $N_{\rm bins} = 164$. Panels are arranged as in Figure 4.5. The model reconstructs all velocity moments accurately, as the residual panels show low values and no structure.

4.4.2 Orbit Fractions

The Schwarzschild model of a galaxy additionally gives information about its intrinsic angular momentum, rather than the projected quantities derived from observations. One useful quantity that we calculate for each orbit in a galaxy model is the circularity parameter, λ_z (Abadi et al., 2003; Zhu et al., 2018b):

$$\lambda_z = \frac{\overline{L_z}}{\overline{r} \cdot \overline{V_c}} \tag{4.8}$$

where:

$$\overline{L_z} = \overline{xV_y - yV_x}$$
$$\overline{r} = \sqrt{\overline{x^2 + y^2 + z^2}}$$
$$\overline{V_c} = \sqrt{\overline{V_x^2 + V_y^2 + V_z^2 + 2V_xV_y + 2V_xV_z + 2V_yV_z}}$$

The bar notation denotes that these values (x, y, z, V_x, V_y, V_z) are averaged over time for the entire orbit's path. $\overline{V_c}$ is equivalent to the angular momentum of a purely circular orbit at $\overline{r}$, which is the maximum possible value of $\overline{L_z}$, and hence λ_z varies between -1 and 1. λ_z can be considered an intrinsic equivalent of λ_{R_e}, as it separates rotation and

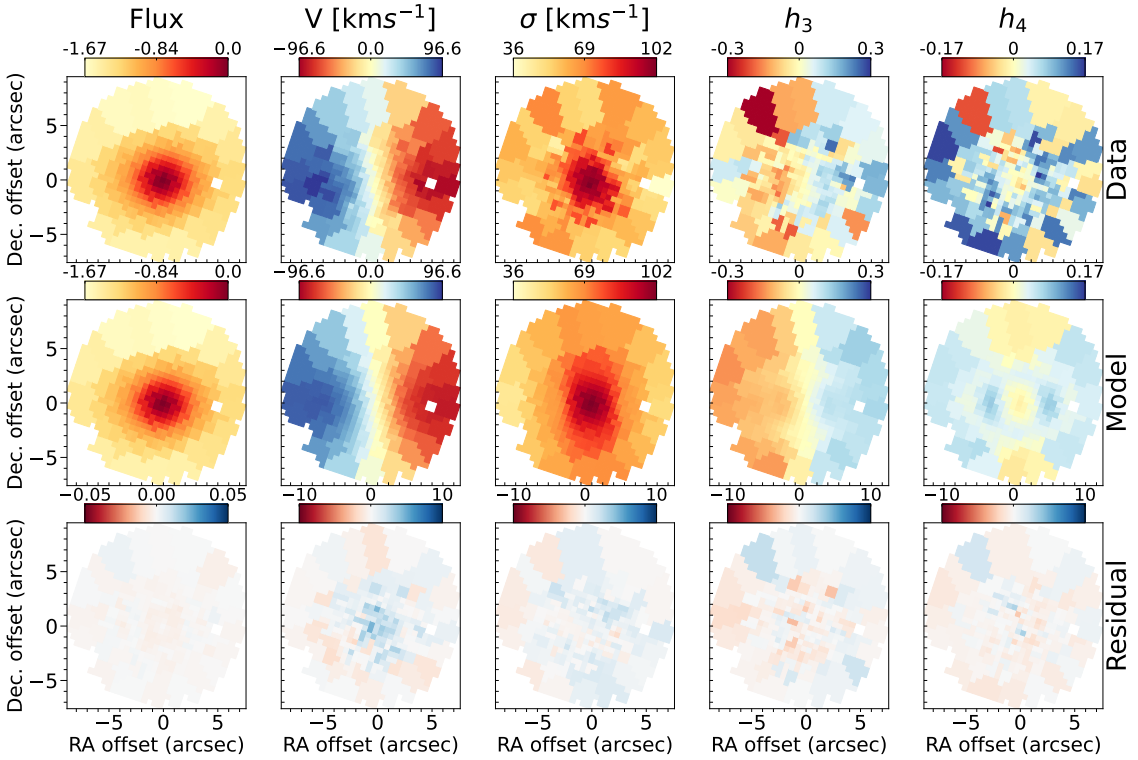

Figure 4.8: The best-fitting Schwarzschild model for SAMI galaxy with CATID = 289102, and $\chi^2_{\rm red}$ = 1.07. This galaxy displays a good fit with an oblate shape, with a stellar mass of $\log_{10}(M_*/M_\odot)$ = 10.14, λ_{R_e} = 0.46, $R_{\rm max}/R_e$ = 1.56, and $N_{\rm bins}$ = 120. Panels are arranged as in Figure 4.5. The model reconstructs all velocity moments accurately, as the residual panels show low values and no structure.

dispersion supported orbits, with hot/box orbits having $\lambda_z \lessapprox 0.3$, and cold/circular orbits having $\lambda_z \gtrapprox 0.5$. We show the $\lambda_z - r$ distribution for 289102 in Figure 4.9. Zhu et al. (2018b) defined four classes of orbits within this distribution according to an orbit's λ_z: hot orbits ($-0.25 \leq \lambda_z \leq 0.25$), warm orbits ($0.25 \leq \lambda_z \leq 0.8$), cold orbits ($\lambda_z \geq 0.8$), and counter-rotating orbits ($\lambda_z \leq -0.25$). We show these classes in Figure 4.9, as well as the maximum radial extent of the SAMI kinematics, and the effective radius.

We show the orbital distribution within 1R$_e$ for our full sample, ordered by stellar age, in Figure 4.10. All stellar orbits are integrated over radii within 1R$_e$, and their relative weights are plotted in bins of λ_z. The x-axis then orders the galaxies by average light-weighted stellar age within 1R$_e$, as this has been shown to be the parameter that correlates best with λ_{R_e}, and hence the angular momentum traced by λ_z. We divide λ_z into the broad categories defined by Zhu et al. (2018b): cold, warm, hot, and counter-rotating, and show and label these groups accordingly. The overall trend is that younger galaxies contain higher fractions of cold orbits, whereas older galaxies are dominated by hot orbits.

We derive orbit fractions (cold, warm, hot, counter-rotating) within 1R$_e$ for each galaxy in our sample. We show the correlations between these fractions and other global galaxy properties in Figure 4.11. This figure presents the hot, warm, cold, and counter-rotating fractions within 1R$_e$ labelled as Hot$_{R_e}$, Warm$_{R_e}$, Cold$_{R_e}$, and CR$_{R_e}$ respectively. We additionally show the stellar mass, $\log_{10}(M_*/M_\odot)$, the mean light-weighted stellar age

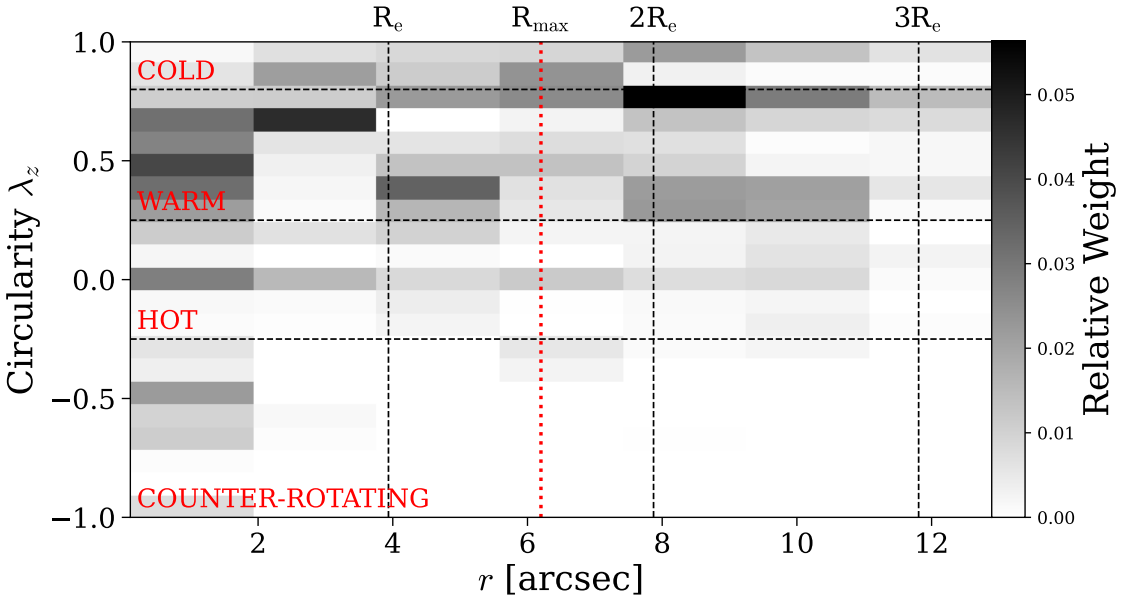

Figure 4.9: The $\lambda_z - r$ phase space distribution of the best fit Schwarzschild model for the galaxy with CATID = 289102. This plot shows the probability density of the orbits used to reconstruct the velocity maps (see Figure 4.8). λ_z is defined in Equation 4.8. The divisions between cold, warm, hot, and counter-rotating orbits are shown in horizontal dashed lines, and labelled. R_e, $2R_e$ and $3R_e$ are shown as vertical dashed black lines, and the maximum radius reached by the SAMI kinematics, R_{max} is shown in a vertical dotted red line. Within $1R_e$, the model predicts a cold orbit fraction of 0.04, warm orbit fraction of 0.22, hot orbit fraction of 0.68, and counter-rotating orbit fraction of 0.06.

within $1R_e$, Age_{LW}/Gyr, the spin parameter proxy, λ_{R_e}, and the sum of hot and counter-rotating orbit fractions, $Hot_{R_e}+CR_{R_e}$. Galaxies with tidal shells, as identified in Rutherford et al. (2024), are circled in black. A best-fitting linear relation is shown for each panel in red, with 68% and 95% confidence intervals, derived using bootstrap resampling, shown in lighter red shading. The p-value for the Pearson correlation coefficient is given for each panel and highlighted in bold when $p < 0.05$, indicating a statistically significant correlation.

There are strong correlations between the orbit fractions, and we note that these are partially driven by the fact that all orbit fractions must sum to one for each galaxy. λ_{R_e} shows a significant correlation with each orbit fraction, as expected since it traces the balance between rotation and dispersion set by the stellar orbits. Among these relations, λ_{R_e} shows the strongest and tightest correlation with the combined hot plus counter-rotating fraction, $Hot_{R_e} + CR_{R_e}$, followed by the warm fraction, $Warm_{R_e}$, and then the hot fraction, Hot_{R_e}. The quantity $Hot_{R_e} + CR_{R_e}$ is mathematically equivalent to $1 - (Cold_{R_e} + Warm_{R_e})$, reflecting the requirement for all fractions to sum to unity. The light-weighted stellar age, Age_{LW}, correlates most strongly with $\log_{10}(M_*/M_\odot)$, followed by, at roughly equal significance, Hot_{R_e} + CR_{R_e}, Hot_{R_e}, $\lambda_{R_e}$and $Cold_{R_e}$. While $Warm_{R_e}$ and Hot_{R_e} both show a strong positive and negative correlation with λ_{R_e}respectively, only Hot_{R_e} shows a strong correlation with Age_{LW}. The Age_{LW}-$\log_{10}(M_*/M_\odot)$ and Age_{LW}/Gyr-λ_{R_e} trends have previously been shown for the full SAMI sample by Croom et al. (2024).

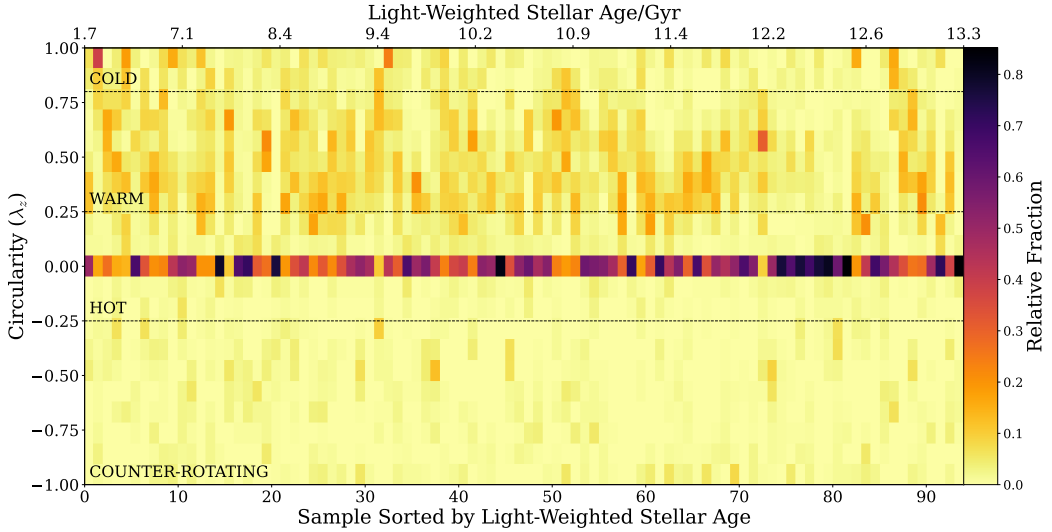

Figure 4.10: Orbit circularity (λ_z) distribution within one effective radius for each galaxy in our sample, ordered by average light-weighted stellar age within one effective radius. The definitions of cold ($\lambda_z > 0.8$), warm ($0.25 < \lambda_z < 0.8$), hot ($-0.25 < \lambda_z < 0.25$), and counter-rotating ($\lambda_z < -0.25$) orbits are labelled and shown in dotted black lines. Darker colours indicate a higher density of orbits, and lighter colours show a lower density. Overall, a trend of more cold orbits is seen in the youngest galaxies, and more hot orbits in the oldest galaxies.

4.4.3 Correlation Analysis

In Figure 4.12, we present correlations between $\mathrm{Hot}_{\mathrm{R_e}}$ and average light-weighted stellar age ($\mathrm{Age}_{\mathrm{LW}}$), environment ($\log(\Sigma_5/\mathrm{Mpc}^{-2})$), and stellar mass ($\log_{10}(M_*/M_\odot)$). We choose to begin this analysis with $\mathrm{Hot}_{\mathrm{R_e}}$ as it shows a strong correlation with $\mathrm{Age}_{\mathrm{LW}}$ in Figure 4.11. We perform this analysis for several samples: the full sample, the full sample without slow rotators (as defined for SAMI in van de Sande et al. 2021a), galaxies with shells, galaxies with streams, and galaxies with shells or streams. However, for each correlation, we account for the linear correlation of the other variables. For example, the correlation between $\mathrm{Hot}_{\mathrm{R_e}}$ and $\mathrm{Age}_{\mathrm{LW}}$is shown after controlling for the correlations with $\log(\Sigma_5/\mathrm{Mpc}^{-2})$ and $\log_{10}(M_*/M_\odot)$. This is known as a partial correlation (e.g. Kendall & Stuart, 1979). Galaxies are coloured by λ_{R_e}, with tidal shells (black circles) and streams (white crosses) indicated too. For each panel, the best-fitting linear relation is shown in red, with 68% and 95% confidence intervals, derived using bootstrap resampling, shaded in lighter red. The Pearson correlation coefficient p-value is given for each partial correlation, and highlighted in bold when $p < 0.05$, indicating statistical significance. We note that the Pearson p-value is not derived from the bootstrap resampled confidence intervals for each linear fit. These two measures generally agree, as when $p < 0.05$, the 95% confidence interval typically excludes a zero correlation, but they are not strictly equivalent.

The choice of parameters for this partial correlation analysis is inspired by Croom et al. (2024), who used partial correlations between $\mathrm{Age}_{\mathrm{LW}}$, $\log_{10}(M_*/M_\odot)$, $\log(\Sigma_5/\mathrm{Mpc}^{-2})$, and λ_{R_e} for the full SAMI sample to determine which parameter λ_{R_e} is most strongly

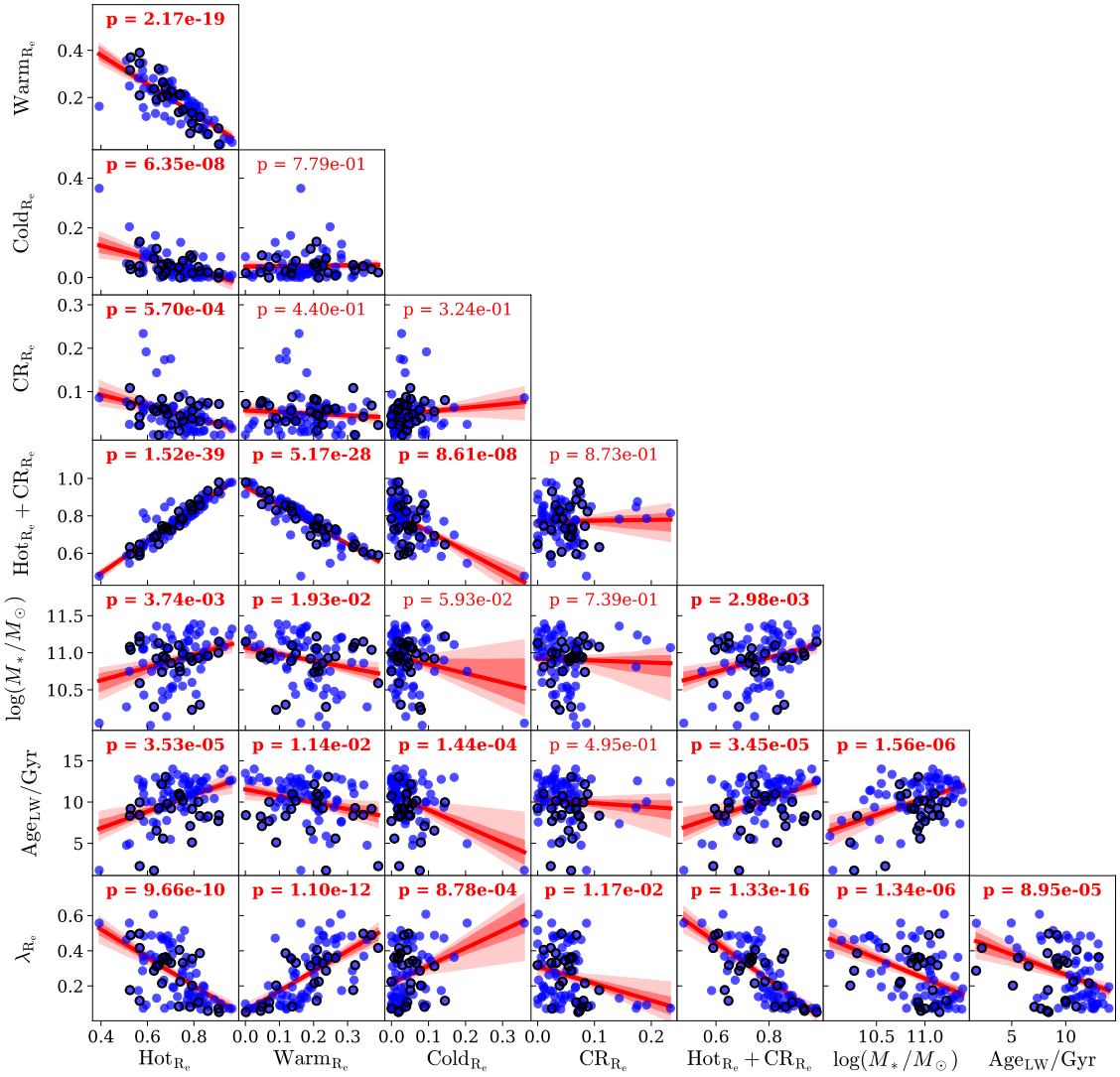

Figure 4.11: Correlations between orbital fractions and global galaxy properties for our sample. $\mathrm{Hot}_{\mathrm{R_e}}$, $\mathrm{Warm}_{\mathrm{R_e}}$, $\mathrm{Cold}_{\mathrm{R_e}}$, and $\mathrm{CR}_{\mathrm{R_e}}$ are the hot orbit fraction, warm orbit fraction, cold orbit fraction, and counter-rotating orbit fraction respectively, all within $1\mathrm{R_e}$. $\log_{10}(M_*/M_\odot)$, $\mathrm{Age_{LW}}$/Gyr, and λ_{R_e} are stellar mass, average light-weighted stellar age within $1\mathrm{R_e}$, and the spin proxy within $1\mathrm{R_e}$, respectively. $\mathrm{Hot}_{\mathrm{R_e}}+\mathrm{CR}_{\mathrm{R_e}}$ is the combined fraction of hot and counter-rotating orbits. Galaxies classified as having a tidal shell by Rutherford et al. (2024) are circled in black. The best-fitting linear relationship for each correlation is shown in red, with the 68% and 95% confidence intervals, derived using bootstrap resampling, shown in lighter red shading. The p-value for the Pearson correlation coefficient is given for each panel, and highlighted in bold when $p < 0.05$, indicating a statistically significant correlation.

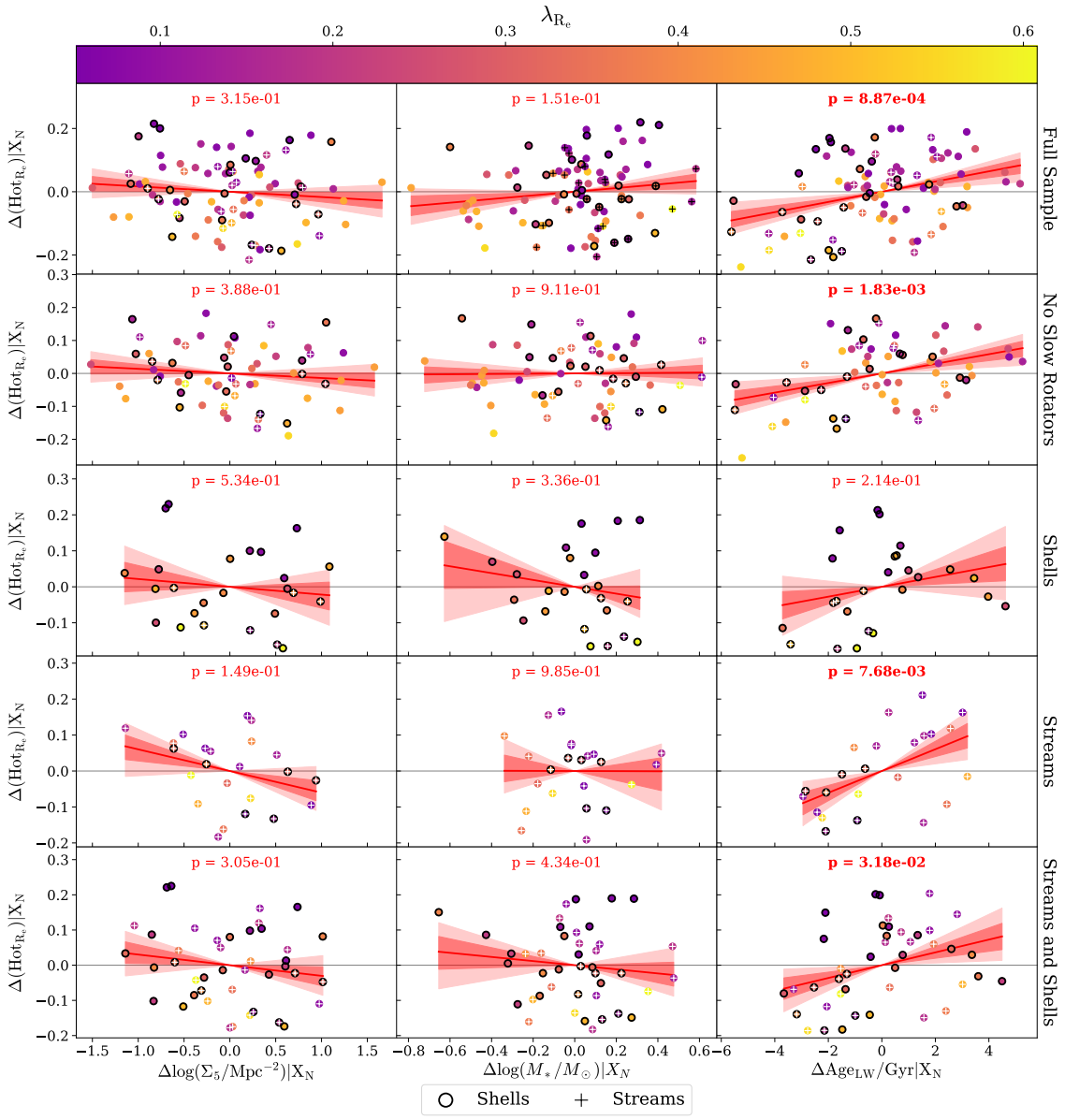

Figure 4.12: Correlations between the hot orbital fraction Hot_{R_e}, and Age_{LW}, $\log(\Sigma_5/\mathrm{Mpc}^{-2})$, and $\log_{10}(M_*/M_\odot)$. For each correlation, the linear correlations of the other variables is controlled for. The top row displays the full sample, and the second row shows the full sample excluding slow rotators (as defined for the SAMI sample in van de Sande et al. 2021a). Subsequent rows display galaxies with shells, galaxies with streams, and galaxies with streams or shells. Galaxies are coloured by λ_{R_e}. Galaxies with tidal shells are circled in black, and galaxies with tidal streams display a white cross. The best-fitting linear relation for each correlation is shown in red, with 68% and 95% confidence intervals shaded. The Pearson correlation coefficient p-value is given for each panel, and highlighted in bold when $p < 0.05$, indicating a statistically significant correlation.

correlated with. They found that λ_{R_e} only showed a significant partial correlation with $\mathrm{Age_{LW}}$. We aim to determine which orbits are driving this relationship. We note here that we are not examining the full SAMI sample, and our sample is biased, only considering massive ($\log_{10}(M_*/M_\odot) > 10$) early-type galaxies with sufficient radial kinematic coverage to build an orbit-superposition dynamical model. Figure 4.12 shows that $\mathrm{Age_{LW}}$ and $\mathrm{Hot_{R_e}}$ are positively correlated even once mass and environment are accounted for, i.e. galaxies with a large proportion of hot orbits within $1\mathrm{R_e}$ have older mean stellar ages within $1\mathrm{R_e}$. This correlation remains when slow rotators are removed, and when only galaxies with tidal streams are considered. Galaxies with tidal shells do not show this correlation, however. Additionally, there is no partial correlation between $\mathrm{Hot_{R_e}}$ and $\log_{10}(M_*/M_\odot)$ or $\log(\Sigma_5/\mathrm{Mpc}^{-2})$ in any sample. Given that hot orbits are dispersion supported and drive low λ_{R_e} values, and we see that $\mathrm{Hot_{R_e}}$ is more correlated with $\mathrm{Age_{LW}}$ than $\log_{10}(M_*/M_\odot)$ or $\log(\Sigma_5/\mathrm{Mpc}^{-2})$ in our full sample, this result is in agreement with the findings of Croom et al. (2024).

In Figure 4.13, we extend the analysis to show how $\mathrm{Age_{LW}}$ correlates with the orbital components $\mathrm{Hot_{R_e}}$, $\mathrm{Warm_{R_e}}$, and $\mathrm{Cold_{R_e}}$, again controlling for $\log_{10}(M_*/M_\odot)$ and $\log(\Sigma_5/\mathrm{Mpc}^{-2})$ as in Figure 4.12. We choose to ignore the partial correlations between orbit fractions and $\log_{10}(M_*/M_\odot)$ or $\log(\Sigma_5/\mathrm{Mpc}^{-2})$ in this figure, as $\mathrm{Age_{LW}}$ seems to be the primary driver of kinematics. The left, middle and right columns show the partial correlations of $\mathrm{Age_{LW}}$ with $\mathrm{Hot_{R_e}}$, $\mathrm{Warm_{R_e}}$, and $\mathrm{Cold_{R_e}}$ respectively. The rows follow the same layout as in Figure 4.12, showing the full sample, the full sample excluding slow rotators, galaxies with shells, galaxies with streams, and galaxies with shells or streams. This figure shows that hot and cold orbits are correlated with $\mathrm{Age_{LW}}$, but warm orbits are not. Given that the relative orbital fractions set the observed V, σ, and thus λ_{R_e} (e.g. Binney & Tremaine, 2008; van den Bosch et al., 2008; Cappellari, 2016), the $\mathrm{Age_{LW}}$–λ_{R_e} relation can, in principle, be re-stated as correlations between $\mathrm{Age_{LW}}$ and the orbital fractions. Figure 4.13 shows that the $\mathrm{Age_{LW}}$-λ_{R_e} relationship is driven by hot and cold orbits, with warm orbits not playing a significant role. Additionally, given the correlations remain when we remove slow rotators, this result is not solely a result of the slow/fast rotator dichotomy. The lack of significant correlation between galaxies with shells and hot orbits is likely due to both low number statistics, and the effect of radial mergers: such events lower λ_{R_e}, leave tidal shells, funnel gas to the centre of the galaxy that drives star formation (e.g. Scott & Kaviraj, 2014; Knapen et al., 2015; Thorp et al., 2019; Bickley et al., 2022), and result in lower stellar ages (e.g. Rutherford et al., 2024; Croom et al., 2024). Although high gas fractions in mergers can lead to the reformation of a stellar disc (e.g. Lagos, 2020a) and increased λ_{R_e}, shell galaxies are likely recent mergers (as the shells have not yet faded) and therefore have not had sufficient time for this process to occur. Overall, these mergers result in a population of galaxies with relatively young stellar ages and reduced rotational support, a trend that goes against the overall SAMI λ_{R_e}-$\mathrm{Age_{LW}}$ result.

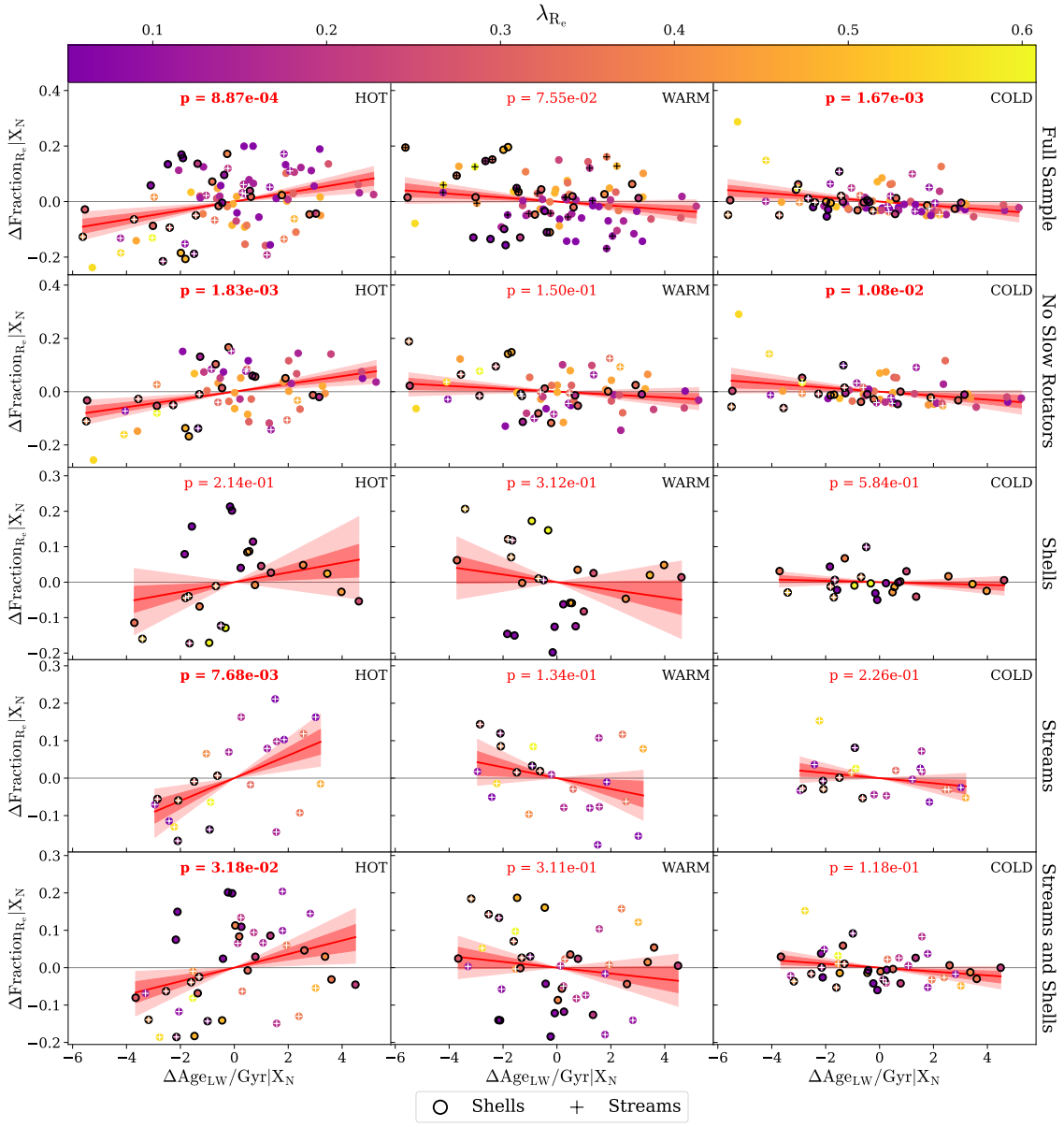

Figure 4.13: Correlations between the hot, warm, and cold orbital fractions, and Age_{LW}. For each correlation, the linear correlations with $\log_{10}(M_*/M_\odot)$ and $\log(\Sigma_5/\text{Mpc}^{-2})$ are controlled for. The points are displayed and rows are ordered as in Figure 4.12. The left, middle, and right columns show the partial correlations for Hot_{R_e}, Warm_{R_e}, and Cold_{R_e} respectively. The Pearson correlation coefficient p-value is given for each panel, and highlighted in bold when $p < 0.05$, indicating a statistically significant correlation.

4.4.4 Mergers and Orbit Fractions

To analyse the impact of mergers on orbital distributions and galaxy shapes, we begin by calculating the triaxiality at $1R_e$, T_{R_e}, defined as:

$$T_{R_e} = \frac{1 - p_{R_e}^2}{1 - q_{R_e}^2} \tag{4.9}$$

where p_{R_e} and q_{R_e} are the intrinsic shape parameters at $1R_e$.

In panel (a) of Figure 4.14, we show the distribution of galaxies in Age_{LW} versus λ_{R_e}, coloured by $\log_{10}(M_*/M_\odot)$. Galaxies with shells identified are circled in black. The panel is further divided into three equally spaced age bins, denoted by black vertical lines. In each age bin, the average λ_{R_e} value for galaxies without shells is shown in blue, and for galaxies with shells in red. Panels (b)-(f) are constructed analogously to panel (a), but they show our sample in Age_{LW} versus $Cold_{R_e}$, $Warm_{R_e}$, Hot_{R_e}, CR_{R_e}, and T_{R_e}, respectively.

We find that, consistent with Rutherford et al. (2024), young and intermediate-age galaxies (the lower two age bins) show significantly lower λ_{R_e} values when they have a shell feature, at 3.6σ and 1.6σ significance for the young and intermediate bins, respectively. We do note, however, that there are only eight galaxies in the lowest age bin. Although Rutherford et al. (2024) didn't show this trend in the lowest age bin, the sample in this work is different, and the broad trend remains. We find that this relationship is primarily driven by changes in the hot and cold orbital fractions (panels (b) and (d)), where the youngest galaxies with shells exhibit moderately higher hot orbit fractions and lower cold orbit fractions, with significances of 1.9σ and 1.9σ, respectively. We find that this relationship is driven by hot and cold orbits, as seen in panels (b) and (d). The youngest galaxies have significantly higher hot orbit fractions and lower cold orbit fractions if they have a shell. Warm and counter-rotating orbits, shown in panels (c) and (e), do not have any significant difference in their distributions for galaxies with and without shells, regardless of age. There is a weak trend towards the youngest galaxies with shells being more triaxial, but the difference is not statistically significant. Finally, the result seen in Figure 4.13 that galaxies without shells increase their hot orbits with age and galaxies with shells do not, can be clearly seen in panel (d) of Figure 4.14.

4.5 Discussion

4.5.1 Spin Transformation is Driven by Hot and Cold Orbits

We have constructed orbit-superposition dynamical models of a subsample of the SAMI galaxy survey to investigate the transformation of galaxy kinematics in massive galaxies as a function of both age and merger history. By deriving the circularity parameter λ_z for the orbits in our models, we find that cold ($\lambda_z > 0.8$) and warm ($0.25 < \lambda_z < 0.8$) orbit fractions correlate positively with λ_{R_e}, while hot ($-0.25 < \lambda_z < 0.25$) and counter-rotating ($\lambda_z < -0.25$) orbit fractions correlate negatively with λ_{R_e}. Correlations between orbital fractions and λ_{R_e} are expected, as λ_{R_e} traces the dynamical contribution of different orbits. While Santucci et al. (2022) demonstrated the same trends for SAMI passive galaxies,

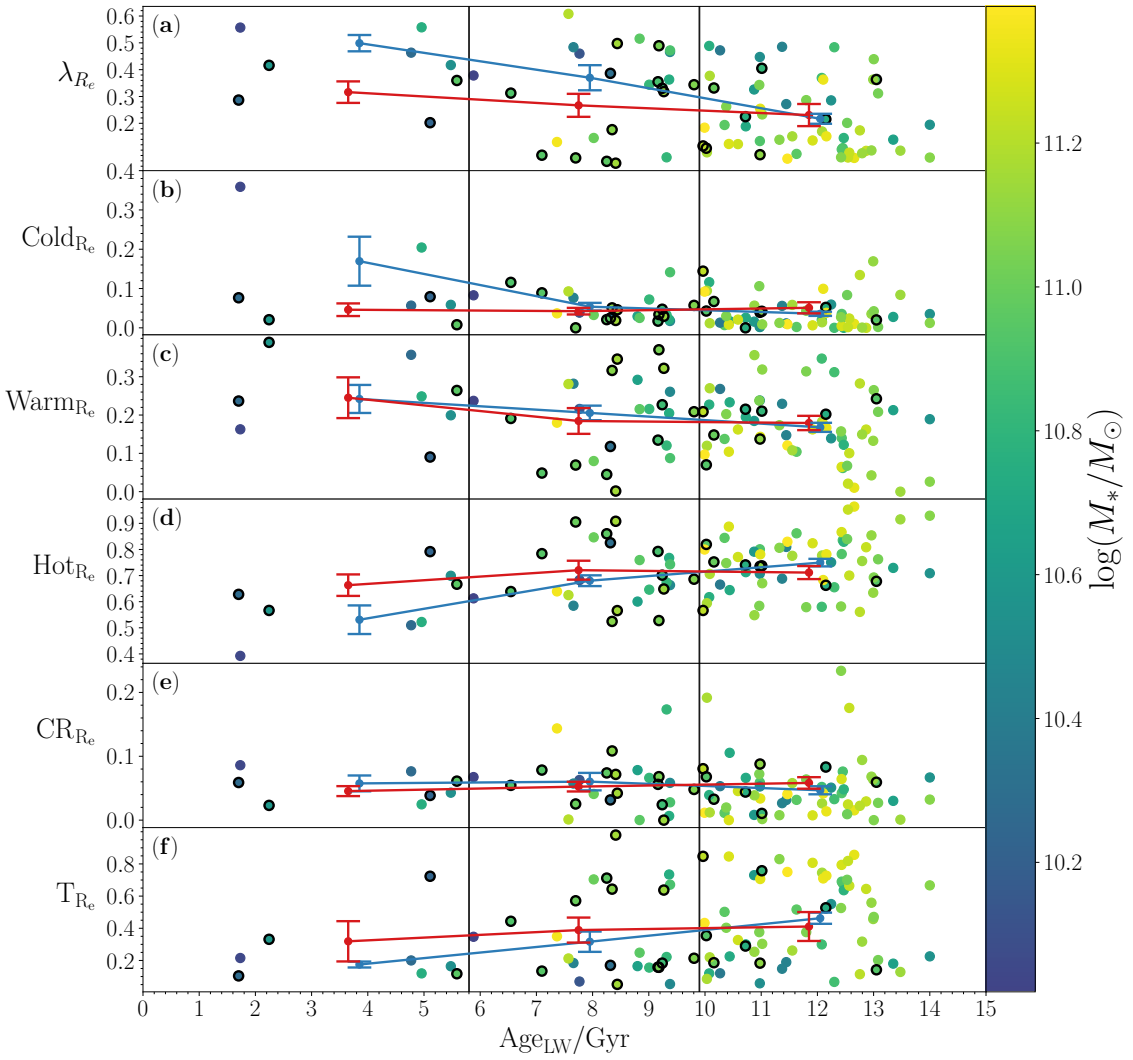

Figure 4.14: The distribution of our sample in $\mathrm{Age_{LW}}$ versus various orbital and shape parameters. Galaxies are coloured by $\log_{10}(M_*/M_\odot)$, and circled in black if they have a tidal shell. Each panel is divided into three equally spaced age bins, denoted by vertical black lines. In panel (a), galaxies are represented by their mean light-weighted stellar age within $1\mathrm{R_e}$ $\mathrm{Age_{LW}}$, against the spin parameter proxy λ_{R_e}. Panels (b)-(f) are displayed by $\mathrm{Age_{LW}}$ versus $\mathrm{Cold_{R_e}}$, $\mathrm{Warm_{R_e}}$, $\mathrm{Hot_{R_e}}$, $\mathrm{CR_{R_e}}$, and $\mathrm{T_{R_e}}$, respectively. In each age bin, the average value of the y-axis parameter for galaxies without shells is shown in blue, and for galaxies with shells in red.

warm orbits are intermediate by definition, and could trace λ_{R_e} differently in rotation-dominated late-type discs. A major advantage of an orbit fraction driven analysis is that it provides a means to disentangle the orbital structure of galaxies, where mergers and secular evolution are expected to leave different imprints in the spin transformation of galaxies (e.g. Debattista et al., 2006; Saha et al., 2010; Martel & Richard, 2020).

The question of what drives spin in galaxies has been investigated in many previous studies. Motivated by the morphology-density relation of Dressler (1980), the role of environment was first identified as a key factor correlated with λ_{R_e} by Cappellari et al.

(2011b), with further studies supporting this trend (e.g. D'Eugenio et al., 2013; Houghton et al., 2013; Scott et al., 2014; Fogarty et al., 2014). Stellar mass has also been proposed as a primary driver of galaxy spin (e.g. Brough et al., 2017; Veale et al., 2017; Greene et al., 2017), although there is evidence from more recent works that mass and environment are independent influences on λ_{R_e} (e.g. Lagos et al., 2017; Graham et al., 2019; Rutherford et al., 2021; van de Sande et al., 2021b). Further complicating the picture, stellar age has been shown to strongly correlate with stellar kinematics (van de Sande et al., 2018), with Croom et al. (2024) finding that stellar age is more strongly correlated with λ_{R_e} than either mass or environment within the SAMI sample.

We take advantage of our derived orbit fractions to further investigate the relationships between λ_{R_e}, $\mathrm{Age_{LW}}$, $\log(\Sigma_5/\mathrm{Mpc}^{-2})$, and $\log_{10}(M_*/M_\odot)$. Using partial correlations, we find that the fraction of hot orbits increases with stellar age ($p = 8.87 \times 10^{-4}$), and the fraction of cold orbits decreases with stellar age ($p = 1.67 \times 10^{-3}$), independent of mass and environment. In contrast, the warm orbit fraction shows no significant correlation with age ($p = 7.55 \times 10^{-2}$) once mass and environment are controlled for. These results are broadly consistent with the λ_{R_e}-stellar age relation reported by Croom et al. (2024), as the relative fractions of orbits determine the observed V, σ, and λ_{R_e} (e.g. Binney & Tremaine, 2008; van den Bosch et al., 2008; Cappellari, 2016). However, the lack of any significant trend between warm orbits and age suggests that the transformation of λ_{R_e} with age occurs with stars transitioning directly from cold to hot orbits. Secular processes such as bar-driven instabilities (e.g. Athanassoula, 2005b; Aumer et al., 2016) and disc/spiral arm torques (e.g. Sellwood, 2014; Agertz et al., 2021; Yi et al., 2024), as well as environmental/group effects (e.g. Bekki & Couch, 2011; Choi & Yi, 2017) are capable of redistributing angular momentum in galaxies, however in these scenarios the orbital transformation is expected to happen smoothly, with stars heated progressively from cold, to warm, and finally to hot orbits (Debattista et al., 2006; Saha et al., 2010). The absence of any significant warm orbit correlation with age implies that these pathways do not dominate the spin evolution of SAMI galaxies in our sample. Rather, the transition from cold to hot orbits appears to happen in more stochastic events.

4.5.2 Mergers as the Driver of Orbit Transformations

The fact that warm orbits do not correlate with age gives valuable insight into the processes that drive the reduction of λ_{R_e} with stellar age. Stochastic events such as major mergers are well known to strongly reduce λ_{R_e} (e.g. Naab et al., 2014; Lagos et al., 2018a), but this also strongly depends on the gas content of the merging galaxies (e.g. Lagos, 2020b), as high gas fractions may result in the re-formation of a spinning disc post-merger. Numerical simulations further demonstrate that mergers generate hot and counter-rotating orbits (e.g. Martel & Richard, 2020), with radial major mergers in particular producing a substantial population of box orbits (Barnes, 1990; Naab & Burkert, 2003; Jesseit et al., 2005). Our initial results support this scenario, as the combined fraction of hot and counter-rotating orbital components provides the strongest correlation with λ_{R_e} ($p = 1.33 \times 10^{-16}$), consistent with a merger-driven origin for the reduction of galaxy spin.

Galaxy mergers leave behind distinct stellar debris structures in the form of tidal streams and shells. As shown by Rutherford et al. (2024), however, the connection between

merger history, identifiable features, and kinematic transformation is not straightforward. They concluded that i) tidal shells trace radial mergers which impact the inner stellar kinematics more significantly than the circularly infalling mergers that form streams, and ii) tidal features can only reliably trace mergers in galaxies with young stellar ages, as such features fade after $\sim 2-4$ Gyr (e.g. Lotz et al., 2008, 2010a,b; Lofthouse et al., 2017; Mancillas et al., 2019; Nevin et al., 2021). A high gas fraction in mergers can increase the detectability timescale of tidal features (e.g. Hood et al., 2018; Lotz et al., 2010a), however this also suppresses the generation of box orbits in central regions (Barnes & Hernquist, 1996; Naab et al., 2006; Hoffman et al., 2010). Consequently, any correlation between tidal features and orbital structure is not perfectly analogous to tracing merger history.

Mergers are expected to influence both stellar ages and kinematics. While any merger can funnel cold gas to the centre of the galaxy, driving star formation and reducing mean stellar age (e.g., Scott & Kaviraj, 2014; Knapen et al., 2015; Thorp et al., 2019; Bickley et al., 2022), the impact on stellar kinematics depends on the merger geometry. Galaxies with shells are produced as the result of radial, typically major mergers (e.g. Quinn, 1984; Hernquist & Quinn, 1989; Karademir et al., 2019) that strongly heat the inner stellar regions and affect the observed stellar kinematics (e.g. Naab & Burkert, 2003; Jesseit et al., 2005; Röttgers et al., 2014). In contrast, circular or tangential mergers that form streams tend to only affect the outer regions (Karademir et al., 2019), and preserve the inner rotational support (Valenzuela & Remus, 2022; Rutherford et al., 2024). However, major mergers will likely impact all regions of a galaxy, independent of impact factor. Even if the merger begins as tangential, it is typically radial just prior to the final coalescence (Vasiliev et al., 2022). This radial behaviour will have a large impact on the inner regions without necessarily leaving behind a shell feature. This framework predicts that while all merger galaxies should show young mean stellar ages, galaxies with shells should show signatures of dynamically hot inner regions, and galaxies with streams should tend to maintain their pre-merger stellar kinematics.

We divide our sample into three equally spaced age bins, and find that for the youngest galaxies ($\mathrm{Age_{LW}} \lessapprox 6$ Gyr), the galaxies that have shells (as identified by Rutherford et al. 2024) show moderately higher hot orbit fractions (1.9σ) and lower cold orbit fractions (1.9σ) than galaxies without shells. No significant difference is found for warm orbits, however. For the intermediate and oldest galaxies, we find no difference in any orbital fraction for galaxies with shells. As discussed by Rutherford et al. (2024) and Croom et al. (2024), this does not necessarily imply that these galaxies did not build their hot orbits through mergers, but rather that the relevant mergers may have occurred sufficiently long ago that any identifiable features have since faded with time.

While these results support the scenario that mergers transform cold orbits to hot orbits, the galaxies that currently display shells differ systematically from the overall population. Although partial correlations show that the fraction of hot orbits increases with age across the full sample ($p = 8.87 \times 10^{-4}$), galaxies with shells do not show this trend ($p = 2.14 \times 10^{-1}$). Conversely, galaxies with streams maintain a significant increase of hot orbits with age ($p = 7.68 \times 10^{-3}$). This again may reflect the short visibility lifetime of shells. In Figure 4.14, the average λ_{R_e}, orbit fraction and triaxiality for galaxies with shells is consistent between the intermediate age bin and the oldest age bin, suggesting that older

galaxies may have experienced the same mergers that leave shells, but their shells have already faded. Alternatively, we note that repeated minor mergers from various different directions have been shown to contribute to galaxy mass growth and dynamical heating (e.g. Bournaud et al., 2007; Khochfar et al., 2011; Moody et al., 2014), thus producing a population of galaxies with hot orbital populations but no apparent merger features.

4.5.3 Disentangling the Role of Slow Rotators and Warm Orbits in Angular Momentum Evolution

The discussion thus far has supported the scenario in which massive SAMI early-type galaxies lose angular momentum through stochastic, merger-driven heating, transforming cold orbits directly into hot ones, and resulting in no significant correlations of the transitionary warm orbits with stellar age. Here we discuss several aspects of the data and methods that warrant further consideration. Firstly, slow rotators are very low spin galaxies (e.g. Emsellem et al., 2011) that increase in fraction in the high-mass regime (van de Sande et al., 2017a) and are primarily formed through mergers (Lagos et al., 2018a). A large proportion of slow rotators in our sample could bias results, particularly if fast rotators lose their angular momentum through different physical processes. Secondly, the behaviour of warm orbits remains ambiguous. They correlate more strongly with λ_{R_e} than hot orbits ($p = 1.10 \times 10^{-12}$ versus $p = 9.66 \times 10^{-10}$), but unlike hot orbits, show no residual correlation with stellar age once mass and environment are controlled for.

Slow rotators present a distinct kinematic class of galaxy (e.g. van de Sande et al., 2021a; Fraser-McKelvie & Cortese, 2022), characterised by low λ_{R_e}, high stellar mass and old stellar age (Emsellem et al., 2011), typically attributed to the remnants of major, gas-poor mergers (e.g. Bois et al., 2011; Naab et al., 2014; Cappellari, 2016; Lagos et al., 2018a). Given their prevalence in the high-mass regime, which we sample from, it is possible that the correlations observed in our full sample are simply reflecting the increasing fraction of slow rotators at high stellar mass and age. To test this, we remove all slow rotator galaxies from our sample (i.e. all galaxies with $\varepsilon < 0.428$ and $\lambda_{R_e} < 0.12 + 0.25\varepsilon$, as defined for SAMI by van de Sande et al. 2021a). After this cut, the broad trends remain the same: controlling for mass and environment, the fraction of hot orbits increases with stellar age ($p = 1.83 \times 10^{-3}$), the fraction of cold orbits decreases with stellar age ($p = 1.08 \times 10^{-2}$), and the fraction of warm orbit shows no significant correlation with stellar age ($p = 1.50 \times 10^{-1}$). Moreover, mass and environment show no significant correlation with any orbit fraction once the other variables are controlled for. These results indicate that stellar age remains the dominant predictor of internal dynamics across the slow and fast rotator dichotomy, and the observed correlations of hot and cold orbits with age are not driven solely by the slow rotator population. Rather, merger-driven kinematic heating appears to operate across the full galaxy population, including the fast rotators.

The correlation of warm orbits with λ_{R_e} is complicated by the absence of a corresponding correlation between warm orbits and stellar age once stellar mass and environment are controlled for. This is unexpected, as λ_{R_e} is known to correlate most strongly with age in the SAMI sample (Croom et al., 2024), and we find that older galaxies in our sample have significantly more hot orbits and fewer cold orbits than younger systems. The lack

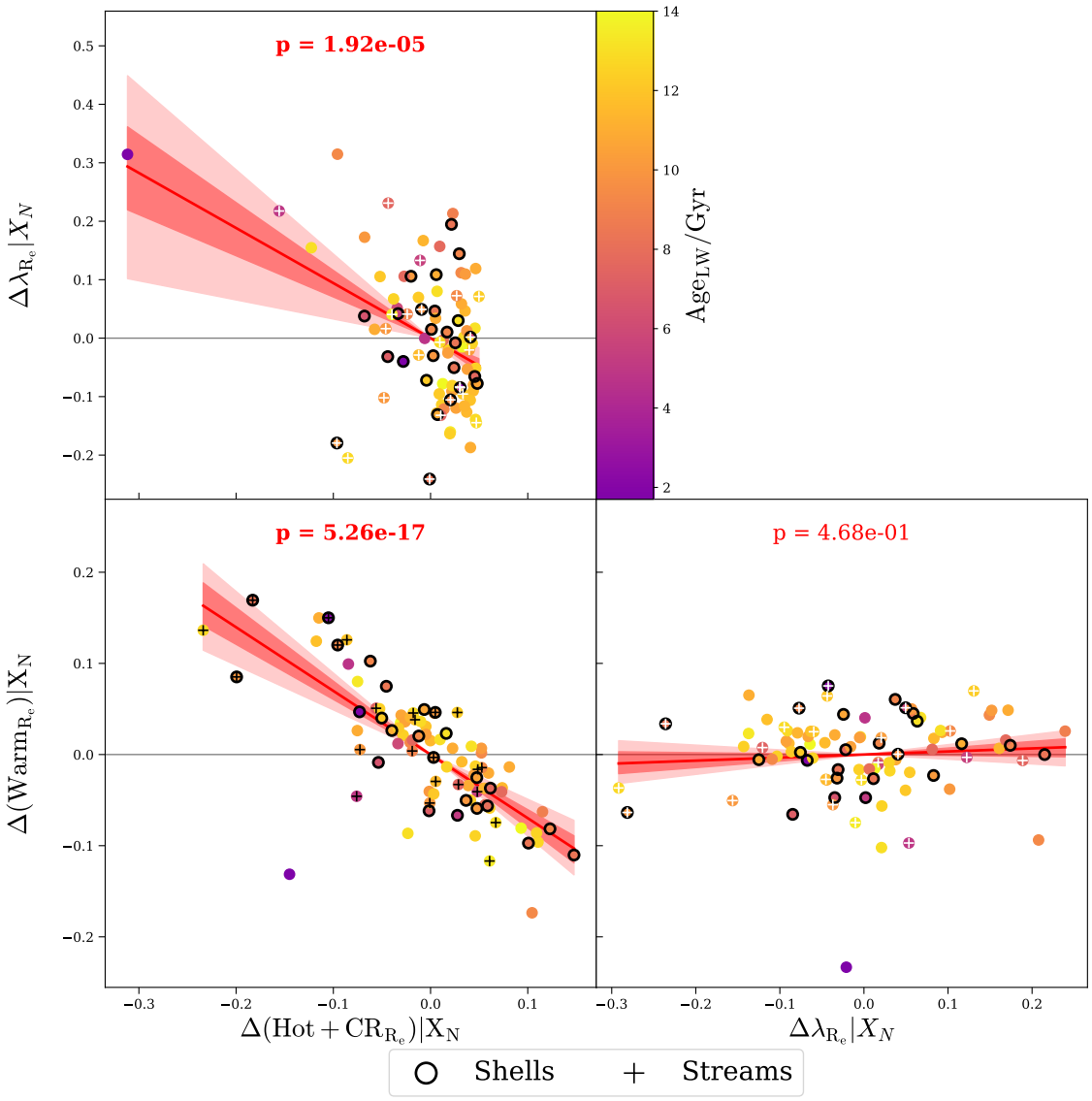

Figure 4.15: Correlations between the hot + counter rotating orbital fraction (Hot_{R_e} + CR_{R_e}), warm orbital fraction (Warm_{R_e}), and λ_{R_e}. For each correlation between two variables, the linear correlation with the third variable is controlled for. Points are coloured by stellar age. Galaxies with shells are circles in black, and galaxies with streams display a white cross. The best-fitting linear relation for each correlation is shown in red, with 68% and 95% intervals shaded. The Pearson correlation coefficient p-value is given for each panel, and highlighted in bold when $p < 0.05$, indicating a statistically significant correlation.

of an age trend for warm orbits therefore suggests that they do not represent a distinct stage in the transformation from high to low spin. One plausible explanation is that "warm" classification traces too large a range in λ_z ($0.25 < \lambda_z < 0.8$), encompassing both near-circular and moderately radial orbits. Such a wide range may mix multiple physical regimes and wash out any underlying age dependence. We tested this by dividing the warm orbit λ_z range in half, creating "cold warm" and "hot warm" fractions. Both subsets independently correlate positively with λ_{R_e} however, and continue to show no trend with age. This reinforces the idea that warm orbits do not represent a distinct stage in spin evolution.

A further possibility is that warm orbits simply represent the largest residual fraction of orbits that are not created by mergers (i.e hot and counter-rotating). Given that the total orbit fraction must sum to unity, the correlation of warm orbits with λ_{R_e} could be partially or entirely driven by the correlation of hot and counter-rotating orbits with λ_{R_e}. We test this in Figure 4.15, by plotting the partial correlation of Warm_{R_e}, $\mathrm{Hot}_{R_e} + \mathrm{CR}_{R_e}$, and λ_{R_e}. Presented similarly to Figure 4.12 but with points coloured by stellar age, we show in each panel the partial correlation of two variables with one another, once the linear correlation of the third variable has been accounted for. We see that when Warm_{R_e} is accounted for, there is still a strong negative correlation between $\mathrm{Hot}_{R_e} + \mathrm{CR}_{R_e}$ and λ_{R_e} ($p = 1.92 \times 10^{-5}$). Further, there exists a strong correlation between $\mathrm{Hot}_{R_e} + \mathrm{CR}_{R_e}$ and Warm_{R_e} independently of λ_{R_e}($p = 5.26 \times 10^{-17}$). However, once correlations with $\mathrm{Hot}_{R_e} + \mathrm{CR}_{R_e}$ are removed, there is no residual trend between Warm_{R_e} and λ_{R_e}($p = 4.68 \times 10^{-1}$). This suggests that the relationship between warm orbits and λ_{R_e} may be an indirect consequence of the correlation between merger-driven orbits and λ_{R_e}, but further work is needed to establish this.

4.6 Conclusions

In this chapter, we investigated the evolution of angular momentum in massive SAMI early-type galaxies through detailed dynamical modelling. Each galaxy's light distribution was modelled with a Multi-Gaussian Expansion (MGE) model, based on KiDS r-band imaging. This MGE was then converted to a total mass model by applying a global mass-to-light ratio and the inclusion of an NFW dark matter halo. We then used these mass models to construct orbit-superposition Schwarzschild models, and derived the fractions of cold, warm, hot, and counter-rotating orbits within one effective radius ($\mathrm{R_e}$) for each galaxy.

We find that the λ_{R_e}-age relation reported by Croom et al. (2024) is driven in our sample primarily by a transition from cold to hot orbits as galaxies age. Partial correlation analysis shows that the fraction of hot orbits increases significantly with stellar age ($p = 8.87 \times 10^{-4}$), while the cold orbit fraction decreases ($p = 1.67 \times 10^{-3}$). Warm orbits show no significant correlation with stellar age, and neither stellar mass nor environment show any residual trend with λ_{R_e}. The absence of a strong warm orbit correlation with age suggests that secular heating processes do not dominate spin evolution in massive early-type galaxies.

Mergers are likely the dominant mechanism driving the transformation from cold to hot

orbits. Using the tidal feature classifications from Rutherford et al. (2024), we find that the youngest galaxies ($\mathrm{Age_{LW}} \lessapprox 6$ Gyr) with shell features exhibit moderately higher hot orbit fractions (1.9σ) and lower cold orbit fractions (1.9σ) compared to galaxies without shells. However, shell galaxies do not show an increase in hot orbits with age as the larger sample does, which is consistent with the short visibility timescale of tidal shells. The similarity in average orbit fractions and triaxialities between intermediate-age shell systems and old-age systems with or without shells suggests that older galaxies may have experienced the same mergers, but their shells have simply faded with time.

We find that merger-driven heating of orbits operates across the full galaxy population, and is not driven solely by slow rotators. After removing slow rotators from our sample, partial correlation analysis again shows that the fraction of hot orbits increases with stellar age ($p = 1.83 \times 10^{-3}$), the fraction of cold orbits decreases ($p = 1.08 \times 10^{-2}$), and warm orbits show no significant trend. Furthermore, the apparent correlation between warm orbits and λ_{R_e} is fully explained by the combined fraction of hot and counter-rotating orbits, which are produced by merger-driven kinematic transformation. Stellar age remains the dominant predictor of stellar kinematics across both slow and fast rotators, while warm orbits play little role in the spin-down of massive early-type galaxies.

Future studies incorporating late-type star-forming discs into the sample would allow for an understanding of kinematic transformation across the full local galaxy population, rather than just early-types. Further, more detailed Schwarzschild implementations that explicitly include bar modelling and orbits would help to disentangle the contributions of different orbital families beyond the broad cold, warm, hot and counter-rotating classifications used in this work. Upcoming instruments such as HARMONI on the ELT (Thatte et al., 2010) will deliver high spatial and spectral resolution observations at cosmic noon ($z \sim 2 - 3$), allowing for the study of galaxies at the peak of the star-formation epoch. HARMONI will also enable analyses of both local galaxies and those at cosmic noon that moves beyond Gauss-Hermite velocity decompositions to direct comparisons of LOSVDs (e.g. Falcón-Barroso & Martig, 2021; Reiter et al., 2025). Finally, similar analyses have been performed for simulated galaxies (e.g. Santucci et al., 2024), demonstrating that Schwarzschild models can recover the dynamical imprints of mergers. Extending this work to higher-resolution simulations would allow finer orbital structures to be resolved and compared, offering a test for how reliably the Schwarzschild technique can reconstruct the true dynamical evolution of galaxies.

Chapter 5

The GECKOS survey: Jeans anisotropic models of edge-on discs uncover the impact of dust and kinematic structures

A straight line may be the shortest distance between two points, but it is by no means the most interesting.

—The Third Doctor

T. H. Rutherford,[1,2] A. Fraser-McKelvie,[1] E. Emsellem,[1] J. van de Sande,[3] S. M. Croom,[2] A. Poci,[4] M. Martig,[5] D. A. Gadotti,[6] F. Pinna,[7,8] L. M. Valenzuela,[9] G. van de Ven,[10] J. Bland-Hawthorn,[2] P. Das,[11] T. A. Davis,[12] R. Elliott,[13] D. B. Fisher,[13] M. R. Hayden,[14] A. Mailvaganam,[15,16] S. Sharma,[17] and T. Zafar[15]

[1]European Southern Observatory, Karl-Schwarzschild-Straße 2, Garching, 85748
[2]Sydney Institute for Astronomy, School of Physics, A28, The University of Sydney, NSW, 2006, Australia
[3]School of Physics, University of New South Wales, NSW, 2052, Australia
[4]Sub-department of Astrophysics, Department of Physics, University of Oxford, Denys Wilkinson Building, Keble Road, Oxford OX1 3RH
[5]Astrophysics Research Institute, Liverpool John Moores University, 146 Brownlow Hill, Liverpool L3 5RF, United Kingdom
[6]Centre for Extragalactic Astronomy, Department of Physics, Durham University, South Road, Durham DH1 3LE, United Kingdom
[7]Instituto de Astrofísica de Canarias, Calle Vía Láctea s/n, E-38205 La Laguna, Tenerife, Spain
[8]Departamento de Astrofísica, Universidad de La Laguna, Av. del Astrofísico Francisco Sánchez s/n, E-38206, La Laguna, Tenerife, Spain
[9]Universitäts-Sternwarte, Fakultät für Physik, Ludwig-Maximilians-Universität München, Scheinerstr. 1, 81679 München, Germany
[10]Department of Astrophysics, University of Vienna, Türkenschanzstraße 17, 1180 Vienna, Austria
[11]Astrophysics Research Group, University of Surrey, Guildford, Surrey, GU2 7XH, United Kingdom
[12]Cardiff Hub for Astrophysics Research & Technology, School of Physics & Astronomy, Cardiff University, Queens Buildings, Cardiff CF24 3AA, United Kingdom
[13]Centre for Astrophysics and Supercomputing, Swinburne University of Technology, PO Box 218, Hawthorn, VIC 3122, Australia
[14]Homer L. Dodge Department of Physics & Astronomy, University of Oklahoma, 440 W. Brooks St, Norman, OK 73019,

USA
[15]School of Mathematical and Physical Sciences, Macquarie University, NSW 2109, Australia
[16]Macquarie University Astrophysics and Space Technologies Research Centre, Sydney, NSW 2109, Australia
[17]Space Telescope Science Institute, 3700 San Martin Drive, Baltimore, MD 21218, USA

This chapter is reproduced from Rutherford et al. (2025), which was published in Astronomy & Astrophysics as "The GECKOS survey: Jeans anisotropic models of edge-on discs uncover the impact of dust and kinematic structures". I wrote all the text, produced all figures, and wrote most of the code for analysis. The JAM code from Cappellari (2008) was used to create the JAM models. Amelia Fraser-McKelvie and Eric Emsellem supervised the work and assisted in revising the text.

Abstract

The central regions of disc galaxies host a rich variety of stellar structures: nuclear discs, bars, bulges, and boxy-peanut bulges. These components are often difficult to disentangle, both photometrically and kinematically, particularly in star-forming galaxies where dust obscuration and complex stellar motions complicate interpretation. In this work, we used data from the GECKOS-MUSE survey to investigate the impact of dust on axisymmetric Jeans Anisotropic Multi-Gaussian Expansion (JAM) models and assess their ability to recover kinematic structures in edge-on disc galaxies. We constructed JAM models for a sample of seven edge-on ($i \gtrapprox 85°$) galaxies that span a range of star formation rates, dust content, and kinematic complexity. We find that when dust is appropriately masked, the disc regions of each galaxy are fit to $\chi^2_{\rm reduced} \leq 5$. We analysed 2D residual velocity fields to identify signatures of non-axisymmetric structure. We find that derived dynamical masses are constant within 10% for each galaxy across all dust masking levels. In NGC 3957, a barred boxy galaxy in our sample, we identified velocity residuals that persist even under aggressive dust masking, aligned with bar orbits and supported by photometric bar signatures. We extended this analysis to reveal a bar in IC 1711 and a possible side-on bar in NGC 0522. Our results highlight both the capabilities and limitations of JAM in dusty, edge-on systems and attempt to link residual velocities to known non-axisymmetric kinematic structure.

5.1 Introduction

The evolution of massive disc galaxies in the local Universe, from their formation to the present day, is a significantly complex picture. The ΛCDM (Lambda Cold Dark Matter) paradigm asserts that gas collapse within a dark matter halo and hierarchical structure formation are the processes through which galaxies build up their mass (White & Rees, 1978; Steinmetz & Navarro, 2002; Abadi et al., 2003; Hopkins et al., 2010), with simulations showing that galaxies experience minor and major mergers over their lifetimes (e.g. Naab et al., 2009; Di Matteo et al., 2009; Lagos et al., 2017; Nevin et al., 2023). Minor mergers (e.g. Choi & Yi, 2017; Schulze et al., 2020), major mergers (e.g. Lagos et al., 2022; Rutherford et al., 2024), gas accretion (e.g. Ho, 2007; Fraternali & Binney, 2008; Ho et al., 2019; Bacchini et al., 2024), stellar feedback (e.g. Übler et al., 2014; Bik et al., 2022), AGN (Active Galactic Nuclei) feedback (e.g. Davies et al., 2020; D'Eugenio et al., 2024), and environmental processes (e.g. Cappellari et al., 2011c; Rutherford et al., 2021) are additionally capable of transforming the stellar motions within a galaxy, primarily through the growth of dispersion-supported bulge-like structures, as well as through scattering into thick-disc orbits and halo orbits (e.g. MW; Bournaud et al., 2011; Sales et al., 2012;

Wilman et al., 2013; Schulze et al., 2020; Barsanti et al., 2022). With the advent of integral-field spectroscopy (IFS; e.g. SAURON, Bacon et al. 2001, MUSE, Bacon et al. 2010, and SAMI, Croom et al. 2012), it is now feasible to examine the spatially resolved stellar kinematic maps of massive disc galaxies and link them to other physical properties and merger history.

Photometric studies have revealed the existence of many morphological substructures in galaxies. The largest diversity (and greatest potential for photometric superposition) is found in the central regions of discs as a result of bars, nuclear discs, and boxy-peanut (BP) bulges (e.g. Sheth et al., 2005b; Coelho & Gadotti, 2011; Athanassoula et al., 2015; Neumann et al., 2017; Seo et al., 2019; Donohoe-Keyes et al., 2019). Stellar bars can form either in the centre of spiral galaxies in isolation (e.g. Hohl, 1971; Ostriker & Peebles, 1973) or be induced through tidal forces arising from galaxy-galaxy interactions and mergers (e.g. Noguchi, 1987; Salo, 1991). Bars can further funnel gas to the centre of galaxies, forming nuclear discs (e.g. Binney et al., 1991; Athanassoula, 1992; Piner et al., 1995; Falcón-Barroso et al., 2006; Wozniak, 2015; Du et al., 2015; Méndez-Abreu et al., 2019; Gadotti et al., 2020; Bittner et al., 2020; Verwilghen et al., 2024) and evolve to buckle vertically out of the disc plane (e.g. Combes & Sanders, 1981; Bureau & Freeman, 1999; Erwin & Debattista, 2017; Kruk et al., 2019), giving rise to BP bulges. Evidently, the study of bulges, bars, nuclear discs, and BP bulges can assist in tracing the evolutionary history of a galaxy. However, while each component manifests itself photometrically, the integrated 2D projection of light we observe on the sky represents all of them together, leading to a highly degenerate problem. Although some work has been carried out using major axis surface brightness profiles to identify bars at certain position angles (e.g. Freeman, 1970; Lütticke et al., 2000a,b; Bureau et al., 2006), one key way to disentangling these components lies in the stellar kinematics, where a line-of-sight velocity distribution (LOSVD) can be determined for each spaxel of a galaxy.

Building on previous work (e.g. Athanassoula, 1992; Bureau & Athanassoula, 2005; Iannuzzi & Athanassoula, 2015; Li et al., 2018), Fraser-McKelvie et al. (2025) employed a Gauss-Hermite parametrisation of stellar kinematics (V, σ, h_3, and h_4) (van der Marel & Franx, 1993; Gerhard, 1993) to qualitatively classify central kinematic structure (e.g. bars and nuclear discs) in 12 edge-on disc galaxies from the GECKOS [1] (van de Sande et al., 2024) sample. However, the physical interpretation of stellar kinematics can be challenging. While Gauss-Hermite parameters quantify the shape of the LOSVD and are sensitive to underlying kinematic structures (e.g. Chung & Bureau, 2004; Bureau & Athanassoula, 2005; Fragkoudi et al., 2020), these quantities are shaped by a combination of intrinsic galaxy properties, such as mass distribution and velocity anisotropy, as well as projection effects, such as inclination and line-of-sight (LoS) integration. This is where dynamical modelling becomes essential, as it can turn observed velocity maps into physically interpretable quantities.

In particular, axisymmetric Jeans anisotropic models (JAMs, Cappellari, 2008, 2020) have been widely applied to early-type and passive disc galaxies (e.g. Cappellari et al., 2013; Li et al., 2017; Ene et al., 2019), which are typically well suited to axisymmetric modelling

[1] Generalising edge-on galaxies and their chemical bimodalities, kinematics, and outflows out to Solar environments

due to their lack of strong internal kinematic structure (e.g. bars) and low levels of dust obscuration. To separate the velocities of JAM models into ordered and random motions, it is necessary to make assumptions about velocity anisotropy. However, enclosed mass profiles and stellar mass-to-light ratios can be recovered from just the $V_{\rm rms}$ field, and JAM models can still reliably recover these for galaxies with modest velocity non-axisymmetries (e.g. Lablanche et al., 2012; Li et al., 2016).

A complete picture of galaxy evolution requires kinematic models not only of passive galaxies, but also of a full sample across all star formation rates. In particular, the GECKOS (van de Sande et al., 2024, van de Sande et al. in prep) sample provides a particularly difficult opportunity, as they were selected with a >2 dex range in star formation rates. In this context, JAM typically struggles with strongly star-forming galaxies, particularly those with complex kinematic structures (e.g. Mitzkus et al., 2017). Dust further complicates modelling, particularly in the edge-on case, where it attenuates light from the far side of the disc, preferentially obscures dynamically cold components, and effectively alters the stellar populations probed. Moreover, the stellar orbits of bars and multiple kinematically decoupled discs (e.g. nuclear discs) are complex and non-axisymmetric (e.g. Skokos et al., 2002a,b; Binney & Tremaine, 2008; Valluri et al., 2016; Tikhonenko et al., 2021). The x_1 orbits in stellar bars (Contopoulos & Papayannopoulos, 1980), for example, generate excess non-axisymmetric LoS velocities at the bar ends (e.g. Athanassoula, 1992; Sellwood & Wilkinson, 1993; Fragkoudi et al., 2017; Kim et al., 2024) that are fundamentally inconsistent with an axisymmetric model. Despite these challenges, modelling GECKOS galaxies comprehensively across a range of star formation rates and dust obscuration levels provides an opportunity to understand how dust affects derived dynamical parameters for edge-on discs, and further enables us to probe how the combination of structures, such as bars and dynamically cold discs, affects kinematic measurements.

Orbit-superposition techniques such as Schwarzschild modelling (Schwarzschild, 1979; Jethwa et al., 2020) offer a more general approach, capable of handling orbits arising from within a non-axisymmetric potential (e.g. Krajnović et al., 2005; van den Bosch et al., 2008; Vasiliev, 2013; Krajnović et al., 2015; Vasiliev & Valluri, 2020; Jethwa et al., 2020; Tahmasebzadeh et al., 2022), and have recently shown success in reproducing barred and multi-component structures (Tahmasebzadeh et al., 2024). Other techniques such as asymmetric drift correction (Leung et al., 2018) have also been applied; however, these techniques are very computationally demanding and suffer from the same dust obscuration issues as JAM.

To improve our understanding of how dust and kinematic structure affect dynamical modelling of edge-on galaxies, we have two goals in this paper: the first, to examine and quantify the effect of dust on the goodness-of-fit criterion and returned dynamical parameters of JAM models applied to edge-on discs; and the second, to explore the diversity of kinematic structures at the centre of GECKOS galaxies. To this end, we propose a simple experiment to understand what would happen if we attempt to model an edge-on galaxy with only simple, axisymmetric disc components. The outer regions of unflared disc galaxies are well modelled (i.e. stellar mass and circular velocity can be well recovered) in most cases with a dynamically cold 'thin' disc, with or without the addition of a dynamically warmer 'thick' disc (Kalinova et al., 2017; Leung et al., 2018). We wish to understand how the velocity residuals obtained after subtracting a JAM model

from the data are affected by dust, and if we can link any coherent residual structure to non-axisymmetric kinematic components present. Edge-on galaxies are the perfect test bed for such an experiment, as the greatest component of LoS velocity is available to us, dust effects are maximised, and central structure light (i.e. structures that 'bulge' out of the disc) is not superimposed with disc light.

In this paper, we construct axisymmetric JAM models of seven galaxies from the GECKOS survey, representative of a range of star formation rates (SFRs), dust levels, and kinematic structures. In Sect. 2.2 we describe the GECKOS data, our sample selection, and surface brightness modelling. In Sect. 5.3 we briefly describe the JAM method and how we applied it to our work. In Sect. 2.4 we describe how different dust masks affect the goodness of fit of our models and describe coherent structures visible in the velocity residuals of our least dusty galaxy, NGC 3957. In Sect. 3.5 we quantify the impact of dust on the dynamical parameters derived from JAM models and extend the analysis of kinematic structures to the remaining galaxies in our sample. Throughout this paper, we use ΛCDM cosmology, with $\Omega_m = 0.30$, $\Omega_\Lambda = 0.70$, and $H_0 = 70$ km s^{-1} Mpc^{-1}, and a Chabrier (2003) stellar initial mass function.

5.2 Data

The GECKOS survey is a European Organisation for Astronomical Research in the Southern Hemisphere (ESO) Very Large Telescope (VLT)/Multi-Unit Spectroscopic Explorer (MUSE) large programme. The GECKOS survey targets 36 edge-on disc galaxies, aiming for a S/N of 40 Å^{-1} per Voronoi bin (Cappellari & Copin, 2003), extending to a surface brightness isophote of $\mu_g = 23.5$ mag arcsec^{-2}—comparable to the Sun's location in the Galactic disc (Melchior et al., 2007). Targets were selected within a heliocentric distance range of 15 to 70 Mpc from the S4G survey (25/36; Sheth et al., 2010) and HyperLeda (11/36; Makarov et al., 2014). Eight galaxies in the sample possess archival data, and we build on these to reach the required surface brightness constraints.

5.2.1 Sample Selection

We selected galaxies for this study based on two criteria: (i) they were observed and reduced prior to December 2023, and (ii) archival Spitzer IRAC 3.6μm photometry is available for use in Multi-Gaussian Expansion (MGE) modelling (see Sect. 5.2.3). We attempted to avoid dust attenuation in our mass and luminosity models by deriving them from Spitzer IRAC 3.6μm imaging. These constraints resulted in a pilot sample of seven galaxies: NGC 5775, UGC 00903, NGC 3279, NGC 0360, IC 1711, NGC 0522, and NGC 3957. NGC 5775 and UGC 00903 exhibit star formation rates exceeding that of the Milky Way, NGC 3279 and NGC 0360 have rates comparable to the Milky Way, while IC 1711, NGC 0522, and NGC 3957 show lower star formation activity. The Spitzer IRAC 3.6μm imaging is presented in Fig. 5.1. Although this sample is limited in size, it covers a range of star formation rates, dust content, and kinematic structures. The properties of this sample are summarised in Table 5.1 and provide a useful test bed for exploring the impact of dust and non-axisymmetric structures on dynamical modelling. We note here that the MUSE spatial coverage varies from galaxy to galaxy, impacting the distribution

Table 5.1: The properties in this table are as follows: Galaxy ID, global star formation rate (WISE W4 band, Cluver et al., 2014), dust proxy (median E(B–V)) (nGIST, Fraser-McKelvie et al., 2025), previously classified kinematic structure (Fraser-McKelvie et al., 2025), and assumed distance from Earth (CF4, Table 5, column 2, Tully et al., 2023).

ID	SFR [$M_\odot$/yr]	Median E(B–V)	Kinematic Structures	Distance [Mpc]
NGC 5775	6.84	0.293	-	18.9
UGC 00903	4.17	0.207	Counter-rotating disc	37.7
NGC 3279	1.99	0.117	Close to pure disc	29.9
NGC 0360	1.46	0.189	-	31.2
IC 1711	1.08	0.107	Boxy-peanut bulge and nuclear disc	44.9
NGC 0522	0.64	0.076	bulge	36.2
NGC 3957	0.27	0.048	Boxy-peanut bulge and nuclear disc	24.8

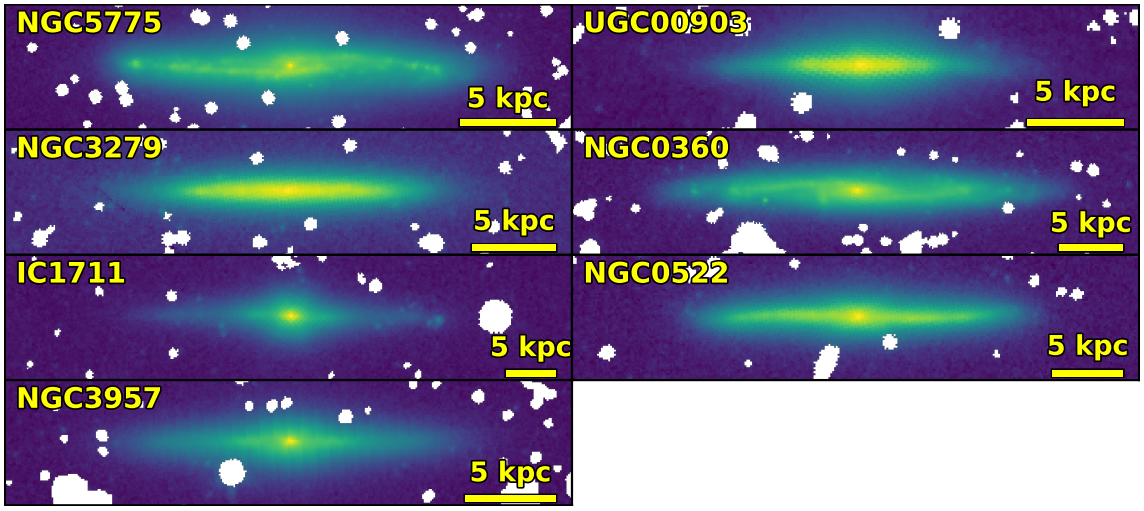

Figure 5.1: Spitzer IRAC 3.6μm imaging of our sample of seven GECKOS galaxies. The images are scaled with an inverse hyperbolic sine (arcsinh) scaling, and masked regions (bright stars, imaging artefacts) are shown in white. There are clear star-forming spiral arms in NGC 5775 and NGC 0360.

of E(B–V) values observed in each system.

5.2.2 Data Reduction and Analysis

Data reduction was performed using the Python package pymusepipe[2] (Emsellem et al., 2022) and is described in Fraser-McKelvie et al. (2025). pymusepipe was used to create mosaicked data cubes from MUSE science exposures. pymusepipe was built around the MUSE Data Reduction Pipeline (Weilbacher et al., 2020) and behaves as a data organiser and wrapper for the ESO Recipe Execution Tool (esorex, ESO CPL Development Team,

[2]https://github.com/emsellem/pymusepipe

2015).

To extract stellar kinematics from our data, we applied the nGIST[3] pipeline (Fraser-McKelvie et al., 2025) on the fully reduced and mosaicked data cubes. nGIST is an upgraded version of the GIST pipeline (Bittner et al., 2019), which is a wrapper for existing spectral fitting routines for the analysis of IFS galaxy data. nGIST is a publicly available, modular, and documented[4] code applicable to any galaxy IFS data.

In this study, we utilised nGIST version 7.2.1 to generate 2D maps of two-moment stellar kinematics, applying Voronoi binning to achieve an S/N of 100 per pixel (equivalent to 80 $Å^{-1}$, calculated over the wavelength range of 4800–7000 Å). This wavelength range was chosen to minimise the inclusion of skylines in the S/N estimate. We chose a binning with S/N = 100 because we focus on the central regions of our galaxies, where S/N is very high and spaxels typically exceed this requirement. The kinematics were derived from a wavelength range of 4800–8700 Å. The Jeans equations, as implemented in JAM, are a function of the true moments V and σ. As a result, we approximate these true moments by enforcing a Gaussian LOSVD (fixing all high-order Gauss-Hermite coefficients to zero).

We utilised the penalised pixel fitting (pPXF) routine, as described by Cappellari & Emsellem (2004) and Cappellari (2017) in the nGIST stellar kinematics (`KIN`) module, in combination with the X-shooter stellar template library (Verro et al., 2022). We chose to use the X-shooter stellar library for its broad wavelength coverage, high spectral resolution near the Calcium II triplet (CaT), and agreement with prior studies suggesting that stellar spectra are generally more reliable than simple stellar populations (SSPs) for determining stellar kinematics (e.g. van de Sande et al., 2017b; Belfiore et al., 2019). Following previous IFS studies including SAURON (Emsellem et al., 2004), ATLAS^{3D} (Cappellari et al., 2011a), SAMI (van de Sande et al., 2017b), MaNGA (Belfiore et al., 2019; Westfall et al., 2019), and PHANGS (Emsellem et al., 2022), a Legendre polynomial was applied to better match the data to the spectral templates. Motivated by the analysis of van de Sande et al. (2017b) and its application to the GECKOS dataset in Fraser-McKelvie et al. (2025), we chose a 23rd-order additive Legendre polynomial. A first-order multiplicative polynomial is also fitted to correct minor continuum variations caused by imperfect sky subtraction and dust attenuation. Initial velocity guesses are sourced from the NASA Extragalactic Database, with a starting stellar velocity dispersion guess of 100 km s^{-1}. In this work, we used the nGIST output mean LoS stellar velocity (V) and stellar velocity dispersion (σ) maps, along with the corresponding Voronoi bin positions. From the nGIST stellar populations and star formation histories module (`SFH`), we used the stellar dust absorption E(B–V) maps for our dust masking, calculated assuming a Calzetti et al. (2000) extinction curve. Additionally, we note that pPXFhas been shown to underestimate formal uncertainties (e.g. Bergamini et al., 2019; Granata et al., 2025), with Bergamini et al. (2019) demonstrating that the true uncertainty in stellar velocity dispersion is 20% higher than the value derived by pPXF. As a result, we increased our σ uncertainty by 20% and conservatively increased our V uncertainty by 20% as well. As a final step, we calculated the median velocity from the V map within a circular aperture of diameter 1 kpc,

[3]https://github.com/geckos-survey/ngist
[4]https://geckos-survey.github.io/gist-documentation/

centred on the galaxy, and subtracted this systemic velocity from the velocity map.

5.2.3 Surface Brightness Modelling

Dynamical modelling with the JAM formalism requires a model for the gravitational potential (which can also include, for example, a dark matter halo) and the tracer stellar population. We thus required both a) imaging of our galaxy sample that accurately represents the stellar distribution (i.e. unaffected by dust) and b) a method for modelling this stellar distribution that is efficient and allows computationally efficient evaluation of the Jeans equations.

Spitzer 3.6μm Imaging

As our sample contains highly inclined galaxies, the impact of dust absorption along the dust lane and/or photometric major axis is strong and requires care with the selection of our photometry. Any imaging in a wavelength band similar to the kinematic maps wavelength range (e.g. SDSS r band) is strongly affected by dust. For this reason, we chose to use 3.6μm mid-IR imaging from the Spitzer Space Telescope (Fazio et al., 2004). Cutouts of each galaxy in our sample were downloaded from the NASA IPAC Infrared Science Archive and are shown in Fig. 5.1.

Multi-Gaussian Expansion Profiles

The majority of previous work with JAM has utilised the MGE parametrisation of Monnet et al. (1992); Emsellem et al. (1994a), which can accurately reproduce the surface brightness of real galaxies and has an efficient and widely used routine (Cappellari, 2002). This approach assumes that the 2D projected luminosity, I, of a galaxy on the sky can be represented by a sum of N Gaussians. Each Gaussian has total luminosity L_k, an observed axial ratio q'_k, and a dispersion σ_k along the major axis. This model may then be convolved with a second sum of Gaussians representing the point-spread function (PSF), which allows the model to stay within the MGE formalism.

We created MGE models of the Spitzer 3.6μm imaging for each galaxy in our sample. We used a Gaussian with a full width at half maximum (FWHM) of 1.66" (the average PSF for IRAC 3.6μm imaging; Khan, 2017) for our PSF. We fixed the position angle of all Gaussians to be the same, as JAM cannot account for non-axisymmetric structures. We show an example of an MGE fit to IC 1711 in Fig. 5.2. Similar fits were created for all galaxies in the sample. These resulting Spitzer MGEs were used as the model for the tracer stellar population, and its contribution to the total gravitational potential.

5.3 Methods

We used the solutions to the Jeans equations (Jeans, 1922) in cylindrical coordinates, using the JAM code of Cappellari (2008). For a more detailed explanation of the formalism, see Cappellari (2008).

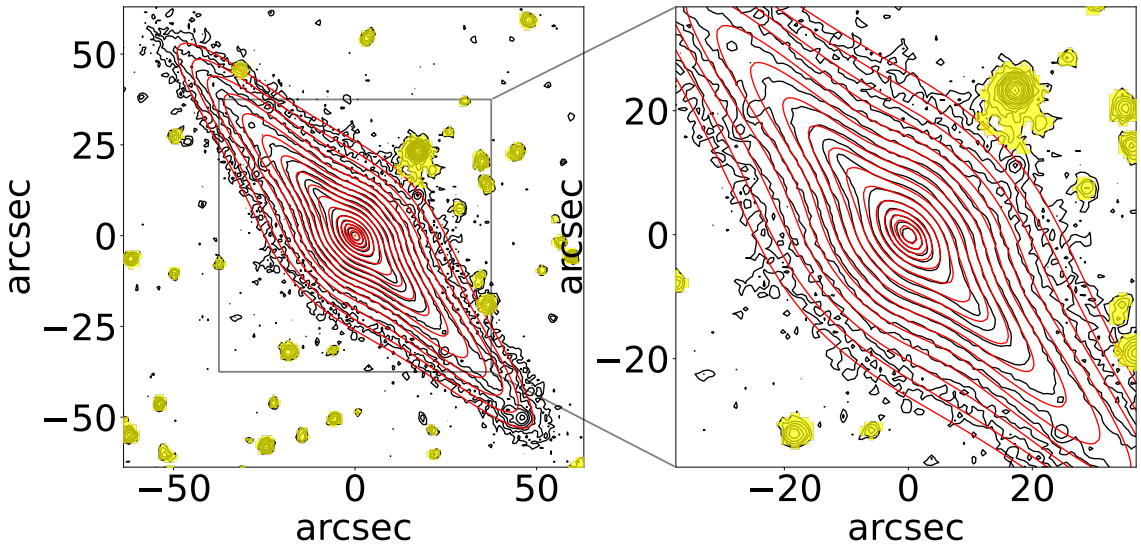

Figure 5.2: MGE fit to the galaxy IC 1711. Spitzer 3.6μm imaging contours are in black, the MGE model contours are in red, and masked regions (other sources) are in yellow. The contours are spaced by 0.5 mag arcsec^{-2}. The right-side panel is a zoomed-in version of the left-side panel, with the scale shown by a box around the central region in the left-side panel.

In this work, we assumed that the velocity ellipsoid is aligned with cylindrical coordinates, which has been shown to be accurate near the equatorial plane and along the minor axis of fast rotators (Cappellari et al., 2007). We used our MGE model as the luminous density for JAM. We then multiplied by a global and constant mass-to-light ratio and added a spherical Navarro–Frenk–White (NFW) (Navarro et al., 1997) dark matter profile to obtain our gravitational potential. The NFW profile is defined by only one parameter – the dark matter fraction within $1R_e$. The NFW slope was set to $\gamma = -1$, as in Navarro et al. (1997), and the halo break radius to $r = 20$ kpc. We made this choice as the halo break radius is not well constrained by typical spectroscopic datasets, which are heavily biased towards the central baryon-dominated regions (of MW-mass galaxies), and setting $r = 20$ kpc provides models of equally good quality as letting it vary (Bellstedt et al., 2018). Given that our GECKOS MUSE data do not extend beyond $r = 20$ kpc, the precise choice of break radius should not significantly affect dynamical parameters, nor the velocity residuals at even smaller radii.

We constructed JAM models for the seven galaxies in our sample. We used the EMCEE package (Foreman-Mackey et al., 2013b) in PYTHON to fit the free parameters of the model for each galaxy, where the likelihood function is simply the JAM procedure of Cappellari (2008) and its derived global $V_{\rm rms}$ $\chi^2_{\rm reduced}$. We used a uniform prior across a reasonable estimation range for each free parameter. These free parameters are stellar mass-to-light ratio, dark matter fraction, inclination, and β_j, the stellar orbital anisotropy of the individual Gaussians that compose the stellar MGE. The JAM model then outputs a $V_{\rm rms}$ map, where $V^2_{\rm rms} = V^2 + \sigma^2$, V is the mean stellar velocity and σ is the stellar velocity dispersion. For each model, we applied a dust mask to the observed kinematic maps based on the E(B–V) stellar dust absorption maps, masking any Voronoi bin with E(B–V) above a given threshold. Our initial models adopt a cut-off value of E(B–V) = 0.7, but we also

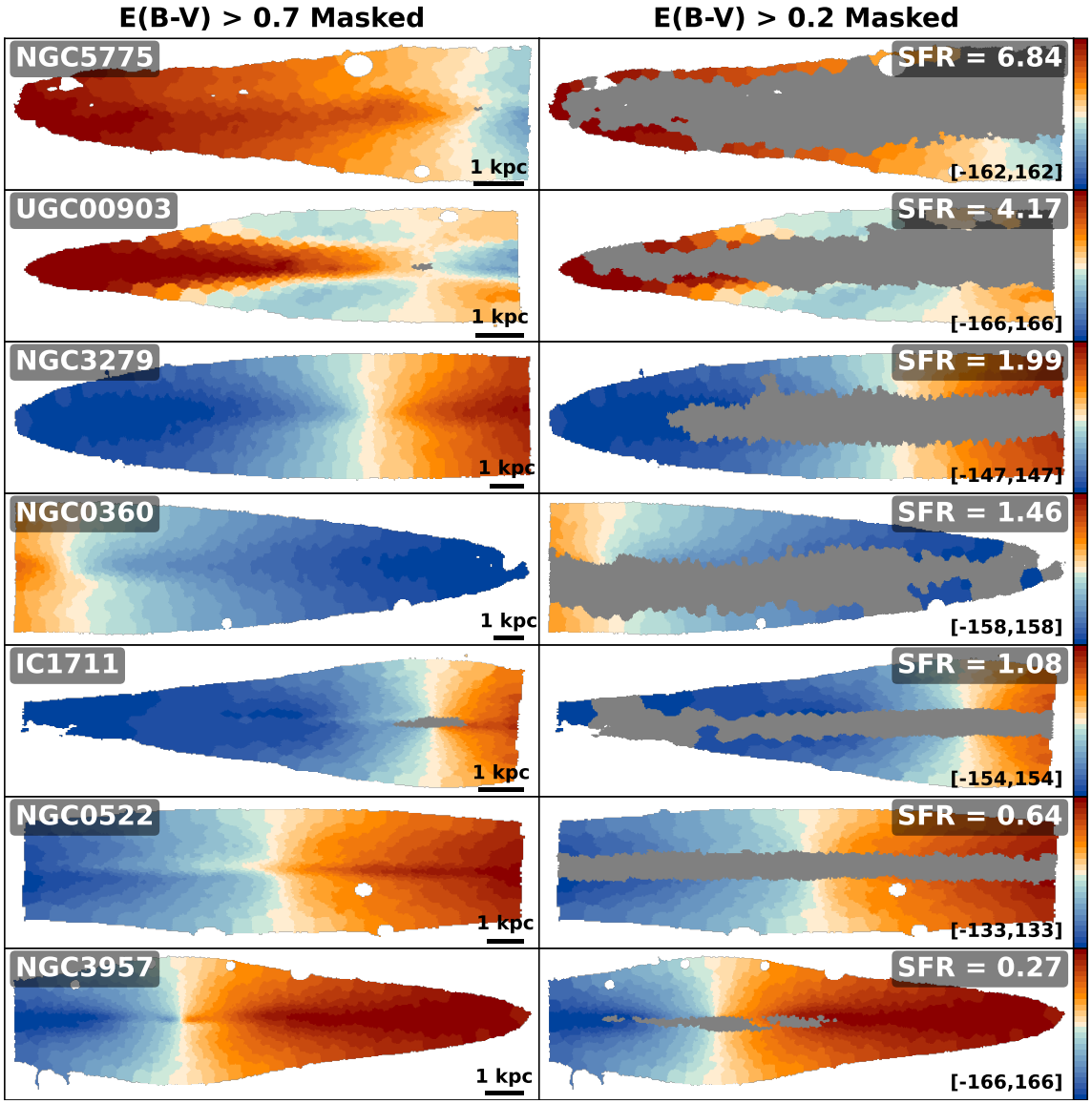

Figure 5.3: Illustration of masking for two E(B–V) thresholds across our sample, overlaid on the V maps. Each row corresponds to a galaxy, ordered from top to bottom by decreasing star formation rate. The left column shows masks where Voronoi bins with E(B–V) > 0.7 are excluded (greyed out), while the right column shows masks for E(B–V) > 0.2. Galaxies are also labelled with their star formation rates in $M_\odot$ yr^{-1}. We show the range in the velocity colour bar in the bottom right of the right-side panels. Aggressive masking removes most mid-plane bins in highly star-forming galaxies.

used several thresholds down to E(B–V) = 0.2 to test the robustness of our results against the impact of dust. Figure 5.3 illustrates the difference between our highest and lowest masking thresholds, with E(B–V) > 0.7 masked in the left column and E(B–V) > 0.2 masked in the right column. Finally, the first velocity moment, V, was found by defining a κ parameter for our luminous Gaussians. The κ parameter defines the amount of rotation in $V_{\rm rms}$. Derived dynamical parameters were not affected by our choice of κ, as they are only dependent on the $V^2_{\rm rms}$ map. In principle, allowing κ to vary across the luminous Gaussians could improve the recovery of the V map, as different components such as

thin discs, thick discs, and nuclear discs have different rotational supports. However, to maintain simplicity, we adopted a single constant κ, scaled so that the model velocity field matched the projected angular momentum of our observed galaxy.

5.4 Results

5.4.1 JAM Models

We fitted the JAM models to each galaxy in our sample, applying our E(B–V) < 0.7 requirement to each Voronoi bin in this first set of models. Maps of $V_{\rm rms}$ and the derived quantities V and σ, are shown in Figs. 5.4-5.6 for NGC 3957, IC 1711, and NGC 0522. The remaining galaxies do not exhibit clear non-axisymmetric structure, and their maps are shown in Figs. B.1-B.4. The left column shows $V_{\rm rms}$, V, and σ derived from NGIST output for the seven GECKOS galaxies, the central column shows the same but from the JAM model, and the right column shows the residuals, i.e. data minus model.

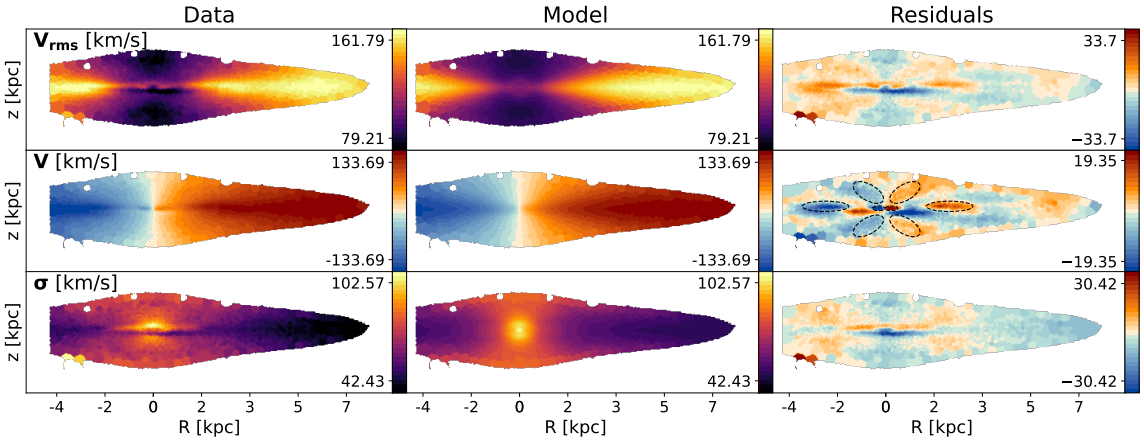

Figure 5.4: JAM model for galaxy NGC 3957. The upper row shows the $V_{\rm rms}$ map, the central row shows the V map, and the lower row shows the σ map. The left column shows NGIST mean light-weighted velocity V and σ binned to S/N=100, as well as the derived quantity $V_{\rm rms} = \sqrt{V^2 + \sigma^2}$. The central column shows the dynamical model, and the right column shows the residuals (data minus model). The model is fit to the $V_{\rm rms}$ map, and a κ value is fit to find the V map from $V_{\rm rms}$. Additionally, we circle structures in the V residual map that we believe corresponds to kinematic components, which JAM failed to successfully model.

Measuring the goodness of fit of our models was not straightforward, particularly given that non-axisymmetric structures are expected to induce systematic discrepancies between the observed and modelled kinematics, particularly in the bulge-dominated regions of our galaxies. One of our aims was to use these discrepancies, where possible, to diagnose these structures. As a result, instead of evaluating $\chi^2_{\rm reduced}$ as a global statistic, we evaluated it as a function of radius. We computed $\chi^2_{\rm reduced}$ as a moving average, within radial bins of

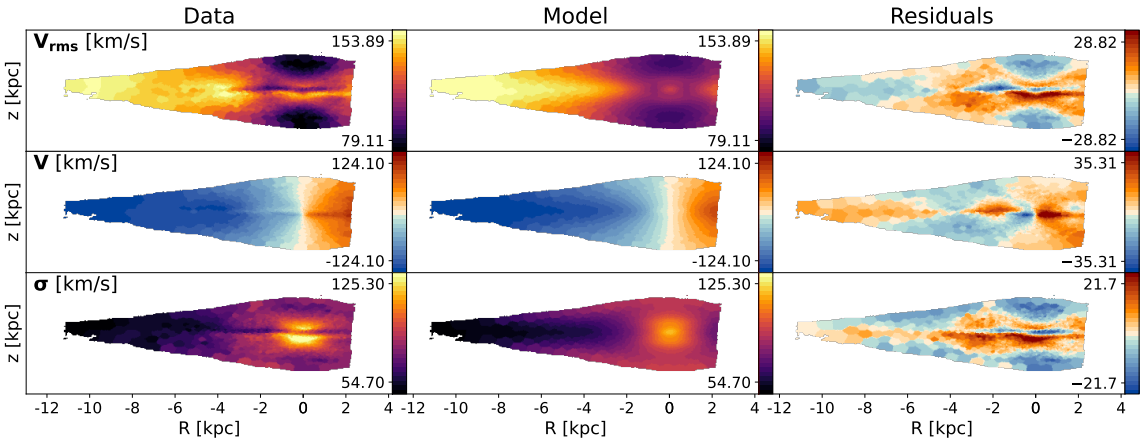

Figure 5.5: Same as Fig. 5.4, but for IC 1711 and without the circling of structures.

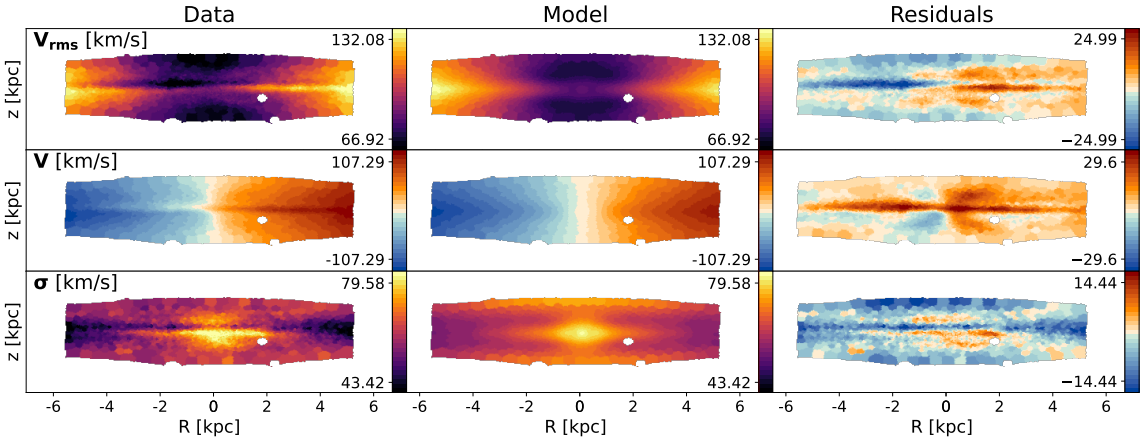

Figure 5.6: Same as Fig. 5.4, but for NGC 0522 and without the circling of structures.

$0.5 \times R_d$, where R_d is the disc scale radius (Salo et al., 2015)[5]. This radial smoothing allowed us to identify how well the different regions of our galaxy (e.g. bulge dominated and disc dominated) were fit.

Figure 5.7 illustrates the goodness of fit for each galaxy in our sample as a function of radius and dust masking level. In each panel, we show the moving average of $\chi^2_{\rm reduced}$, for each mask threshold in E(B–V). The x-axis is shown as a function of disc scale radius, and the y-axis range is kept the same for each galaxy to aid in comparison. We show $\chi^2_{\rm reduced} = 1$ as a dotted line, and $R_d = 0.5$ (the bulge-dominated region, e.g. Fisher & Drory 2010) and $R_d = 2.2$ (the disc-dominated region, e.g. Freeman 1970; Persic et al. 1996) as vertical dashed lines. Finally, we plot the $\chi^2_{\rm reduced}$ measure for our E(B–V) ≤ 0.7 model, but only applied to E(B–V) ≤ 0.2 bins in grey. We first find that in the disc-dominated region ($0.5 < R/R_d < 2.2$), most galaxies approach $\chi^2_{\rm reduced} \lessapprox 5$, indicating a reasonable fit for the disc component of the galaxy, in comparison to the bulge. In our most actively star-forming galaxies (NGC 5775, UGC 00903, and NGC 3279), more aggressive dust masking results in strong improvement. This is less apparent but remains true

[5]Disc scale-radii for Spitzer 3.6 μm imaging were derived for multi-component Sérsic fits. We estimated R_d for NGC 3957 from a second-component Sérsic fit to its photometry, as this was not calculated by Salo et al. (2015).

within the bulge-dominated region ($R/R_d < 0.5$) of NGC 0360 and NGC 0522. However, IC 1711 and NGC 3957 show little improvement with stronger masking. Interestingly, these galaxies have previously been identified as hosting non-axisymmetric structures (bars, Fraser-McKelvie et al., 2025). This may hence indicate that these non-improving galaxies possess non-axisymmetric structures. However, as these galaxies also have the lowest SFRs and thus presumably lower dust content, the smaller improvement from dust masking might reflect fewer bins being masked. The $\chi^2_{\rm reduced}$ measure for our E(B–V) ≤ 0.7 model applied to E(B–V) ≤ 0.2 bins generally follows the E(B–V) ≤ 0.2 model for most galaxies, with the exception of NGC 5775. This is because for most galaxies, there are not enough dusty bins with $0.2 <$ E(B–V) < 0.7 to affect the fit significantly, and $\chi^2_{\rm reduced}$ is driven almost entirely by only measuring dust-free bins. In the case of NGC 5775, there are enough dusty bins to affect the E(B–V) ≤ 0.7 model. Overall, in the disc-dominated region ($0.5 < R/R_d < 2.2$), we find that most galaxies approach $\chi^2_{\rm reduced} \lessapprox 5$, indicating a reasonable fit for the disc component of the galaxy in comparison to the bulge.

5.4.2 Kinematic Residual Map Structure

We now examine the spatial distribution of kinematic residuals. These residual maps contain valuable information about localised deviations from axisymmetry. Nonetheless, we must be careful to take into consideration the effect of dust and masking. We note here that JAM fits a symmetrised transformation of the input kinematics. Thus, some velocity residual structures are introduced purely by this symmetrisation process and should not be misinterpreted as non-axisymmetric velocity components. To illustrate this we show the V maps for our sample as well as the symmetrised $V_{\rm sym}$ maps in Fig. 5.8. We also compare the residuals $V - V_{\rm sym}$, $V - V_{\rm model}$, and $V_{\rm sym} - V_{\rm model}$. The $V_{\rm sym} - V_{\rm model}$ residual should be free of any structures due to symmetrisation, and thus we only classify structures that are clearly visible in this and the $V - V_{\rm model}$ residual.

We begin our analysis with NGC 3957, which has the lowest SFR, the lowest median E(B–V), and the best-fit model that exhibits only small variations with changes in our masking threshold. We thus expect the JAM models of NGC 3957 to have the least impact from dust obscuration, with any deviations from a good model fit due to non-axisymmetric structure rather than dust. However, we take care to consider only structures in the kinematic residuals that are not impacted by dust (i.e. visible even with E(B–V) < 0.2 masking applied; see Fig. 5.3). Finally, we obtain the kinematic structure classification from Fraser-McKelvie et al. (2025), which suggests that NGC 3957 has a BP bulge and nuclear disc. In Fig. 5.4 we highlight coherent structures in the V residual maps of NGC 3957 by circling these structures in dashed ellipses.

A compact, symmetric (around $R = 0$) feature of residual velocity exceeding that of its surroundings is apparent in the V residual map ($R \lessapprox 1$ kpc), suggestive of a nuclear disc. This residual feature peaks at approximately 0.25kpc along the major axis in agreement with the size of the nuclear disc in NGC 3957 found by Fraser-McKelvie et al. (2025, 0.28kpc). Although nuclear discs are, to a good approximation, axisymmetric (although some host nuclear bars) and could, in principle, be modelled with JAM, accurate recovery would require finely tuned low-dispersion, highly flattened Gaussians in the MGE. We acknowledge a larger structure below the mid-plane, with inverted signs at a similar scale,

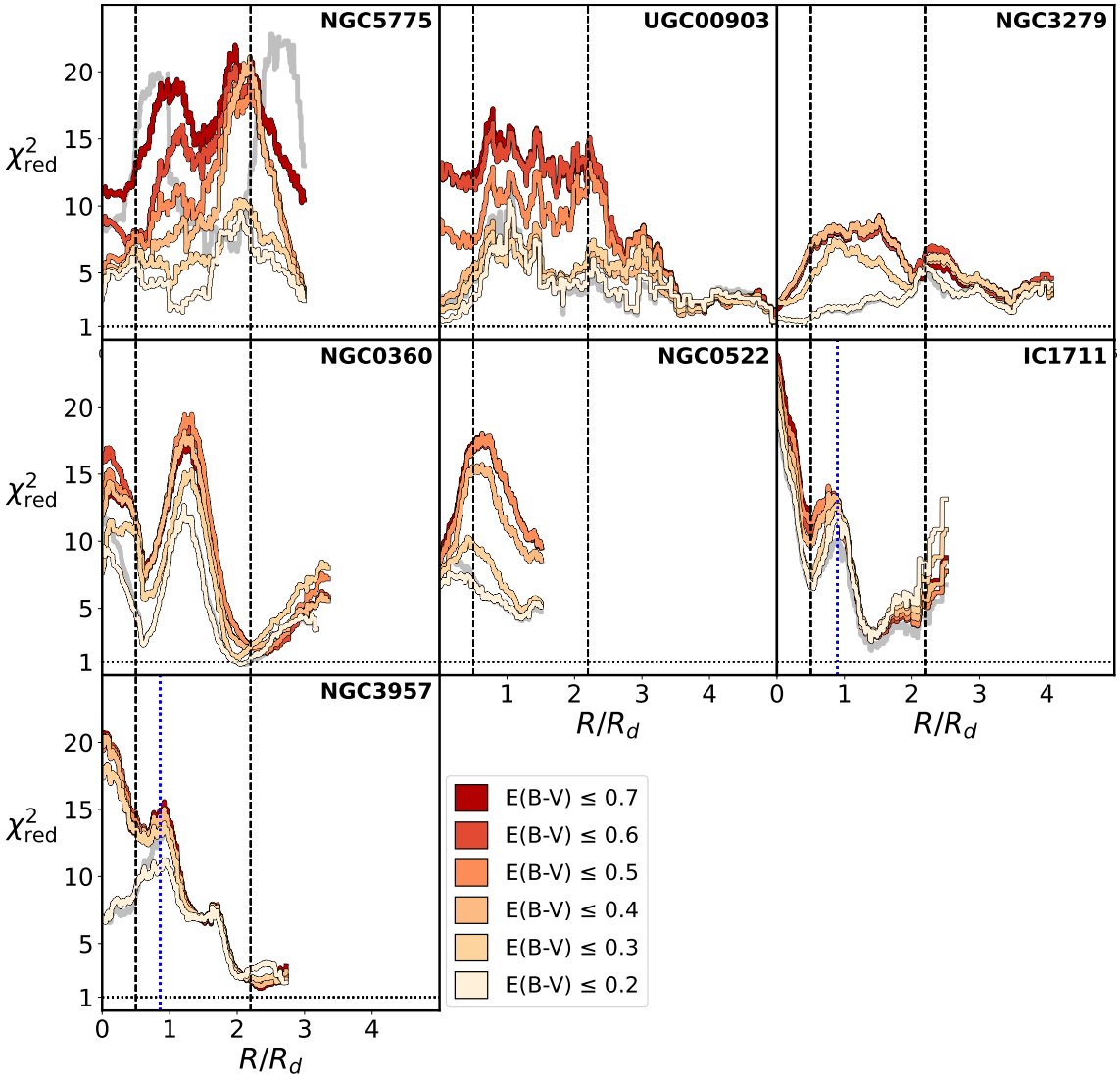

Figure 5.7: Moving-average $\chi^2_{\rm reduced}$ value for each galaxy in our sample, plotted as a function of R/R_d, where R_d is the disc scale length. For each galaxy and each dust masking cut-off, we measure $\chi^2_{\rm reduced}$ in a $0.5 \times R_d$ bin, spaced in radius along the major axis. $\chi^2_{\rm reduced} = 1$ is represented by a dotted line, and $R_d = 0.5$ (bulge-dominated region, e.g. Fisher & Drory, 2010) and $R_d = 2.2$ (disc-dominated region, e.g. Freeman, 1970; Persic et al., 1996) are represented by vertical dashed lines. We also plot in grey the $\chi^2_{\rm reduced}$ measure for our E(B–V) ≤ 0.7 model, but applied to E(B–V) ≤ 0.2 bins. Dotted blue lines are plotted at 3.5 kpc for IC 1711 and at 2.5 kpc for NGC 3957, the radius at which their photometric shoulders end (see Sect. 5.5.2). We note that NGC 5775 and NGC 0360 are not perfectly edge-on and show clear spiral arms in their photometry. This explains their strong peaks in $\chi^2_{\rm reduced}$. A general trend of decreasing $\chi^2_{\rm reduced}$ with mask level is shown, as well as discs fit better than bulges.

which we have not circled. However, as seen in Fig. 5.8, this is an artefact of the velocity symmetrisation process of the JAM model. Thus, we do not consider it correlated with any physical structure.

At intermediate radii ($\sim$ 2.5 kpc), we identify and circle prominent residuals in the V

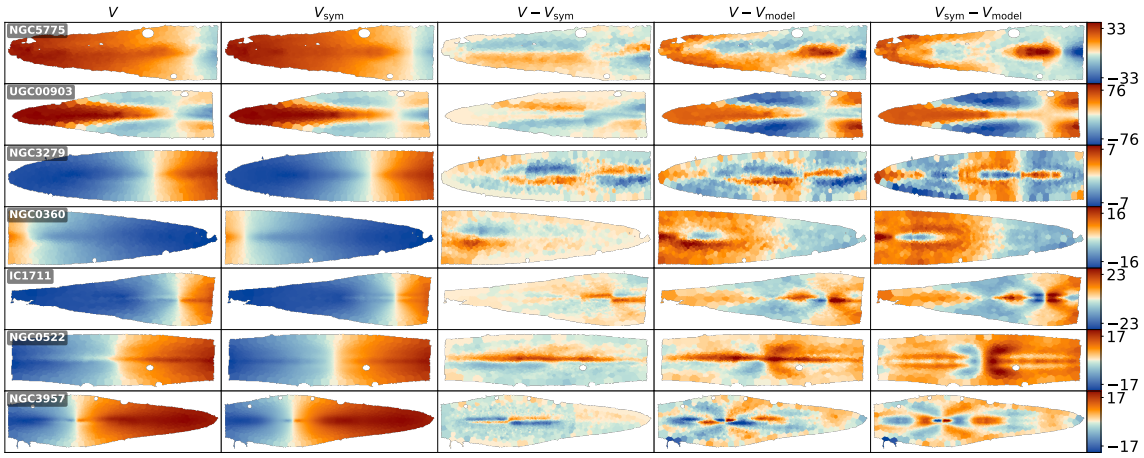

Figure 5.8: Velocity maps for all seven galaxies in our sample, demonstrating the effect of symmetrisation within the JAM model. The leftmost column shows the observed velocity (V) maps. The $V_{\rm sym}$ column presents the same velocity maps after applying the symmetrisation procedure used by the JAM model. The $V - V_{\rm sym}$ column shows the residuals between the observed and symmetrised velocities. The $V - V_{\rm model}$ column shows the residuals between the observed velocity and the best-fitting JAM model (with a mask of E(B–V)<0.7). Finally, The $V_{\rm sym} - V_{\rm model}$ column shows the residuals between the symmetrised velocity field and the JAM model. Our diagnosis of non-axisymmetric velocity structures consider only features that are also clearly visible in the $V_{\rm sym} - V_{\rm model}$ residuals, as these are unaffected by the symmetrisation process.

residual map along the major axis that stand out in magnitude and structure, exhibiting opposite signs across the disc and exceeding the surrounding residual levels. These structures suggest an excess of mean velocity, a few kiloparsecs along the major axis of the disc, on both sides of the galaxy centre. This is consistent with the kinematic signatures expected from a bar, where non-circular motions generate excess LoS velocities near the bar ends (e.g. Athanassoula, 1992; Sellwood & Wilkinson, 1993; Fragkoudi et al., 2017; Kim et al., 2024).

Finally, the V residual maps reveal an X-shaped structure. Such features are known indicators of BP bulges when observed photometrically via unsharp masking (e.g. Bureau et al., 2006; Fraser-McKelvie et al., 2025), tracing stars on vertically resonant orbits. The detection of an X-shaped residual in the stellar kinematic V map supports the interpretation of a BP bulge, as velocity moments can trace this structure off the plane of the disc (Iannuzzi & Athanassoula, 2015; Fragkoudi et al., 2017) due to the bifurcated x_1 orbits that populate BP bulges (e.g. Skokos et al., 2002a; Patsis & Xilouris, 2006).

We use NGC 3957 as an illustrative example, given its clear kinematic signatures and known structures. The remaining galaxies with notable residuals are IC 1711 and NGC 0522, and are discussed in Sect. 5.5.2. The remaining galaxies in our sample (NGC 0360, NGC 3279, NGC 5775, and UGC 00903) do not show residuals consistent with known structures, and hence we do not discuss their residuals in detail.

5.5 Discussion

5.5.1 The Impact of Dust on JAM Models of Edge-on Disc Galaxies

Most previous applications of JAM modelling have been applied to passive, dust-free, and unbarred galaxies, where the model assumption of axisymmetry is likely to hold. Early work with the JAM formalism (e.g. Monnet et al., 1992; Emsellem et al., 1994a,b, 1999; Cappellari, 2008; Cappellari et al., 2009, 2013) was primarily performed on early-type galaxies from the SAURON and ATLAS^{3D} surveys. These studies demonstrated that JAM models could robustly recover the mass-to-light ratio (M/L), velocity anisotropy, and dark matter fraction for elliptical and lenticular galaxies. There has been work done on barred systems (e.g. Lablanche et al., 2012; Li et al., 2016), but these have mostly been simulation studies.

In contrast, dusty, star-forming disc galaxies pose significant challenges to dynamical modelling. These systems are affected by prominent dust lanes that distort both the observed light distribution and the weighting of the stellar kinematics. As a result, they violate JAM assumptions and are generally under-represented in the JAM literature. While some work has been carried out on JAM's reliability in more complex systems (e.g. Lablanche et al., 2012; Li et al., 2016), observational applications to highly spatially resolved, dusty, star-forming discs remain rare. Some work has been done on samples that contain spiral galaxies (e.g. Scott et al., 2015; Zhu et al., 2023), but a thorough discussion of the impact of dust was not included. This study therefore represents one of the first applications of JAM to such galaxies with the intention of studying the effects of dust. By focusing on a small but representative sample of edge-on discs with a range of dust distributions and star formation rates, we explore whether JAM can still provide reliable dynamical constraints under these more difficult conditions.

To test whether reliable dynamical parameters could be extracted from partially masked data, we compared derived enclosed masses at 2.5kpc, 4.0kpc, and 10.0kpc, as well as derived inclinations, across a range of dust masks from E(B–V) > 0.2 to E(B–V) > 1.0. The enclosed mass values are a function of the derived M/L and dark matter fraction, as the MGE light model for each galaxy remains consistent. All galaxies show stable values within 10%, indicating that global dynamical properties remain robust even when excluding the kinematics of the dust-dominated central regions. Interestingly, UGC 00903 has both a comparable $V_{\rm rms}$ fit and reliably determined dynamical parameters relative to the rest of the sample, despite hosting the most unusual kinematic structure, with a clearly visible counter-rotating thick disc (see Fig. B.4). This is because dynamical parameters are recovered solely from the $V_{\rm rms}$ field, which is independent of how the kinematics separate into ordered and random motions, does not depend on the sign of V, and makes no assumptions about the anisotropy. Indeed, JAM has been used previously to find the mass distribution of galaxies with counter-rotating discs (Mitzkus et al., 2017).

Our results are consistent with previous simulation-based studies, demonstrating that global M/L ratios in edge-on discs can be reliably recovered with JAM modelling, even in the presence of non-axisymmetric structures (Lablanche et al., 2012), and that the enclosed mass can be recovered to within 10% when the true mass distribution is known

(Li et al., 2016). We extend these findings by showing that, although the true enclosed mass is unknown for our galaxies, the recovered mass remains consistent within 10% and is not biased across a wide range of dust masking thresholds.

5.5.2 Connecting Residuals to Physical Structure

NGC 3957 as a Benchmark System

NGC 3957 provides a particularly clean case for interpreting residuals, due to its combination of low dust content, low star formation rate, and clear photometric features suggestive of non-axisymmetry. Most importantly, we are more confident that these features are due to non-axisymmetries, because the dust content is low (Fig. 5.3), our model changes little when we apply more aggressive masking (Fig. 5.7), and the features are not apparent in the symmetrised velocity residuals (Fig. 5.8). As our best-fitting system, it provides an ideal benchmark for interpreting residuals in terms of physical substructures.

Photometric evidence supports the presence of a bar in NGC 3957. As discussed by Bureau & Athanassoula (2005), Freeman Type II surface brightness profiles (Freeman, 1970) are suggestive evidence of bar structure (e.g. Gadotti & de Souza, 2003; Erwin et al., 2008; Kim et al., 2016), due to resonances and instabilities in the bar leading to a redistribution of disc material. A Freeman Type II profile occurs when the major-axis surface brightness exhibits a local depression beyond the central component, followed by a flat or slightly rising plateau (depending on the bar orientation) before transitioning into an outer exponential decline. Of the seven GECKOS galaxies in our sample, only NGC 3957 and IC 1711 clearly display this shoulder in their major-axis 3.6μm surface brightness profiles, which we show in Fig. 5.9. We also note that NGC 0522 shows possible kinematic evidence for a bar (see Sect. 5.5.2), and its surface brightness profile shows noticeable flattening but less pronounced shoulders than NGC 3957 and IC 1711. We caution that this signature is only visible when the bar is not oriented end-on, as projection effects can obscure the shoulder (e.g. Lütticke et al., 2000b; Athanassoula, 2005a).

In Sect. 5.4.2, we highlighted the different structures visible in the V map residuals for NGC 3957. Here, we attempt to correlate these velocity residuals with photometric evidence for a bar. If a bar is present, we expect non-axisymmetric stellar motions, particularly those from elongated x_1 orbits in the disc plane, to manifest as velocity excesses along the disc major axis. For this, we extract velocities from the data, model, and residual maps along three slices, each 1.5" thick: one along the mid-plane (0 kpc offset), one just above it (0.1 kpc), and one further off-plane (0.75 kpc). All slices were taken on one side of the mid-plane, on the opposite side of the dust lane. This allows us to probe both in-plane structures and off-plane structures away from the dust lane.

In Fig. 5.9, we show the velocity profiles along these slits for NGC 3957 and IC 1711, with the data represented by the orange line, the model by the purple line, and the residual by the black line. We also show the photometric shoulders from Spitzer IRAC 3.6 μm imaging. The vertical dashed lines are drawn to approximately where the photometric shoulders end. For NGC 3957, this corresponds to a radius of $\sim$ 2.5kpc, almost exactly where the peak is in the residual velocities, seen most strongly in the 0.1 kpc offset slit.

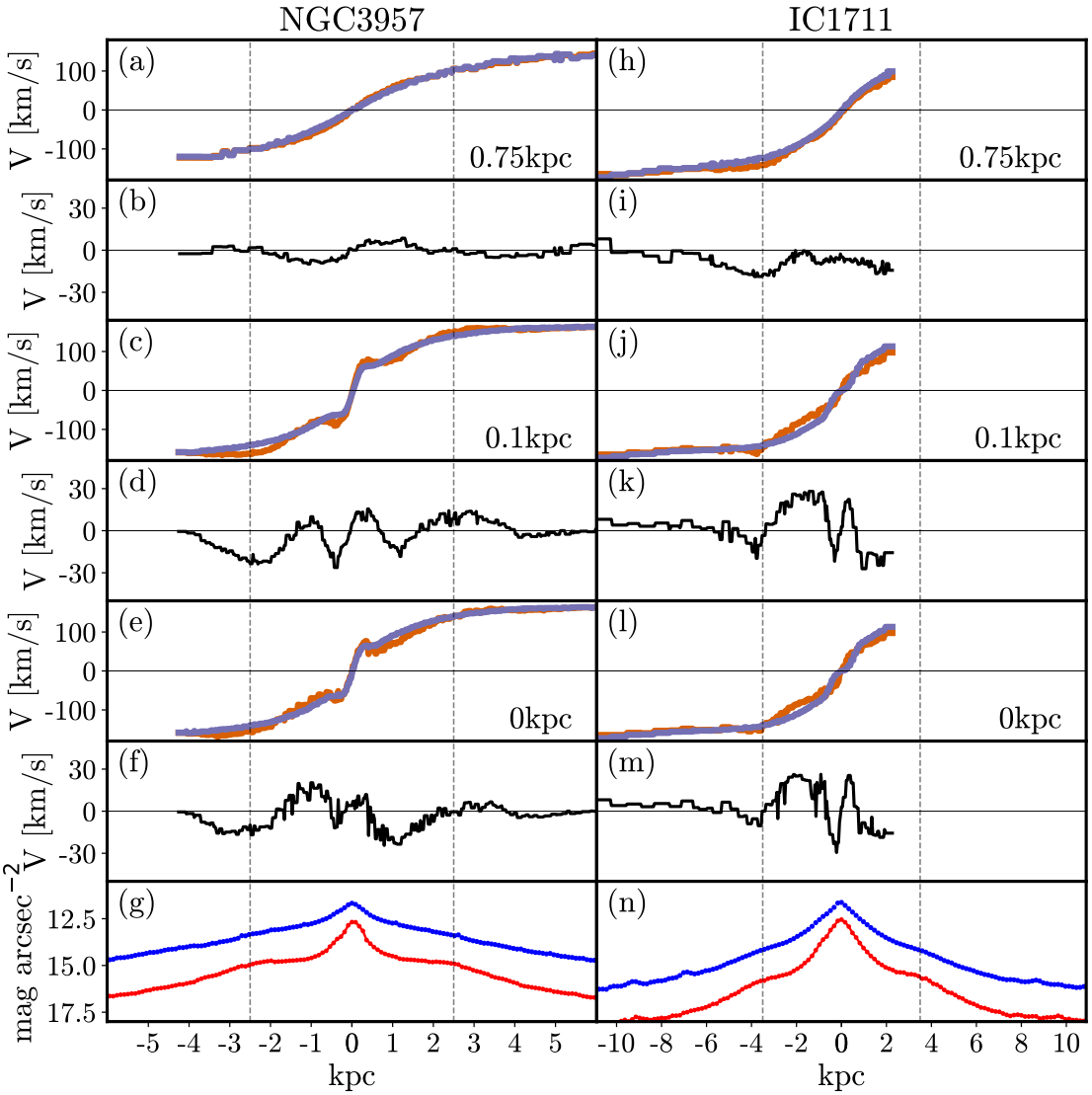

Figure 5.9: Stellar velocities and surface brightness profiles for NGC 3957 and IC 1711. For NGC 3957, panels (a), (c), and (e) show velocities extracted from horizontal slits parallel to the major axis, with the data in orange and the model in purple. Panel (a) shows a slit offset from the major axis by 0.75 kpc,
panel (c) by 0.1 kpc, and panel (e) by 0 kpc. Panels (b), (d), and (f) show the residual velocity from the slits in the panels above, (a), (c), and (e) respectively. Panel (g) shows the surface brightness profiles from Spitzer IRAC 3.6 μm imaging. The total flux summed along the minor axis for each point along the major axis is shown in blue, and the flux along the major axis is shown in red. The dashed black vertical lines at ±2.5 kpc indicate where the photometric shoulders in the major axis profile end. The same is shown for IC 1711 with panels (h), (j), and (l) indicating corresponding velocities; (i), (k), and (m) indicating residuals; and panel (n) indicating surface brightness profiles. Dashed black vertical lines shown at 3.5 kpc indicate where the photometric shoulders end.

We include IC 1711 in the same figure for comparison. Although this galaxy has more dust, it also exhibits a Freeman Type II profile and strong velocity residuals. The photometric shoulders for IC 1711 are at a radius of ~ 3.5kpc, corresponding almost exactly to where the excess velocities drop to zero after a peak, seen most strongly in the 0 kpc and 0.1 kpc offset slits. While this is different from NGC 3957, where the shoulders spatially corresponded to a peak in velocity residuals, the resemblance to NGC 3957 still lends further support to the interpretation that such kinematic structures can trace bar-like components, even in dustier systems. Further to this, we see strong peaks in χ^2_{reduced} at 2.5 kpc for NGC 3957 and 3.5 kpc for IC 1711 in Fig. 5.7. As modelled V_{rms} requires fewer assumptions than modelled V, this lends greater weight to the correlation between these kinematic residuals and the presence of a bar. We emphasise here that we are simply showing that there is a spatial correlation between the kinematic residuals and photometric major-axis shoulders in both NGC 3957 and IC 1711. We do not make predictions on what orbital structures cause this, nor any implied bar size or position angle.

Extending Lessons from NGC 3957 to Our Remaining Sample

Building on the lessons from NGC 3957, we explore whether similar interpretations of residuals can be extended to dustier, more star-forming galaxies in our sample. We note here that NGC 3957 has been identified as hosting a BP bulge in previous studies (Bureau & Freeman, 1999; Lütticke et al., 2000b; Fraser-McKelvie et al., 2025), as well as IC 1711 (Buta et al., 2015; Fraser-McKelvie et al., 2025) and NGC 0522 (Lütticke et al., 2000b; Buta et al., 2015; Fraser-McKelvie et al., 2025). While increased dust complicates the analysis, we suggest several possible structures due to non-axisymmetric orbits in the residual maps of galaxies IC 1711 and NGC 0522.

IC 1711 (Fig. 5.5) was shown to share several key properties with NGC 3957 in Sect. 5.5.2: both exhibit clear Freeman Type II surface brightness profiles (Fig. 5.9) and coherent residual structures in their velocity maps. Here, we note that the major axis residuals in IC 1711 are indeed still somewhat visible even with our most aggressive mask (E(B–V) > 0.2). This supports the interpretation that, despite IC 1711's higher dust content (median E(B–V) of 0.107, c.f. 0.048 for NGC 3957), its kinematic residuals are still spatially correlated with photometric evidence for a bar and could trace bar orbits.

NGC 0522 presents a more ambiguous case. Unlike NGC 3957 and IC 1711, it does not exhibit a clear Freeman Type II profile, though it does show noticeable flattening in its major-axis surface brightness distribution. The velocity residuals in NGC 0522 (Fig. 5.6) also lack the distinct major-axis excess seen in NGC 3957 and IC 1711. Nevertheless, the residuals in NGC 0522 show a notable X-shaped pattern in the off-plane regions of the residual map, qualitatively similar to the pattern we previously noted for NGC 3957 in Sect. 5.4.2. Importantly for this analysis, this pattern is still visible regardless of our dust mask. This structure is morphologically similar to the residuals produced by BP bulges: vertically thickened inner bar structures that arise from dynamical instabilities (Combes & Sanders, 1981; Bureau & Athanassoula, 2005). Indeed, Laurikainen et al. (2014) and Fraser-McKelvie et al. (2025) found that NGC 0522 shows this structure in unsharp-masked 3.6 μm imaging. Buckled BP bulges have been shown to induce complex

non-circular motions, especially in edge-on projections. Iannuzzi & Athanassoula (2015) found that higher-order h_3 and h_4 maps trace BP off the plane of the disc, and Fragkoudi et al. (2017) found the same for mean velocities. While we cannot conclusively identify a bar in NGC 0522, the presence of this X-shaped kinematic signature, as well as the flattened major-axis surface brightness distribution, provides evidence for a BP bulge. Given that previous work has established the presence of a BP bulge in imaging, the lack of strong kinematic evidence for a bar implies a side-on bar orientation, which is the same conclusion reached by Fraser-McKelvie et al. (2025) for this galaxy.

General Trends Across the Sample and Practical Guidelines

While we focus on a detailed residual interpretation for the three systems, Fig. 5.7 shows that all galaxies in our sample achieve acceptable JAM disc fits, with dust masking being important for our most star-forming galaxies (NGC 5775, UGC 00903, and NGC 3279), consistent with the expected correlation between dust content and SFR in star-forming discs (e.g. Calzetti, 2001; Martis et al., 2019; Pappalardo et al., 2021; Tacchella et al., 2022). Despite this, derived enclosed mass remains consistent across mask levels, with variations below 10%, in line with earlier JAM analyses (Lablanche et al., 2012; Li et al., 2016).

Crucially, velocity residuals still reveal coherent kinematic signatures of non-axisymmetric structures in NGC 3957, IC 1711, and NGC 0522 even when an aggressive E(B–V) > 0.2 mask is applied and masked bins are not considered. These detections are supported, in the case of NGC 3957 and IC 1711, by photometric evidence for a bar. We suggest that residual-based identification of internal structure remains viable under substantial dust masking, provided the features persist.

We therefore acknowledge that applying a dust mask of at least E(B–V) > 0.7 is sufficient to recover reliable dynamical parameters in edge-on systems. However, given that these derived dynamical parameters are consistent across dust maskings and residual-based identification of non-axisymmetric structure is most reliable when a strong dust mask is applied, we recommend applying a dust mask of E(B–V) > 0.2 for general application of JAM models to edge-on disc galaxies.

5.6 Summary & Conclusions

In this paper, we investigated the limitations of axisymmetric dynamical modelling of edge-on disc galaxies, focusing on the combined effects of dust attenuation and non-axisymmetric structure on stellar kinematic residuals. We constructed Jeans Anisotropic MGE (JAM) models for seven galaxies in the GECKOS VLT/MUSE survey, using 3.6μm Spitzer IRAC photometry for the light and mass model, with an additional NFW dark matter profile included in the mass model.

One of the goals of this work was to assess what information about non-axisymmetric kinematic structures could be recovered from edge-on galaxies by subtracting a simple, axisymmetric dynamical model. By creating JAM models of a sample of GECKOS galaxies with varying dust content and structural complexity, we tested whether coherent

features in the velocity residuals could reveal underlying non-axisymmetric structure. The velocity residuals between data and model in NGC 3957, our least dusty target, revealed coherent patterns aligned with expected bar orbits and photometry, suggesting a clear link between residual structure and underlying non-axisymmetric kinematics. We extended this analysis to dustier galaxies, which showed velocity residuals similar to NGC 3957. IC 1711 showed similar coherent patterns aligned with photometry, despite the impact of dust. NGC 0522 also had residuals strongly impacted by dust, but off-plane structures showed promise of a diagnostic of vertical bar instabilities. Our results therefore suggest that residual maps from JAM can be a powerful diagnostic for barred structure, provided that regions with dust extinctions of E(B–V) > 0.2 are masked.

We found that JAM fits discs well in all galaxies, and applying stricter E(B–V) masks (e.g. > 0.2 or > 0.4) resulted in $\chi^2_{\text{reduced}} \leq 5$ in the disc region. Additionally, all galaxies showed consistent (within 10%) values of enclosed mass and inclination across a range of dust masks. Notably, galaxies previously classified as containing central non-axisymmetric structure by Fraser-McKelvie et al. (2025) showed the smallest changes with increased masking. This is likely due to a combination of factors: these galaxies having low dust content and hence fewer masked bins in general, along with non-axisymmetric structures imposing an upper bound on how well-fit these galaxies can be.

Future studies incorporating radiative transfer modelling or higher-resolution multi-band imaging could help disentangle the effects of dust and stellar populations on observed kinematics in regions where the dust is optically thin. Extending this analysis to the full GECKOS sample of edge-on galaxies, with a range of structural properties and inclinations, will provide stronger statistical constraints on when and where JAM residuals can be reliably used to detect kinematic structure. For example, the three galaxies in our sample with previously identified bars (NGC 3957, IC 1711, and NGC 0522) are the three least dusty galaxies, so a sample of galaxies with higher dust content and kinematic structure would provide new insights into the upper limit on dust extinction where kinematic components can still be identified. Additionally, a comparison of our work to simulations will allow a more confident determination of whether residual structure truly corresponds to non-axisymmetric orbits. Finally, this work provides a starting point for the GECKOS dynamical modelling effort, and the lessons learned on dust masking and MGE fitting will inform future papers. Future GECKOS studies will employ more complex techniques such as orbit-superposition modelling to explicitly model stellar bars (Tahmasebzadeh et al., 2022, 2024) and derive parameters such as bar pattern speed. Alternative approaches are also possible, such as the method of Fridman et al. (2005), who derived bar pattern speeds from Hα residual velocity maps with appropriate dust masking.

We emphasise caution when applying axisymmetric models to edge-on galaxies. Dust along the line of sight affects the observed kinematics, especially in the mid-plane, tracing only a subset of stars. While using near-infrared imaging helps reduce this bias in the mass model, this imaging introduces a mismatch in our stellar tracer model when compared to optical kinematics, which appears, for example, in poor modelling of nuclear discs. However, the impact of this mismatch between tracer wavelengths could be improved in the future by allowing M/L to vary with each luminous Gaussian, for example. Despite these limitations, global parameters such as enclosed mass and inclination are robustly recovered, even under aggressive masking. A mask of E(B–V) > 0.7 is sufficient for stable

global results, whereas the stricter mask of E(B–V) > 0.2 should be applied when using residual maps for diagnosing non-axisymmetric structures. This suggests that, independent of their kinematic complexity, dusty star-forming edge-on discs can be reliably modelled axisymmetrically at a global level, while residual maps can serve as a window into their more complex kinematic substructure, shedding light on the internal dynamics that trace their evolution.

5.7 Acknowledgements

This work is based on observations obtained with ESO telescopes at the La Silla Paranal Observatory under programme ID 110.24AS. We gratefully acknowledge the support of the ESO staff, and in particular the dedicated team at Paranal Observatory, for their efforts in executing the GECKOS observations.

This research was partially supported by the Australian Research Council Centre of Excellence for All Sky Astrophysics in 3 Dimensions (ASTRO 3D), through project number CE170100013. THR acknowledges the support and funding of an ESO Studentship. AFM acknowledges the support and funding of an ESO Fellowship. AP acknowledges support from the Hintze Family Charity Foundation. MM acknowledges support from the UK Science and Technology Facilities Council through grant ST/Y002490/1. DAG acknowledges support from the UK Science and Technology Facilities Council through grant ST/X001075/1. FP acknowledges support from the Horizon Europe research and innovation programme under the Maria Skłodowska-Curie grant "TraNSLate" No 101108180, and from the Agencia Estatal de Investigación del Ministerio de Ciencia e Innovación (MCIN/AEI/10.13039/501100011033) under grant (PID2021-128131NB-I00) and the European Regional Development Fund (ERDF) "A way of making Europe". PD is supported by a UKRI Future Leaders Fellowship (grant reference MR/S032223/1).

Chapter 6

Thesis Conclusions

You want weapons? We're in a library. Books are the best weapon in the world. This room's the greatest arsenal we could have. Arm yourself!

—The Tenth Doctor

The aim of this thesis was to investigate the physical drivers of galaxy spin evolution. This was achieved by combining the statistical power of the SAMI Galaxy Survey with the exquisite spatial detail of the GECKOS survey, enabling a multi-scale view of how environment, mergers, age, and internal structure shape stellar kinematics. In this chapter, I will summarise the results of this thesis and show their connection to advancing the field of galaxy evolution. Then, I will highlight and discuss the prospects for future studies enabled by my work.

6.1 Summary

We began at the largest scales in Chapter 2, by investigating the connection between large-scale structure and stellar kinematics in the SAMI Galaxy Survey. It has been known since at least the work of Dressler (1980) that there exists a relationship between galaxy morphology and environment, such that early-type galaxies tend to cluster in dense environments. This was extended by Cappellari et al. (2011c), who proposed a kinematic morphology-density relation where the proportion of galaxies with low spin parameter proxy λ_{R_e} increases with local galaxy density. However, it was not clear whether this relationship was independent of the clustering of galaxies by stellar mass through dynamical friction (e.g. Scott et al., 2014; Brough et al., 2017; Graham et al., 2019). By utilising galaxies from the GAMA survey (Driver et al., 2011) as a background galaxy distribution, we marked SAMI galaxies by their ranked stellar mass and ranked λ_{R_e} to calculate marked correlation functions.

Our marked correlation functions confirmed that stellar mass is positively correlated with environment to a 2.4σ level, and λ_{R_e} is negatively correlated with environment to a 3.2σ level. By defining mass bins of 0.1 dex, we randomised λ_{R_e} values within each bin and

further showed that this cannot maintain the negative correlation of λ_{R_e} with environment, and hence the relation is not purely driven by stellar mass. We also removed slow rotators from the sample, and showed that the negative correlation of λ_{R_e} with environment exists within the fast rotator population as well.

Finally, we applied the same technique to a mass-matched sample of galaxies from the EAGLE hydrodynamical cosmological simulations. EAGLE displayed the same broad trend as SAMI, with a positive mass and negative λ_{R_e} correlation with environment. These results demonstrate that in both observations and simulations, environmental effects play an important role in shaping a galaxy's angular momentum. Further, this relationship is not as straightforward as a restatement of the mass-environment correlation, nor a result of the dichotomy of fast and slow rotators. To understand the physical processes that drive this environmental trend, we then turned to the scale of individual galaxies and investigated how galaxy mergers drive kinematic transformations.

In Chapter 3, we examined the role of galaxy mergers in the spin-down of galaxies and formation of slow rotators. Simulations suggest that mergers can reduce λ_{R_e} in galaxies (e.g. Bois et al., 2011; Naab et al., 2014; Choi & Yi, 2017; Lagos, 2020b); however, the timing of these mergers, the importance of gas, and the impact of the geometry of the collision have not been conclusively examined in observational studies. We performed an inspection of deep Hyper-Suprime Cam images of SAMI ETGS with $\log_{10}(M_*/M_\odot)$>10, utilising interactive dynamic ranges and surface-brightness model subtracted residuals. We identified low surface brightness tidal features around these galaxies, classifying features as either shells, which exist at constant radii around a galaxy, or streams, which spiral inwards towards a galaxy.

We found that tidal features are associated with lower values of λ_{R_e}in SAMI galaxies, although the relationship is complex and not strictly one-to-one. Across the full sample, there is no significant difference in the spin of galaxies with and without features. However, when only considering the younger half of the sample (Age/Gyr < 10.8), galaxies with shell features show a significant negative correlation with $\lambda_{R_e}(p = 3.82 \times 10^{-2})$, whereas no such trend is observed for galaxies with streams. We further find that for this younger half of our sample, slow rotators have a significantly higher fraction of shells than fast rotators. The strongest result is for intermediate age galaxies (7.39 < Age/Gyr < 12.55), where galaxies with shells display significantly lower values of λ_{R_e} than those without. Both streams and shells are also strongly correlated with higher stellar masses, but we found the λ_{R_e} correlation for younger galaxies is not driven by stellar mass.

Radial galaxy mergers have been shown to produce shells in post-merger remnants (Karademir et al., 2019), and are therefore the most plausible drivers of the spin-down observed in younger SAMI galaxies with shells. The older, low-spin galaxies that lack visible shells have multiple possible formation pathways. One possibility is that they may were born hot in the early Universe, with any subsequent mergers having no effect on their spin. Alternatively, the absence of shells may simply reflect the fading timescales of shells and streams. Although dependent on factors such as gas fraction and morphology, most studies agree that features remain detectable in deep imaging for about 2 – 4 Gyr post-merger (e.g. Lotz et al., 2010b; Pop et al., 2018; Hood et al., 2018; Mancillas et al., 2019). Thus, galaxies that experienced early mergers could have lost their visible tidal features, erasing

any present day correlation between shells and spin.

Taken together, these results present observational evidence for the merger-driven formation pathway of slow rotator galaxies, as well as the general spin-down of galaxies over cosmic time, as observed for example in simulations (e.g. Zavala et al., 2016; Choi & Yi, 2017). This is consistent with an environmental effect, as central galaxies are a preferred location for merging in simulations (e.g. Fakhouri & Ma, 2009; Oser et al., 2010; Davison et al., 2020). However, the strong observed dependence on stellar age, as well as recent results that suggest that stellar age is more strongly correlated with λ_{R_e} than either stellar mass or environment (Croom et al., 2024), suggests that the imprint of kinematic evolution in galaxies extends beyond averaged λ_R values within an effective radius. To further investigate the relationship between internal stellar dynamics and age, as well as the exact kinematic structural changes driven by mergers, we required an understanding of the detailed orbital structures within each galaxy.

In Chapter 4, we constructed orbit-superposition Schwarzschild dynamical models of a subset of our sample of galaxies from Chapter 3, dependent on a large enough radial coverage in the stellar kinematics. We modelled each galaxy's light distribution with detailed Multi-Gaussian Expansion fits to KiDS r-band imaging, before multiplying by a mass-to-light ratio and adding an NFW halo to create a full mass distribution. We then populated the gravitational potential defined by our mass distribution with a representative library of stellar orbits, and fit to the observed 4-moment velocity maps for each galaxy. From the best-fitting model, we further derived the fraction of hot, warm, cold, and counter-rotating orbits within $1R_e$ in each galaxy, defined by the circularity parameter λ_z.

We found that hot and counter-rotating orbits show a strong negative correlation with λ_{R_e} ($p = 9.66 \times 10^{-10}$ and $p = 1.17 \times 10^{-2}$ respectively), and cold and warm orbits show a strong positive correlation with λ_{R_e} ($p = 8.78 \times 10^{-4}$ and $p = 1.10 \times 10^{-12}$ respectively). Given that λ_{R_e} traces the dynamical contribution of different orbits and their angular momentum, this is an expected result (e.g. van den Bosch et al., 2008; Cappellari, 2016). By calculating partial correlations where stellar mass and environment are controlled for, we found that while hot and cold orbits show correlations with stellar age, there is no such result for warm orbits. This suggests that the transformation of λ_{R_e} with age that has been shown for SAMI galaxies occurs with stars transitioning directly from cold to hot orbits.

Stochastic events such as major mergers are known to reduce λ_{R_e}, as shown in Chapter 3, as well as in simulations (e.g. Naab et al., 2014; Lagos et al., 2018a; Lagos, 2020b). Numerical simulations also suggest that mergers generate a substantial fraction of hot and counter-rotating orbits (e.g. Martel & Richard, 2020), which is supported by our results, as the combined fraction of hot and counter-rotating orbits provides the strongest correlation with λ_{R_e} ($p = 1.13 \times 10^{-16}$). This is consistent with a merger-driven origin for the reduction of galaxy spin. We further investigated this, by examining the younger galaxies in our sample that are likely to display tidal shells as evidence of recent mergers. The result from Chapter 3 that young shell galaxies have significantly lower spin remains, while a higher proportion of hot orbits and a lower proportion of cold orbits is observed in shell galaxies. Interestingly, warm orbits do not show any correlation with shells.

The results from Chapter 4 collectively support a picture where in massive early-type galaxies, mergers drive a transition from cold to hot orbits, which is the primary pathway for the reduction of λ_{R_e} with stellar age. Secular processes are also capable of redistributing angular momentum, but the orbital transformation in these scenarios is expected to happen smoothly, with stars heated from cold, to warm, and finally hot orbits (e.g. Debattista et al., 2006; Saha et al., 2010). The absence of any correlation of warm orbits and stellar age in this sample implies that these processes do not dominate the spin evolution of massive early-type SAMI galaxies.

While the results presented thus far paint a clear picture of the merger driven spin-down of early-type SAMI galaxies, the λ_{R_e}-environment relationship presented in Chapter 2 did not discriminate between early and late-type morphologies. This raises the natural question, how do disc-dominated galaxies respond to galaxy-galaxy interactions? In such systems, external perturbations may trigger instabilities rather than destroy ordered rotation. One of the most prominent of these is the formation or enhancement of stellar bars, which can be triggered by tidal interactions (e.g. Noguchi, 1987; Salo, 1991). Bars are known to redistribute angular momentum within a galaxy (e.g. Fraser-McKelvie et al., 2020), providing a secular process to potentially spin down late-types. Understanding the stellar kinematics of bars within disc galaxies is therefore key to developing a complete picture of how angular momentum evolves across all morphological types.

In Chapter 5, we built axisymmetric Jeans Anisotropic MGE (JAM) models for seven edge-on ($i \gtrapprox 85°$) disc galaxies from the GECKOS-MUSE survey. Our goal was to assess what information about non-axisymmetric kinematic structures could be recovered from edge-on galaxies by subtracting an axisymmetric dynamical model. By modelling the luminosity and mass distribution of each galaxy with Multi-Gaussian Expansion models of Spitzer 3.6μm imaging, we attempted to mitigate the effect of dust in the model input. We compared the output velocity field of JAM to the exquisitely spatially resolved stellar kinematics from MUSE for each galaxy, and used this as a goodness of fit. We additionally masked spaxels in the MUSE data above threshold E(B-V) values, in a further attempt to try and mitigate the effect of dust.

We investigated the three barred galaxies in our sample (previously identified by Fraser-McKelvie et al., 2024). As bars are non-axisymmetric and JAM models are axisymmetric, we expect that strong residual velocities along the major axis should indicate stellar velocities that were unable to be modelled, and hence the presence of a bar. Residual maps from these comparisons revealed clear, spatially coherent velocity excesses along the major axes of two barred galaxies, consistent with the orbital structure expected for bars. These signatures persisted even under conservative dust masking, demonstrating that bar-driven deviations from axisymmetry can be identified kinematically even in edge-on galaxies. The third barred galaxy was more strongly impacted by dust along the major axis, but showed off-plane residual velocity structures typical of barred galaxies. These results show that residual maps from JAM models can be a powerful diagnostic for barred structure, provided that regions with dust extinction are appropriately masked.

Taken in its totality, this thesis establishes a coherent, multi-scale view of the evolution of angular momentum in galaxies. Starting from the environmental dependence of spin measured across thousands of galaxies, we further examined the physical mechanisms of

spin-down through mergers and extended this to their imprints in stellar orbital structure. Finally, we detailed the effect of bars on non-axisymmetric stellar kinematics in disc galaxies, with a future possibility to determine how this impacts the measured λ_{R_e}. The combination of large-scale statistical studies (SAMI) with spatially detailed dynamical modelling (GECKOS) has revealed how angular momentum connects galaxy environment, morphology, and stellar age across multiple evolutionary pathways.

6.2 Future Work

We have measured the evolution of galaxy spin in this thesis, from the large-scale correlations of λ_{R_e} with galaxy density, to the impact of individual mergers on dynamical support, and the non-axisymmetric bar orbits in individual massive edge-on discs, thought to result from past interactions. There are many future studies that are motivated by the work presented in this thesis, and I will summarise them here.

While this thesis provides valuable insight into the spin-evolution of early-type galaxies, there is a missing equivalent study for late-type discs. Morphology is inherently connected to galaxy evolution, with the major merging of discs expected to be the primary formation pathway for elliptical galaxies (e.g. Toomre & Toomre, 1972; Barnes, 1992). Galaxy surveys such as the Hector Survey (Bryant et al., 2016), along with deep imaging surveys such as the LSST (Ivezić et al., 2019; Brough et al., 2020; Martin et al., 2022) will provide the detailed data needed to extend the analysis of merger features and orbital fractions across the full galaxy population. The Euclid mission (Euclid Collaboration et al., 2025) has recently demonstrated the capability of a sky survey with high spatial resolution, depth, and wide coverage to derive merger histories. Using data from Euclid's Early Release Observations, Urbano et al. (2025) identified tidal features and deduced a recent merger history for several galaxies in the Dorado group (Huchra & Geller, 1982).

Additionally, Hector will probe stellar kinematics to a larger effective radius than SAMI. As the inner effective radius is often dominated by bulge structure and stellar bars, extending the radius coverage will allow for a more thorough characterisation of a galaxy's internal dynamics, as well as placing better constraints on the orbital fractions in orbit-superposition modelling. Hector will also help to examine the lack of correlation between shell tidal features and stellar kinematics in old galaxies we found in this thesis. We speculated that mean light-weighted stellar age is a proxy for the time since the last merger, as mergers are expected to drive a starburst period, and old galaxies simply merged long ago and their visible tidal features have since faded. Detailed SED models of Hector galaxies will allow for the derivation of star formation histories across a variety of ages and environments, to examine if the young galaxies we observe with tidal features and low λ_{R_e} have a young age driven by a major starburst, or a more constant star-formation rate over cosmic time. Finally, this thesis didn't examine galaxy mergers in cluster environments due to a lack of available deep imaging for SAMI clusters. Hector will provide even more diverse environments such as the outskirts of clusters, which when combined with the comprehensive imaging of the LSST, will allow the opportunity to examine the spin-evolution of galaxies in detail across a wide variety of environments.

An alternate pathway to examining the evolution of disc galaxies is through the detailed

study of a small number of very highly-spatially resolved galaxies. In a survey such as GECKOS (van de Sande et al., 2024), the exquisite spatial resolution and visible off-plane structure allows for individual kinematic and morphological components such as bars, nuclear discs, pseudo-bulges and classical bulges to be identified and measured, as was done in Chapter 5 of this thesis. However, while this thesis has focused on the growth of dispersion dominated structure from mergers, the Milky Way's thin/thick disc for example is thought to be the result of either mergers (e.g. Renaud et al., 2021) or a combination of secular processes (e.g. Minchev et al., 2015; Clarke et al., 2019). A full chemo-dynamical model of GECKOS galaxies, as well as deep imaging to reveal existing tidal features will provide an opportunity to connect the merger history of disc galaxies with the dynamics, age, and metallicity of its stellar orbits. Moreover, orbit-superposition models may be used to reconstruct merger histories directly, constraining both the mass and timing of past major mergers (e.g. Zhu et al., 2022).

The examination of the impact of mergers on stellar dynamics in this thesis was limited to the local Universe, as SAMI only covers galaxies out to $z \sim 0.1$. Recent and upcoming instruments such as JWST (Gardner et al., 2006) and ELT's HARMONI (Thatte et al., 2010) provide integral field spectroscopy at infrared wavelengths, enabling the possibility of measuring stellar kinematics at high redshifts (e.g. fast rotators at cosmic noon, Slob et al., 2025). This will allow for the direct measurement of how λ_{R_e} evolves with time in the Universe, rather than using light-weighted stellar age as a proxy. Additionally, measuring stellar kinematics at cosmic noon ($z \sim 2-3$) provides valuable insight into the time period where many galaxies assembled their angular momentum. It will be possible to test galaxy evolution models during the time of disk settling and bulge growth, and the transition from turbulent to ordered rotation.

Appendix A

Appendix to Chapter 3

A.1 Stellar Mass, Age, λ_{R_e} and Tidal Features

In this section we show that although stellar mass is strongly correlated with tidal features, it does not drive the relationship between λ_{R_e}, mean stellar age and shells seen in Figure 3.9.

In Figure A.1, we see that when we restrict to galaxies with a stellar mass above the median ($\log_{10}(M_*/M_\odot) = 10.75$), stellar mass is no longer correlated with tidal features. As discussed in Section 3.5.5, we still see a significant split in feature fraction with age at this mass. Additionally, the same qualitative results from Figure 3.9 are found for this mass group.

We further show in Figure A.1 that the correlation between shells and age becomes *stronger* when we restrict to higher stellar masses, as also seen in panel (b) of Figure 3.3. Although there are a high number of shells at all ages at high mass, the fraction of shells is clearly much higher at low stellar ages.

A.2 Example Shells

Here we present examples of shell galaxy cutouts with colour images as well. In Figure A.2, we show galaxies which despite being classified as having a shell, display relatively high λ_{R_e} or low light-weighted mean stellar age. These are examples of galaxies in which it is possible that a ring or weak spiral arm was mis-characterised as a shell.

In Figure A.3, we show examples galaxies which were classified as having a strong shell, i.e. a shell strength of at least 3/5.

A.3 Magneticum ETG Definition

Here we show the cut in the star forming main sequence of Magneticum galaxies, used to classify them as either ETGs or LTGs. In Figure A.4, we show all SAMI galaxies, and our ETG sample on the SAMI star forming main sequence. We then make a cut on

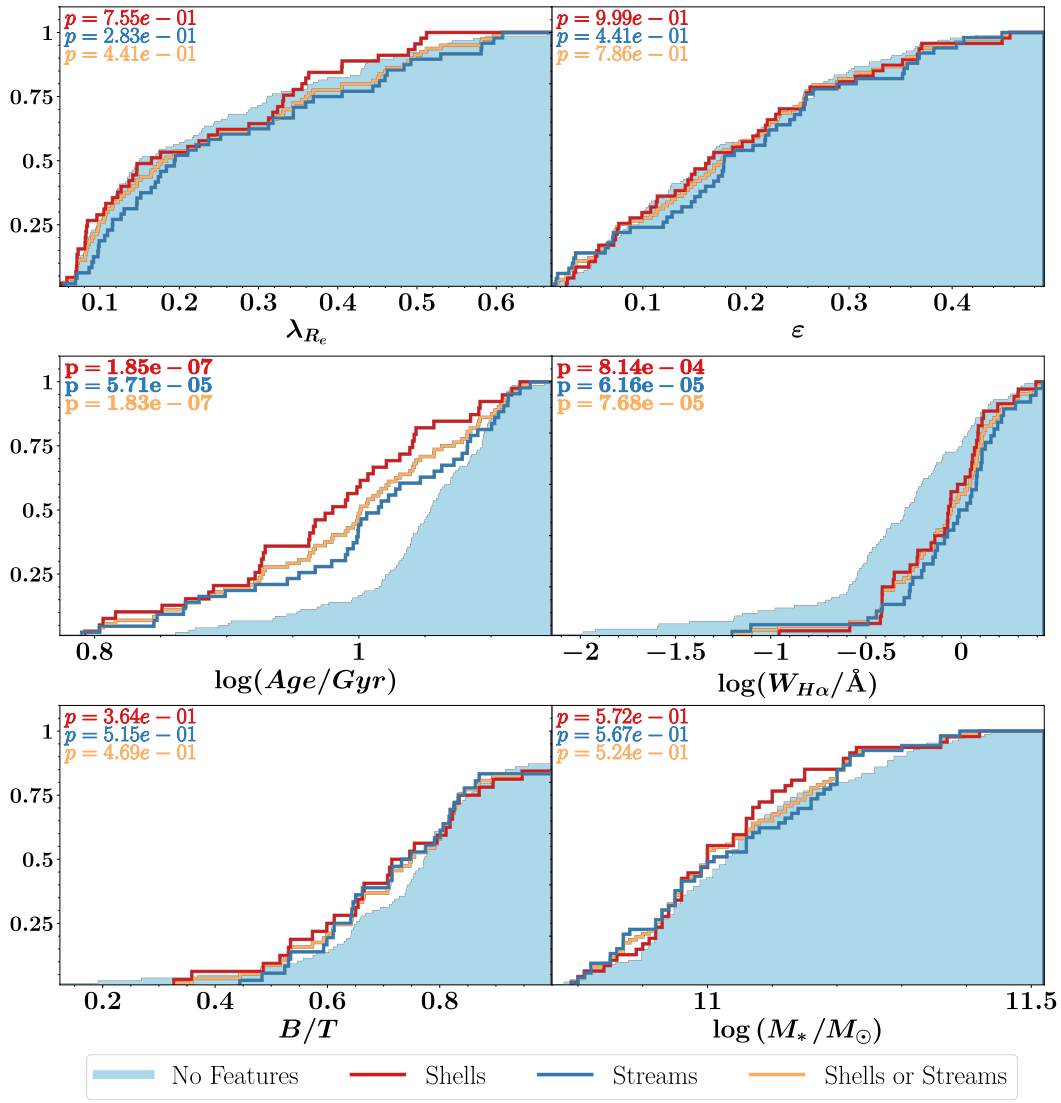

Figure A.1: The cumulative distribution for all relevant parameters and tidal feature samples, for galaxies with stellar masses above the median stellar mass ($\log_{10}(M_*/M_\odot)$= 10.75). All cumulative distributions and labels are the same as Figure 3.4. We find that for these galaxies with high stellar mass, there is no correlation between stellar mass and tidal features.

Magneticum galaxies, based on a fit to our star forming main sequence, shifted down in SFR by 1 dex. The functional form (shown in Equations A.1 and A.2) was used by Fraser-McKelvie et al. (2021) and Leslie et al. (2020), inspired by Lee et al. (2015).

$$\log(SFR) = S_0 - a_1 t - \log\left(1 + \left(\frac{10^{M'_t}}{10^{M}}\right)\right), \tag{A.1}$$

$$M'_t = M_0 - a_2 t \tag{A.2}$$

where t is the age of the universe (taken to be 13.5 Gyr for SAMI data by Fraser-McKelvie et al. (2021)) and M is $\log_{10}(M_*/M_\odot)$. S_0, a_1, a_2 and M_0 are parameters which are fit[1].

[1]Parameters are fit using a linear least squares method (Virtanen et al., 2020)

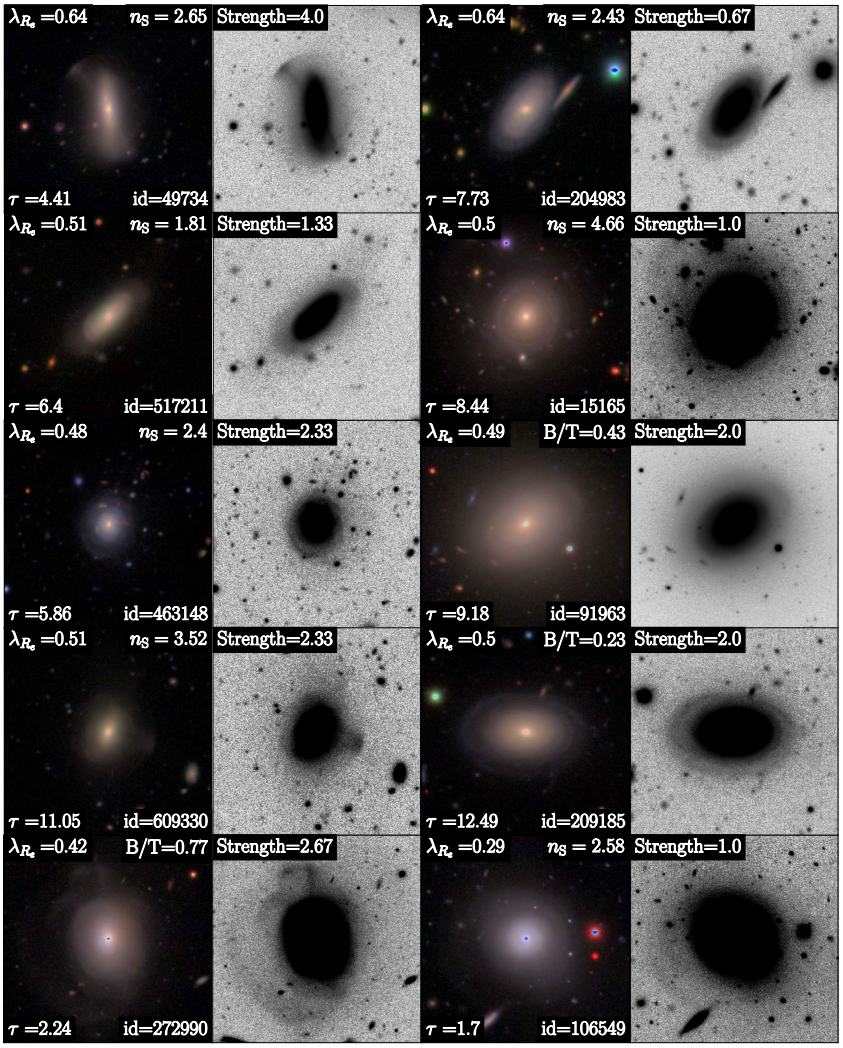

Figure A.2: Galaxies which were both classified as containing a shell, and have relatively high λ_{R_e} or low mean light-weighted stellar age. Each black and white cutout corresponds to the colour image to its left. We include values for the galaxy's λ_{R_e}, age (τ, measured in Gyr), CATAID (id), B/T (or Sérsic index if B/T is not available), and its classified feature strength.

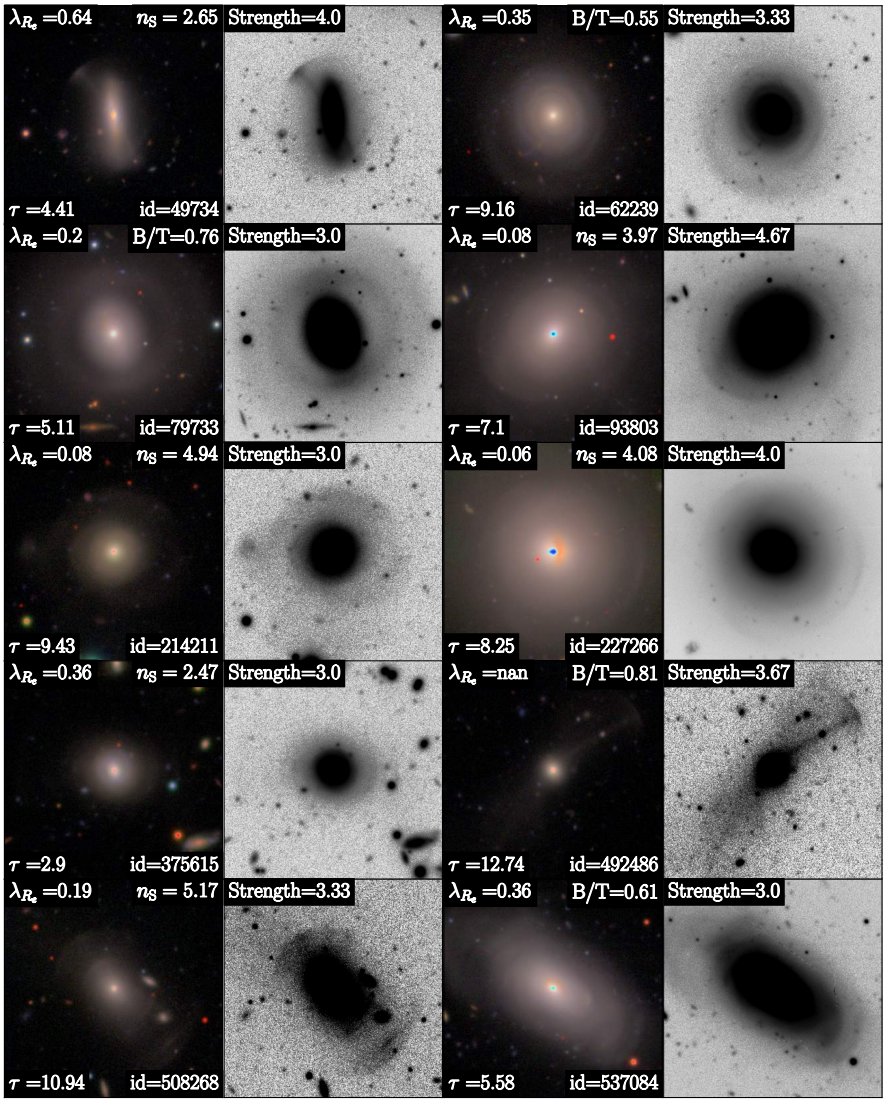

Figure A.3: Galaxies which were both classified as containing a shell, and have a classified strength of at least 3/5. The image layout is similar to Figure A.2.

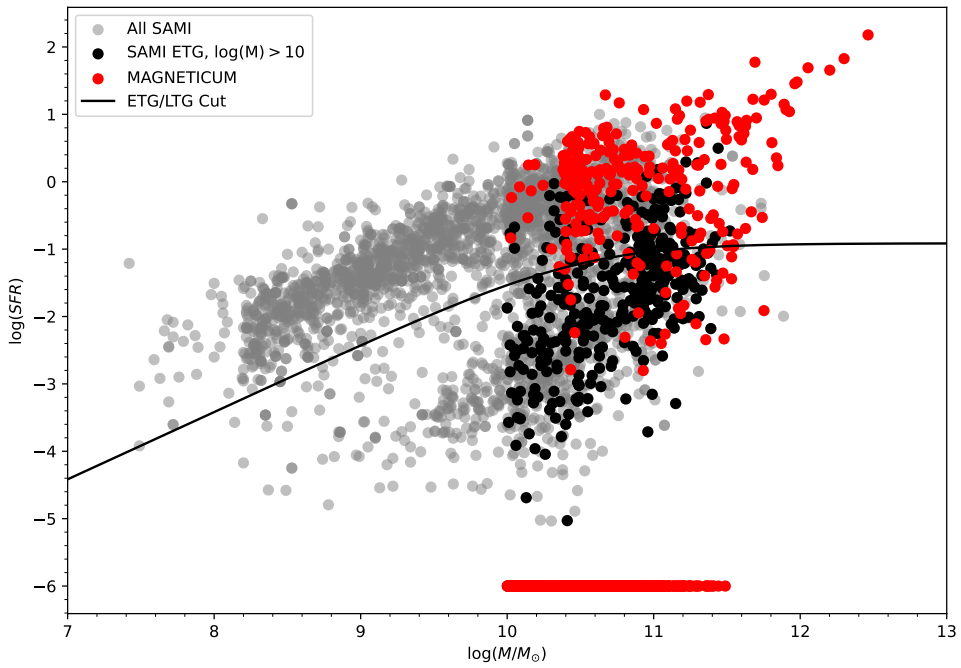

Figure A.4: The star forming main sequence for SAMI galaxies, with Magneticum overplotted. We make a cut based on the SAMI ETGs in order to defne Magneticum ETGs, with all Magneticum galaxies below the line being classified as ETGs. The cut is based on a parametrised form taken from Leslie et al. (2020). The majority of Magneticum ETGs can be seen to have $\log(SFR) = -6$, essentially entirely passive galaxies.

Our best fit can be seen in Equations A.3 and A.4.

$$\log(SFR) = 2.91 - 0.209 \times 13.5 - \log\left(1 + \left(\frac{10^{M'_t}}{10^{M}}\right)\right), \tag{A.3}$$

$$M'_t = 13.201 - 0.200 \times 13.5 \tag{A.4}$$

This was then shifted down by 1 dex, and can be seen in Figure A.4.

Appendix B

Appendix to Chapter 5

B.1 JAM Models

In this section we present JAM model maps for galaxies NGC 3279, NGC 5775, NGC 0360, and UGC 00903, in Figs. B.1-B.4. The left column shows $V_{\rm rms}$, V and σ derived from NGIST output for the seven GECKOS galaxies, the central column shows the same but from the JAM model, and the right column shows the residuals, i.e. data minus model. The velocity residuals for these galaxies do not show clear non-axisymmetric structure.

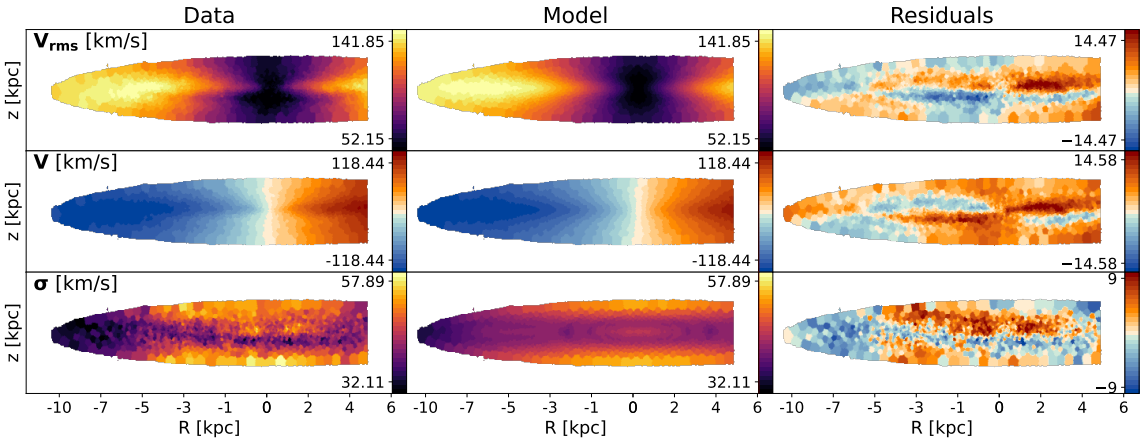

Figure B.1: Same as Fig. 5.4, but for NGC 3279 and without the circling of structure.

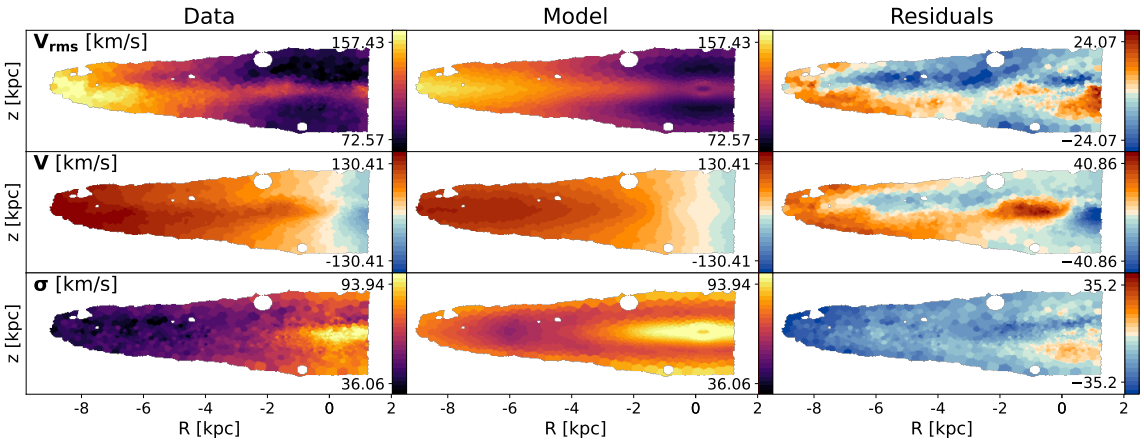

Figure B.2: Same as Fig. 5.4, but for NGC 5775 and without the circling of structure.

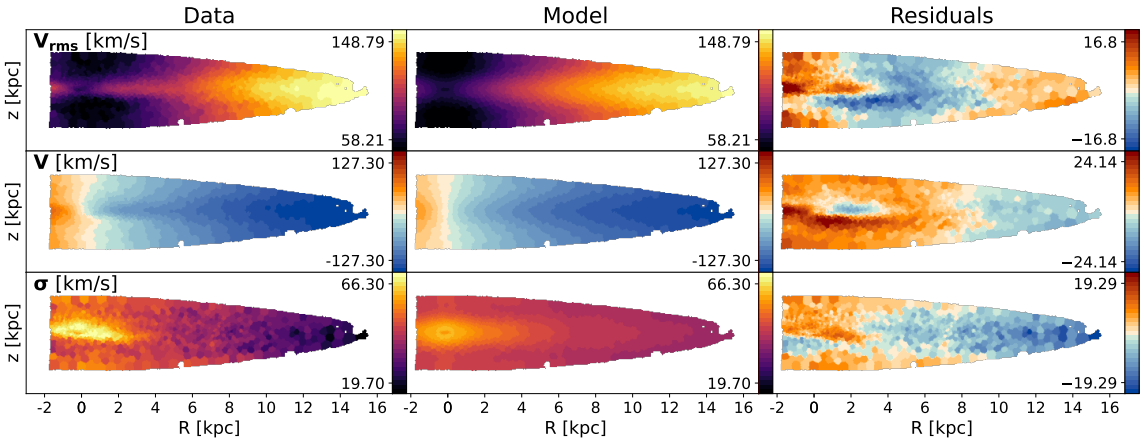

Figure B.3: Same as Fig. 5.4, but for NGC 0360 and without the circling of structure.

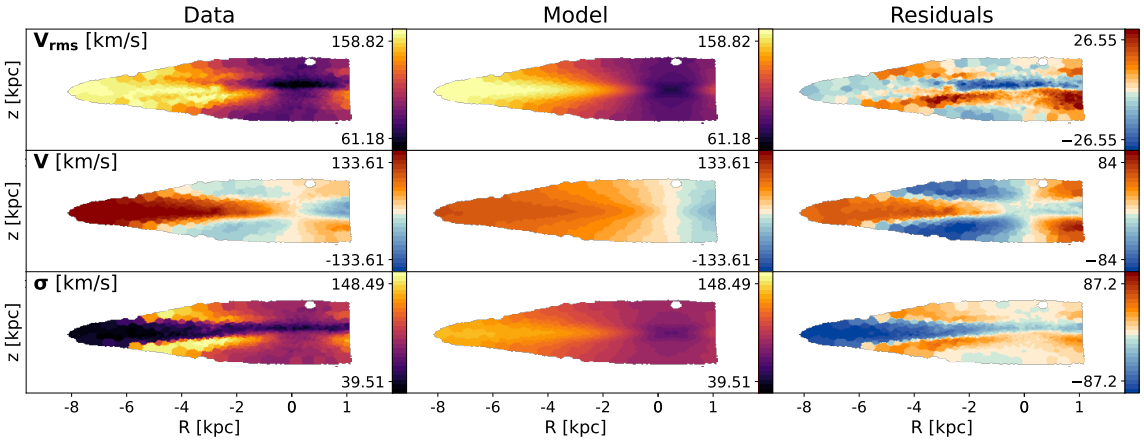

Figure B.4: Same as Fig. 5.4, but for UGC 00903 and without the circling of structure.

We're all stories in the end. Just make it a good one, eh?

—The Eleventh Doctor

Bibliography

Abadi M. G., et al., 2003, ApJ, 597, 21

Abazajian K. N., et al., 2009, ApJS, 182, 543

Abbott B. P., et al., 2016, Phys. Rev. Lett., 116, 061102

Adelman-McCarthy J. K., et al., 2008, ApJS, 175, 297

Agertz O., et al., 2021, MNRAS, 503, 5826

Ahn C. P., et al., 2012, ApJS, 203, 21

Aihara H., et al., 2018a, PASJ, 70, S4

Aihara H., et al., 2018b, PASJ, 70, S8

Aihara H., et al., 2019, PASJ, 71, 114

Allen J. T., et al., 2015, MNRAS, 446, 1567

Aller L. H., 1942, ApJ, 95, 52

Alpher R. A., Bethe H., Gamow G., 1948, Physical Review, 73, 803

Amorisco N. C., 2015, MNRAS, 450, 575

Amram P., et al., 2002, Ap&SS, 281, 389

Angel J. R. P., et al., 1977, ApJ, 218, 776

Athanassoula E., 1992, MNRAS, 259, 345

Athanassoula E., 2005a, MNRAS, 358, 1477

Athanassoula E., 2005b, in Szczerba R., Stasińska G., Gorny S. K., eds, American Institute of Physics Conference Series Vol. 804, Planetary Nebulae as Astronomical Tools. AIP, pp 333–340 (arXiv:astro-ph/0510808), doi:10.1063/1.2146306

Athanassoula E., et al., 2015, MNRAS, 454, 3843

Atkinson A. M., Abraham R. G., Ferguson A. M. N., 2013, ApJ, 765, 28

Aumer M., Binney J., Schönrich R., 2016, MNRAS, 462, 1697

Babcock H. W., 1939, Lick Observatory Bulletin, 498, 41

Bacchini C., et al., 2024, A&A, 687, A115

Bacon R., et al., 1995, A&AS, 113, 347

Bacon R., et al., 2001, MNRAS, 326, 23

Bacon R., et al., 2010, in McLean I. S., Ramsay S. K., Takami H., eds, Society of Photo-Optical Instrumentation Engineers (SPIE) Conference Series Vol. 7735, Ground-based and Airborne Instrumentation for Astronomy III. p. 773508 (arXiv:2211.16795), doi:10.1117/12.856027

Bacon R., et al., 2014, The Messenger, 157, 13

Barnabè M., et al., 2012, MNRAS, 423, 1073

Barnes J., 1990, in Wielen R., ed., , Dynamics and Interactions of Galaxies. pp 186–195

Barnes J. E., 1992, ApJ, 393, 484

Barnes J. E., Hernquist L., 1996, ApJ, 471, 115

Barsanti S., et al., 2022, MNRAS, 516, 3569

Bekki K., Couch W. J., 2011, MNRAS, 415, 1783

Belfiore F., et al., 2019, AJ, 158, 160

Bell E. F., et al., 2006, ApJ, 640, 241

Bellstedt S., et al., 2018, MNRAS, 476, 4543

Bender R., Saglia R. P., Gerhard O. E., 1994, MNRAS, 269, 785

Benedetti J. P. V., et al., 2023, MNRAS, 522, 2570

Bergamini P., et al., 2019, A&A, 631, A130

Bershady M. A., et al., 2010, ApJ, 716, 198

Bertin E., Arnouts S., 1996, A&AS, 117, 393

Bezanson R., et al., 2018, ApJ, 858, 60

Bickley R. W., et al., 2022, MNRAS, 514, 3294

Bik A., et al., 2022, A&A, 666, A161

Bílek M., et al., 2020, MNRAS, 498, 2138

Bílek M., Duc P. A., Sola E., 2023, A&A, 672, A27

Binney J., Tremaine S., 1987, Galactic dynamics. Princeton University Press

Binney J., Tremaine S., 2008, Galactic Dynamics: Second Edition

Binney J., et al., 1991, MNRAS, 252, 210

Bittner A., et al., 2019, A&A, 628, A117

Bittner A., et al., 2020, A&A, 643, A65

Bland-Hawthorn J., Gerhard O., 2016, ARA&A, 54, 529

Bland-Hawthorn J., et al., 2011, Optics Express, 19, 2649

Blanton M. R., Moustakas J., 2009, ARA&A, 47, 159

Bois M., et al., 2010, MNRAS, 406, 2405

Bois M., et al., 2011, MNRAS, 416, 1654

Bottrell C., 2022, in SciOps 2022: Artificial Intelligence for Science and Operations in Astronomy (SCIOPS). Proceedings of the ESA/ESO SCOPS Workshop held 16-20 May. p. 2, doi:10.5281/zenodo.6551859

Bottrell C., et al., 2022, MNRAS, 511, 100

Bournaud F., Jog C. J., Combes F., 2007, A&A, 476, 1179

Bournaud F., et al., 2011, in Brummell N. H., et al., eds, IAU Symposium Vol. 271, Astrophysical Dynamics: From Stars to Galaxies. pp 160–169 (arXiv:1012.5227), doi:10.1017/S1743921311017571

Breddels M. A., Helmi A., 2014, ApJ, 791, L3

Brough S., et al., 2017, ApJ, 844, 59

Brough S., et al., 2020, arXiv e-prints, p. arXiv:2001.11067

Bryant J. J., et al., 2014, MNRAS, 438, 869

Bryant J. J., et al., 2015, MNRAS, 447, 2857

Bryant J. J., et al., 2016, in Evans C. J., Simard L., Takami H., eds, Society of Photo-Optical Instrumentation Engineers (SPIE) Conference Series Vol. 9908, Ground-based and Airborne Instrumentation for Astronomy VI. p. 99081F (arXiv:1608.03921), doi:10.1117/12.2230740

Bryant J. J., et al., 2020, in Evans C. J., Bryant J. J., Motohara K., eds, Society of Photo-Optical Instrumentation Engineers (SPIE) Conference Series Vol. 11447, Ground-based and Airborne Instrumentation for Astronomy VIII. p. 1144715, doi:10.1117/12.2560309

Bundy K., et al., 2015, ApJ, 798, 7

Burbidge E. M., Burbidge G. R., Prendergast K. H., 1960, ApJ, 132, 640

Bureau M., Athanassoula E., 2005, ApJ, 626, 159

Bureau M., Freeman K. C., 1999, AJ, 118, 126

Bureau M., et al., 2006, MNRAS, 370, 753

Buta R. J., et al., 2015, ApJS, 217, 32

Byrd G. G., Howard S., 1992, AJ, 103, 1089

Calzetti D., 2001, PASP, 113, 1449

Calzetti D., et al., 2000, ApJ, 533, 682

Cameron E., 2011, PASA, 28, 128

Cappellari M., 2002, MNRAS, 333, 400

Cappellari M., 2008, MNRAS, 390, 71

Cappellari M., 2016, ARA&A, 54, 597

Cappellari M., 2017, MNRAS, 466, 798

Cappellari M., 2020, MNRAS, 494, 4819

Cappellari M., Copin Y., 2003, MNRAS, 342, 345

Cappellari M., Emsellem E., 2004, PASP, 116, 138

Cappellari M., et al., 2006, MNRAS, 366, 1126

Cappellari M., et al., 2007, MNRAS, 379, 418

Cappellari M., et al., 2009, ApJ, 704, L34

Cappellari M., et al., 2011a, MNRAS, 413, 813

Cappellari M., et al., 2011b, MNRAS, 416, 1680

Cappellari M., et al., 2011c, MNRAS, 416, 1680

Cappellari M., et al., 2012, Nature, 484, 485

Cappellari M., et al., 2013, MNRAS, 432, 1709

Casura S., et al., 2022, MNRAS, 516, 942

Chabrier G., 2003, PASP, 115, 763

Chiosi C., Carraro G., 2002, MNRAS, 335, 335

Choi H., Yi S. K., 2017, ApJ, 837, 68

Choi H., et al., 2018, ApJ, 856, 114

Chung A., Bureau M., 2004, AJ, 127, 3192

Cid Fernandes R., et al., 2011, MNRAS, 413, 1687

Clarke A. J., et al., 2019, MNRAS, 484, 3476

Clarkson C., et al., 2017, Nature, 547, 306

Cluver M. E., et al., 2014, ApJ, 782, 90

Coelho P., Gadotti D. A., 2011, ApJ, 743, L13

Cole S., et al., 2000, MNRAS, 319, 168

Colless M., et al., 2001, MNRAS, 328, 1039

Combes F., Sanders R. H., 1981, A&A, 96, 164

Conselice C. J., 2006, ApJ, 638, 686

Conselice C. J., et al., 2016, ApJ, 830, 83

Contopoulos G., Papayannopoulos T., 1980, A&A, 92, 33

Contreras S., et al., 2019, MNRAS, 484, 1133

Copernicus N., 1543, De revolutionibus orbium coelestium

Cortese L., et al., 2016, MNRAS, 463, 170

Courteau S., 1997, AJ, 114, 2402

Courtès G., 1972, Vistas in Astronomy, 14, 81

Cretton N., et al., 1999, ApJS, 124, 383

Croom S. M., Shanks T., 1996, MNRAS, 281, 893

Croom S. M., et al., 2012, MNRAS, 421, 872

Croom S. M., et al., 2021, MNRAS, 505, 991

Croom S. M., et al., 2024, MNRAS, 529, 3446

D'Eugenio F., et al., 2013, MNRAS, 429, 1258

D'Eugenio F., et al., 2021, MNRAS, 504, 5098

D'Eugenio F., et al., 2024, Nature Astronomy, 8, 1443

Davies J. J., et al., 2020, MNRAS, 491, 4462

Davison T. A., et al., 2020, MNRAS, 497, 81

Debattista V. P., et al., 2006, ApJ, 645, 209

Derkenne C., et al., 2024, MNRAS, 533, 1300

Desmons A., Brough S., Lanusse F., 2023a, arXiv e-prints, p. arXiv:2307.04967

Desmons A., et al., 2023b, MNRAS, 523, 4381

Di Matteo P., et al., 2009, A&A, 501, L9

Domínguez Sánchez H., et al., 2023, MNRAS, 521, 3861

Donne J., 1624, in , Devotions upon Emergent Occasions, Meditation XVII. Printed for Thomas Jones, London

Donohoe-Keyes C. E., et al., 2019, MNRAS, 489, 4992

Dressler A., 1980, ApJ, 236, 351

Dressler A., Gunn J. E., 1983, ApJ, 270, 7

Drinkwater M. J., et al., 2000, PASA, 17, 227

Driver S. P., et al., 2011, MNRAS, 413, 971

Du M., Shen J., Debattista V. P., 2015, ApJ, 804, 139

Duc P.-A., Renaud F., 2013, in Souchay J., Mathis S., Tokieda T., eds, , Vol. 861, Lecture Notes in Physics, Berlin Springer Verlag. p. 327, doi:10.1007/978-3-642-32961-6_9

Duc P.-A., et al., 2015, MNRAS, 446, 120

Dutton A. A., Macciò A. V., 2014, MNRAS, 441, 3359

ESO CPL Development Team 2015, Astrophysics Source Code Library, p. ascl:1504.003

Efstathiou G., et al., 1988, MNRAS, 235, 715

Einstein A., 1916, Annalen der Physik, 354, 769

Einstein A., 1918, Sitzungsberichte der Königlich Preussischen Akademie der Wissenschaften, pp 154–167

Einstein A., 1936, Science, 84, 506

Eisenhauer F., Raab W., 2015, ARA&A, 53, 155

Eisenstein D. J., et al., 2005, ApJ, 633, 560

Elmegreen B. G., Elmegreen D. M., 2005, ApJ, 627, 632

Emsellem E., Monnet G., Bacon R., 1994a, A&A, 285, 723

Emsellem E., et al., 1994b, A&A, 285, 739

Emsellem E., Dejonghe H., Bacon R., 1999, MNRAS, 303, 495

Emsellem E., et al., 2004, MNRAS, 352, 721

Emsellem E., et al., 2007, MNRAS, 379, 401

Emsellem E., et al., 2011, MNRAS, 414, 888

Emsellem E., et al., 2022, A&A, 659, A191

Ene I., et al., 2019, ApJ, 878, 57

Epinat B., et al., 2008, MNRAS, 388, 500

Erwin P., Debattista V. P., 2017, MNRAS, 468, 2058

Erwin P., Pohlen M., Beckman J. E., 2008, AJ, 135, 20

Euclid Collaboration et al., 2025, A&A, 697, A1

Fakhouri O., Ma C.-P., 2009, MNRAS, 394, 1825

Falcón-Barroso J., Martig M., 2021, A&A, 646, A31

Falcón-Barroso J., et al., 2006, MNRAS, 369, 529

Falcón-Barroso J., Lyubenova M., van de Ven G., 2015, in Cappellari M., Courteau S., eds, IAU Symposium Vol. 311, Galaxy Masses as Constraints of Formation Models. pp 78–81 (arXiv:1409.7786), doi:10.1017/S1743921315003439

Fall S. M., Efstathiou G., 1980, MNRAS, 193, 189

Fazio G. G., et al., 2004, ApJS, 154, 10

Feldmeier-Krause A., et al., 2017, MNRAS, 466, 4040

Filippenko A. V., 1982, PASP, 94, 715

Fisher D. B., Drory N., 2010, ApJ, 716, 942

Fisher K. B., et al., 1994, MNRAS, 266, 50

Fogarty L. M. R., et al., 2014, MNRAS, 443, 485

Fogarty L. M. R., et al., 2015, MNRAS, 454, 2050

Foreman-Mackey D., et al., 2013a, PASP, 125, 306

Foreman-Mackey D., et al., 2013b, PASP, 125, 306

Foster C., et al., 2021, PASA, 38, e031

Fragkoudi F., et al., 2017, A&A, 606, A47

Fragkoudi F., et al., 2020, MNRAS, 494, 5936

Franx M., Illingworth G. D., 1988, ApJ, 327, L55

Fraser-McKelvie A., Cortese L., 2022, ApJ, 937, 117

Fraser-McKelvie A., et al., 2020, MNRAS, 499, 1116

Fraser-McKelvie A., et al., 2021, MNRAS, 503, 4992

Fraser-McKelvie A., et al., 2024, arXiv e-prints, p. arXiv:2411.03430

Fraser-McKelvie A., et al., 2025, A&A, 700, A237

Fraternali F., Binney J. J., 2008, MNRAS, 386, 935

Fraunhofer J., 1817, Annalen der Physik, 56, 264

Freeman K. C., 1970, ApJ, 160, 811

Fridman A. M., et al., 2005, A&A, 430, 67

Friedmann A., 1922, Zeitschrift fur Physik, 10, 377

Gadotti D. A., 2009, MNRAS, 393, 1531

Gadotti D. A., de Souza R. E., 2003, ApJ, 583, L75

Gadotti D. A., et al., 2019, MNRAS, 482, 506

Gadotti D. A., et al., 2020, A&A, 643, A14

Galilei G., 1610, Sidereus nuncius magna, longeque admirabilia spectacula pandens lunae facie, fixis innumeris, lacteo circulo, stellis nebulosis, ... Galileo Galileo : nuper a se reperti beneficio sunt observata in apprime vero in quatuor planetis circa Iovis stellam disparibus intervallis, atque periodis, celeritate mirabili circumvolutis ... atque Medicea sidera nuncupandos decrevit, doi:10.3931/e-rara-695.

Gardner J. P., et al., 2006, Space Sci. Rev., 123, 485

Gebhardt K., et al., 2003, ApJ, 583, 92

Gerhard O. E., 1993, MNRAS, 265, 213

Gerssen J., Kuijken K., Merrifield M. R., 1997, MNRAS, 288, 618

Gerssen J., Kuijken K., Merrifield M. R., 2000, MNRAS, 317, 545

Gott III J. R., Gunn J. E., 1971, ApJ, 169, L13

Graham A. W., et al., 1998, A&AS, 133, 325

Graham M. T., et al., 2019, arXiv e-prints, p. arXiv:1910.05139

Granata G., et al., 2025, A&A, 697, A94

Green A. W., et al., 2010, Nature, 467, 684

Green A. W., et al., 2018, MNRAS, 475, 716

Greene J. E., et al., 2017, ApJ, 851, L33

Guth A. H., 1981, Phys. Rev. D, 23, 347

Habas R., et al., 2020, MNRAS, 491, 1901

Hamacher D. W., Banks K., 2018, arXiv e-prints, p. arXiv:1806.02462

Harborne K. E., et al., 2020, MNRAS, 497, 2018

Harker G., et al., 2006, MNRAS, 367, 1039

Harrison B. K., et al., 1965, Gravitation Theory and Gravitational Collapse

Heath T. L., Aristarchus of Samos 1913, Aristarchus of Samos, the ancient Copernicus; a history of Greek astronomy to Aristarchus, together With Aristarchus's Treatise on the sizes and distances of the sun and moon

Hermit S., et al., 1996, MNRAS, 283, 709

Hernquist L., Quinn P. J., 1989, ApJ, 342, 1

Herpich F., et al., 2018, MNRAS, 481, 1774

Hilker M., et al., 1999, A&AS, 134, 75

Hill J. M., et al., 1980, ApJ, 242, L69

Ho L. C., 2007, ApJ, 668, 94

Ho S. H., Martin C. L., Turner M. L., 2019, ApJ, 875, 54

Hoffman L., et al., 2010, ApJ, 723, 818

Hohl F., 1971, ApJ, 168, 343

Hood C. E., et al., 2018, ApJ, 857, 144

Hopkins P. F., et al., 2010, ApJ, 724, 915

Houghton R. C. W., et al., 2013, MNRAS, 436, 19

Hoyle F., 1948, MNRAS, 108, 372

Huang Q., Fan L., 2022, ApJS, 262, 39

Hubbard E. N., Angel J. R. P., Gresham M. S., 1979, ApJ, 229, 1074

Hubble E. P., 1926a, ApJ, 64, 321

Hubble E., 1926b, Contributions from the Mount Wilson Observatory / Carnegie Institution of Washington, 324, 1

Hubble E. P., 1929, ApJ, 69, 103

Huchra J. P., Geller M. J., 1982, ApJ, 257, 423

Husser T.-O., et al., 2016, A&A, 588, A148

Iannuzzi F., Athanassoula E., 2015, MNRAS, 450, 2514

Ibata R. A., et al., 2017, ApJ, 848, 128

Ivezić Ž., et al., 2019, ApJ, 873, 111

Jeans J. H., 1922, MNRAS, 82, 122

Jesseit R., Naab T., Burkert A., 2005, MNRAS, 360, 1185

Jesseit R., et al., 2009, MNRAS, 397, 1202

Jethwa P., et al., 2020, DYNAMITE: DYnamics, Age and Metallicity Indicators Tracing Evolution, Astrophysics Source Code Library, record ascl:2011.007

Ji I., Peirani S., Yi S. K., 2014, A&A, 566, A97

Jian H.-Y., Lin L., Chiueh T., 2012, ApJ, 754, 26

Jin Y., et al., 2019, MNRAS, 486, 4753

Jin Y., et al., 2020, MNRAS, 491, 1690

Johnston K. V., et al., 2008, ApJ, 689, 936

Kado-Fong E., et al., 2018, ApJ, 866, 103

Kalinova V., et al., 2017, MNRAS, 464, 1903

Kamann S., et al., 2018, MNRAS, 473, 5591

Karademir G. S., et al., 2019, MNRAS, 487, 318

Kassin S. A., et al., 2012, ApJ, 758, 106

Kauffmann G., White S. D. M., 1993, MNRAS, 261, 921

Kelvin L. S., et al., 2014, MNRAS, 439, 1245

Kemp S. N., Meaburn J., 1991, MNRAS, 251, 10P

Kendall M., Stuart A., 1979, The advanced theory of statistics. Vol.2: Inference and relationship

Kenney J. D. P., van Gorkom J. H., Vollmer B., 2004, AJ, 127, 3361

Kepler J., 1609, Astronomia nova ..., seu physica coelestis, tradita commentariis de motibus stellae martis, doi:10.3931/e-rara-558.

Khalid A., et al., 2024, MNRAS, 530, 4422

Khan R., 2017, ApJS, 228, 5

Khochfar S., et al., 2011, MNRAS, 417, 845

Kim T., et al., 2016, MNRAS, 462, 3430

Kim T., et al., 2024, ApJ, 976, 220

Kirchhoff G., 1860, Annalen der Physik, 185, 148

Kirchhoff G., Bunsen R., 1860, Annalen der Physik, 186, 161

Kluge M., et al., 2020, ApJS, 247, 43

Knapen J. H., Cisternas M., Querejeta M., 2015, MNRAS, 454, 1742

Koopmann R. A., Kenney J. D. P., 2004, ApJ, 613, 866

Kormendy J., 1989, ApJ, 342, L63

Krajnović D., et al., 2005, MNRAS, 357, 1113

Krajnović D., et al., 2006, MNRAS, 366, 787

Krajnović D., et al., 2009, MNRAS, 399, 1839

Krajnović D., et al., 2011, MNRAS, 414, 2923

Krajnović D., et al., 2015, MNRAS, 452, 2

Kruk S. J., et al., 2019, MNRAS, 490, 4721

Kuijken K., 2011, The Messenger, 146, 8

Kuijken K., et al., 2019, A&A, 625, A2

Lablanche P.-Y., et al., 2012, MNRAS, 424, 1495

Lacey C., Cole S., 1993, MNRAS, 262, 627

Lagos C. D. P., 2020a, in IAU General Assembly. pp 208–214, doi:10.1017/S1743921319004095

Lagos C. d. P., 2020b, IAU Focus Meeting, 30, 208

Lagos C. d. P., et al., 2017, MNRAS, 464, 3850

Lagos C. d. P., et al., 2018a, MNRAS, 473, 4956

Lagos C. d. P., et al., 2018b, MNRAS, 476, 4327

Lagos C. d. P., et al., 2022, MNRAS, 509, 4372

Larson R. B., 1974, MNRAS, 166, 585

Larson R. B., Tinsley B. M., Caldwell C. N., 1980, ApJ, 237, 692

Lauer T. R., et al., 2021, ApJ, 906, 77

Laurikainen E., et al., 2014, MNRAS, 444, L80

Lawson C. L., Hanson R. J., 1974, Solving least squares problems

Le Fèvre O., et al., 2005, A&A, 439, 845

Lee N., et al., 2015, ApJ, 801, 80

Lemaître G., 1927, Annales de la Société Scientifique de Bruxelles, 47, 49

Lemaître A. G., 1931, Nature, 128, 704

Leslie S. K., et al., 2020, ApJ, 899, 58

Leung G. Y. C., et al., 2018, MNRAS, 477, 254

Levan A. J., et al., 2017, ApJ, 848, L28

Li H., et al., 2016, MNRAS, 455, 3680

Li H., et al., 2017, ApJ, 838, 77

Li Z.-Y., et al., 2018, ApJ, 854, 65

Li J., et al., 2022, MNRAS, 515, 5335

Liller M. H., 1966, ApJ, 146, 28

Lin L., et al., 2008, ApJ, 681, 232

Linde A. D., 1982, Physics Letters B, 108, 389

Liske J., et al., 2015, MNRAS, 452, 2087

Lofthouse E. K., et al., 2017, MNRAS, 465, 2895

López-Sánchez Á. R., 2010, A&A, 521, A63

Lotz J. M., et al., 2008, MNRAS, 391, 1137

Lotz J. M., et al., 2010a, MNRAS, 404, 575

Lotz J. M., et al., 2010b, MNRAS, 404, 590

Lütticke R., Dettmar R. J., Pohlen M., 2000a, A&AS, 145, 405

Lütticke R., Dettmar R. J., Pohlen M., 2000b, A&A, 362, 435

Ma C.-P., et al., 2014, ApJ, 795, 158

Madgwick D. S., et al., 2003, MNRAS, 344, 847

Makarov D., et al., 2014, A&A, 570, A13

Mancillas B., et al., 2019, A&A, 632, A122

Mantha K. B., et al., 2019, MNRAS, 486, 2643

Martel H., Richard S., 2020, MNRAS, 498, 940

Martin G., et al., 2022, MNRAS, 513, 1459

Martis N. S., et al., 2019, ApJ, 882, 65

Matthews B. W., 1975, Biochimica et Biophysica Acta (BBA) - Protein Structure, 405, 442

Mayall N. U., 1946, ApJ, 104, 290

McDermid R. M., et al., 2015, MNRAS, 448, 3484

McIntosh D. H., et al., 2008, MNRAS, 388, 1537

Melchior A. L., Combes F., Gould A., 2007, A&A, 462, 965

Méndez-Abreu J., et al., 2019, MNRAS, 482, L118

Menéndez-Delmestre K., et al., 2007, ApJ, 657, 790

Minchev I., et al., 2015, ApJ, 804, L9

Minkowski R., 1962, in McVittie G. C., ed., IAU Symposium Vol. 15, Problems of Extra-Galactic Research. p. 112

Mitzkus M., Cappellari M., Walcher C. J., 2017, MNRAS, 464, 4789

Miyazaki S., et al., 2015, ApJ, 807, 22

Moffat A. F. J., 1969, A&A, 3, 455

Monnet G., Bacon R., Emsellem E., 1992, A&A, 253, 366

Moody C. E., et al., 2014, MNRAS, 444, 1475

Morton D. C., Thuan T. X., 1973, ApJ, 180, 705

Mountford C. P., 1958, in , Chapter 7 of "The Tiwi: their art. p. 170

Mukhanov V. F., Chibisov G. V., 1981, Soviet Journal of Experimental and Theoretical Physics Letters, 33, 532

Mukhanov V. F., Feldman H. A., Brandenberger R. H., 1992, Phys. Rep., 215, 203

NASA 1968, LUNAR TELEVISION CAMERA PRE-INSTALLATION ACCEPTANCE (PIA) TEST PLAN, https://history.nasa.gov/alsj/MSC-SESD-28-105.pdf

Naab T., Burkert A., 2003, ApJ, 597, 893

Naab T., Jesseit R., Burkert A., 2006, MNRAS, 372, 839

Naab T., Johansson P. H., Ostriker J. P., 2009, ApJ, 699, L178

Naab T., et al., 2014, MNRAS, 444, 3357

Navarro J. F., Frenk C. S., White S. D. M., 1996, ApJ, 462, 563

Navarro J. F., Frenk C. S., White S. D. M., 1997, ApJ, 490, 493

Neugebauer O., 1975, A history of ancient mathematical astronomy. Part 1; Part 2; Part 3

Neumann J., et al., 2017, A&A, 604, A30

Neureiter B., et al., 2021, MNRAS, 500, 1437

Nevin R., et al., 2019, ApJ, 872, 76

Nevin R., et al., 2021, ApJ, 912, 45

Nevin R., et al., 2023, MNRAS, 522, 1

Newton I., 1671, Philosophical Transactions of the Royal Society of London Series I, 6, 3075

Newton I., 1687, Philosophiae Naturalis Principia Mathematica., doi:10.3931/e-rara-440.

Noguchi M., 1987, MNRAS, 228, 635

Noordermeer E., Merrifield M. R., Aragón-Salamanca A., 2008, MNRAS, 388, 1381

Norberg P., et al., 2001, MNRAS, 328, 64

Norberg P., et al., 2002, MNRAS, 332, 827

Oh S. H., et al., 2008, ApJ, 683, 94

Oh S., et al., 2016, ApJ, 832, 69

Oke J. B., Gunn J. E., 1983, ApJ, 266, 713

Oppenheimer J. R., Snyder H., 1939, Physical Review, 56, 455

Oser L., et al., 2010, ApJ, 725, 2312

Ostriker J. P., Peebles P. J. E., 1973, ApJ, 186, 467

Owers M. S., et al., 2017, MNRAS, 468, 1824

Pappalardo C., et al., 2021, A&A, 655, A104

Parikh T., et al., 2019, MNRAS, 483, 3420

Pasquini L., et al., 2002, The Messenger, 110, 1

Patsis P. A., Xilouris E. M., 2006, MNRAS, 366, 1121

Patterson F. S., 1940, Harvard College Observatory Bulletin, 914, 9

Pawlik M. M., et al., 2019, Nature Astronomy, 3, 440

Peebles P. J. E., 1980, The Large-Scale Structure of the Universe

Peng C. Y., et al., 2002, AJ, 124, 266

Penoyre Z., et al., 2017, MNRAS, 468, 3883

Penzias A. A., Wilson R. W., 1965, ApJ, 142, 419

Persic M., Salucci P., Stel F., 1996, MNRAS, 281, 27

Pietrinferni A., et al., 2004, ApJ, 612, 168

Pietrinferni A., et al., 2006, ApJ, 642, 797

Piner B. G., Stone J. M., Teuben P. J., 1995, ApJ, 449, 508

Planck Collaboration et al., 2016, A&A, 594, A13

Planck Collaboration et al., 2020, A&A, 641, A6

Plummer H. C., 1911, MNRAS, 71, 460

Poci A., et al., 2019, MNRAS, 487, 3776

Poggianti B. M., et al., 2017, ApJ, 844, 48

Pontzen A., et al., 2017, MNRAS, 465, 547

Pop A.-R., et al., 2018, MNRAS, 480, 1715

Press W. H., Schechter P., 1974, ApJ, 187, 425

Quenneville M. E., Liepold E. R., Ma C.-P., 2021, ApJS, 254, 25

Quinn P. J., 1984, ApJ, 279, 596

Rees M. J., Ostriker J. P., 1977, MNRAS, 179, 541

Reines A. E., Volonteri M., 2015, ApJ, 813, 82

Reiter S., et al., 2025, A&A, 701, A12

Renaud F., et al., 2021, MNRAS, 503, 5846

Riess A. G., et al., 1998, AJ, 116, 1009

Riffel R., et al., 2023, MNRAS, 524, 5640

Ristea A., et al., 2022, MNRAS, 517, 2677

Robotham A. S. G., et al., 2011, MNRAS, 416, 2640

Robotham A. S. G., et al., 2017, MNRAS, 466, 1513

Robotham A. S. G., et al., 2018, MNRAS, 476, 3137

Robotham A. S. G., et al., 2020, MNRAS, 495, 905

Robotham A. S. G., Bellstedt S., Driver S. P., 2022, MNRAS, 513, 2985

Röttgers B., Naab T., Oser L., 2014, MNRAS, 445, 1065

Rutherford T. H., et al., 2021, ApJ, 918, 84

Rutherford T. H., et al., 2024, MNRAS, 529, 810

Rutherford T. H., et al., 2025, arXiv e-prints, p. arXiv:2509.08371

Saha K., Tseng Y.-H., Taam R. E., 2010, ApJ, 721, 1878

Sales L. V., et al., 2012, MNRAS, 423, 1544

Salo H., 1991, A&A, 243, 118

Salo H., et al., 2015, ApJS, 219, 4

Sánchez S. F., et al., 2012, A&A, 538, A8

Santucci G., et al., 2022, ApJ, 930, 153

Santucci G., et al., 2024, MNRAS, 528, 2326

Sargent W. L. W., et al., 1977, ApJ, 212, 326

Sarzi M., et al., 2006, MNRAS, 366, 1151

Schaefer A. L., et al., 2019, MNRAS, 483, 2851

Schaye J., et al., 2015, MNRAS, 446, 521

Schulze F., et al., 2020, MNRAS, 493, 3778

Schwarzschild M., 1979, ApJ, 232, 236

Schwarzschild M., 1982, ApJ, 263, 599

Schweizer F., Seitzer P., 1988, ApJ, 328, 88

Scott C., Kaviraj S., 2014, MNRAS, 437, 2137

Scott N., et al., 2009, MNRAS, 398, 1835

Scott N., et al., 2014, MNRAS, 441, 274

Scott N., et al., 2015, MNRAS, 451, 2723

Scott N., et al., 2017, MNRAS, 472, 2833

Scott N., et al., 2018, MNRAS, 481, 2299

Sellwood J. A., 2014, Reviews of Modern Physics, 86, 1

Sellwood J. A., Wilkinson A., 1993, Reports on Progress in Physics, 56, 173

Seo W.-Y., et al., 2019, ApJ, 872, 5

Sérsic J. L., 1963, Boletin de la Asociacion Argentina de Astronomia La Plata Argentina, 6, 41

Shajib A. J., et al., 2023, A&A, 673, A9

Shakeshaft J. R., et al., 1955, MmRAS, 67, 106

Shapiro K. L., Gerssen J., van der Marel R. P., 2003, AJ, 126, 2707

Sharp R., et al., 2006, in McLean I. S., Iye M., eds, Society of Photo-Optical Instrumentation Engineers (SPIE) Conference Series Vol. 6269, Ground-based and Airborne Instrumentation for Astronomy. p. 62690G (arXiv:astro-ph/0606137), doi:10.1117/12.671022

Sharp R., et al., 2015, MNRAS, 446, 1551

Sheth R. K., Tormen G., 2004, MNRAS, 350, 1385

Sheth R. K., Connolly A. J., Skibba R., 2005a, arXiv e-prints, pp astro–ph/0511773

Sheth K., et al., 2005b, ApJ, 632, 217

Sheth K., et al., 2010, PASP, 122, 1397

Silk J., 1977, ApJ, 211, 638

Simard L., et al., 2011, ApJS, 196, 11

Skibba R., et al., 2006, MNRAS, 369, 68

Skibba R. A., et al., 2009, MNRAS, 399, 966

Skokos C., Patsis P. A., Athanassoula E., 2002a, MNRAS, 333, 847

Skokos C., Patsis P. A., Athanassoula E., 2002b, MNRAS, 333, 861

Slipher V. M., 1915, Popular Astronomy, 23, 21

Slob M., et al., 2025, A&A, 702, A110

Sola E., et al., 2022, A&A, 662, A124

Sola E., et al., 2025, arXiv e-prints, p. arXiv:2503.18480

Sparre M., Springel V., 2017, MNRAS, 470, 3946

Spitzer L., 1978, Physical processes in the interstellar medium, doi:10.1002/9783527617722.

Stäckel P., 1891, Über die integration der Hamilton-Jacobischen differentialgleichung mittelst separation der variabeln...

Starobinsky A. A., 1982, Physics Letters B, 117, 175

Steigman G., 2007, Annual Review of Nuclear and Particle Science, 57, 463

Steinmetz M., Navarro J. F., 2002, New Astron., 7, 155

Stewart K. R., 2009, in Jogee S., et al., eds, Astronomical Society of the Pacific Conference Series Vol. 419, Galaxy Evolution: Emerging Insights and Future Challenges. p. 243 (arXiv:0902.2214), doi:10.48550/arXiv.0902.2214

Tacchella S., et al., 2022, MNRAS, 513, 2904

Tahmasebzadeh B., et al., 2022, ApJ, 941, 109

Tahmasebzadeh B., et al., 2024, MNRAS, 534, 861

Tal T., et al., 2009, AJ, 138, 1417

Tanvir N. R., et al., 2017, ApJ, 848, L27

Taylor P., Kobayashi C., 2017, MNRAS, 471, 3856

Taylor E. N., et al., 2011, MNRAS, 418, 1587

Teklu A. F., et al., 2015, ApJ, 812, 29

Thater S., et al., 2019, A&A, 625, A62

Thater S., et al., 2022, A&A, 667, A51

Thatte N., et al., 2010, in McLean I. S., Ramsay S. K., Takami H., eds, Society of Photo-Optical Instrumentation Engineers (SPIE) Conference Series Vol. 7735, Ground-based and Airborne Instrumentation for Astronomy III. p. 77352I, doi:10.1117/12.857445

Thompson D., Djorgovski S. G., 1995, AJ, 110, 982

Thorp M. D., et al., 2019, MNRAS, 482, L55

Tikhonenko I. S., Smirnov A. A., Sotnikova N. Y., 2021, A&A, 648, L4

Toomre A., Toomre J., 1972, ApJ, 178, 623

Tully R. B., et al., 2023, ApJ, 944, 94

Tyndall J., 1873, Nature, 8, 432

Übler H., et al., 2014, MNRAS, 443, 2092

Übler H., et al., 2019, ApJ, 880, 48

Urbano M., et al., 2025, A&A, 700, A104

Valenzuela L. M., Remus R.-S., 2022, arXiv e-prints, p. arXiv:2208.08443

Valluri M., Merritt D., Emsellem E., 2004, ApJ, 602, 66

Valluri M., et al., 2016, ApJ, 818, 141

Vasiliev E., 2013, MNRAS, 434, 3174

Vasiliev E., Athanassoula E., 2015, MNRAS, 450, 2842

Vasiliev E., Valluri M., 2020, ApJ, 889, 39

Vasiliev E., Belokurov V., Evans N. W., 2022, ApJ, 926, 203

Vaughan S. P., et al., 2022, MNRAS, 516, 2971

Vazdekis A., et al., 2015, MNRAS, 449, 1177

Veale M., et al., 2017, MNRAS, 471, 1428

Verro K., et al., 2022, A&A, 660, A34

Verwilghen P., et al., 2024, A&A, 687, A53

Virtanen P., et al., 2020, Nature Methods, 17, 261

Wagoner R. V., Fowler W. A., Hoyle F., 1967, ApJ, 148, 3

Walo-Martín D., et al., 2020, MNRAS, 494, 5652

Wang B., et al., 2020, MNRAS, 495, 1958

Watkins L. L., et al., 2013, MNRAS, 436, 2598

Weil M. L., Bland-Hawthorn J., Malin D. F., 1997, ApJ, 490, 664

Weilbacher P. M., et al., 2020, A&A, 641, A28

Westfall K. B., et al., 2019, AJ, 158, 231

White S. D. M., 1979, MNRAS, 189, 831

White S. D. M., Rees M. J., 1978, MNRAS, 183, 341

Wild V., et al., 2007, MNRAS, 381, 543

Willman B., et al., 2005a, AJ, 129, 2692

Willman B., et al., 2005b, ApJ, 626, L85

Wilman D. J., et al., 2013, MNRAS, 433, 2986

Wisnioski E., et al., 2015, ApJ, 799, 209

Wozniak H., 2015, A&A, 575, A7

Yi S. K., et al., 2024, ApJS, 271, 1

Yoon Y., et al., 2024, ApJ, 965, 158

York D. G., et al., 2000, AJ, 120, 1579

Zavala J., et al., 2016, MNRAS, 460, 4466

Zel'dovich Y. B., 1970, A&A, 5, 84

Zhu L., et al., 2014, ApJ, 792, 59

Zhu L., et al., 2018a, Nature Astronomy, 2, 233

Zhu L., et al., 2018b, MNRAS, 473, 3000

Zhu L., et al., 2022, A&A, 664, A115

Zhu K., et al., 2023, MNRAS, 522, 6326

de Fontenelle B. L. B., Gardiner W., 1715, Conversations on the plurality of worlds.

de Jong J. T. A., et al., 2013, Experimental Astronomy, 35, 25

de Vaucouleurs G., 1948, Annales d'Astrophysique, 11, 247

de Vaucouleurs G., 1959, Handbuch der Physik, 53, 275

de Zeeuw T., 1985, MNRAS, 216, 273

de Zeeuw T., Franx M., 1989, ApJ, 343, 617

de Zeeuw T., Franx M., 1991, ARA&A, 29, 239

de Zeeuw P. T., et al., 2002, MNRAS, 329, 513

van Dokkum P. G., 2005, AJ, 130, 2647

van de Sande J., et al., 2017a, MNRAS, 472, 1272

van de Sande J., et al., 2017b, ApJ, 835, 104

van de Sande J., et al., 2018, Nature Astronomy, 2, 483

van de Sande J., et al., 2019, MNRAS, 484, 869

van de Sande J., et al., 2020, arXiv e-prints, p. arXiv:2011.08199

van de Sande J., et al., 2021a, MNRAS, 505, 3078

van de Sande J., et al., 2021b, MNRAS, 508, 2307

van de Sande J., et al., 2024, in Tabatabaei F., Barbuy B., Ting Y.-S., eds, IAU Symposium Vol. 377, Early Disk-Galaxy Formation from JWST to the Milky Way. pp 27–33 (arXiv:2306.00059), doi:10.1017/S1743921323001138

van de Ven G., et al., 2006, A&A, 445, 513

van de Ven G., et al., 2010, ApJ, 719, 1481

van den Bergh S., et al., 1996, AJ, 112, 359

van den Bosch R. C. E., et al., 2008, MNRAS, 385, 647

van der Marel R. P., Franx M., 1993, ApJ, 407, 525